Physics of Atomic Nuclei, Vol. 66, No. 3, 2003, pp. 423–434. From Yadernaya Fizika, Vol. 66, No. 3, 2003, pp. 451–462.

NEW PHYSICS BEYOND THE STANDARD MODEL

Puzzles in Astrophysics in the Past and Present*

V. S. Berezinsky[1)]

Istituto Nazionale di Fisica Nucleare, Laboratori Nazionali del Gran Sasso, Assergi, Italy

Received February 13, 2002

Abstract—About 400 years have passed since the great discoveries by Galileo, Kepler, and Newton, but astronomy still remains an important source of discoveries in physics. They start with puzzles, with phenomena difficult to explain, and phenomena which in fact need new physics for explanation. Do such puzzles exist now? There are at least three candidates: absence of absorption of TeV gamma radiation in extragalactic space (violation of Lorentz invariance?), absence of GZK cutoff in the spectrum of ultrahigh-energy cosmic rays (new particle physics?), tremendous energy (up to 10^{54} erg) released in gamma ray bursts on a time scale of a second (collapsing stars or sources of a new type?). Do these puzzles really exist? A critical review of these phenomena is given. © *2003 MAIK "Nauka/Interperiodica"*.

1. INTRODUCTION

Not many good things fall down on us from the sky, but discoveries do. Below, I will give a short list of astrophysical discoveries of the last four decades, separating intuitively astrophysics from cosmology.

Quasars were discovered in the early 1960s as compact radio sources. In 1960, Mathews and Sandage identified radio source 3C48 with a stellar-like object. In 1963, Schmidt deciphered the optical spectrum of quasar 3C273 assuming its redshift, $z = 0.158$. Surmounting resistance of skeptics, this explanation moved the source to the distance of 630 Mpc and made its luminosity uncomfortably large, $L \sim 10^{46}$ erg/s. This puzzling energy release resulted in the long run in the discovery of a black hole, an object of general relativity.

Pulsars were discovered first in 1967 by a student of A. Hewish, Jocelyn Bell. She observed a puzzling periodicity of radiopulses from an unknown source. After a short but intense discussion of different possible sources, including extraterrestrial civilizations and little green men, magnetized rotating neutron stars, pulsars, were found to be responsible. It opened a new field of cosmic physics: relativistic electrodynamics.

The atmospheric neutrino anomaly and the solar neutrino problem went along the most difficult road to the status of discovery. The puzzling phenomenon in both cases was a neutrino deficit as compared with calculations. But skepticism of the community, especially in the case of the solar neutrino problem, was strong. Pushed mostly by Davis and Bahcall, the solar neutrino problem moved like a slow coach along a road two decades long. Fortunately, physics differs from democracy: the opinion of the majority means usually less than that of one. These two obscure puzzles have turned (or have almost turned) into discovery of the most fascinating phenomenon, neutrino oscillations.

Supernova SN 1987a became an elementary-particle laboratory in the sky for the study of properties of neutrinos, axions, majorons, etc. Detection of neutrinos [1] became a triumph of the theory: the number of detected neutrinos, duration of the neutrino pulse, and estimated neutrino luminosity turned out to be in agreement with theoretical prediction. Gravitational collapse as a phenomenon providing the SN explosion was confirmed.

However, some puzzles remain. The presupernova is a blue supergiant, not a red one as the theory of stellar evolution prescribes. But what is more puzzling is rotation. The asymmetric ring around SN 1987a implies that the presupernova was a rotating star (it would be a surprise if not!). But the striking agreement of neutrino observations with calculations was obtained for a nonrotating presupernova. Inclusion of rotation in calculations is a very difficult task. The simplified calculations [2] demonstrate that rotation changes the predictions dramatically: the temperature of the neutrinosphere decreases by a factor of 2, the total energy of the emitted neutrinos becomes six times smaller, and the number of detected neutrinos should be an order of magnitude smaller.

False discoveries often have a greater impact on physics than true ones.

*This article was submitted by the author in English.

[1)]and Institute for Nuclear Research, Russian Academy of Sciences, pr. Shestidesyatiletiya Oktyabrya 7a, Moscow 117312 Russia; E-mail: berezinsky@lngs.infn.it

1063-7788/03/6603-0423$24.00

At the end of the 1960s and the beginning of the 1970s, it was found by using long-baseline interferometry that in some cases gas clouds in quasars and radiogalaxies had velocities exceeding the speed of light by a factor of 4–10. In fact, the measured velocity was a projection of the velocity on the plane perpendicular to the line of view. Accurately written in relativistic mechanics, this (apparent) velocity is

$$v_{\rm app} = v \sin\theta \left[1 - \frac{v}{c}\cos\theta\right]^{-1}. \qquad (1)$$

Provided by the ultrarelativistic velocity of an object $v \sim c$, the apparent velocity can exceed the speed of light. Astrophysics of relativistic objects, now a subject of university courses, was born.

The Cyg X-3 saga is a story of a different kind. Cyg X-3 is a galactic binary system well studied in all types of radiations, most notably in x rays. In the 1980s, many EAS (extensive air showers) arrays detected a periodic 4.8-h gamma-ray signal from it in the VHE (very high energy, $E \geq 1$ TeV) and UHE (ultrahigh energy, $E \geq 0.1$–1 PeV) ranges. The list of these arrays included Kiel, Haverah Park, Fly's Eye, Akeno, Carpet-Baksan, Tien Shan, Platey Rosa, Durham, Ooty, Ohya, Gulmarg, Crimea, Dugway, Whipple, and others. Probably, it is easy to say that there was no single EAS array which claimed no-signal observation. Additionally, some underground detectors (Nusex, Soudan, MUTRON) marginally observed a high-energy muon signal from the direction of this source. Apart from the Kiel array, which claimed a 6σ signal, the confidence level of detection was not high (3–4σ). In 1990–1991, two new-generation detectors, CASA-MIA and SYGNUS, put a stringent upper limit to the signal from Cyg X-3, which excluded early observations.

Apart from two lessons—(i) good detectors are better than bad ones and (ii) 3σ discoveries should not be trusted even if many detectors confirm them—experience of Cyg X-3 has taught us how to evaluate statistical significance in searching for periodic signals.

The false discovery of high-energy radiation from Cyg X-3 had a great impact on theoretical high-energy astrophysics, stimulating study of acceleration in binary systems, production of high-energy gamma and neutrino radiation and creation of high-energy astrophysics with new particles, such as light neutralinos and gluinos.

2. VIOLATION OF LORENTZ INVARIANCE

Violation of Lorentz Invariance (LI) is often suspected in astrophysics because of large Lorentz factors sometimes being involved. Before describing these suspicions, we will discuss the aesthetic side of the problem: Is there an aesthetically attractive theory with broken LI?

Breaking of LI, even extremely weak, leads to existence of the absolute Lorentz frame. This is a qualitative difference between the two theories. Absence of continuous transition from one theory to another looks disturbing. Lorentz invariance is a basic principle for building a Lagrangian for any interaction. How is it possible to abandon it?

All questions raised above disappear in spontaneously broken LI. Equations of motion remain Lorentz-invariant. The violation occurs spontaneously in the solutions. Lagrangians for all interactions are constructed as Lorentz scalars and spontaneous LI breaking occurs due to nonzero values of field components in vacuum states. Breaking of LI can be made arbitrarily small, and all physical effects accompanied by LI breaking are small too. The absolute Lorentz frame exists, but all physical effects, which distinguish it from other frames, are small, and thus all frames are nearly equivalent, similar to the Lorentz-invariant theory.

2.1. Spontaneously Broken Lorentz Invariance

Lorentz invariance is spontaneously broken when the time component of the vector or tensor field obtains a nonzero value. The necessary condition for the phase transition to such a configuration is existence of a potential minimum at this value. Such a condition can be fulfilled only in some exceptional cases, e.g., in superstring theories [3] and in some specific D-brane models with extra dimensions [4, 5]. The interactions responsible for such a potential minimum usually do not appear in conventional four-dimensional renormalizable theories.

Consider for example the Lorentz-invariant interaction of a superheavy tensor field $T_{\mu\nu\ldots}$ with an ordinary field described by spinor ψ. If, for example, string interactions set nonzero vev for the time components of this tensor field, the interaction term considered is reduced to a term that explicitly breaks LI [6]:

$$\mathcal{L}_{\rm int} = \frac{\epsilon}{M^k} v_k \bar{\psi} \Gamma (i\partial_0)^k \psi, \qquad (2)$$

where $v_k = \langle T_{00\ldots} \rangle$ is vev, Γ is build from γ's, ϵ is a dimensionless constant, and M is a superstring mass scale. Such an LI-breaking term modifies the dispersion relation for a particle ψ and results in astrophysical consequences [7]. We shall give here a simple example of spontaneous LI breaking accompanied by modification of the dispersion relation for an ordinary particle. Let us consider the Lagrangian for an ordinary spinor particle

$$\mathcal{L} = i\bar{\psi}\gamma_\mu \partial_\mu \psi - m\bar{\psi}\psi + \mathcal{L}_{\rm int}, \qquad (3)$$

where interaction with the superheavy field $T_{\mu\nu}$ is described by

$$\mathcal{L}_{\rm int} = \frac{\epsilon}{M^2} T_{\mu\nu} \bar{\psi} \gamma_\mu \partial_\nu \psi. \quad (4)$$

After spontaneous symmetry breaking $\langle T_{00} \rangle = v^2$, the associate Klein–Gordon equation [8] for a noninteracting particle can be readily obtained as

$$\left(\partial_\mu^2 + m^2 - \frac{\epsilon}{M^2} v^2 E^2 \right) \psi = 0. \quad (5)$$

The corresponding dispersion relation is

$$p_\mu^2 - m^2 + \frac{\epsilon}{M^2} v^2 E^2 = 0. \quad (6)$$

2.2. Modified Dispersion Relations and Threshold of Reactions

In astrophysical applications, one often considers a collision of a very high energy particle with a low-energy particle from background radiation. This is the case of absorption of TeV gamma radiation on infrared photons and the so-called Greisen–Zatsepin–Kuzmin (GZK) [9] cutoff, when a very-high-energy proton collides with a microwave photon, producing a pion. The threshold of such reactions is determined by the momentum of the particle in the center-of-mass system, which has a very large Lorentz factor in the laboratory system. At large Lorentz factors, i.e., at large energy of one of the colliding particles in the laboratory system, the dispersion relation is modified and affects the threshold of the reaction in the laboratory system.

Let us consider this effect in the $\gamma + \gamma \to e^+ + e^-$ collision when one photon has large energy E_γ and the other has small energy ϵ_γ. Conservation of energy and momentum requires

$$(k_\mu + k'_\mu)^2 = (p_\mu + p'_\mu)^2, \quad (7)$$

where k_μ and p_μ are the 4-momenta of the photon and the electron, respectively, and their 4-momenta after collision are shown by primes. In the LI case, $k_\mu^2 = k_\mu'^2 = 0$ and $p_\mu^2 = p_\mu'^2 = m_e^2$, and energy–momentum conservation requires

$$\sqrt{E_\gamma \epsilon_\gamma} > m_e \quad (8)$$

as the threshold condition. In the case of the modified dispersion relation, $p_\mu^2 = E_e^2 - \mathbf{p}_e^2 \approx m_e^2 + \epsilon v^2 E^2 / M^2$, as in [6], and the threshold shifts towards higher energies in the laboratory system.

2.3. Astrophysical Tests of Special Relativity

The GZK cutoff involves Lorentz transformations with the Lorentz factor $\Gamma \sim m_\pi / \epsilon_\gamma \sim 10^{11}$, where m_π is the pion mass and $\epsilon_\gamma \sim 10^{-3}$ eV is a typical energy of the microwave photon participating in the photopion reaction. It gives the largest Lorentz factor presently known, up to which LI can be tested. Such a test and proposal to explain the absence of the GZK cutoff in the experimental data were first suggested by Kirzhnitz and Chechin [10] in 1971 and later in [7, 11–13].

Another similar process is absorption of TeV gamma radiation on IR background photons. It will be considered in more detail in the next section. There are some other astrophysical processes where LI can reveal itself. They are constancy of the velocity of light [14], vacuum Cherenkov radiation [12], vacuum Faraday rotation [12], and high-energy photon decay [12].

3. TeV GAMMA-RAY CRISIS?

Propagating through the space filled by IR background radiation, TeV photons are absorbed in $\gamma + \gamma_{\rm IR} \to e^+ + e^-$ collisions. A photon with energy E_γ is absorbed by IR photons with wavelengths shorter than

$$\lambda_{\rm IR} \approx \frac{E_\gamma}{4 m_e^2} = 1.2 \frac{E_\gamma}{1\ {\rm TeV}}\ (\mu{\rm m}). \quad (9)$$

Thus, photons with energies of 1–20 TeV are absorbed on IR background radiation with wavelengths $1 \le \lambda_{\rm IR} \le 20\,\mu$m. For this wavelength range, there are both direct measurements and detailed calculations.

The DIRBE instrument [15] (diffuse infrared background experiment) on the COBE spacecraft measures IR diffuse radiation in the band from 1.25 to 240 μm. The measured fluxes are shown in Fig. 1. Note that the measured flux is very close to that produced by interplanetary dust and, after subtraction of this major component, the residual is about a factor of 20 smaller.

The data of another COBE instrument, FIRAS (far-infrared absolute spectrometer) in the range 125–2000 μm are consistent [16] with DIRBE at overlapping frequencies. An estimate of the intergalactic diffuse IR flux from integrating the 15-μm count of IR sources at ISOCAM [17] is also consistent with the DIRBE data. However, a count of sources is always incomplete, and thus the ISOCAM flux at 15 μm can be considered as a lower limit.

The diffuse IR flux was calculated in many works, most notably in two recent works [18, 19] (see the references to early calculations there). In [18], a

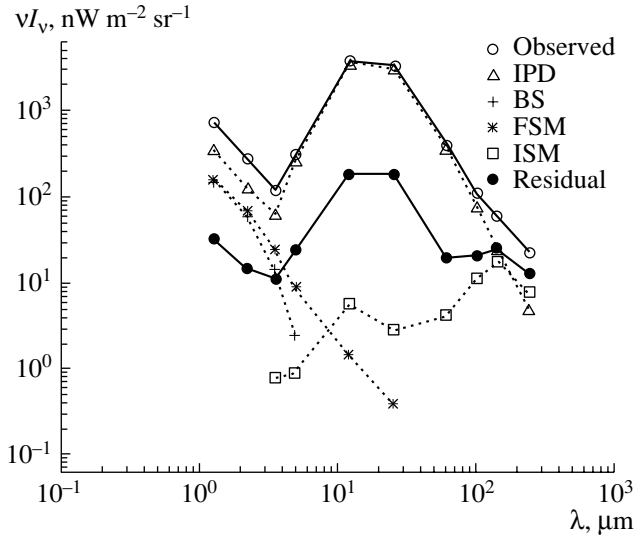

Fig. 1. IR diffuse spectra as measured by DIRBE–COBE in the range 1.25–240 μm (from [15]). The extragalactic diffuse flux, shown by filled circles, is obtained by subtraction of contributions due to interplanetary dust (IPD) shown by triangles, bright galactic sources (BS) shown by crosses, and others.

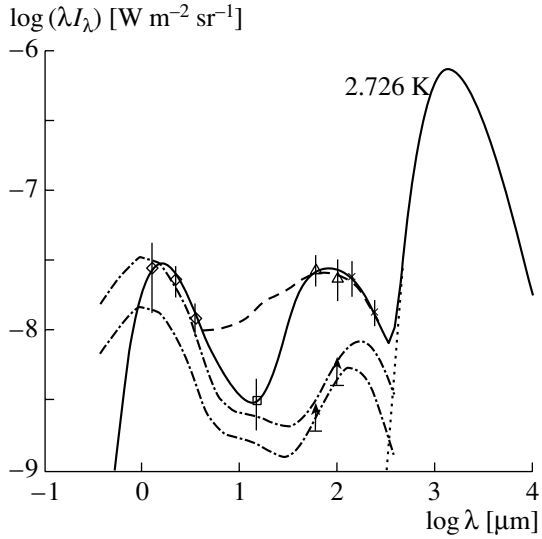

Fig. 2. Intergalactic diffuse IR fluxes [20]. The data points are from DIRBE (diamonds), ISOCAM (square), and FIRAS (crosses). These data can be described by a solid curve or by a dashed curve. Two theoretical curves (dash-dotted ones) have emerged from the calculations by Malkan and Stecker [18].

semiempirical method is used, while calculations of [19] are based on galaxy-formation models. A feature common to both calculations is a bimodal frequency distribution. A peak at about 1 μm is direct radiation during the star-formation epoch, and a second peak at about 100 μm is due to dust reradiating the starlight at lower frequencies. It could be (Fig. 2) that observational data confirm this feature. Both calculations give the IR flux lower than that of DIRBE. The results of observations and comparison with calculations are given in Fig. 2 taken from [20].

As was discussed above, the gamma radiation with energy 1–10 TeV is absorbed by IR radiation in the range 1–10 μm. A gamma-ray source with relevant properties is a nearby blazar Mrk 501. This powerful TeV source is located at a suitable distance 155 Mpc ($z = 0.0336$), and its measured spectrum extends from 400 GeV up to 24 TeV without noticeable steepening. However, the expected absorption at the end of the spectrum is appreciable, and to have the observed spectrum without a cutoff, the production ("corrected") spectrum must be unnatural, as is shown in Fig. 3 from [20]. In fact, this unnatural increase in the production spectrum corresponds to the spectrum cutoff if the production spectrum is smooth. The cutoff appears when a path length decreases with energy, as happens when the density of target photons increases with the wavelength λ. This is the case of dependence of the IR flux on λ presented in Fig. 2.

If the IR flux is taken according to the theoretical calculations [18, 19], the TeV gamma-ray crisis disappears. In Fig. 4, the observed spectrum Mrk 501 in the flaring state (low curve) is given together with the production spectrum (upper curve). The absorption in intergalactic space is taken according to the IR flux calculated by the authors of [18] in one of their models. The source spectrum is quite natural with no indication of the crisis. Similar calculations were made in [21]. The source (production) spectrum of TeV radiation from Mrk 501 was calculated from the observed spectrum by using the theoretical IR flux, according to the LCDM model of [19]. The production spectrum is found to be natural.

In conclusion, the TeV gamma-ray crisis does not look dramatic. It could be that the IR flux measured by DIRBE is slightly overestimated due to incomplete subtraction of galactic or interplanetary components. The frequency dependence of the flux plays a crucial role. The spectrum cutoff appears if the flux increases with λ sharply enough. If the ISOCAM point in Fig. 2 is in fact a lower limit, the frequency dependence of the IR flux can be smooth (as the dashed curve shows), and the sharp cutoff is absent. It could also be that steepening in the TeV gamma-ray spectrum will be discovered.

At present, there is no need to involve LI breaking for solving this problem. A clear test of Lorentz invariance can be done with the help of radiation for which the density of target photons and their energy spectrum are reliably known. This case is given by 2.7-K radiation. As Fig. 2 shows, at the wavelength

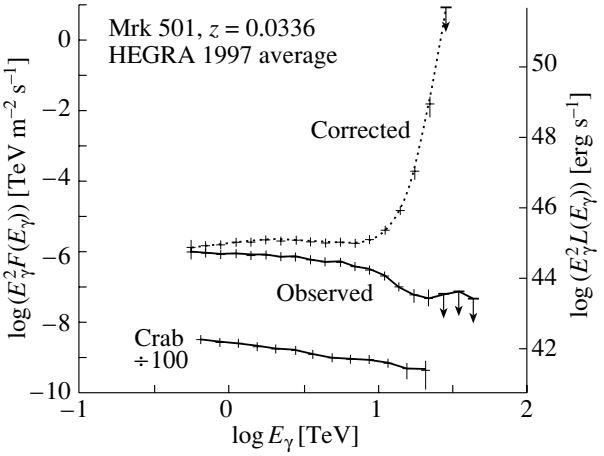

Fig. 3. Production ("corrected") spectrum for Mrk 501 calculated [20] from the observed spectrum and with $\gamma\gamma$ absorption taken into account. Unnaturalness of the production spectrum is illustrated by luminosity shown on the right-hand axis.

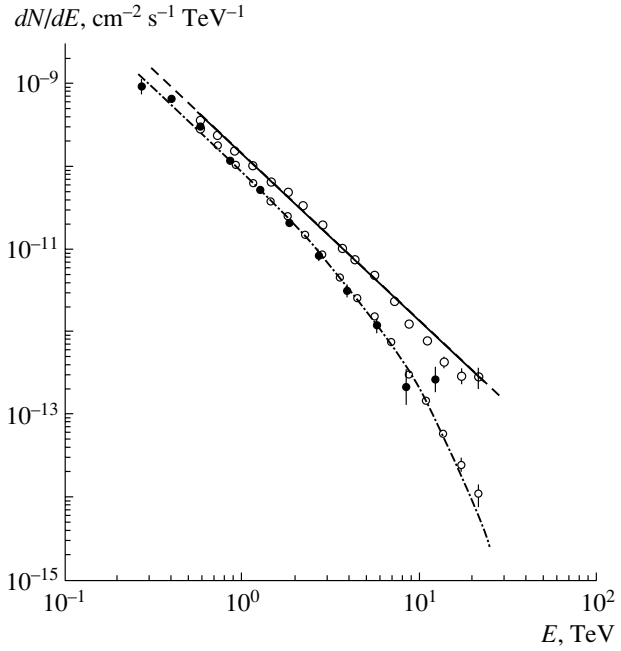

Fig. 4. Observed (lower curve) and production (upper curve) spectra of TeV gamma radiation for Mrk 501 (from [18]). The production spectrum is calculated using the absorption on IR radiation with the flux calculated in one of the models of [18].

$\lambda \sim 300$ μm, there is a sharp increase in the photon density with λ, which results in the cutoff of the gamma-ray spectrum at $E_\gamma \sim 250$ TeV. Absence of such a cutoff for a source with known distance to our galaxy (redshift) can be explained only by LI breaking.

4. UHECR: HOW SERIOUS IS THE PROBLEM?

The problem with ultrahigh-energy cosmic rays (UHECR) consists in observation of particles with very high energies, up to $(2–3) \times 10^{20}$ eV, while ordinary signal carriers such as protons, nuclei, electrons, and photons have a small path length in intergalactic space. UHE protons lose energy due to production of pions in collisions with microwave photons, and their spectra should have a steepening (GZK cutoff [9]) that starts at $E \sim 3 \times 10^{19}$ eV. UHE nuclei lose energy due to e^+e^- pair production in collisions with microwave photons [22]. Electrons lose their energy very fast by microwave radiation. UHE photons are absorbed on the extragalactic radio background [23].

UHE particles are observed by EAS produced in the atmosphere. Doubts in existence of the UHECR problem are usually expressed in the form of two questions: Are energies measured correctly? Could the sources of UHECR be located nearby, e.g., in our Galaxy or at a small distance from it? I will address these questions below and analyze the status of the UHECR problem.

4.1. Energy Determination

The energy of a primary particle is determined by measuring some characteristics of EAS (for a review see [24]). The methods are different and agree for determination of UHE energies within 20–30%. The error in energy determination is estimated at 15–20% for the good events. The most traditional method of energy measurement is based on the relation between the cascade particle density at a distance of 600 m from the shower axis and the primary energy E. This method (ρ_{600}) was first suggested by Hillas [25] and later confirmed by many Monte Carlo simulations. It was demonstrated that this relation depends slightly on the EAS development model and on chemical composition of the primaries. The density fluctuations also have a minimum at a distance of 600 m from the core. For UHE EAS, this relation between ρ_{600} and the primary energy has been confirmed by calorimetric measurements at Yakutsk for energies up to 4×10^{18} eV. The ρ_{600} method was used in the Haverah Park, Yakutsk, and AGASA arrays. In the case of Haverah Park, the ρ_{600} signal is given by energy release in water Cherenkov detectors.

The Fly's Eye array detects fluorescence light produced by EAS in the atmosphere. The intensity and arrival time of fluorescent radiation to the collecting mirrors allow one to reconstruct the longitudinal development of EAS in the atmosphere, and the primary energy is thus obtained practically calorimetrically.

In two cases, the primary energy was measured very reliably.

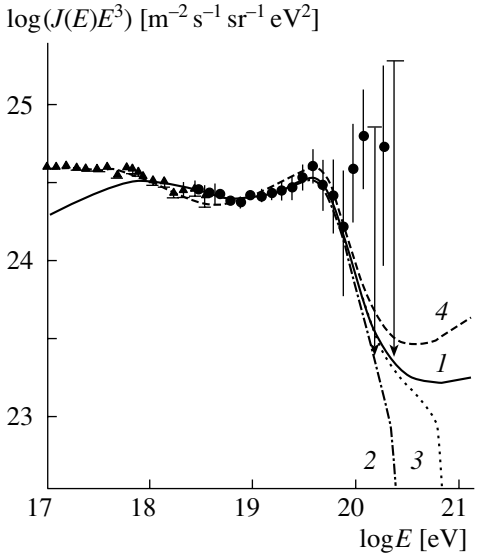

Fig. 5. Calculated diffuse spectra [29] for the uniform distribution of UHECR sources in the Universe in the case of cosmological evolution of the sources (curve *4*) and without evolution (curves *1–3*). The latter are given for different cutoff energies in the production spectra $E_{\max} = \infty, 3 \times 10^{20}$, and 1×10^{21} eV for curves *1, 2,* and *3,* respectively (see also [30]).

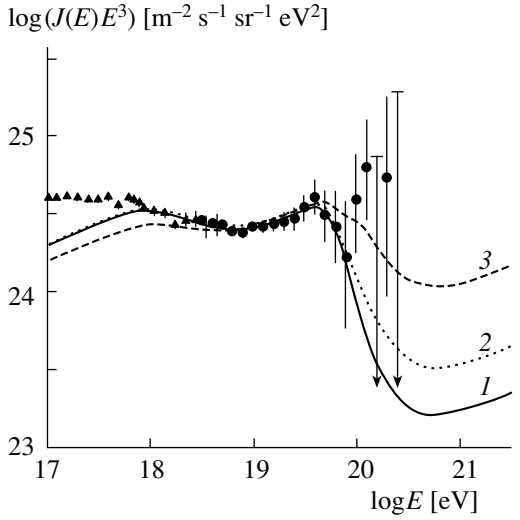

Fig. 6. Diffuse energy spectra with local overdensity of UHECR sources. Curves *1, 2*, and *3* are given for the uniform distribution of the sources and for overdensity $n/n_0 = 2$ and 10, respectively. The linear size of the overdensity region is 30 Mpc.

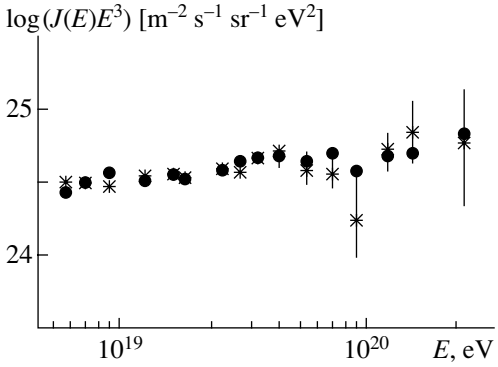

Fig. 7. Energy spectrum of UHE iron nuclei of galactic origin according to the simulation [40] for the generation spectrum with $\gamma_g = 2.3$. Black circles show the calculated flux (*ad hoc* normalization); stars are the AGASA data.

The Fly's Eye detector had an event [26] with a very accurately measured longitudinal profile, and the primary energy was found to be $E = (3^{+0.36}_{-0.54}) \times 10^{20}$ eV. This is the highest energy event.

The AGASA array detected [27] a shower with the core in the dense part of the array, Akeno. The lateral distribution of cascade particles, including muons, was measured in the total range of distances from the core up to 3 km. The primary energy is estimated to be in the range $(1.7–2.6) \times 10^{20}$ eV.

The total number of detected showers with energy higher than 1×10^{20} eV is about 20. A skeptic, taking an event after an event, could doubt the energy of some of them, but even in the most critical analysis, several of them survive as cases with energy higher than 1×10^{20} eV. It is already enough to claim existence of the problem.

4.2. What Is the GZK Cutoff?

The Greisen–Zatsepin–Kuzmin cutoff [9] is caused by interaction of high-energy protons with microwave (2.73 K) radiation. At an energy of 3×10^{19} eV, the total energy loss of the proton starts sharply (exponentially) increasing with energy due to pion production $p + \gamma_{2.7\text{-K}} \to N + \pi$. The exponential character of this increase is caused by the fact that production of pions needs photons from the high-energy tail of their distribution, and the number of these photons exponentially increases when the proton energy becomes higher. A similar phenomenon occurs for nuclei Z, but the relevant process is pair production, $Z + \gamma_{2.7\text{-K}} \to Z + e^+ + e^-$ [22]. If a source is at a large distance, this process causes the cutoff in the observed spectrum. Numerically, the energy of this cutoff is usually given for a model where sources are distributed uniformly in extragalactic space. In this case, the cutoff starts at $E = 3 \times 10^{19}$ eV and the flux becomes half of its power-law extrapolation at $E_{1/2} = 5.3 \times 10^{19}$ eV (for these and other details of energy losses and absorption of different kind of primaries, see [28]).

In Fig. 5, the calculated spectra of protons are

displayed for a model where the sources are distributed uniformly in the Universe with cosmological evolution of the sources (curve *4*) and without it (curves *1–3*). The evolutionary case is given for the generation spectrum with the spectral index $\gamma_g = 2.45$ and with evolution described as $(1+z)^m$ with $m = 4$. The case without evolution, $m = 0$, is presented for the power-law generation spectrum with the index $\gamma_g = 2.7$ and with different cutoffs of generation spectra described by the maximal energies $E_{\max} = 3 \times 10^{20}$, 1×10^{21} eV, and ∞ [29]. The calculations are compared with the recent AGASA data. The GZK cutoff in the calculated spectra is clearly seen, in contrast to the observed spectrum.

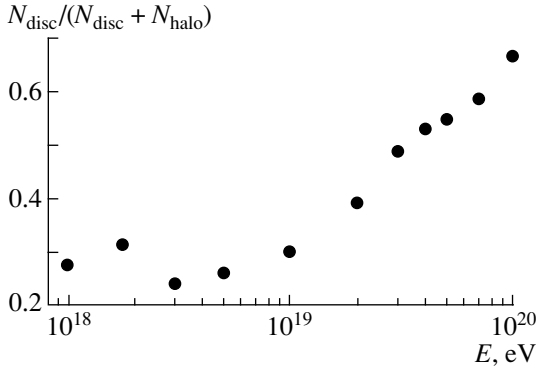

Fig. 8. Disc anisotropy of UHE iron nuclei according to the simulation [40].

4.3. Extragalactic UHECR from Astrophysical Sources

An often asked question is: There could be a few extragalactic sources so close to us that the observed spectrum does not suffer the GZK cutoff, so what is the problem then?

The problem is the low-energy part of the spectrum. It is formed by sources at large distances, and because of the GZK cutoff these sources do not contribute to the high-energy part of the observed spectrum. One must specify his assumption about the distribution of sources in the Universe, and the uniform distribution is the simplest one.

The GZK cutoff shifts to higher energies and becomes softer if the population of the sources has local (within 30–50 Mpc) overdensity (for early calculations see [31], described in [28]). The count of galaxies show local overdensity with the factor ~ 2 within the local supercluster. Since overdensity is a gravitational phenomenon, one must expect similar overdensity for all galaxy-like sources of UHECR, i.e., ones with acceleration by stars, AGN, and other intragalactic objects. In Fig. 6, the spectra of UHECR are shown for three cases: uniform distribution of the sources (curve *1*), distribution with local overdensity $n/n_0 = 2$ within the radius $R = 30$ kpc, and distribution with local overdensity $n/n_0 = 10$ within the radius $R = 30$ kpc. The calculations of the spectra for the observed distribution of galaxies were performed in [32]. From Fig. 6, one can see that, to reconcile the data with the observations, the overdensity of the sources must be considerably larger than that observed for the galaxies. This disfavors the idea. Another possibility of making the GZK cutoff less pronounced is given by the one-source model.

Let us assume that there are a few sources of UHECR in the Universe and by chance our Galaxy is located near one of them. In this case, the GZK cutoff is absent, but the price to be paid is anisotropy. In an early work [33], the Virgo cluster was considered as such a source, and the cutoff energy and anisotropy were reconciled assuming diffusive propagation of UHE particles. With new data on particle energies and anisotropy, this model is excluded. An interesting revival of this idea was suggested in [34]. Particles generated in the M87 galaxy in the Virgo cluster are propagating almost rectilinearly and are focusing to the Sun by the galactic magnetic field. It provides arrival at the Sun from different directions in agreement with absence of large anisotropy. Quasi-rectilinear propagation from Virgo provides absence of the GZK cutoff. A model of a nearby source with nonstationary diffusion was suggested [35].

4.4. Galactic Origin of UHECR

UHECR have no GZK cutoff in the case of their galactic origin. Starting with Syrovatsky [36], the galactic origin of UHECR was advocated in many works (see, for example, [37–39]). Observational data are in favor of pure proton composition at the highest energies. As numerous simulations show, the galactic magnetic field cannot confine UHECR in the Galaxy if they are protons. It is more difficult to draw a conclusion that they are the heaviest (iron) nuclei. We shall present here results of the simulation of propagation of UHE particles in our Galaxy [40] with conclusions concerning the iron nuclei as primaries.

The model is similar to the one used in [41]. The disc with UHECR sources is surrounded by an extended spherical halo with a radius that varies from 15 to 30 kpc. The magnetic field in the disc has a spiral structure with spiral arms and is given by a complicated analytic expression that fits observational data. The field is dominated by the azimuthal component. The thickness of the magnetic disc is 0.4 kpc. The magnetic field in the halo is taken according to the theoretical model [42] and is described by complicated analytic formulas (see also [41]). The flux of

UHE particles from a given direction is calculated in the following way. An antiparticle with energy E is emitted in this direction, and its trajectory is followed step by step until its exit from the halo. The particle can cross the disc several times due to deflection by the magnetic field in the halo. The intensity in the given direction is proportional to the total time T_d that a particle spends in the disc. The energy spectrum is given by the product of the generation spectrum $KE_g^{-\gamma_g}$ and $T_d(E)$. The calculated spectrum with $\gamma_g = 2.3$ is shown in Fig. 7 in comparison with the AGASA data. One can see excellent agreement.

However, the real problem is given by anisotropy. In Fig. 8, the disc anisotropy is calculated as the ratio of the flux from the direction of the disc to the total flux. At energy $E \geq 4 \times 10^{19}$ eV, the calculated anisotropy exceeds the observed value.

4.5. New Physics

Although is not yet excluded, the astrophysical solution to the UHECR problem is strongly disfavored. We shall briefly describe here the elementary-particle solutions without giving references (for a review of elementary-particle solutions see [43]).

Superheavy Dark Matter. Long-lived superheavy dark matter particles are accumulated in galactic halos. These particles are naturally produced in the postinflationary epoch and can close the Universe or contribute some fraction to cold dark matter. These particles can be long-lived, with the lifetime exceeding the age of the Universe. Decays of these particles produce UHECR without the GZK cutoff (most of the UHE particles come from the galactic halo). The dominant component is photons.

Topological Defects (TD). There are different mechanisms of production of UHE particles by TD. In some cases, TD become unstable and decompose into constituent fields (superheavy Higgs and gauge bosons), which then decay into ordinary particles. This mechanism works for cusps and superconducting cosmic strings. In the case of monopoles and antimonopoles connected by strings, high-energy particles are produced upon annihilation of monopole–antimonopole pairs. The most promising candidates are necklaces and monopole–antimonopole pairs connected by strings. UHECR from TD has a spectrum with a soft GZK cutoff that does not contradict observations.

Resonant neutrinos. Very high energy neutrinos are resonantly absorbed by target neutrinos comprising hot dark matter (HDM): $\nu + \bar{\nu}_{\rm HDM} \to Z^0 \to$ hadrons. In the case where HDM neutrinos have locally enhanced density, the GZK cutoff is absent or softened. A very large flux of primary neutrinos with superhigh energies is needed for this hypothesis.

Light gluino. Light gluinos can be effectively produced by TD or in pp collisions in astrophysical sources. They weakly degrade in energy, interacting with microwave radiation. The interaction of the UHE light gluino with nucleons is similar to that of the UHE proton. The light gluino is disfavored by accelerator experiments.

Strongly interacting neutrino. In extradimensional theories, for example, the neutrino can have a large cross section of scattering off the nucleon. In this case, the neutrino can be a carrier of the UHE signal from remote astrophysical sources.

Lorentz invariance breaking. In this case, for protons with energies of 10^{20} eV and higher, the c.m. energy could not be enough for production of pions in collisions with microwave photons (see Section 2).

5. MYSTERY OF GRB ENGINE

Gamma-ray bursts (GRBs) strike our imagination. On the one hand, the tremendous energy release up to 2×10^{54} erg during a short time on the order of a few seconds within a volume on the order of the Moon implies a catastrophic event in the Universe. On the other, we observe them once a day. All observed characteristics of GRBs vary within a very wide range, fluences vary within 10^{-8}–10^{-4} erg/s, durations vary from a few milliseconds up to a few thousand seconds, and energy releases vary from 10^{50} to 10^{54} erg in the case of isotropic radiation. It is very plausible that there are several types of GRBs of different origin. In particular, short bursts, shorter than 1 s, and long bursts form two distinctive groups of GRBs.

The mechanism of radiation in GRBs is well understood. The unknown compact GRB engine explosively produces a fireball expanding in the surrounded plasma. An important parameter that determines the hydrodynamic expansion is the inverse baryon content η of the initial fireball, which is given by the relation $\eta = \mathcal{E}_{\rm GRB}/M_b c^2$, where $\mathcal{E}_{\rm GRB}$ is the total energy of the GRB and M_b is the baryonic mass. The value of η gives the Lorentz factor of the fireball at the stage of saturation, which follows the acceleration stage of expansion.

Electrons accelerated in the fireball by multiple internal shocks and external and reversed shocks produce soft gamma-ray radiation by the synchrotron mechanism. When the external shock starts decelerating, the synchrotron emission of electrons occurs in the x-ray and optical range. This is the so-called afterglow radiation.

For most of the GRBs, the host galaxies are not found. This could be explained by a large error box determined for GRBs and by weakness of host galaxies. Only in 1996 did Beppo-SAX discover the first

host galaxy due to afterglow radiation. Since that time, the host galaxies were reliably found for more than 20 GRBs. All galaxy-hosted GRBs have long durations and are located at large distances.

The Beppo-SAX discovery gave us a clear indication of the location of the sources: at least some of them (and maybe all) are galactic objects. For astrophysical objects, the greatest energy release is given by gravitational collapse. In principle, energy release at the collapse can reach 29% of the collapsed mass in the case of a black hole with maximal rotation. It gives $\sim 1 \times 10^{54}$ erg for a collapse of 1 $M_\odot$ stellar core, but it is difficult to imagine that all this energy can be transferred to a GRB.

Strong beaming can solve the energy problem, and this beaming looks like an inevitable element of any realistic astrophysical model of the GRB engine.

Moderate beaming is a common feature observed, e.g., in AGNs and miniquasars in our Galaxy, e.g., SS433, but it is hard to imagine a model of a collapsar with a beaming factor, e.g., $\sim 10^{-2}$–10^{-3}. As Blandford said [44]: "Are GRBs beamed? ... The argument that the bursts must be beamed, otherwise they would have energies in excess of stellar rest mass, reminds me of a similar argument in favor of them being local!"

Although general principles allow collapsars as GRB engines with required energy release up to $\mathcal{E}_{\rm GRB} \sim 10^{54}$ erg, there are no models which practically realize this possibility. We shall describe briefly four recent collapsar models for GRB engines.

The most elaborated model is a binary neutron star merger, NS–NS, or a similar binary system of a neutron star and a black hole, NS–BH. This was first suggested in [45]; for the recent calculations and references, see [46]. Merging of two NSs or an NS and BH results in collapse with emission of neutrinos. The latter annihilate, $\nu + \bar{\nu} \to e^+ + e^-$, producing a relativistically expanding fireball. Numerical simulations [46] give the total energy of neutrinos in the burst of $\sim 3 \times 10^{52}$ erg, but the annihilation efficiency is very low (1–3%). Apart from the small total energy $\mathcal{E}_{\rm GRB} \sim 10^{51}$ erg, this model predicts a very short burst duration $\tau \leq 0.1$ s, which corresponds to a small fraction of the observed GRBs.

The second model [47], "failed SN," starts with the collapse of a single rotating Wolf–Rayet star. As the core of this star collapses, it accretes gas from the mantle. Neutrinos interact with the accretion disc, producing a fireball. The total energy transferred to the fireball is estimated as $E_{\rm GRB} \sim 10^{51}$ erg. One cannot expect large beaming in this model. Duration of the bursts is rather short, less than 10 s. The model predicts too large a baryon contamination, in contradiction with the hydrodynamic part of the model. This model is based on the estimates and should be called a scenario.

The two models described above use neutrino radiation, which has a low efficiency of conversion into fireball energy. An interesting collapse scenario (hypernova) without involving neutrinos was suggested in [48]. A massive black hole with mass $M_{\rm BH} \sim 10 M_\odot$ is produced at the end of the evolution of a single star. It has a superstrong magnetic field $B \sim 10^{15}$ G and fast rotation corresponding to rotational energy $E_{\rm rot} \sim 5 \times 10^{54}$ erg. The magnetic field by its pressure expels the outer shell. A small fraction of it moving in the region with decreasing density is accelerated to relativistic velocities by the Colgate mechanism. The hypernova scenario does not need narrow beaming and predicts large GRB duration. However, it predicts too large a baryonic contamination. This scenario involves a possible sequence of physical phenomena taken with extreme values of parameters. It is hard to perform numerical calculations for such a scenario.

The weakness of the hypernova scenario (large baryon contamination) is evaded in the supranova scenario [49]. A massive neutron star is stabilized by rotation. The loss of the angular momentum results in collapse as in the hypernova scenario, and a fireball is produced by the expanding magnetic field. In this scenario the baryon contamination is low; it is provided by swept-up baryons from the interstellar region.

In conclusion, the astrophysical models for the GRB engine, which allow numerical calculations, predict too low an energy release and need narrow beaming, which does not naturally exist in these models. In some scenarios, most notably the hypernova, there could be a set of physical phenomena that, when taken with extreme parameters, can provide the energy release and durations needed for explanation of the observed GRBs. However, as it stands, these scenarios do not give numerical predictions and, strictly speaking, cannot be called models.

5.1. GRBs from Superconducting Strings

Can the problem of the GRB engine with its tremendous energy release, probably beamed, be solved with the help of new physics?

Such a solution, utilizing the cusps of superconducting strings, was first suggested in [50] and has been recently revived in [51].

Cosmic strings are linear defects that could be formed at a symmetry-breaking phase transition in the early Universe [52]. In space, they exist in the form of endless strings and closed loops. Strings predicted in most Grand Unified Models respond to external electromagnetic fields as thin superconducting wires

[53]. As they move through cosmic magnetic fields, such strings develop electric currents. Oscillating loops of a superconducting string emit short bursts of highly beamed electromagnetic radiation through small string segments, centered at peculiar points on a string, cusps, where velocity reaches the speed of light [54, 55].

The beam of low-frequency electromagnetic radiation propagating in a plasma produces a beam of accelerated particles. For an electromagnetic wave in vacuum, a test particle would be accelerated to a very large Lorentz factor. But the maximum Lorentz factor of the beam is saturated at the value γ_b, when the energy of the beam reaches the energy of the original electromagnetic pulse: $N_b m\gamma_b \sim \mathcal{E}_{\rm em}$. This results in the Lorentz factor of the beam on the order of 10^2–10^4, as in an ordinary fireball. The beam of accelerated particles pushes the gas with the frozen magnetic field ahead of it, producing an external shock in the surrounding plasma and a reverse shock in the beam material, as in the case of an ordinary fireball. Therefore, the hydrodynamic development of a fireball is essentially the same as in the case of the astrophysical GRB engine.

In contrast to astrophysical models, a cusp produces a pulse of electromagnetic radiation with the energy and beaming fixed by the parameters of cosmic strings and ambient gas. In fact, the cusp model is very rigid. In a simplified version [51], there is only one free parameter, the string scale of symmetry breaking $\eta \sim 10^{14}$ GeV, and two physical quantities that characterize the gas in filaments and sheets, where most of the GRBs are originated. Formally, there are three such quantities: a magnetic field, parametrized as $B = B_{-7} \times 10^{-7}$ G; redshift of its origin z_m; and gas density n_g. But dependence on gas density is extremely weak. It influences only the hydrodynamic flow through the Lorentz factor of the contact discontinuity surface, $\gamma_{\rm CD}$, with $\gamma_{\rm CD} \propto n_g^{-1/8}$.

The only genuine free parameter, η, or an equivalently dimensionless parameter $\alpha = k_g G\eta^2$, where G is the gravitational constant and $k_g \sim 50$ is a numerical coefficient, determines the space properties of the loops: a typical length of a loop in the epoch t, $l \sim \alpha t$ and the number density of loops

$$n_l(t) \sim \alpha^{-1} t^{-3}. \tag{10}$$

A string segment near the cusp moves with the Lorentz factor γ and radiates an electromagnetic pulse within a cone with the opening angle $\theta \sim 1/\gamma$. The energy radiated per unit of solid angle in the direction θ is given by [54]

$$d\mathcal{E}_{\rm em}/d\Omega \sim k_{\rm em} J_0^2 \alpha t/\theta^3, \tag{11}$$

where J_0 is the initial current induced by the external magnetic field in the loop.

The fluence, defined as the total energy per unit area of the detector, is

$$S \sim (1+z)(d\mathcal{E}_{\rm em}/d\Omega) d_L^{-2}(z), \tag{12}$$

where $d_L(z) = 3t_0(1+z)^{1/2}[(1+z)^{1/2} - 1]$ is the luminosity distance.

After simple calculations [51], one obtains the GRB rate as a function of the fluence. For relatively small fluences,

$$\dot{N}_{\rm GRB}(>S) \approx 3 \times 10^2 S_{-8}^{-2/3} B_{-7}^{4/3} \ ({\rm yr}^{-1}), \tag{13}$$

while for large fluences $\dot{N}_{\rm GRB}(>S) \propto S^{-3/2}$. Both the absolute value of $\dot{N}_{\rm GRB}(>S)$ and its dependence on S agree with observations. The duration of the cusp event as seen by a distant observer is [50]

$$\tau_c \sim (1+z)(\alpha t/2)\gamma^{-3} \sim (\alpha t_0/2)(1+z)^{-1/2}\theta^3. \tag{14}$$

The duration of the cusp event coincides with the duration of the GRB found as the duration of fireball emission [51]. The duration of GRBs originating at redshift z and having fluence S can be readily calculated as

$$\tau_{\rm GRB} \approx 200 \frac{\alpha_{-8}^4 B_{-7}^2}{S_{-8}} (1+z)^{-1} (\sqrt{1+z} - 1)^{-2} \ (s). \tag{15}$$

Analysis of (15) shows [51] that it correctly describes the range of observed GRB durations.

Therefore, the simplified one-parameter cusp model correctly describes the total energies of GRBs (or fluences S), the GRB rates and their dependence on S, and GRB durations (absolute values and range).

The signatures of this model are simultaneous powerful bursts of gravitational radiation [51, 56] from a cusp and repeaters for GRBs of very short durations.

The cusp model faces basically one difficulty: it predicts too low a GRB rate from galaxies. This discrepancy could be eliminated if the model strongly underestimates the capture rate of string loops by galaxies. For example, if $\alpha \gg k_g G\eta^2$, then the loops are nonrelativistic and may be effectively captured by galaxies. Another possibility is that the cusp model could describe some subclass of the sources not associated with galaxies. Such a subclass could include short-duration GRBs for which host galaxies are not found or another subclass of no-host GRBs.

6. CONCLUSIONS

Astronomy and astrophysics were in the past and remain now a source of fundamental discoveries in physics. What phenomena can we suspect now as the challengers for such discoveries?

Most probably, UHECR is challenger number one. The presence of detected particles with energies above the GZK cutoff is reliably established. An astrophysical solution to the UHECR problem is disfavored, though not excluded. UHE heavy nuclei (iron) accelerated in our Galaxy, local (10–30 Mpc) enhancement of UHECR sources, and exotic one-source models remain disfavored but not rigorously excluded possibilities. One might expect surprises here, but each of them will be a small revolution in a special field. There are many elementary-particle solutions to the UHECR problem. All of them seem exotic to nonspecialists, but eventually many of them will not. For example, the idea of UHECR from superheavy DM is based only on known theoretical physics. The light gluino as a carrier of the UHE signal is also based on reliable physics and may be saved by reexamination or reinterpretation of accelerator data. Only future experiments can solve the UHECR problem. Observations of UHECR in the Southern Hemisphere (the Auger detector), measurement of longitudinal profiles of EAS in the atmosphere (High-Res), and search for particles with energies of 1×10^{21} eV and higher (Auger, telescope array, and space detectors) may result in fundamental discovery in physics.

GRB engines with their tremendous energy output, most probably beamed, are a new type of source even if they are collapsars. Further observational evidence for their origin (more precise positions in the galaxies, no-host GRBs, etc.) will help to establish the nature of these objects, though they are well hidden in the debris of the bursts. Search for gravitational bursts and very short GRBs can bring evidence for nonastrophysical origin of at least some GRBs.

I think the TeV gamma-ray crisis will be peacefully solved by reconsideration of the observed diffuse flux of IR radiation, or the TeV gamma-ray spectrum, or both. It will result then in a better constraint on Lorentz invariance violation, not in its discovery.

ACKNOWLEDGMENTS

This work has been performed as part of INTAS, project no. 99-1065.

REFERENCES

1. K. Hirata *et al.*, Phys. Rev. Lett. **58**, 1490 (1987); R. M. Bionta *et al.*, Phys. Rev. Lett. **58**, 1494 (1987); E. N. Alexeev *et al.*, Pis'ma Astron. Zh. **14**, 99 (1988) [Sov. Astron. Lett. **14**, 41 (1988)].
2. V. S. Imshennik and D. K. Nadyozhin, Pis'ma Astron. Zh. **3**, 353 (1977) [Sov. Astron. Lett. **3**, 188 (1977)].
3. V. A. Kostelecki and S. Samuel, Phys. Rev. D **39**, 683 (1989).
4. G. Dvali and M. Shifman, Phys. Rep. **320**, 107 (1999).
5. J. Ellis, N. E. Mavromatos, and D. V. Nanopolos, in *Proceedings of the 4th International Symposium on Sources and Detection of Dark Matter in the Universe (DM 2000)*; gr-qc/0005100.
6. Don Colladay and V. A. Kostelecky, Phys. Rev. D **55**, 6760 (1997).
7. S. Colemam and S. L. Glashow, Phys. Lett. B **405**, 249 (1997); Phys. Rev. D **59**, 116008 (1999).
8. V. B. Berestetskiĭ, E. M. Lifshitz, and L. P Pitaevskiĭ, *Course of Theoretical Physics,* Vol. 4: *Quantum Electrodynamics* (Nauka, Moscow, 1989; Pergamon Press, Oxford, 1982).
9. K. Greisen, Phys. Rev. Lett. **16**, 748 (1966); G. T. Zatsepin and V. A. Kuzmin, Pis'ma Zh. Éksp. Teor. Fiz. **4**, 114 (1966) [JETP Lett. **4**, 78 (1966)].
10. D. A. Kirzhnitz and V. A. Chechin, Pis'ma Zh. Éksp. Teor. Fiz. **14**, 261 (1971) [JETP Lett. **14**, 172 (1971)]; Yad. Fiz. **15**, 1051 (1972) [Sov. J. Nucl. Phys. **15**, 585 (1972)].
11. L. Gonzáles-Mestres, in *Proceedings of the 25th International Cosmic Ray Conference, ICRC, Durban, 1997,* Vol. 6. p. 109; in *Proceedings of the 26th International Cosmic Ray Conference, ICRC, Salt Lake City, 1999*, Vol. 1, p. 179.
12. S. L. Glashow, Nucl. Phys. B (Proc. Suppl.) **70**, 180 (1999).
13. R. Aloisio, P. Blasi, P. L. Ghia, and A. F. Grillo, Phys. Rev. D **62**, 053010 (2000).
14. J. Ellis *et al.*, Astrophys. J. **535**, 139 (2000).
15. M. G. Hauser *et al.*, Astrophys. J. **508**, 25 (1998).
16. D. J. Fixsen *et al.*, Astrophys. J. **508**, 123 (1998).
17. A. Biviano *et al.*, astro-ph/9910314.
18. M. A. Malkan and F. W. Stecker, astro-ph/0009500; F. W. Stecker, in *Proceedings of the IAU Symposium no. 204 "The Extragalactic Infrares Background and its Cosmological Implications," Manchester, 2000,* Ed. by M. Harwit and G. Hauser; astro-ph/0010015.
19. J. R. Primack, Astropart. Phys. **11**, 93 (1999); D. MacMinn and J. R. Primack, Space Sci. Rev. **75**, 413 (1996).
20. R. J. Protheroe and N. Meyer, Phys. Lett. B **493**, 1 (2000).
21. J. Guy, C. Renault, F. A. Aharonian, *et al.*, Astron. Astrophys. **359**, 419 (2000).
22. V. S. Berezinsky, S. I. Grigorieva, and G. T. Zatsepin, in *Proceedings of the 14th International Cosmic Ray Conference, ICRC, Munich, 1975,* Vol. 2, p. 711; Izv. Akad. Nauk SSSR, Ser. Fiz. **40**, 524 (1976).

23. V. Berezinskiĭ, Yad. Fiz. **11**, 399 (1970) [Sov. J. Nucl. Phys. **11**, 222 (1970)].
24. M. Nagano and A. A. Watson, Rev. Mod. Phys. **72**, 689 (2000).
25. A. M. Hillas *et al.*, in *Proceedings of the 12th International Cosmic Ray Conference, ICRC, 1971,* Vol. 3, p. 1001.
26. D. J. Bird *et al.*, Astrophys. J. **424**, 491 (1994).
27. S. Yoshida *et al.*, Astropart. Phys. **3**, 105 (1995).
28. V. S. Berezinskii, S. V. Bulanov, V. A. Dogiel, *et al.*, *Astrophysics of Cosmic Rays* (North-Holland, Amsterdam, 1990).
29. V. S. Berezinsky, A. R. Gazizov, and S. I. Grigorieva, in *Proceedings of the International Cosmic Ray Conference, ICRC, 2001* (in press).
30. S. T. Scully and F. W. Stecker, astro-ph/0006112.
31. V. S. Berezinsky and S. I. Grigorieva, in *Proceedings of the 16th International Cosmic Ray Conference, ICRC, Kyoto, 1979,* Vol. 2, p. 81.
32. M. Blanton, P. Blasi, and A. Olinto, Astropart. Phys. **15**, 275 (2001).
33. J. Wdowczyk and A. Wolfendale, Nature **281**, 356 (1980); M. Giler, J. Wdowczyk, and A. Wolfendale, J. Phys. G **6**, 1561 (1980).
34. E.-J. Ahn, G. Medino-Tanco, P. L. Biermann, and T. Stanev, Nucl. Phys. B (Proc. Suppl.) **87**, 417 (2000).
35. V. S. Berezinsky, S. I. Grigorieva, and V. A. Dogiel, Astron. Astrophys. **232**, 582 (1990).
36. S. I. Syrovatsky, Comments Appl. Phys. **3**, 155 (1969).
37. G. V. Kulikov, Yu. A. Fomin, and G. B. Khristiansen, Pis'ma Zh. Éksp. Teor. Fiz. **11**, 543 (1969) [JETP Lett. **11**, 374 (1970)].
38. M. Giller and M. Zielinska, in *Proceedings of the 25th International Cosmic Ray Conference, ICRC, Durban, 1997,* Vol. 4, p. 469.
39. V. N. Zirakashvili *et al.*, Astrophys. Lett. **24**, 139 (1998).
40. V. Berezinsky, S. Grigorieva, and M. Marchesini, in preparation.
41. V. S. Berezinsky *et al.*, in *Astrophysical Aspects of Most Energetic Cosmic Rays,* Ed. by M. Nagano and F. Takahara (World Sci., Singapore, 1991), p. 134.
42. D. D. Sokoloff and A. M. Shukurov, Nature **347**, 51 (1990).
43. V. S. Berezinsky, Nucl. Phys. B (Proc. Suppl.) **87**, 387 (2000).
44. R. D. Blandford, astro-ph/0001498.
45. D. Eichler, M. Livio, T. Piran, and D. N. Schramm, Nature **340**, 126 (1989).
46. H.-Th. Janka *et al.*, Astrophys. J. **527**, L39 (1999); astro-ph/0101357.
47. S. E. Woosley, Astrophys. J. **405**, 273 (1993); **527**, L55 (1999).
48. B. Paczynski, Astrophys. J. **494**, L45 (1998); astro-ph/9706232.
49. M. Vietri and L. Stella, Astrophys. J. **507**, L45 (1998); **527**, L43 (1999).
50. A. Babul, B. Paczynski, and D. N. Spergel, Astrophys. J. Lett. **316**, L49 (1987); B. Paczynski, Astrophys. J. **335**, 525 (1988).
51. V. Berezinsky, B. Hnatyk, and A. Vilenkin, astro-ph/0102366.
52. A. Vilenkin and E. P. S. Shellard, *Cosmic Strings and Other Topological Defects* (Cambridge Univ. Press, Cambridge, 1994).
53. E. Witten, Nucl. Phys. B **249**, 557 (1985).
54. A. Vilenkin and T. Vachaspati, Phys. Rev. Lett. **58**, 1041 (1987).
55. D. N. Spergel, T. Piran, and J. Goodman, Nucl. Phys. B **291**, 847 (1987).
56. T. Damour and A. Vilenkin, Phys. Rev. Lett. **85**, 3761 (2000).

Physics of Atomic Nuclei, Vol. 66, No. 3, 2003, pp. 435–437. From Yadernaya Fizika, Vol. 66, No. 3, 2003, pp. 463–465.

NEUTRINO PHYSICS AND ASTROPHYSICS

Medium Energy Neutrinos from Solar Flares*

O. G. Ryazhskaya, L. V. Volkova, and G. T. Zatsepin**

Institute for Nuclear Research, Russian Academy of Sciences, pr. Shestidesyatiletiya Oktyabrya 7a, Moscow, 117312 Russia

Received April 17, 2002

Abstract—The production of neutrinos with energies higher than 0.1 GeV in the solar atmosphere during solar flares is discussed. Neutrinos and muons are generated in decays of $\pi^{\pm}$ mesons produced in nuclear interactions of accelerated solar flare protons with matter of the Sun. Muons themselves decay yielding neutrinos. These neutrinos could come to the Earth and be detected with neutrino telescopes. Estimations of fluxes of such neutrinos are given. © *2003 MAIK "Nauka/Interperiodica"*.

1. INTRODUCTION

In recent years, the problem of neutrino oscillations has been discussed very seriously. There were many neutrino experiments made with different neutrino sources: the center of the Sun, the Earth's atmosphere, reactors, accelerators. Long baseline neutrino experiments are under construction now. One of them has been running since 1999. An additional neutrino source exists. It is a solar flare and the atmosphere of the Sun.

2. A SCHEME OF NEUTRINO PRODUCTION IN SOLAR FLARES

Protons are accelerated during a flare in the solar corona (see figure). The protons that are accelerated in the direction from the Sun do not have enough matter in their way and leave the Sun going into outer space. But the other protons accelerated in the direction to the Sun can interact with the matter of the chromosphere, photosphere, and in the outer layers of the convective zone (B). In these interactions, pions and kaons are produced. Neutrinos and antineutrinos are created in pion and kaon decays:

$$p + p \to \pi, K \to \mu, \nu_\mu, \nu_e, \bar{\nu}_\mu, \bar{\nu}_e.$$

In decays of muons, neutrinos and antineutrinos are produced again:

$$\mu \to e, \nu_\mu, \nu_e, \bar{\nu}_\mu, \bar{\nu}_e.$$

These neutrinos, having gone through the Sun with almost no attenuation (neutrinos with energies <10 GeV), could be detected with apparatus on the Earth. The conditions in zone B are such that protons have enough matter in their way to interact with protons and yield pions and kaons. The density of matter in the way of pions, kaons, and muons is such that these particles have time to decay and yield neutrinos.

3. ESTIMATIONS OF FLUXES OF NEUTRINOS PRODUCED IN SOLAR FLARES

The equations for propagation of protons, pions, and neutrinos through the matter of the corona, the chromosphere, the photosphere, and the outer layers of the convective zone of the Sun are solved analytically using the following assumptions:

(i) The differential energy spectra of protons accelerated during a flare have a pure power law with degree $\gamma + 1$,

$$F^p(E_p)dE_p = AE_p^{-(\gamma+1)}dE_p, \qquad (1)$$

and it is valid up to the proton energy $E_p = E_0$. Here, $F^p(E_p)$ is in proton/(flash GeV).

(ii) Acceleration in flares has an isotropic character.

(iii) Pions are produced in proton–proton interactions with inclusive cross sections that were found in accelerator experiments at proton energies of ~ 20 GeV (it is supposed that the cross sections have a scaling behavior in the entire energy interval considered in this work).

(iv) Nuclear interactions of pions are taken into account (critical energies for pions are equal to $\sim$5000 GeV in the place of effective pion production in the matter of the convective zone).

*This article was submitted by the authors in English.

**e-mail: volkova@inr.npd.ac.ru

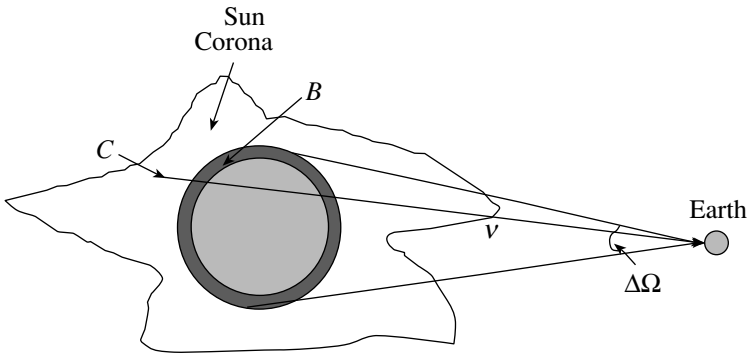

Scheme of arrival of neutrinos produced in solar corona flares to the Earth: a proton accelerated during a flare (C) comes to zone B (chromosphere + photosphere + beginning of the convective zone) and produces pions and kaons in interactions with a proton; pions and kaons decay and yield muons and neutrinos; neutrinos are also produced in decays of muons. All neutrinos produced within the angle $\Delta\Omega$ come to the Earth.

3.1. On Solar Flares

Nobody knows the nature of solar flares in detail. Two types of flares are discussed further in the work. One is similar to the flare that took place on February 23, 1956. It was a very huge flare. Its power was estimated to be $N = 10^{33}$ protons with $E_p > 1$ GeV.

The other is an averaged flare. Its power is $N = 2 \times 10^{29}$ protons with energy $E_p > 1$ GeV. The number of such flares is about 5/yr. It was supposed that the mean time duration of a flare was about 20 minutes.

Table 1. Differential spectra $F_\nu^{\text{flare}}(E_\nu)dE_\nu$ of neutrinos produced in $\pi_{\mu 2}$ and μ_{e3} decays in solar corona flares (proton spectrum (1) for $A = 1$; E_p in GeV, $F_\nu^{\text{flare}}(E_\nu)$ in neutrino/(flash GeV))

γ	$E_{\nu_\mu+\bar\nu_\mu}$, GeV			
	0.1	0.3	1.0	3.0
1.1	7.70	1.15	0.105	1.05×10^{-2}
1.7	3.95	0.405	1.90×10^{-2}	9.85×10^{-4}
2	2.95	0.270	9.05×10^{-3}	3.40×10^{-4}
3	1.30	8.75×10^{-2}	1.20×10^{-3}	1.45×10^{-5}
5	0.390	1.95×10^{-2}	7.90×10^{-5}	1.10×10^{-7}
γ	$E_{\nu_e+\bar\nu_e}$, GeV			
	0.1	0.3	1.0	3.0
1.1	3.75	0.580	5.50×10^{-2}	5.45×10^{-3}
1.7	1.90	0.205	9.65×10^{-3}	5.00×10^{-4}
2	1.40	0.135	4.55×10^{-3}	1.70×10^{-4}
3	0.630	4.40×10^{-2}	6.00×10^{-4}	7.45×10^{-6}
5	0.190	9.85×10^{-3}	3.95×10^{-5}	5.50×10^{-8}

3.2. The Results of the Calculations

All data that are available today on production of accelerated protons in solar flares show that not only values of A from (1) differ from flare to flare very much but also values of γ differ very much (γ is in a wide interval of values from 1.1 to 5). Table 1 shows the differential neutrino fluxes calculated for different values of γ (for $A = 1$) for given neutrino energies E_ν.

The ratio of the differential fluxes of neutrinos produced in a solar corona flare to that of atmospheric neutrinos $\alpha^{\text{flare-atm}}$ per 1 s during a flare per 1 cm^2 within the angle $\Delta\Omega$ for a flare with an intensity A/τ

Table 2. The values of the ratios $\alpha^{\text{flare-atm}}$ of the differential fluxes of neutrinos produced in a solar corona flare to that of atmospheric neutrinos per 1 s during a flare per 1 cm^2 within the angle $\Delta\Omega$ for a flare with the intensity $N(>1\text{ GeV}) = 2 \times 10^{29}$ protons/flash

γ	$E_{\nu_\mu+\bar\nu_\mu}$, GeV			
	0.1	0.3	1.0	3.0
1.1	3.70×10^3	3.50×10^3	5.35×10^3	1.05×10^4
1.7	3.60×10^3	2.70×10^3	1.85×10^3	1.90×10^3
3	3.40×10^3	1.40×10^3	3.20×10^2	7.90×10^1
5	3.30×10^3	1.00×10^3	7.15×10^1	1.95×10^0
γ	$E_{\nu_e+\bar\nu_e}$, GeV			
	0.1	0.3	1.0	3.0
1.1	3.75×10^3	4.30×10^3	8.15×10^3	2.15×10^4
1.7	3.65×10^3	2.95×10^3	2.75×10^3	3.80×10^3
3	3.40×10^3	1.55×10^3	4.80×10^2	1.60×10^2
5	2.80×10^3	1.30×10^3	1.05×10^2	3.85×10^0

is

$$\alpha^{\text{flare–atm}} = \frac{1}{4\pi R^2_{\text{Earth–Sun}}} \frac{F^{\text{flare}}(E_\nu)}{P^{\text{atm}}(E_\nu)\Delta\Omega} \frac{A}{\tau}, \quad (2)$$

where $P^{\text{atm}}(E_\nu)$ is the differential energy spectrum of atmospheric neutrinos coming to sea level in the vertical direction (in units of neutrino/(cm^2 sr GeV)), $R_{\text{Earth–Sun}}$ is the distance from the Earth to the Sun (in cm), τ is the averaged flare duration (in s/flash), $\Delta\Omega = \pi R^2_{\text{Sun}}/R^2_{\text{Earth–Sun}}$ (in sr), and R_{Sun} is the radius of the Sun (in cm). These values of the ratios $\alpha^{\text{flare–atm}}$ are given in Table 2.

The ratios $\alpha^{\text{flare–atm}}$ for electron neutrinos for higher energies begin to be higher than those for muon neutrinos due to the different probability of muon decay in the Earth's and the Sun's atmosphere. The higher the neutrino energy, the higher the ratio $\alpha^{\text{flare–atm}}$. If we consider a flare with $N(>1\text{ GeV}) = 10^{33}$, then all values in Table 2 are to be increased by a factor of 5000.

4. CONCLUSION

The apparatus detecting about 3000 events/yr from atmospheric neutrinos (like Super-Kamiokande) during a flare with $N = 10^{33}$ protons/flash could observe about 25 events with an energy of 1 GeV within the angle $\Delta\Omega$ from neutrinos produced in the solar flash if $\gamma = 1.7$.

The calculations of fluxes of neutrinos were performed under the assumption that the differential energy spectra of protons accelerated in solar flares had a pure power character up to very high energies ($E_p \sim \infty$). If it is assumed that protons are accelerated only up to 10, 20, or 50 GeV, then the corresponding neutrino fluxes are to be reduced. For example, when $\gamma = 1.7$, these fluxes for $E_\nu = 0.3$ GeV are 0.8, 0.95, and 1.0 of the fluxes presented in the tables (the corresponding values for $E_\nu = 1$ GeV are about 0.3, 0.6, and 0.9).

The authors are grateful to G.A. Bazilevskaya for a fruitful discussion of the problem on proton acceleration in solar corona flares and to L.B. Okun for interest in this work and very useful remarks.

This work was supported by the Russian Foundation for Basic Research (project nos. 00-15-96632 and 00-02-16112).

Physics of Atomic Nuclei, Vol. 66, No. 3, 2003, pp. 438–443. From Yadernaya Fizika, Vol. 66, No. 3, 2003, pp. 466–471.

Symmetry Violations in Nuclear Hamiltonians and Their Consequences for Electroweak Decays*

D. R. Bes and O. Civitarese[1)]

Departamento de Fisica, CNEA, and Departamento de Fisica, Universidad Favaloro, Argentina

Received February 13, 2002

Abstract—We discuss the results of the treatment of nuclear Hamiltonians in terms of collective and intrinsic variables. The BRST method is adapted to identify spurious and physical sectors of the wave functions and operators. Counterterms are added to the Hamiltonian to enforce the symmetries broken by the single-particle field and/or by the residual two-body interactions. We focus on the study of Fermi and Gamow–Teller transitions, with reference to the nuclear double-beta-decay processes, and on the study of vector operators ($\lambda^\pi = 1^-$), with reference to (μ, e^-) conversion processes. We address the following aspects of the problem: (a) Isospin symmetry and the calculation of 0^+ and 1^+ states; sensitivity of the Fermi and Gamow–Teller response in double-beta-decay processes; (b) Restoration of the translational and Galilean invariance of the nuclear Hamiltonians and the calculation of $I^\pi = 1^-$ states; sensitivity of the nuclear response to the spurious center-of-mass motion and μ-electron lepton-flavor-violation processes.

1. ISOSPIN SYMMETRY AND THE PAIRING HAMILTONIAN

In most cases, the short-range part of the two-body interaction in nuclei is described in terms of monopole pairing forces. From first principles, one may expect that both $T = 0$ and $T = 1$ channels of the interaction should be present [1–3]. The experimental evidence, however, favors the isovector ($T = 1$) pairing, and it is less conclusive about the existence of $T = 0$ (isoscalar) pairing. At the same time, the conventional treatment of the nuclear pairing force implies that the interaction is operative among nucleons with the same charge, and occasionally the interaction between protons and neutrons is also considered. In general, we may say that the pairing channels of the nuclear two-body interaction are not treated in a fully symmetric way. Another source of symmetry breaking is, naturally, the adoption of the empirical single-particle basis. Clearly, the consideration of both sources of symmetry breaking is of some importance, particularly, in dealing with the calculation of observables that are isospin-dependent. Let us start with the analysis of the pairing force problem with reference to isospin-dependent excitations and transitions in nuclei.

The separable pairing Hamiltonian is written as

$$H = H_{\rm sp} + H_{\rm pair}$$

with

$$H_{\rm sp} = \epsilon_{vj}\tau_{vj},$$
$$H_{\rm pair} = -g_p S_p^+ S_p - g_n S_n^+ S_n - \frac{1}{2} g_\perp S_\perp^+ S_\perp,$$
$$S_v^+ = c_{vjm}^+ c_{vj\bar{m}}^+ \quad (\text{with } v = p, n),$$
$$S_\perp^+ = c_{pjm}^+ c_{nj\bar{m}}^+ + c_{njm}^+ c_{pj\bar{m}}^+$$

(with summation over repeated indices). The Hamiltonian allows for differences between proton and neutron single-particle energies and pairing strengths, and for an (arbitrary) strength of the neutron–proton isovector pairing component. As a consequence of the presence of the isovector and isoquadrupole terms in this Hamiltonian, it does not in general conserve isospin. Therefore, we are faced with the problem of discriminating between unphysical violations of the symmetries introduced by the formalism (through the use of the basic set of states determined by the mean field approximation) and violations produced by the lack of invariance of the effective nuclear Hamiltonian. After transforming to collective and intrinsic variables, this Hamiltonian reads

$$H = H_0 + H_1 + H_2,$$

where we define its different terms as

$$H_0 = \epsilon_{aj}\tau_{aj} - g_0 \left(S_p^+ S_p + S_n^+ S_n + \frac{1}{2} S_\perp^+ S_\perp \right),$$
$$H_1 = \epsilon_{0j} D^1_{0\sigma} \tau_{\sigma j} - g_1 D^1_{00} (S_p^+ S_p - S_n^+ S_n)$$

*This article was submitted by the authors in English.

[1)]Departamento de Fisica, UNLP, La Plata, Argentina; e-mail: civitare@venus.fisica.unlp.edu.ar

$$- g_1 \frac{1}{\sqrt{2}} D^1_{01}(S^+_p S_\perp + S^+_\perp S_n)$$
$$+ g_1 \frac{1}{\sqrt{2}} D^1_{0\bar{1}}(S^+_n S_\perp + S^+_\perp S_p),$$
$$H_2 = -g_2 D^2_{00}(S^+_p S_p + S^+_n S_n - S^+_\perp S_\perp)$$
$$+ g_2 \sqrt{\frac{3}{2}} D^2_{01}(S^+_\perp S_n - S^+_p S_\perp)$$
$$+ g_2 \sqrt{\frac{3}{2}} D^2_{0\bar{1}}(S^+_\perp S_p - S^+_n S_\perp)$$
$$+ g_2 \sqrt{6}(D^2_{02} S^+_p S_n + D^2_{0\bar{2}} S^+_n S_p).$$

The coupling constants entering into this expression are defined by

$$g_0 = \frac{1}{3}(g_p + g_n + g_\perp), \quad g_1 = \frac{1}{2}(g_p - g_n),$$
$$g_2 = \frac{1}{6}(g_p + g_n - 2g_\perp),$$
$$\epsilon_{aj} = \epsilon_{pj} + \epsilon_{nj}, \quad \epsilon_{0j} = \epsilon_{pj} - \epsilon_{nj},$$
$$\tau_{aj} = \frac{1}{2}(\tau_{pj} + \tau_{nj}), \quad \tau_{0j} = \frac{1}{2}(\tau_{pj} - \tau_{nj}).$$

1.1. Definition of the Intrinsic Frame

We choose $\mathrm{Im}\langle S_p\rangle = \mathrm{Im}\langle S_n\rangle = \langle S_\perp\rangle = 0$. This choice leads to the usual Bogolyubov–Valatin transformation between identical particles. This selection of a gauge constitutes a violation of isospin and gauge symmetries occuring in the intrinsic frame. The *np* pairing is incorporated through the collective rotations in the isospace and the gauge space [3]. The two remaining expectation values $\langle S_p\rangle$ and $\langle S_n\rangle$ are real and considered to be the order parameters, i.e., the large quantities of the system. If the isospin T is also large, the D functions may be treated within a boson description through generalization of the Holstein–Primakoff algebra (Marshalek's expansion).

1.2. Boson Image of the Hamiltonian

The leading orders of the Hamiltonian are simplified to

$$H_\perp = \omega_{\perp\iota}\Gamma^+_{\perp\iota}\Gamma_{\perp\iota} + \omega_\xi \xi^+\xi$$
$$- g_2 \frac{3}{T}\langle S_p\rangle\langle S_n\rangle(\beta^4\xi^{+2} + \beta^{-4}\xi^2)$$
$$- \left(\beta^2\xi^+\Gamma_{\perp\iota} + \mathrm{h.c.}\right)\phi_{a\iota} - \left(\beta^2\xi^+\Gamma^+_{\perp\iota} + \mathrm{h.c.}\right)\phi_{b\iota}$$
$$- \frac{1}{2\mathcal{I}_\perp}\left[\tau^{(20)}_1, \tau^{(20)}_{\bar{1}}\right]_+.$$

In the present treatment, the proton–neutron interaction is replaced by the isospin-independent nuclear interaction which gives rise to the well-behaved bosons $\Gamma^+_{\perp\iota}$, creating the so-called antianalog states. The operator ξ^+ acts in the collective space by increasing the value of $m = T - M$ (it excites the band of analog states having $M = T$ for the ground state). Therefore, the "badly behaved" operator τ_1 is replaced by the "well-behaved" operator ξ^+. The excitation frequency ω_ξ includes the single-particle Coulomb displacements

$$\omega_\xi = -\frac{1}{T}\epsilon_{0j}\langle\tau_{0j}\rangle + \frac{3g_2 + g_1}{T}\langle S_p\rangle^2 + \frac{3g_2 - g_1}{T}\langle S_n\rangle^2. \quad (1)$$

The spectrum of states associated with the neutron–proton sector is labeled by the quantum numbers $(A, T, M, (n_\xi, n_{\perp\iota}, n_{d\iota}))$. It displays a signature

$$(-1)^{\sum_\iota (n_{\perp\iota} + n_{d\iota}) + T - \frac{1}{2}A} = 1. \quad (2)$$

The operator β^2 increases the value of the isospin by one unit ($\beta^2|T\rangle = |T+1\rangle$). Therefore, the product $\beta^2\xi^+$ conserves the projection M in the laboratory frame. The operator $\beta^4\xi^{+2}$ mixes the ground state of a nucleus having isospin $T-2$ and projection $T-2$ with the double IAS with spin T. It is proportional to the isoquadrupole strength g_2. The operator $\beta^2\xi^+\Gamma^+_{\perp\iota}$ creates the antianalog states $\Gamma^+_{\perp\iota}|0\rangle$ in the neighboring odd–odd nucleus with isospin $T-1$, laboratory projection $M = T-1$, simultaneously with the IAS carrying isospin T, $M = T-1$. There are also transitions in which the antianalog state is destroyed, while the analog is created.

1.3. Transition Operators

The β^- transition operators, being isovectors, should also be transformed to the intrinsic frame. For the Fermi and Gamow–Teller (GT) operators, we obtain

$$\beta^{(\mathrm{F}-)} = -\sqrt{2}\tau_1 \to -\sqrt{2T}\xi^+, \quad (3)$$

$$\beta^{(\mathrm{GT}-)}_q = \sigma_{q1} \equiv \frac{1}{\sqrt{3}}\langle j_1||\sigma||j_2\rangle[c^+_{pj_1}c_{nj_2}]^1_q \quad (4)$$
$$\to \beta^{-2}\left(q_{f\iota}\Gamma^+_{d\iota q} + (-1)^q_{b\iota}\Gamma_{d\iota(-q)}\right).$$

We note that for Fermi transitions the operator τ_1 is again replaced by ξ^+. Therefore, there are only Fermi beta-decay processes within the isobaric analog band. However, the isospin mixing admixtures make possible the transition between the initial state (ATT) and the final state $(A(T-2)(T-2))$. It may proceed through either the intermediate IAS $(AT(T-1)(1,0,0))$ or through the states $(A(T-1)(T-1)(0,1,0))$. The reduced matrix elements of the spin operator are included in the GT operator. In that expression, there appears the isospin-decreasing operator β^{-2}, which allows occurrence of

the double-beta-decay process without recourse to the isospin nonconserving terms of the Hamiltonian. The coefficients $q_{f\iota}, q_{b\iota}$ are obtainable within the RPA calculation of $I^\pi = 1^+$ excitations.

1.4. Mixing between Components

The mixing between different components for each of the states belonging to the above-discussed level scheme may be calculated by direct diagonalization. As an example, we discuss the perturbative approach. The mixing is therefore expressed as

$$\delta|AT(T-1)(n_\xi=1)\rangle = -a_\iota|A(T-1)(T-1)(n_{\perp\iota}=1)\rangle,$$
$$\delta|A(T-2)(T-2)\rangle = b_\iota|A(T-1)(T-2)(n_\xi=1)(n_{\perp\iota}=1)\rangle + c|AT(T-2)(n_\xi=2)\rangle,$$

where

$$a_\iota = \frac{\phi_{a\iota}}{\omega_{\perp\iota} - 2\kappa T - \omega_\xi},$$
$$b_\iota = -\frac{\phi_{b\iota}}{2\kappa(T-1) + \omega_\xi + \omega_{\perp\iota}},$$
$$c = \frac{3g_2\langle S_n\rangle\langle S_p\rangle}{\sqrt{2}T\,(\kappa(2T-1)+\omega_\xi)}.$$

1.5. Transition Matrix Elements

With the wave functions of the previous subsection, we have calculated the matrix elements for allowed Fermi transitions from the initial $(A, T, M = T)$ state. The results are

$$M_{1\xi} = \langle AT(T-1)(n_\xi=1)|\beta^{l(\mathrm{F}-)}|ATT\rangle = -\sqrt{2T},$$
$$M_{1\perp\iota} = \langle AT(T-1)(n_{\perp\iota}=1)|\beta^{l(\mathrm{F}-)}|ATT\rangle = -\sqrt{2T}a_\iota,$$
$$M_{2\xi} = \langle A(T-2)(T-2)|\beta^{l(\mathrm{F}-)}|AT(T-1)(n_\xi=1)\rangle = -\sqrt{2T}(c - a_\iota b_\iota),$$
$$M_{2\perp\iota} = \langle A(T-2)(T-2)|\beta^{l(\mathrm{F}-)}|AT(T-1)(n_{\perp\iota}=1)\rangle = -\sqrt{2T}b_\iota.$$

The matrix element corresponding to double Fermi transitions is

$$M^{(\mathrm{F})}_{2\nu} = \frac{M_{1\xi}M_{2\xi}}{\Delta + E(\mathrm{IAS})} + \frac{M_{1\perp\iota}M_{2\perp\iota}}{\Delta + \omega_{\perp\iota}}.$$

In the same way, we can write the expression for the double Gamow–Teller matrix element

$$M_{1\diamond jq} = \sigma_{fj}, \qquad M_{2\diamond jq} = \sigma_{bj},$$
$$M^{(\mathrm{GT})}_{2\nu} = \frac{(-1)^q M_{1\diamond\iota q}M_{2\diamond\iota(-q)}}{\Delta + \omega_{\diamond\iota}} = \frac{3\sigma_{f\iota}\sigma_{b\iota}}{\Delta + \omega_{\diamond\iota}}.$$

To summarize, we have developed a collective treatment for motion in the isospace and the gauge space. The system is described within a moving frame of reference by using both collective variables (determining the orientation of the moving frame) and intrinsic variables (describing the motion of the particles with respect to the moving frame) [1]. Two difficulties have to be overcome: (i) a zero-frequency RPA mode and subsequent infrared problems should be expected if the Hamiltonian is an isoscalar, and (ii) the Hamiltonian is not an isoscalar. Thus, we must disentangle the real isospin mixing effects produced by the Hamiltonian from those produced by our isospin-violating treatment. The solution has been checked against exact results for the case of particles moving in a single-j shell and coupled by the isovector pairing interaction [2]. The agreement is very satisfactory. This is not the case for other procedures used previously to treat the same problem (as the renormalized version of the RPA, etc.).

2. CENTER-OF-MASS EFFECTS IN ELECTROWEAK DECAYS

We now turn to the discussion of spurious center-of-mass effects in nuclear Hamiltonians [4]. The problem is perhaps one of the most studied ones and, together with the particle number and angular momentum symmetries, received a lot of attention in the past, mainly in connection with the development of projection techniques. We shall discuss the spurious center-of-mass motion as we have discussed the isospin case, by the way of the separation between collective and intrinsic variables. We shall also discuss the structure of the counterterms that should be introduced to fulfill translational and Galilean invariances [4].

2.1. The Hamiltonian

The degree of violation of the translational and Galilean invariances of a given Hamiltonian H is measured by the commutators

$$\pi_\mu \equiv [H, p_\mu], \qquad \rho_\mu \equiv [H, r_\mu] - \frac{i}{m}p_\mu,$$

which are, in general, nonvanishing operators.

2.2. Counterterms

In order to restore the invariances, we may add counterterms to the Hamiltonian; they are formally defined by

$$H_p = \mathbf{P}\cdot\mathbf{r}, \qquad H_r = \mathbf{R}\cdot\mathbf{p},$$
$$0 = \pi_\mu + iAP_\mu + (-1)^\nu[P_{-\nu}, p_\mu]r_\nu + (-1)^\nu[R_{-\nu}, p_\mu]p_\nu,$$
$$0 = \rho_\mu - iAR_\mu + (-1)^\nu[P_{-\nu}, r_\mu]r_\nu + (-1)^\nu[R_{-\nu}, r_\mu]p_\nu,$$

and these equations have to be solved for each order of the expansion in powers of $1/A$. The systematic application of the previous procedure associates residual interactions to any single-particle Hamiltonian. In what follows we study some applications to the most frequent single-particle contributions, namely, the harmonic oscillator potential, the spin–orbit and l^2 terms, and the empirical single-particle Hamiltonian.

2.3. Single-Particle Hamiltonians

(i) The harmonic oscillator case is

$$H_{\rm sp}^{\rm ho} = \frac{1}{2m}p^2 + \frac{m\omega^2}{2}r^2.$$

The resulting interaction is

$$H_p^{\rm ho} = -\chi_{\rm ho}\mathbf{r}\cdot\mathbf{r}, \qquad \chi_{\rm ho} = \frac{m\omega^2}{2A}.$$

The single-particle and residual interactions are

$$H^{\rm ho} = \frac{1}{2m}p^2 + \frac{\chi_{\rm ho}}{2}\sum_{ab}|\mathbf{r}_a - \mathbf{r_b}|^2.$$

(ii) Spin–orbit interaction. The single-particle term is

$$H_{\rm sp}^{so} = -\chi_{so}(\mathbf{l}\cdot\mathbf{s})_{(1v)}.$$

The two-body interactions are

$$H_p^{so} = \frac{\chi_{so}}{A}\sum_w(\mathbf{p}\times\mathbf{s})_{(1(v-w))}\cdot\mathbf{r}_{(1w)},$$

$$H_r^{so} = -\frac{\chi_{so}}{A}\sum_w(\mathbf{r}\times\mathbf{s})_{(1(v-w))}\cdot\mathbf{p}_{(1w)}.$$

The total Hamiltonian is

$$H^{so} = H_{\rm sp}^{so} + H_p^{so} + H_r^{so}$$
$$= -\frac{\chi_{so}}{2A}\sum_{ab}(\mathbf{r}_a - \mathbf{r}_b)\times(\mathbf{p}_a - \mathbf{p}_b)\cdot(\mathbf{s}_a + \mathbf{s}_b) + \frac{\chi_{so}}{2A}(\mathbf{l}\cdot\mathbf{s})_{(2v)},$$

$$P_\mu = \frac{\chi_{so}}{A}\left((\mathbf{p}\times\mathbf{s})_{\mu(1v)} - \frac{1}{2A}\times\sum_w\left(\mathbf{p}_{(1(v-w))}\times\mathbf{s}_{(1w)}\right)_{\mu(2v)}\right),$$

$$R_\mu = -\frac{\chi_{so}}{A}\left((\mathbf{r}\times\mathbf{s})_{\mu(1v)} - \frac{1}{2A}\times\sum_w\left(\mathbf{r}_{(1(v-w))}\times\mathbf{s}_{(1w)}\right)_{\mu(2v)}\right).$$

(iii) The l^2 terms are

$$H_{\rm sp}^{ll} = -\chi_{ll}(\mathbf{l}\cdot\mathbf{l}).$$

The interactions are

$$H_p^{ll} = \frac{\chi_{ll}}{A}(\mathbf{p}\times\mathbf{l})\cdot\mathbf{r} - \frac{\chi_{ll}}{A}(\mathbf{l}\times\mathbf{p})\cdot\mathbf{r} - \frac{2\chi_{ll}}{3A^2}\langle p^2\rangle\mathbf{r}\cdot\mathbf{r},$$
$$H_r^{ll} = \frac{\chi_{ll}}{A}(\mathbf{l}\times\mathbf{r})\cdot\mathbf{p} - \frac{\chi_{ll}}{A}(\mathbf{r}\times\mathbf{l})\cdot\mathbf{p} - \frac{2\chi_{ll}}{3A^2}\langle r^2\rangle\mathbf{p}\cdot\mathbf{p}.$$

The sum of the contributions is

$$H_{\rm sp}^{ll} + H_p^{ll} + H_r^{ll}$$
$$= -\frac{\chi_{ll}}{2A}\sum_{ab}|(\mathbf{r}_a - \mathbf{r}_b)\times(\mathbf{p}_a - \mathbf{p}_b)|^2 - \frac{2\chi_{ll}}{3A}\langle p^2\rangle\left(\frac{\mathbf{r}\cdot\mathbf{r}}{A} - (\mathbf{r}\cdot\mathbf{r})_{(11)+(10)}\right) - \frac{2\chi_{ll}}{3A}\langle r^2\rangle\left(\frac{1}{A}\mathbf{p}\cdot\mathbf{p} - (\mathbf{p}\cdot\mathbf{p})_{(11)+(10)}\right) + \frac{\chi_{ll}}{A}\mathbf{l}\cdot\mathbf{l} + \frac{\chi_{ll}}{A}\sum_{ab}\mathbf{r}_b\times\mathbf{p}_a\cdot\mathbf{r}_a\times\mathbf{p}_b + \frac{\chi_{ll}}{A}(\mathbf{r}\cdot\mathbf{r})_{(11)+(10)}(\mathbf{p}\cdot\mathbf{p})_{(11)+(10)} - \frac{\chi_{ll}}{A}\times\sum_{\mu,a,b}(-1)^\mu r_{a,\mu}p_{b,\mu}(r_{a,\mu+1}p_{b,\mu+1} + r_{a,\mu-1}p_{b,\mu-1}).$$

2.4. The Collective Formalism

The above-described solution guarantees that there is a zero-frequency RPA boson for each direction of space. This consequence of the homogeneity of space gives rise to infrared divergences, which should be taken into account. One way to solve the problem is to introduce collective coordinates, which in the present case represent the coordinates $\mathcal{R}_\mu$ determining the position of the moving frame of reference relative to the laboratory frame. Within this description, there is no way to distinguish between the motion of the body in one direction and the displacement of the frame of reference in the opposite one. This gauge-type invariance is expressed by the constraint $p_\mu - \mathcal{P}_\mu = 0$, where $\mathcal{P}_\mu$ is the generator of displacements of the moving frame, hereon the collective momentum ($[\mathcal{R}_{-\mu}, \mathcal{P}_\nu] = i(-1)^\mu\delta_{\mu\nu}$). Physical

states $|\text{phys}\rangle$ are annihilated by the constraint, and physical operators $\mathcal{O}_{\text{phys}}$ commute with it. As is well known, the constraints may be taken into account by adding to the Hamiltonian the terms proportional to the Lagrange multipliers $\mathbf{\Omega}$

$$H \to H - \mathbf{\Omega} \cdot (\mathbf{p} - \boldsymbol{\mathcal{P}})$$

and requiring the vanishing of $\mathbf{B}$, the momentum conjugate to $\mathbf{\Omega}$ ($[\Omega_{-\mu}, B_\nu] = i(-1)^\mu \delta_{\mu\nu}$).

The BRST Hamiltonian reads

$$H_{\text{BRST}} = H - \mathbf{\Omega} \cdot (\mathbf{p} - \boldsymbol{\mathcal{P}}) + i\boldsymbol{\pi} \cdot \bar{\boldsymbol{\pi}} + \omega^2 \left(\frac{\mathbf{r} \cdot \mathbf{B}}{A} - \frac{\mathbf{B} \cdot \mathbf{B}}{2mA} - i\bar{\boldsymbol{\eta}} \cdot \boldsymbol{\eta} \right)$$

and the different elements entering into the BRST Hamiltonian are the Hermitian and nilpotent operator $\mathcal{Q}$, the fermion ghost operators, and their conjugate momenta. The BRST charge is given by

$$\mathcal{Q} = (\mathbf{p} - \boldsymbol{\mathcal{P}}) \cdot \boldsymbol{\eta} + \mathbf{B} \cdot \bar{\boldsymbol{\pi}}.$$

In the same manner, we can write the operator for the transformation to a moving frame

$$T = \exp\left[\frac{i}{A} \boldsymbol{\mathcal{P}} \cdot \left(\frac{\mathbf{B}}{m} - \mathbf{r} \right) \right],$$

$$T H_{\text{BRST}} T^+ = H'_{\text{BRST}} + \frac{1}{2mA} \mathcal{P}^2.$$

By applying this procedure, we may transform the coordinate to (transformed operator)

$$TF(\mathbf{r}_i + \boldsymbol{\mathcal{R}})T^{-1} = F\left(\mathbf{r}_i + \frac{1}{A}\left(\frac{\mathbf{B}}{m} - \mathbf{r} \right) + \boldsymbol{\mathcal{R}} \right) \to F\left(\mathbf{r}_i - \frac{\mathbf{r}}{A} + \boldsymbol{\mathcal{R}} \right).$$

In the moving frame of reference, the collective variables $\boldsymbol{\mathcal{R}}$ are considered to be real, and thus, as a tradeoff, some original degrees of freedom must join the spurious sector. At the level of elementary modes of excitation, these are given by the RPA zero-frequency modes. In addition to the spurious sector $|n_{0\mu}, n_{1\mu}\rangle$, the intrinsic sector displays elementary modes of excitation, which are represented by the finite-frequency RPA modes $|n_\nu\rangle$ ($\omega_\nu > 0$). The physical operator is $\mathbf{r} + A\boldsymbol{\mathcal{R}}$, and it reduces to $A\boldsymbol{\mathcal{R}}$ after being boosted: the vector $\mathbf{r}$ disappeares from the calculation (and the associated infrared divergencies as well). The problem is reduced to the calculation of the well-behaved operator $\boldsymbol{\mathcal{R}}$ within the collective sector of the Hilbert space.

2.5. Empirical Single-Particle Energies

We have performed three sets of RPA calculations using the empirical single-particle energies (as in ^{208}Pb) and introducing as interaction (i) an $\mathbf{r} \cdot \mathbf{r}$ term with a self-consistent strength; (ii) the same interaction as in (i) but with such a strength that there is an eigenvalue as close to zero as allowed by the computational facilities; and (iii) the counterterms with the values of $\mathbf{P}_{(11)}, \mathbf{R}_{(11)}$. The results are given in [4], where the matrix elements of the operator $\mathbf{r}$ corresponding to transitions between the ground state and the excited states are calculated as a function of the excitation energy. Although calculation (i) with the self-consistent strength displays a prominent peak at low energies, the peak is finite and located at an energy significantly larger than zero. On the contrary, results (ii) and (iii) show the peak at zero energy (within the numerical accuracy of the calculation). This similarity apparently supports the use of procedure (ii) appearing in the literature. Let us consider now the matrix elements to finite frequency modes, which are the ones that interest us from the physical point of view. In this case, calculations (i) and (ii) yield very similar results, while the scale is smaller by two orders of magnitude for (iii), although the excitation pattern is quite similar. We conclude that the admixture of the spurious and the finite-frequency modes is not changed significantly by varying the strength of the $\mathbf{r} \cdot \mathbf{r}$ interaction and thus the use of this interaction does not insure that we obtain correct matrix elements for excited states [4].

2.6. Transition Operator

Conversion of muons into electrons may proceed according to the lepton-flavor-violating processes. Such a process is mainly of interest because of necessary mixing of muon and electron neutrinos. So far, there are experimental upper limits for this process. Considering the dominance of the contributions due to excitation of 1^- states in the context of the RPA diagonalization, it is obvious that from the nuclear structure point of view one has to estimate the nuclear matrix elements involved in the transitions as accurately as possible. The vector operator exciting $I^\pi = 1^-$ states may be written as

$$j_1(qr) Y_{1\mu}|_{(11)} = \sum_{n_\nu} \langle n_\nu | j_1 Y_1 | \rangle \left(\gamma^+_{n_\nu,\mu} - (-1)^\mu \gamma_{n_\nu,(-\mu)} \right) - \frac{i}{A}(-1)^\mu \langle [j_1 Y_{1\mu}, p_{-\mu}] \rangle r_{\mu(11)}, \quad (5)$$

where n_ν denotes the finite-frequency RPA mode and a similar expression should be used for the dipole axial-vector term of the weak current. Its contribution is not affected by the treatment of the spurious sector. The amplitude in the second line may be regularized. The results corresponding to the transition matrix elements of the shifted operator, obtained in the RPA

diagonalization, are given in [4]. The similarity of the results obtained with the three different Hamiltonians supports the claim about the validity of the procedure. The same effects are expected to materialize in the case of realistic calculations, and work is in progress to include the counterterms obtained in the previous sections, starting with realistic two-body forces.

3. CONCLUSIONS

We have treated the problem of broken symmetries in two steps: (i) reconstruction of the invariance of the Hamiltonian by introducing counterterms, and (ii) inclusion of collective variables in order to eliminate infrared singularities.

The comparison between the available exact results and those obtained by using the present approach shows the accuracy of the method. We thus suggest the use of the present approach in cases where, as in (μ^-, e^-) conversion, the dominance of the $I^\pi = 1^-$ channels is apparent or, as in the case of double Fermi and Gamow–Teller transitions in double-beta-decay processes, the strong dependence of the theoretical results on model parameters may limit the predictive power of the theory.

REFERENCES

1. D. R. Bes and J. Kurchan, *The Treatment of Collective Coordinates in Many-Body Systems* (World Sci., Singapore, 1990).
2. D. R. Bes, O. Civitarese, and N. N. Scoccola, Phys. Lett. B **446**, 93 (1999).
3. D. R. Bes, O. Civitarese, E. Maqueda, and N. N. Scoccola, Phys. Rev. C **61**, 024315 (2000).
4. D. R. Bes and O. Civitarese, Phys. Rev. C **63**, 044323 (2001).

Physics of Atomic Nuclei, Vol. 66, No. 3, 2003, pp. 444–451. From Yadernaya Fizika, Vol. 66, No. 3, 2003, pp. 472–479.

DOUBLE BETA DECAY

Majorana Neutrinos, *CP* Violation, Neutrinoless Double Beta and Tritium Beta Decays*

S. Pascoli** **and** **S. T. Petcov**[1)]**

Scuola Internazionale Superiore di Studi Avanzati and Istituto Nazionale di Fisica Nucleare, Trieste, Italy

Received February 13, 2002

Abstract—If the present or upcoming searches for neutrinoless double beta ($(\beta\beta)_{0\nu}$) decay give a positive result, the Majorana nature of massive neutrinos will be established. From the determination of the value of the $(\beta\beta)_{0\nu}$-decay effective Majorana mass parameter ($|\langle m\rangle|$), it would be possible to obtain information on the type of neutrino mass spectrum. Assuming 3-ν mixing and massive Majorana neutrinos, we discuss the information that a measurement of, or an upper bound on, $|\langle m\rangle|$ can provide on the value of the lightest neutrino mass m_1. With additional data on the neutrino masses obtained in ^{3}H β-decay experiments, it might be possible to establish whether the CP symmetry is violated in the lepton sector. This would require very high precision measurements. If CP invariance holds, the allowed patterns of the relative CP parities of the massive Majorana neutrinos would be determined. © *2003 MAIK "Nauka/Interperiodica"*.

1. INTRODUCTION

With the accumulation of more and stronger evidence for oscillations of the atmospheric [1] and solar [2] neutrinos, caused by neutrino mixing (see, e.g., [3]), the problem of the nature of massive neutrinos emerges as one of the fundamental problems in the studies of neutrino mixing. Massive neutrinos can be Dirac or Majorana particles. In the former case, they possess a conserved lepton charge and distinctive antiparticles, while in the latter there is no conserved lepton charge and massive neutrinos are truly neutral particles identical with their antiparticles [3]. Thus, the question of the nature of massive neutrinos is directly related to the question of the basic symmetries of the fundamental particle interactions.

The present and upcoming neutrino oscillation experiments will allow one to make a big step forward in understanding the patterns of neutrino mass-squared differences and of ν mixing, but will not be able to determine the absolute values of the neutrino masses or to answer the question regarding the nature of massive neutrinos. The ^{3}H β-decay experiments studying the electron spectrum are sensitive to the electron (anti)neutrino mass m_{ν_e} and can give information on the absolute value of neutrino masses. The present bounds on m_{ν_e} from the Troitsk [4] and Mainz [5] experiments (at 95% C.L.) are $m_{\nu_e} < 2.5$ eV [4] and $m_{\nu_e} < 2.9$ eV [5]. There are prospects (the KATRIN project) to increase the sensitivity of the ^{3}H β-decay experiments to $m_{\nu_e} \sim 0.3$–1.0 eV [6].

The problem of the nature of massive neutrinos can be addressed in experiments studying processes in which the total lepton charge L is not conserved and changes by two units, $\Delta L = 2$. The process most sensitive to the existence of massive Majorana neutrinos (coupled to the electron) is the neutrinoless double beta ($(\beta\beta)_{0\nu}$) decay of certain even–even nuclei $(A, Z) \to (A, Z+2) + e^- + e^-$ (see, e.g., [3]). If the $(\beta\beta)_{0\nu}$ decay is generated only by the left-handed charged-current weak interaction through the exchange of virtual light massive Majorana neutrinos, the probability amplitude of this process is proportional to the "effective Majorana mass parameter"

$$|\langle m\rangle| \equiv \left||U_{e1}|^2 m_1 + |U_{e2}|^2 e^{i\alpha_{21}} m_2 + |U_{e3}|^2 e^{i\alpha_{31}} m_3\right|, \quad (1)$$

where m_j is the mass of the Majorana neutrino ν_j; U_{ej} is the element of the Pontecorvo–Maki–Nakagawa–Sakata (PMNS) neutrino (lepton) mixing matrix [7, 8]; and α_{j1}, $j = 2, 3$, are two Majorana CP-violating phases [9]. If CP parity is conserved, we have [10, 11] $\alpha_{j1} = k\pi$, $k = 0, 1, 2, \ldots$ Many experiments are searching for $(\beta\beta)_{0\nu}$ decay. No indications that this process takes place have been found so far. The most stringent constraint on the value of $|\langle m\rangle|$ was obtained in the ^{76}Ge Heidelberg–Moscow experiment [12] $|\langle m\rangle| < 0.35$ eV (90% C.L.).

*This article was submitted by the authors in English.

[1)]Institute of Nuclear Research and Nuclear Energy, Bulgarian Academy of Sciences, Sofia, Bulgaria.

**e-mail: pascoli@sissa.it

The IGEX collaboration has obtained [13] $|\langle m\rangle| < 0.33-1.35$ eV (90% C.L.). Higher sensitivity to the value of $|\langle m\rangle|$ is planned to be reached in several $(\beta\beta)_{0\nu}$-decay experiments of a new generation [14]. The NEMO 3 and the planned CUORE experiments aim to achieve a sensitivity to values of $|\langle m\rangle| \cong 0.1$ eV. A sensitivity to $|\langle m\rangle| \cong 10^{-2}$ eV is planned to be reached in the GENIUS and EXO experiments.

The present article represents a continuation of the studies of the physical implications of the possible future results on $|\langle m\rangle|$ and on m_{ν_e} performed in [15–17]. The article is based on the work done in [17]. We generalize the results, derived in [17] by using the best fit values of the input neutrino oscillation parameters, to the case when some of these parameters take values in their 90% C.L. allowed regions. Earlier studies on the subject were performed, e.g., in [18–20]. Recent relevant studies include [21].

2. CONSTRAINING OR DETERMINING THE LIGHTEST NEUTRINO MASS m_1 AND/OR THE MAJORANA CP-VIOLATING PHASES

In this section, assuming 3-ν mixing, we discuss the information that future $(\beta\beta)_{0\nu}$-decay and/or ^{3}H β-decay experiments can provide on the lightest neutrino mass m_1 and on the CP violation generated by the Majorana CP-violating phases α_{21} and α_{31}. We number the three neutrinos with definite mass ν_j in such a way that their masses obey $m_1 < m_2 < m_3$. The two cases of neutrino mass spectrum are analyzed: spectrum with normal hierarchy, $\Delta m^2_\odot \equiv \Delta m^2_{21}$, and with inverted hierarchy, $\Delta m^2_\odot \equiv \Delta m^2_{32}$, $\Delta m^2_\odot > 0$ being the neutrino mass-squared difference characterizing the solar neutrino oscillations (see, e.g., [15, 17]). In both cases, we use in the analysis that follows fixed values of the mixing parameters $|U_{e3}|^2$ (or $|U_{e1}|^2$) and of the angle $\theta_\odot$, which are constrained by the CHOOZ and the solar neutrino data, respectively. In our further discussion, we assume $\cos 2\theta_\odot \geq 0$, which is favored by the analyses of the solar neutrino data [22]. The modification of the relevant formulas and of the results in the case $\cos 2\theta_\odot < 0$ is rather straightforward.

We allow $\Delta m^2_\odot$ and $\Delta m^2_{\rm atm}$, which characterizes the oscillations of atmospheric neutrinos, to vary within their 90% C.L. allowed intervals found in the analyses of the solar and atmospheric neutrino data in [22, 23]. We denote the minimal and maximal values in these intervals by $(\Delta m^2_\odot)_{\min}$, $(\Delta m^2_\odot)_{\max}$, $(\Delta m^2_{\rm atm})_{\min}$, and $(\Delta m^2_{\rm atm})_{\max}$. The results thus obtained are summarized in Fig. 1 (normal neutrino mass hierarchy) and in Fig. 2 (inverted hierarchy).

2.1. Normal Mass Hierarchy: $\Delta m^2_\odot \equiv \Delta m^2_{21}$

If $\Delta m^2_\odot = \Delta m^2_{21}$, for any given solution of the solar neutrino problem LMA MSW, LOW-QVO, and SMA MSW, $|\langle m\rangle|$ can lie anywhere between 0 and the present upper limits, as Fig. 1 indicates. This conclusion does not change even under the most favorable conditions for the determination of $|\langle m\rangle|$, namely, even when $\Delta m^2_{\rm atm}$, $\Delta m^2_\odot$, $\theta_\odot$, and θ are known with negligible uncertainty. The further conclusions in the case of the LMA MSW solution of the solar neutrino problem, which are illustrated in Fig. 1, are now summarized.

Case A. An experimental upper limit on $|\langle m\rangle|$, $|\langle m\rangle| < |\langle m\rangle|_{\rm exp}$, will determine a maximal value of m_1, $m_1 < (m_1)_{\max}$. The value $(m_1)_{\max}$ is fixed by one of the two equalities

$$|\langle m\rangle|_{\rm exp} = \left|\left(m_1\cos^2\theta_\odot - \sqrt{m_1^2 + (\Delta m^2_\odot)_{\max}}\sin^2\theta_\odot\right)\times(1-|U_{e3}|^2) - \sqrt{m_1^2+(\Delta m^2_{\rm atm})_{\max}}|U_{e3}|^2\right|, \quad (2)$$

$$|\langle m\rangle|_{\rm exp} = \left|\left(m_1\cos^2\theta_\odot - \sqrt{m_1^2 + (\Delta m^2_\odot)_{\min}}\sin^2\theta_\odot\right)\times(1-|U_{e3}|^2) + \sqrt{m_1^2+(\Delta m^2_{\rm atm})_{\max}}|U_{e3}|^2\right|. \quad (3)$$

Equation (2) is valid for $\cos 2\theta_\odot > (\Delta m^2_\odot/m_1^2)\sin^4\theta_\odot$; otherwise, (3) should be used.

For the quasi-degenerate mass spectrum, one has $m_1 \gg \Delta m^2_\odot, \Delta m^2_{\rm atm}$, $m_1 \cong m_2 \cong m_3 \cong m_{\nu_e}$, and [17, 21]

$$(m_1)_{\max} \cong \frac{|\langle m\rangle|_{\rm exp}}{|\cos 2\theta_\odot(1-|U_{e3}|^2) - |U_{e3}|^2|}. \quad (4)$$

If $|\cos 2\theta_\odot(1-|U_{e3}|^2) - |U_{e3}|^2|$ is sufficiently small, the upper limit on m_{ν_e} obtained in ^{3}H β-decay experiments could yield a more stringent upper bound on m_1 than the bound from the limit on $|\langle m\rangle|$.

Case B. A measurement of $|\langle m\rangle| = (|\langle m\rangle|)_{\rm exp} \gtrsim 0.02$ eV would imply that $m_1 \gtrsim 0.02$ eV and thus a mass spectrum with partial hierarchy or of quasi-degenerate type [15]. The lightest neutrino mass will be constrained to lie in the interval $(m_1)_{\min} \leq m_1 \leq (m_1)_{\max}$, where $(m_1)_{\max}$ and $(m_1)_{\min}$ are determined, respectively, by (2) and (3) and by the equation [17]

$$(m_1\cos^2\theta_\odot + \sqrt{m_1^2+(\Delta m^2_\odot)_{\max}}\sin^2\theta_\odot) \times(1-|U_{e3}|^2) + \sqrt{m_1^2+(\Delta m^2_{\rm atm})_{\max}}|U_{e3}|^2 \quad (5)$$

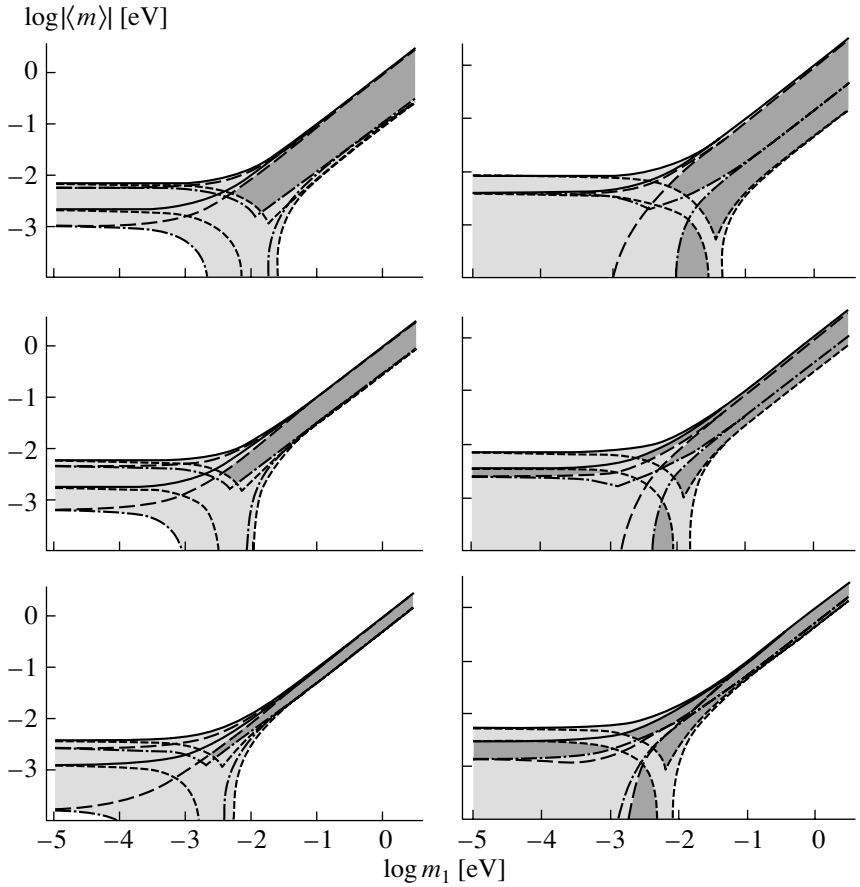

Fig. 1. The dependence of $|\langle m\rangle|$ on m_1 for $\Delta m^2_{\odot} = \Delta m^2_{21}$ in the case of 3-ν mixing and of the LMA MSW solution obtained at 90% C.L. in [23], for 0.1 (upper panels), 0.3 (middle panels), 0.54 (lower panels), and for $|U_{e3}|^2 = 0.05$ (right panels) and 0.01 (left panels). The allowed values of $|\langle m\rangle|$ are constrained to lie in the case of CP conservation (i) in the medium-gray region between the two solid curves if $\eta_{21} = \eta_{31} = 1$, (ii) in the medium-gray region between the two long-dashed curves and the axes if $\eta_{21} = -\eta_{31} = 1$, (iii) in the medium-gray region between the dash-dotted curves and the axes if $\eta_{21} = -\eta_{31} = -1$, and (iv) in the medium-gray region between the short-dashed curves if $\eta_{21} = \eta_{31} = -1$. In the case of CP violation, the allowed region for $|\langle m\rangle|$ covers all the gray region. Values of $|\langle m\rangle|$ in the dark gray region signal CP violation.

$$= |\langle m\rangle|_{\rm exp}.$$

The limiting values of m_1 correspond to the case of CP conservation. If it holds that $\Delta m^2_{\odot} \ll m_1^2$ (i.e., for $\Delta m^2_{\odot} \lesssim 10^{-4}$ eV^2), $(m_1)_{\rm min}$ to a good approximation is independent of $\theta_{\odot}$, and for $\sqrt{\Delta m^2_{\rm atm}}|U_{e3}|^2 \ll m_1$, which takes place in the case we consider as $|U_{e3}|^2 \lesssim 0.05$, we have $(m_1)_{\rm min} \cong (|\langle m\rangle|)_{\rm exp}$. For $|U_{e3}|^2 \ll \cos 2\theta_{\odot}$, which is realized in Fig. 1 for $|U_{e3}|^2 \lesssim 0.01$, practically all the region between $(m_1)_{\rm min}$ and $(m_1)_{\rm max}$, $(m_1)_{\rm min} < m_1 < (m_1)_{\rm max}$, corresponds to violation of the CP symmetry. If $|U_{e3}|^2$ is nonnegligible with respect to $\cos 2\theta_{\odot}$, e.g., if $|U_{e3}|^2 \cong 0.02$–0.05 for the values of $\cos 2\theta_{\odot}$ used to derive the right panels in Fig. 1, one can have $(m_1)_{\rm min} < m_1 < (m_1)_{\rm max}$ if the CP symmetry is violated, as well as in two specific cases of CP conservation [17]. One of these two CP-conserving values of m_1, corresponding to $\eta_{21} = -\eta_{31} = -1$, can differ considerably from the two limiting values (Fig. 1). In general, the knowledge of the value of $|\langle m\rangle|$ alone will not allow one to distinguish the case of CP conservation from that of CP violation.

Case C. It might be possible to determine whether CP violation due to the Majorana phases takes place in the lepton sector if both $|\langle m\rangle|$ and m_{ν_e} are measured. Since prospective measurements are limited to $(m_{\nu_e})_{\rm exp} \gtrsim 0.35$ eV, the relevant neutrino mass spectrum is of quasi-degenerate type, $m_1 \cong m_2 \cong m_3 \cong m_{\nu_e}$ (see, e.g., [15]), and one has $m_1 > 0.35$ eV. If we can neglect $|U_{e3}|^2$ (i.e., if $\cos 2\theta_{\odot} \gg |U_{e3}|^2$), a value of $m_{\nu_e} \cong m_1$, satisfying $(m_1)_{\rm min} < m_{\nu_e} < (m_1)_{\rm max}$, where $(m_1)_{\rm min}$ and $(m_1)_{\rm max}$ are determined by (5) and (2) or (3), would imply that the CP symmetry does not hold in the lepton sector. In this case, one would obtain correlated constraints on the CP violating phases α_{21} and α_{31} [15, 24]. This appears to

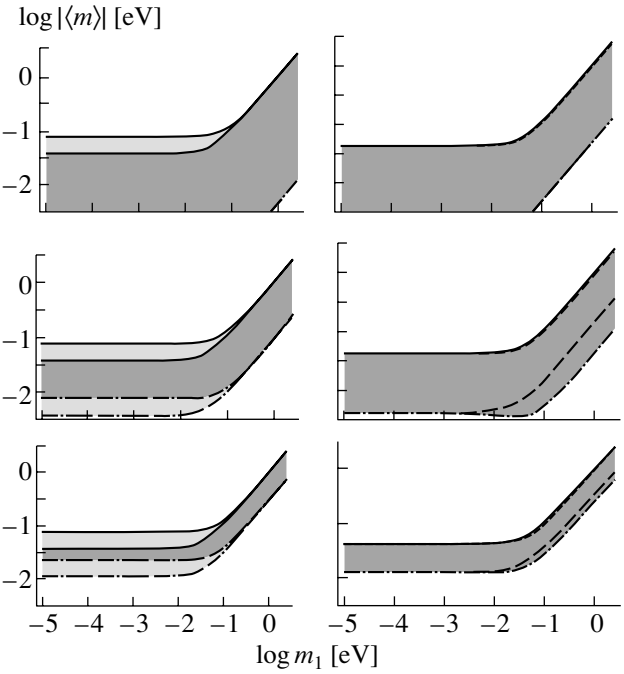

Fig. 2. The dependence of $|\langle m\rangle|$ on m_1 for $\Delta m^2_{\odot} = \Delta m^2_{32}$ in the case of 3-ν mixing and of the LMA MSW solution obtained at 90% C.L. in [23], for $\cos 2\theta_{\odot} = 0$ (upper panels), 0.1 (middle panels), 0.3 (lower panels), and for $|U_{e1}|^2 = 0.05$ (right panels) and 0.005 (left panels). The allowed regions for $|\langle m\rangle|$ correspond to, for $|U_{e1}|^2 = 0.005$, (i) the medium-gray regions between the solid curves if $\eta_{21} = \eta_{31} = \pm 1$, (ii) the medium-gray regions between the dashed curves (lowest left and middle left panels) or the dashed line (upper left panel) if $\eta_{21} = -\eta_{31} = \pm 1$, and all the gray regions if CP invariance does not hold, and, for $|U_{e1}|^2 = 0.05$, (iii) the solid curves if $\eta_{21} = \eta_{31} = 1$, (iv) the long-dashed curves if $\eta_{21} = -\eta_{31} = 1$, (v) the dash-dotted curves if $\eta_{21} = -\eta_{31} = -1$, (vi) the short-dashed curves if $\eta_{21} = \eta_{31} = -1$, and all the gray regions if CP invariance does not hold. Values of $|\langle m\rangle|$ in the dark gray region signal CP violation.

be the only possibility for demonstrating CP violation due to Majorana CP-violating phases in the case of $\Delta m^2_{\odot} \equiv \Delta m^2_{21}$ under discussion [17]. In order to reach a definite conclusion concerning CP violation due to the Majorana CP violating phases, considerable accuracy in the measured values of $|\langle m\rangle|$ and m_{ν_e} is required. For example, if the oscillation experiments give the result $\cos 2\theta_{\odot} \leq 0.3$ and $|\langle m\rangle| = 0.3$ eV, a value of m_{ν_e} between 0.3 eV and 1.0 eV would demonstrate CP violation. This requires better than 30% accuracy on both measurements. The accuracy requirements become less stringent if the upper limit on $\cos 2\theta_{\odot}$ is smaller.

If $\cos 2\theta_{\odot} > |U_{e3}|^2$ but $|U_{e3}|^2$ cannot be neglected in $|\langle m\rangle|$, there exist two CP-conserving values of m_{ν_e} in the interval $(m_1)_{\min} < m_{\nu_e} < (m_1)_{\max}$ [17]. The one that can significantly differ from the extreme values of the interval corresponds to the specific case of CP conservation with $\eta_{21} = -\eta_{31} = -1$ (Fig. 1).

Case D. A measured value of m_{ν_e}, $(m_{\nu_e})_{\exp} \gtrsim 0.35$ eV, satisfying $(m_{\nu_e})_{\exp} > (m_1)_{\max}$, where $(m_1)_{\max}$ is determined from the upper limit on $|\langle m\rangle|$, (2) or (3), in the case where $(\beta\beta)_{0\nu}$ decay is not observed, might imply that the massive neutrinos are Dirac particles. If $(\beta\beta)_{0\nu}$ decay has been observed and $|\langle m\rangle|$ measured, the inequality $(m_{\nu_e})_{\exp} > (m_1)_{\max}$ would lead to the conclusion that there exist contribution(s) to the $(\beta\beta)_{0\nu}$-decay rate other than that due to the light Majorana neutrino exchange (see, e.g., [25] and the references quoted therein) that partially cancel the one from the Majorana neutrino exchange.

Case E. An actual measurement of $|\langle m\rangle| \lesssim 10^{-2}$ eV is unlikely, but it is illustrated in Fig. 1 to show the interpretation of such a result. There always remains an upper limit on m_1, $(m_1)_{\max}$, determined by (2) or by (3). For $|U_{e3}|^2 \geq \widehat{|U_{e3}|^2}$, where $\widehat{|U_{e3}|^2} \equiv (\sqrt{(\Delta m^2_{\odot})_{\min}}\sin^2\theta_{\odot})/\sqrt{(\Delta m^2_{\mathrm{atm}})_{\max}}$, the cancellations between the different terms allow one to have $(m_1)_{\min} = 0$. Both the cases of CP conservation and CP violation are allowed. In principle, there exists the possibility of having regions of the parameter space where only the case of CP violation is allowed. However, in order to establish that $|\langle m\rangle|$ and m_1 lie in those regions, they must be known with a precision which is far beyond that aimed at in the currently planned future experiments.

If $|U_{e3}|^2 < \widehat{|U_{e3}|^2}$ and $|\langle m\rangle|$ lies in the interval $|\langle m\rangle|_- \leq |\langle m\rangle| \leq |\langle m\rangle|_+$, defined by

$$|\langle m\rangle|_+ = \Big|\sqrt{(\Delta m^2_\odot)_{\max}}(\sin^2\theta_\odot)_{\max}(1-|U_{e3}|^2) + \sqrt{(\Delta m^2_{\rm atm})_{\max}}|U_{e3}|^2\Big|, \quad (6)$$

$$|\langle m\rangle|_- = \Big|\sqrt{(\Delta m^2_\odot)_{\min}}(\sin^2\theta_\odot)_{\min}(1-|U_{e3}|^2) - \sqrt{(\Delta m^2_{\rm atm})_{\max}}|U_{e3}|^2\Big|, \quad (7)$$

where $(\sin^2\theta_\odot)_{\min}$ and $(\sin^2\theta_\odot)_{\max}$ are respectively the minimal and maximal allowed values of $\sin^2\theta_\odot$ in the LMA solution region, the lower limit on m_1 goes to zero. All the CP-parity patterns in the case of CP conservation as well as the violation of the CP symmetry are possible. If $|U_{e3}|^2 < \widehat{|U_{e3}|^2}$ and $|\langle m\rangle| < |\langle m\rangle|_-$, $(m_1)_{\min}$ is determined by the following equation:

$$|\langle m\rangle|_{\rm exp} = \Big|(m_1\cos^2\theta_\odot - \sqrt{m_1^2+(\Delta m^2_\odot)_{\min}}\sin^2\theta_\odot) \times (1-|U_{e3}|^2) + \sqrt{m_1^2+(\Delta m^2_{\rm atm})_{\max}}|U_{e3}|^2\Big|. \quad (8)$$

Under the above conditions, the case of CP conservation corresponding to $\eta_{21} = \pm\eta_{31} = 1$ will be excluded. At the same time, both the case of CP conservation with $\eta_{21} = \pm\eta_{31} = -1$ and that of CP violation will be allowed.

It should be noted also that one can have $|\langle m\rangle| = 0$ for $m_1 = 0$ in the case of CP invariance if $\eta_{21} = -\eta_{31}$ and the relation $\sqrt{\Delta m^2_\odot}\sin^2\theta_\odot(1-|U_{e3}|^2) = \sqrt{\Delta m^2_{\rm atm}}|U_{e3}|^2$ holds. Finally, there would seem to be no practical possibility of determining the Majorana CP-violating phases.

The analysis of the Cases A–E for the LOW-QVO solution of the solar neutrino problem leads to the same qualitative conclusions as those obtained above for the LMA MSW solution. The conclusions differ, however, in the case of the SMA MSW solution, and we will discuss them next briefly [17]. An experimental upper limit on $|\langle m\rangle|$ (Case A) in the range $|\langle m\rangle|_{\rm exp} \geq 10^{-2}$ eV would imply, in the case of the SMA MSW solution, $m_1 < |\langle m\rangle|_{\rm exp}(1-2|U_{e3}|^2)^{-1}$. For values of $|\langle m\rangle| \gtrsim 10^{-2}$ eV, the maximum and minimum values of m_1 are extremely close: $(m_1)_{\min} \cong |\langle m\rangle|_{\rm exp}$. As a result, a measurement of $|\langle m\rangle|$ (Case B) practically determines m_1, $m_1 \cong |\langle m\rangle|$. However, no information about CP violation generated by the Majorana phases can be obtained by the measurement of $|\langle m\rangle|$ (or of $|\langle m\rangle|$ and m_{ν_e}) [15]. If both $|\langle m\rangle| \gtrsim 0.02$ eV and $m_{\nu_e} \gtrsim 0.35$ eV were measured (Case C), the relation $m_1 \cong (|\langle m\rangle|)_{\rm exp} \cong (m_{\nu_e})_{\rm exp}$ should hold. The conclusions in the Cases D and E are qualitatively the same as for the LMA MSW solution.

2.2. Inverted Mass Hierarchy: $\Delta m^2_\odot \equiv \Delta m^2_{32}$

Consider next the possibility of a neutrino mass spectrum with inverted hierarchy, which is illustrated in Fig. 2. A comparison of Figs. 1 and 2 reveals two major differences in the predictions for $|\langle m\rangle|$: if $\Delta m^2_\odot \equiv \Delta m^2_{32}$, (i) even in the case of $m_1 \ll m_2 \cong m_3$ (i.e., even if $m_1 \ll 0.02$ eV), $|\langle m\rangle|$ can exceed $\sim 10^{-2}$ eV and can reach the value of ~ 0.08 eV [15], and (ii) a more precise determination of $\Delta m^2_{\rm atm}$, $\Delta m^2_\odot$, $\theta_\odot$, and $\sin^2\theta = |U_{e1}|^2$ can lead to a lower limit on the possible values of $|\langle m\rangle|$ [15]. For the LMA and the LOW-QVO solutions, $\min(|\langle m\rangle|)$ will depend, in particular, on whether CP invariance holds or not in the lepton sector, and if it holds, it will depend on the relative CP parities of the massive Majorana neutrinos. All these possibilities are parametrized by the values of the two CP-violating phases, α_{21} and α_{31}, entering into the expression for $|\langle m\rangle|$. The existence of a significant lower limit on the possible values of $|\langle m\rangle|$ depends crucially in the cases of the LMA and LOW-QVO solutions on the minimal value of $|\cos 2\theta_\odot|$, $|\cos 2\theta_\odot|_{\min}$, allowed by the data. Up to corrections of $\sim 5\times 10^{-3}$ eV, the minimum value of $|\langle m\rangle|$ for these two solutions is (see, e.g., [15])

$$(|\langle m\rangle|)_{\min} \simeq \Big|\sqrt{(\Delta m^2_{\rm atm})_{\min}}|(\cos 2\theta_\odot)|_{\min}(1-|U_{e1}|^2)\Big|. \quad (9)$$

The $\min(|\langle m\rangle|)$ in (9) is reached in the case of CP invariance and $\eta_{21} = -\eta_{31} = \pm 1$.

We shall discuss next briefly the implications of the results of future $(\beta\beta)_{0\nu}$-decay and ^{3}H β-decay experiments. We follow the same line of analysis that we have used for the neutrino mass spectrum with normal hierarchy. Consider the case of the LMA MSW solution of the solar neutrino problem.

Case A. An experimental upper limit on $|\langle m\rangle|$, $|\langle m\rangle| < |\langle m\rangle|_{\rm exp}$, which is larger than the minimal value of $|\langle m\rangle|$, $|\langle m\rangle|^{\rm ph}_{\min}$, predicted by taking into account all uncertainties in the values of the relevant input parameters ($\Delta m^2_{\rm atm}$, $\Delta m^2_\odot$, $\theta_\odot$, etc.), $|\langle m\rangle|_{\rm exp} \geq |\langle m\rangle|^{\rm ph}_{\min}$, will imply an upper limit on

m_1, $m_1 < (m_1)_{\max}$. The latter is determined by the equality

$$\left| \left(\sqrt{m_1^2 + (\Delta m^2_{\rm atm})_{\min} - (\Delta m^2_{\odot})_{\max}} \cos^2\theta_{\odot} - \sqrt{m_1^2 + (\Delta m^2_{\rm atm})_{\min}} \sin^2\theta_{\odot} \right) (1 - |U_{e1}|^2) \pm m_1 |U_{e1}|^2 \right| = |\langle m \rangle|_{\rm exp}, \quad (10)$$

where the $+\,(-)$ corresponds to a negative (positive) value of the expression in the big round brackets [17]. For the quasi-degenerate neutrino mass spectrum ($m_1 \gg \Delta m^2_{\odot}, \Delta m^2_{\rm atm}$, $m_1 \cong m_2 \cong m_3 \cong m_{\nu_e}$), $(m_1)_{\max}$ is given by (4) in which $|U_{e3}|^2$ is replaced by $|U_{e1}|^2$. Correspondingly, the conclusion that, if $|\cos 2\theta_{\odot}(1 - |U_{e1}|^2) - |U_{e1}|^2|$ is sufficiently small, the upper limit on $m_1 \cong m_{\nu_e}$, obtained in ^{3}H β decay, can be more stringent than the upper bound on m_1, implied by the limit on $|\langle m \rangle|$, remains valid.

An experimental upper limit on $|\langle m \rangle|$, which is smaller than the minimal possible value of $|\langle m \rangle|$, $|\langle m \rangle|_{\rm exp} < |\langle m \rangle|^{\rm ph}_{\min}$, would imply that either (i) the neutrino mass spectrum is not of the inverted hierarchy type, or (ii) there exist contributions to the $(\beta\beta)_{0\nu}$-decay rate other than due to the light Majorana neutrino exchange (see, e.g., [25]) that partially cancel the contribution from the Majorana neutrino exchange. The indicated result might also suggest that the massive neutrinos are Dirac particles.

Case B. A measurement of $|\langle m \rangle| = (|\langle m \rangle|)_{\rm exp} \gtrsim \sqrt{(\Delta m^2_{\rm atm})_{\max}}(1 - |U_{e1}|^2) \cong 0.04$–$0.08$ eV, where we have used the 90% C.L. allowed regions of $\Delta m^2_{\rm atm}$ and $|U_{e1}|^2$ from [23], would imply the existence of a finite interval of possible values of m_1, $(m_1)_{\min} \leq m_1 \leq (m_1)_{\max}$, with $(m_1)_{\max}$ and $(m_1)_{\min}$ given, respectively, by (10) and by the equality

$$m_1 |U_{e1}|^2 + \left(\sqrt{m_1^2 + (\Delta m^2_{\rm atm})_{\max} - (\Delta m^2_{\odot})_{\min}} \cos^2\theta_{\odot} + \sqrt{m_1^2 + (\Delta m^2_{\rm atm})_{\max}} \sin^2\theta_{\odot} \right) \times (1 - |U_{e1}|^2) = |\langle m \rangle|_{\rm exp}. \quad (11)$$

In this case, $m_1 \gtrsim 0.04$ eV and the neutrino mass spectrum is with partial inverted hierarchy or of quasi-degenerate type [15]. The limiting values of m_1 correspond to CP conservation. For $\Delta m^2_{\odot} \ll m_1^2$, i.e., for $\Delta m^2_{\odot} \lesssim 10^{-4}$ eV^2, $(m_1)_{\min}$ is to a good approximation independent of $\theta_{\odot}$ and we have $\sqrt{((m_1)_{\min})^2 + (\Delta m^2_{\rm atm})_{\max}}(1 - |U_{e1}|^2) \cong (|\langle m \rangle|)_{\rm exp}$.

For negligible $|U_{e1}|^2$ (i.e., $|U_{e1}|^2 \lesssim 0.01$ for the values of $\cos 2\theta_{\odot}$ in Fig. 2), essentially all of the interval between $(m_1)_{\min}$ and $(m_1)_{\max}$, $(m_1)_{\min} < m_1 < (m_1)_{\max}$, corresponds to violation of the CP symmetry. If the term $\sim m_1 |U_{e1}|^2$ cannot be neglected in (10) and (11) (i.e., if $|U_{e1}|^2 \cong 0.02$–0.05 for the values of $\cos 2\theta_{\odot}$ in Fig. 2), there exists for a fixed $|\langle m \rangle|_{\rm exp}$ two CP-conserving values of m_1 in the indicated interval [17], one of which differs noticeably from the limiting values $(m_1)_{\min}$ and $(m_1)_{\max}$ and corresponds to $\eta_{21} = -\eta_{31} = 1$ (Fig. 2).

In general, measuring the value of $|\langle m \rangle|$ alone will not allow one to distinguish the case of CP conservation from that of CP violation. In principle, a measurement of m_{ν_e}, or even an upper limit on m_{ν_e} smaller than $(m_1)_{\max}$, could be a signal of CP violation, as Fig. 2 (upper panels) shows. However, unless $\cos 2\theta_{\odot}$ is very small, the required values of m_{ν_e} are less than prospective measurements. For example, as is seen in Fig. 2, middle left panel, for $\cos 2\theta_{\odot} = 0.1$ and $|\langle m \rangle| = 0.03$ eV, one needs to find $m_{\nu_e} < 0.35$ eV to demonstrate CP violation.

If the measured value of $|\langle m \rangle|$ lies in the interval $(|\langle m \rangle|_-)_{\max} \leq |\langle m \rangle| \leq (|\langle m \rangle|_+)_{\min}$, where

$$(|\langle m \rangle|_+)_{\max} = \left| \sqrt{(\Delta m^2_{\rm atm})_{\max} - (\Delta m^2_{\odot})_{\min}} \cos^2\theta_{\odot} + \sqrt{(\Delta m^2_{\rm atm})_{\max}} \sin^2\theta_{\odot} \right| (1 - |U_{e1}|^2), \quad (12)$$

$$(|\langle m \rangle|_-)_{\min} = \left| \sqrt{(\Delta m^2_{\rm atm})_{\min} - (\Delta m^2_{\odot})_{\max}} \cos^2\theta_{\odot} - \sqrt{(\Delta m^2_{\rm atm})_{\min}} \sin^2\theta_{\odot} \right| (1 - |U_{e1}|^2), \quad (13)$$

we would have $(m_1)_{\min} = 0$. Furthermore, if one finds that $|\langle m \rangle| < (|\langle m \rangle|_+)_{\min}$ with

$$(|\langle m \rangle|_+)_{\min} = \left| \sqrt{(\Delta m^2_{\rm atm})_{\min} - (\Delta m^2_{\odot})_{\max}} \cos^2\theta_{\odot} + \sqrt{(\Delta m^2_{\rm atm})_{\min}} \sin^2\theta_{\odot} \right| (1 - |U_{e1}|^2),$$

the case of CP conservation corresponding to $\eta_{21} = \eta_{31} = \pm 1$ will be excluded. If $(|\langle m \rangle|_-)_{\max} < |\langle m \rangle| < (|\langle m \rangle|_+)_{\min}$, where

$$(|\langle m \rangle|_-)_{\max} = \left| \sqrt{(\Delta m^2_{\rm atm})_{\max} - (\Delta m^2_{\odot})_{\min}} \cos^2\theta_{\odot} \right.$$

$$- \sqrt{(\Delta m^2_{\rm atm})_{\rm max}}\sin^2\theta_\odot \Big| (1-|U_{e1}|^2)$$

and $0 < m_1 < (m_1)_{\rm max}$, one will conclude that the CP symmetry is violated.

Case C. As Fig. 2 indicates, the discussions and conclusions are identical to the ones in the same cases for the neutrino mass spectrum with normal hierarchy, except that $(m_1)_{\rm max}$ and $(m_1)_{\rm min}$ are determined by (10) and (12), and $|U_{e3}|^2$ must be substituted by $|U_{e1}|^2$ in the relevant parts of the analysis.

Case E. It is possible to have a measured value of $|\langle m\rangle| \lesssim 10^{-2}$ eV in the case of the LMA MSW solution and neutrino mass spectrum with inverted hierarchy under discussion only if $\cos 2\theta_\odot$ is rather small, $\cos 2\theta_\odot \lesssim 0.2$. A measured value of $|\langle m\rangle| < |\langle m\rangle|^{\rm ph}_{\rm min}$ would imply that either the neutrino mass spectrum is not of the inverted hierarchy type, or that there exist contributions to the $(\beta\beta)_{0\nu}$-decay rate other than due to the light Majorana neutrino exchange that partially cancel the contribution from the Majorana neutrino exchange.

The above conclusions hold with minor modifications (essentially of the numerical values involved) for the LOW-QVO solution as well. In the case of the SMA MSW solution, we have, as is well known, $\sin^2\theta_\odot \ll 1$ and $\Delta m^2_\odot \lesssim 10^{-5}$ eV^2 (see, e.g., [24]). Consequently, the analog of (4) in Case A reads $(m_1)_{\rm max} \cong |\langle m\rangle|_{\rm exp}(1-2|U_{e1}|^2)^{-1}$. The conclusions in the Cases B–D are qualitatively the same as in the case of a neutrino mass spectrum with normal hierarchy. In particular, a measured value of $|\langle m\rangle| > |\langle m\rangle|_+ \cong \sqrt{(\Delta m^2_{\rm atm})_{\rm max}}(1-|U_{e1}|^2)$, would essentially determine m_1, $m_1 \cong (|\langle m\rangle|)_{\rm exp}$. No information about CP violation generated by the Majorana phases can be obtained by the measurement of $|\langle m\rangle|$, or of $|\langle m\rangle|$ and m_{ν_e}. If both $|\langle m\rangle|$ and $m_{\nu_e} \gtrsim 0.35$ eV are measured, the relation $m_1 \cong (|\langle m\rangle|)_{\rm exp} \cong (m_{\nu_e})_{\rm exp}$ should hold. If it is found that $|\langle m\rangle| = \sqrt{\Delta m^2_{\rm atm}}(1-|U_{e1}|^2)$, one would have $0 \le m_1 \le (m_1)_{\rm max}$, where $(m_1)_{\rm max}$ is determined by (10) in which effectively $\sin^2\theta_\odot = 0$, $\cos^2\theta_\odot = 1$, and $\Delta m^2_\odot = 0$. Finally, a measured value of $|\langle m\rangle| < (|\langle m\rangle|_-)_{\rm min} \cong (|\langle m\rangle|_+)_{\rm min} \cong \sqrt{(\Delta m^2_{\rm atm})_{\rm min}}(1-|U_{e1}|^2)$ would either indicate that there exist new additional contributions to the $(\beta\beta)_{0\nu}$-decay rate or that the SMA MSW solution is not the correct solution of the solar neutrino problem.

3. CONCLUSIONS

If $(\beta\beta)_{0\nu}$ decay is detected by present or upcoming experiments, we will conclude that neutrinos are massive Majorana particles and that the total lepton charge L is not conserved. The observation of the $(\beta\beta)_{0\nu}$ decay with a rate corresponding to $|\langle m\rangle| \gtrsim 0.02$ eV, which is in the range of sensitivity of the future $(\beta\beta)_{0\nu}$-decay experiments, can provide unique information on the type of neutrino mass spectrum and on the absolute values of neutrino masses. With additional information on the value of neutrino masses from ^{3}H β-decay experiments or the type of neutrino mass spectrum, one could also obtain information on the CP violation in the lepton sector and (if CP invariance holds) on the relative CP parities of the massive Majorana neutrinos. The possibility of establishing CP nonconservation requires high precision measurements. Given the precision of the future planned $(\beta\beta)_{0\nu}$-decay and ^{3}H β-decay experiments, it holds for a limited range of the values of the parameters involved.

ACKNOWLEDGMENTS

S.P. is grateful to the organizers of this workshop for having being invited to such an interesting meeting that took place in a nice and stimulating atmosphere.

The work of S.P. was partly supported by the Marie Curie Fellowship of the European Community program HUMAN POTENTIAL under contract no. HPMT-CT-2000-00096.

REFERENCES

1. SuperKamiokande Collab. (H. Sobel), in *Proceedings of the 19th International Conference "Neutrino'2000,"* Nucl. Phys. B (Proc. Suppl.) **91** (2001).
2. SuperKamiokande Collab. (Y. Suzuki), in *Proceedings of the 19th International Conference "Neutrino'2000,"* Nucl. Phys. B (Proc. Suppl.) **91** (2001); SNO Collab. (Q. R. Ahmad *et al.*), nucl-ex/0106015.
3. S. M. Bilenky and S. T. Petcov, Rev. Mod. Phys. **59**, 671 (1987).
4. V. Lobashev *et al.*, in *Proceedings of the 19th International Conference "Neutrino'2000,"* Nucl. Phys. B (Proc. Suppl.) **91** (2001).
5. C. Weinheimer *et al.*, in *Proceedings of the 19th International Conference "Neutrino'2000,"* Nucl. Phys. B (Proc. Suppl.) **91** (2001).
6. A. Osipowicz *et al.* (KATRIN Project), hep-ex/0109033.
7. B. Pontecorvo, Zh. Éksp. Teor. Fiz. **33**, 549 (1957) [Sov. Phys. JETP **6**, 429 (1958)]; **34**, 247 (1958) [**7**, 172 (1958)].
8. Z. Maki, M. Nakagawa, and S. Sakata, Prog. Theor. Phys. **28**, 870 (1962).
9. S. M. Bilenky *et al.*, Phys. Lett. B **94B**, 495 (1980).
10. L. Wolfenstein, Phys. Lett. B **107B**, 77 (1981).
11. S. M. Bilenky, N. P. Nedelcheva, and S. T. Petcov, Nucl. Phys. B **247**, 589 (1984); B. Kayser, Phys. Rev. D **30**, 1023 (1984).

12. L. Baudis *et al.*, Phys. Rev. Lett. **83**, 41 (1999); H. V. Klapdor-Kleingrothaus, Nucl. Phys. B (Proc. Suppl.) **100**, 350 (2001).
13. C. E. Aalseth, F. T. Avignone III, R. L. Brodzinski, *et al.*, Yad. Fiz. **63**, 1299 (2000) [Phys. At. Nucl. **63**, 1225 (2000)].
14. NEMO-3 Collab. (C. Marquet *et al.*), Nucl. Phys. B (Proc. Suppl.) **87**, 298 (2000); E. Fiorini, Phys. Rep. **307**, 309 (1998); H. V. Klapdor-Kleingrothaus *et al.*, J. Phys. G **24**, 483 (1998); L. Baudis *et al.*, Phys. Rep. **307**, 301 (1998); M. Danilov *et al.*, Phys. Lett. B **480**, 12 (2000).
15. S. M. Bilenky, S. Pascoli, and S. T. Petcov, Phys. Rev. D **64**, 053010 (2001).
16. S. M. Bilenky, S. Pascoli, and S. T. Petcov, Phys. Rev. D **64**, 113003 (2001).
17. S. Pascoli, S. T. Petcov, and L. Wolfenstein, hep-ph/0110287.
18. S. T. Petcov and A. Yu. Smirnov, Phys. Lett. B **322**, 109 (1994).
19. S. M. Bilenky *et al.*, Phys. Rev. D **54**, 4432 (1996); Phys. Lett. B **465**, 193 (1999); V. Barger and K. Whisnant, Phys. Lett. B **456**, 194 (1999); H. Minakata and O. Yasuda, Nucl. Phys. B **523**, 597 (1998); T. Fukuyama *et al.*, Phys. Rev. D **57**, 5844 (1998); hep-ph/9804262.
20. F. Vissani, JHEP **06**, 022 (1999); M. Czakon *et al.*, hep-ph/0003161; H. V. Klapdor-Kleingrothaus, H. Päs, and A. Yu. Smirnov, Phys. Rev. D **63**, 073005 (2001); hep-ph/0003219.
21. M. Czakon *et al.*, hep-ph/0110166.
22. G. F. Fogli *et al.*, hep-ph/0106247; J. N. Bachall, M. C. González-García, and C. Peña-Garay, hep-ph/0106258; A. Bandyopadhyay *et al.*, hep-ph/0106264; M. V. Garzelli and C. Giunti, hep-ph/0108191.
23. M. C. González-García *et al.*, Phys. Rev. D **63**, 033005 (2001).
24. W. Rodejohann, hep-ph/0008044.
25. K. S. Babu and R. N. Mohapatra, Phys. Rev. Lett. **75**, 2276 (1995); H. Paes *et al.*, Phys. Lett. B **459**, 450 (1999).

Physics of Atomic Nuclei, Vol. 66, No. 3, 2003, pp. 452–457. From Yadernaya Fizika, Vol. 66, No. 3, 2003, pp. 480–485.

A Cryogenic Underground Observatory for Rare Events: CUORE, an Update*

A. Alessandrello, C. Arnaboldi, F. T. Avignone III[1)], J. Beeman[2),3)], M. Barucci[4)], M. Balata[5)], C. Brofferio, C. Bucci[5)], S. Cebrian[6)], R. J. Creswick[1)], S. Capelli, L. Carbone, O. Cremonesi, A. de Ward[7)], E. Fiorini, H. A. Farach[1)], G. Frossati[7)], A. Giuliani[8)], D. Giugni, E. E. Haller[2),3)], I. G. Irastorza[6)], R. J. McDonald[2)], A. Morales[6)], E. B. Norman[2)], P. Negri, A. Nucciotti, M. Pedretti[8)], C. Pobes[5)], V. Palmieri[9)], M. Pavan, G. Pessina, S. Pirro, E. Previtali, C. Rosenfeld[1)], A. R. Smith[2)], M. Sisti, G. Ventura[4)], M. Vanzini, and L. Zanotti**

The CUORE Collaboration

Dipartimento di Fisica dell'Università di Milano–Bicocca e Sezione di Milano dell'INFN, Italy

Received April 17, 2002

Abstract—CUORE is a proposed tightly packed array of 1000 TeO_2 bolometers, each being a cube 5 cm on a side with a mass of 750 g. The array consists of 25 vertical towers, arranged in a square of 5 towers by 5 towers, each containing ten layers of four crystals. The design of the detector is optimized for ultralow-background searches for neutrinoless double beta decay of ^{130}Te (33.8% abundance), cold dark matter, solar axions, and rare nuclear decays. A preliminary experiment involving 20 crystals of various sizes (MIBETA) has been completed, and a single CUORE tower is being constructed as a smaller scale experiment called CUORICINO. The expected performance and sensitivity, based on Monte Carlo simulations and extrapolations of present results, are reported. © *2003 MAIK "Nauka/Interperiodica".*

1. INTRODUCTION

Neutrinoless double beta decay is a process by which two neutrons in a nucleus beta decay by exchanging a virtual Majorana neutrino and each emitting an electron. This violates lepton number conservation ($\Delta L = 2$) [1]. There are many reviews on the subject [2–4].

The decay rate for the process involving the exchange of a Majorana neutrino can be written as follows:

$$\lambda^{0\nu}_{\beta\beta} = G^{0\nu}(E_0, Z)\langle m_\nu\rangle^2 |M^{0\nu}_{\rm F} - (g_A/g_V)^2 M^{0\nu}_{\rm GT}|^2. \quad (1)$$

Here $G^{0\nu}$ is the two-body phase-space factor including coupling constant; $M^{0\nu}_{\rm F}$ and $M^{0\nu}_{\rm GT}$ are the Fermi and Gamow–Teller nuclear matrix elements, respectively; and g_A and g_V are the axial-vector and vector weak coupling constants, respectively. The quantity $\langle m_\nu\rangle$ is the effective Majorana neutrino mass given by

$$\langle m_\nu\rangle \equiv \left|\sum_{k=1}^{2n} \lambda^{CP}_k (U^L_{lk})^2 m_k\right|, \quad (2)$$

where λ^{CP}_k is the CP eigenvalue associated with the kth neutrino mass eigenstate (± 1 for CP conservation); U^L_{lk} is the (l,k) matrix element of the transformation between flavor eigenstates $|\nu_l\rangle$ and mass

*This article was submitted by the authors in English.

[1)]Department of Physics and Astronomy, University of South Carolina, Columbia, SC 29208, USA.
[2)]Lawrence Berkeley National Laboratory, California, USA.
[3)]Department of Materials Science and Mineral Engineering, University of California, Berkeley, CA 94720, USA.
[4)]Dipartimento di Fisica dell'Università di Firenze e Sezione di Firenze dell'INFN, Italy.
[5)]Laboratori Nazionali del Gran Sasso, Assergi (L'Aquila), Italy.
[6)]Laboratorio de Física Nuclear y Altas Energías, Universidad de Zaragoza, Spain.
[7)]Kamerling Onnes Laboratory, Leiden University, The Netherlands.
[8)]Dipartimento di Scienze Chimiche, Fisiche e Matematiche dell'Università dell'Insubria e Sezione di Milano dell'INFN, Como, Italy.
[9)]Laboratori Nazionali de Legnaro, Padova, Italy.
**e-mail: waters@sc.edu

eigenstates $|\nu_k\rangle$ for left handed neutrinos,

$$|\nu_l\rangle = \sum U^L_{lk}|\nu_k\rangle; \tag{3}$$

and m_k is the mass of the kth neutrino mass eigenstate.

The effective Majorana neutrino mass, $\langle m_\nu\rangle$, is directly derivable from the measured half-life of the decay as follows:

$$\langle m_\nu\rangle = m_e(F_N T^{0\nu}_{1/2})^{-1/2}\ \text{eV}, \tag{4}$$

where $F_N \equiv G^{0\nu}|M^{0\nu}_{\rm F} - (g_A/g_V)M^{0\nu}_{\rm GT}|^2$ and m_e is the electron mass. This quantity derives from nuclear structure calculations and is model-dependent as shown later.

The most sensitive experiments thus far utilize germanium detectors isotopically enriched in ^{76}Ge from 7.78% abundance to ~86%. This activity began with natural abundance Ge detectors in Milan [5] evolving over the years to the first experiments with small isotopically enriched Ge detectors [6], and finally to the two present multikilogram isotopically enriched ^{76}Ge experiments: Heidelberg–Moscow [7] and IGEX [8]. These experiments have achieved lower bounds on the half-life of the decay $^{76}\text{Ge} \rightarrow {}^{76}\text{Se} + 2e^-$: $T^{0\nu}_{1/2} > 1.9\times 10^{25}$ yr [7] and $T^{0\nu}_{1/2} > 1.6\times 10^{25}$ yr [8]. The former [7] has about six times the exposure as the latter [8] with data of similar quality. This strongly implies that these experiments with the order of 100 moles of ^{76}Ge each have reached their point of diminishing returns. Their continuation will yield little more information of fundamental interest. The latest large-space shell-model calculation yields $F_N = 1.41\times 10^{-14}\ \text{yr}^{-1}$ [9]. This value implies that the above half-lives yield $\langle m_\nu\rangle \le 1.0$ eV. Other calculations, discussed later, yield values as small as 0.3 eV.

Where should the field of $\beta\beta$ decay go from here? Suppose we consider the observed neutrino oscillations in the data from atmospheric neutrinos [10] and solar neutrinos [11]. Considering these data, what probable range of $\langle m_\nu\rangle$ is implied? Would it be large enough for a direct observation of $0\nu\beta\beta$ decay? If so, what technique would be the best for a possible discovery experiment? How much would such an experiment cost? We will address these questions in an effort to demonstrate that CUORE, an array of 1000, 750-g TeO_2 bolometers, is the best approach presently available. It can be launched without isotopic enrichment or extensive R&D, and it can achieve next generation sensitivity.

2. THEORETICAL MOTIVATION: PROBABLE NEUTRINO SCENARIOS

The Super-Kamiokande (SK) data imply maximal mixing of ν_μ with ν_τ with $\delta m^2_{23} \simeq 3\times 10^{-3}$ eV^2. The solar neutrino data from SK and from SNO also imply that the small mixing angle solution to the solar neutrino problem is disfavored, so that $\delta m^2_{(\text{solar})} \simeq 10^{-5}$–$10^{-4}$ eV^2. Based on these interpretations, one possible scenario for the neutrino mixing matrix has the following approximate form:

$$\begin{pmatrix}\nu_e\\ \nu_\mu\\ \nu_\tau\end{pmatrix} = \begin{pmatrix}1/\sqrt{2} & 1/\sqrt{2} & 0\\ -1/2 & 1/2 & 1/\sqrt{2}\\ 1/2 & -1/2 & 1/\sqrt{2}\end{pmatrix}\begin{pmatrix}\nu_1\\ \nu_2\\ \nu_3\end{pmatrix}. \tag{5}$$

The neutrino masses can be arranged in two hierarchical patterns in which $\delta m^2_{31} \simeq \delta m^2_{32} \sim 3\times 10^{-3}$ eV^2 and $\delta m^2_{21} \simeq 10^{-5}$–$10^{-4}$ eV^2. With the available data, it is not possible to determine which hierarchy, $m_3 \gg m_1(m_2)$ or $m_1(m_2) \gg m_3$, is the correct one, nor do we know the absolute value of any of the mass eigenstates.

The consideration of reactor neutrino and atmospheric neutrino data together strongly implies that the atmospheric neutrino oscillations are predominantly $\nu_\mu \rightarrow \nu_\tau$ ($\bar\nu_\mu \rightarrow \bar\nu_\tau$), which implies, as seen from (5), that ν_e is predominantly a mixture of ν_1 and ν_2. In this case, there will be one relative CP phase, ϵ, and the equation reduces to the approximate form

$$\langle m_\nu\rangle = \frac{m_1 + \epsilon m_2}{2}, \tag{6}$$

where we recall that the large mixing angle solution of the solar neutrino problem implies

$$m^2_2 - m^2_1 = 10^{-5}\text{–}10^{-4}\ \text{eV}^2. \tag{7}$$

This yields four cases to be analyzed:

(a) $m_1 \simeq 0$. If $m_1 = 0$, then $m_2 = 0.003$–0.01 eV and $\langle m_\nu\rangle = m_2/2$.

(b) $m_1 \gg 0.01$ eV. If $m_1 \equiv M \gg 0.01$ eV, then $\langle m_\nu\rangle \simeq M(1+\epsilon)/2 = 0$ or M.

(c) $m_3 \simeq 0$. If $m_3 = 0$, then $m_1 \simeq m_2 \simeq 0.055$ eV and $\langle m_2\rangle \simeq 0$ or 0.055 eV.

(d) The existence of a mass scale, M, where $M \gg 0.055$ eV. If $M \gg 0.055$ eV, then $m_1 \simeq m_2 \simeq M + 0.055$ eV and $\langle m_\nu\rangle \simeq m_1(1+\epsilon)/2$. If we assume then that $\epsilon \simeq +1$ and that neutrinos are Majorana particles, then it is very probable that $\langle m_\nu\rangle$ lies between 0.01 eV and the present bound from ^{76}Ge experiments.

The requirements for a next generation experiment can easily be deduced from the relation

$$T^{0\nu}_{1/2} = \frac{(\ln 2)Nt}{c}, \tag{8}$$

Table 1. Theoretical values of F_N for the double beta decay of ^{76}Ge and ^{130}Te computed with five nuclear models ($R(t)^+$ is the ratio of $F_N(^{130}\mathrm{Te})/F_N(^{76}\mathrm{Ge})$, $R(\epsilon)^* = \sqrt{R(t)^+}$ is the relative sensitivity to $\langle m_\nu \rangle$ of ^{130}Te to that of ^{76}Ge)

F_N, yr^{-1}		$R(t)^+$	$R(\epsilon)^*$	Model	Ref.
^{76}Ge	^{130}Te				
1.54×10^{-13}	1.63×10^{-12}	10.6	3.3	Shell Model	[19]
1.14×10^{-13}	1.08×10^{-12}	9.6	3.1	Generalized Seniority	[20]
1.86×10^{-14}	3.96×10^{-13}	21.8	4.7	QRPA	[21]
1.24×10^{-13}	4.98×10^{-13}	3.9	2.0	QRPA	[22]
1.14×10^{-13}	5.33×10^{-13}	4.7	2.2	QRPA	[23]

where N is the number of parent nuclei; t is the counting time; and c is the total number of counts, predominantly background. To improve the sensitivity to $\langle m_\nu \rangle$ by a factor of 10^{-2} from the present 1 to 0.01 eV, one must increase the quantity Nt/c by a factor of 10^4. The quantity N can feasibly be increased by a factor of $\sim 10^2$ over present experiments, so that t/c must also be improved by that amount. Since the present counting times are probably about a factor of 5 less than a practical counting time, the background should be reduced by a factor of between 10 and 20 below present levels. These are approximately the target parameters of the next generation neutrinoless double-beta-decay experiments.

Georgi and Glashow [12] give further motivation for more sensitive next-generation double-beta-decay experiments. They discuss six "facts" deduced from atmospheric neutrino experiments, solar neutrino experiments, and the constraints imposed by the reactor neutrino experiments. They conclude that, if neutrinos play an essential role in the large structure of the Universe, their six facts are mutually consistent if and only if solar neutrino oscillations are nearly maximal. They further state that stronger bounds on $0\nu\beta\beta$ decay could possibly constrain solar neutrino data to allow only the just-so solution.

If, on the other hand, the small-angle MSW solution somehow were the correct one, next-generation $0\nu\beta\beta$ decay experiments could "exclude the cosmological relevance of relic neutrinos" [12].

3. PROPOSED NEXT-GENERATION EXPERIMENTS

There are six large volume experimental proposals in various stages of development. CUORE will be discussed in detail later. The remaining five in alphabetical order are CAMEO, EXO, GENIUS, MAJORANA, and MOON.

The CAMEO proposal would place enriched parent isotopes in and near the center of the BOREXINO detector and Counting Test Facility (CTF) [13].

The proposed EXO detector would be either a large high-pressure ^{136}Xe gas time projection chamber (TPC) or a liquid TPC. It would contain tons of Xe isotopically enriched in ^{136}Xe [14].

The GENIUS proposal involves between 1 and 10 t of "naked" germanium detectors, isotopically enriched to 86% in ^{76}Ge, directly submerged in a large tank of liquid nitrogen as a "clean" shield [15].

The MAJORANA proposal is a significant expansion of the IGEX experiment with new segmented detectors in a highly dense-packed configuration and new pulse shape discrimination techniques developed by PNNL and USC. The proposal involves the production of 250 2-kg isotopically enriched (86%) Ge detectors, each segmented into 12 electrically independent segments.

The Molybdenum Observatory of Neutrinos (MOON) proposal is a major extension of the ELEGANTS detector [16]. It involves between 1 and 3 t of molybdenum foils isotopically enriched to 85% in ^{100}Mo inserted between plastic scintillators.

All of these experiments will require significant time, R&D, and funding for isotopic enrichment as well as the development of new techniques. The CUORE experiment, on the other hand, requires no isotopic enrichment because the natural abundance of ^{130}Te is $(33.80 \pm 0.01)\%$, and the technique has already been developed. A preliminary experiment, MIBETA, has already been completed [17]. In addition, a preliminary trial experiment, CUORICINO, is being constructed at this time [18]. It is one of the 25 towers of 40 of the 1000 750-g TeO_2 bolometers, which is a slight change in the configuration initially designed [18]. CUORICINO will contain 8.11 kg of ^{130}Te. The most conservative nuclear structure calculations imply that ^{130}Te is 2 times more effective in $\langle m_\nu \rangle$ sensitivity than ^{76}Ge, so that CUORICINO will be equal to at least 16.22 kg of Ge enriched to

Table 2. Projected sensitivities of CUORICINO depending on energy resolution and background

Background, count/(keV kg yr)	FWHM = 5 keV		FWHM = 2 keV	
	$\tau_{1/2}$, yr	$\langle m_\nu \rangle$, eV	$\tau_{1/2}$, yr	$\langle m_\nu \rangle$, eV
0.5	$3.6 \times 10^{24} t^{1/2}$	$0.38 t^{-1/4}$	$5.7 \times 10^{24} t^{1/2}$	$0.30 t^{-1/4}$
0.1	$8.1 \times 10^{24} t^{1/2}$	$0.25 t^{-1/4}$	$1.3 \times 10^{25} t^{1/2}$	$0.20 t^{-1/4}$
0.01	$2.6 \times 10^{25} t^{1/2}$	$0.14 t^{-1/4}$	$2.9 \times 10^{25} t^{1/2}$	$0.14 t^{-1/4}$

86% in ^{76}Ge. CUORE would be equivalent to 407 kg of 86% ^{76}Ge with the most conservative nuclear matrix elements or 957 kg of 86% ^{76}Ge according to the largest theoretical matrix elements. There are five nuclear structure calculations presented in Table 1 [19–23].

The results of the preliminary experiment MIBETA reported by the Milano–INFN group [17] involved 20 natural TeO_2 crystal bolometers averaging 340 g each for a total mass of 6.8 kg. This is equivalent to 1.84 kg of ^{130}Te. The array was run in a number of configurations with various detectors operating at any one time, as the array was used for development of the technique. These experiments ran over a total of 80 613 h of operation but with several detector configurations. The total exposure was $Nt = 4.31 \times 10^{24}$ yr with a bound on the number of counts in the $0\nu\beta\beta$ decay region of $6.9^{+6.7}_{-5.9}$ for an upper bound to 90% C.L. of 17.96. The most recent bound on the half-life is $T^{0\nu}_{1/2} > 1.6 \times 10^{23}$ yr. This corresponds to the following upper bounds on $\langle m_\nu \rangle$ for eight nuclear structure calculations: 1.1 [3], 2.1 [21], 1.5 [20], 1.8 [23], 2.4 [24], 1.9 [22], 2.6 [25], and 1.5 eV [26]. The range is from 1.1 to 2.6 eV, not much larger than the conservative result from the ^{76}Ge experiments [7, 8].

The average background for this experiment was 0.5 count/(kg keV yr); however, it was discovered later that the crystals were polished with cerium oxide, which was measured in the Gran Sasso Laboratory and found to be radioactive. In addition, there is clear evidence of neutron-induced background. We have conservatively estimated that the background can be reduced by a factor of at least 10 in CUORICINO. The goal will be to reduce the background significantly below this level, by a factor of 40 or even more.

The final spectrum of the MIBETA 20 crystal experiment reported in [17] is shown in Fig. 1. While improvements are being made at present in the background as well as in the energy resolution, it is clear that this technology has been clearly demonstrated by the results of the MIBETA experiment and will be further demonstrated by the CUORICINO experiment being constructed at this time (Table 2).

4. THE CUORE DETECTOR

The CUORE will consist of an array of 1000 TeO_2 bolometers arranged in a square configuration of 25 towers of 40 crystals each. The geometry of a single tower is shown in Fig. 2*a*. A sketch of CUORE is shown in Fig. 2*b*.

The principle of operation of these bolometers is now well understood [27]. TeO_2 is a dielectric and diamagnetic crystal, which when maintained at very low temperature (~5–10 mK) has a very low heat capacity. In fact, the specific heat is proportional to the ratio $(T/T_0)^3$, where T_0 is the Debye temperature. Accordingly, a very small energy absorbed by the crystal via a nuclear decay or recoil by collision can result in a measurable increase in temperature. This temperature change can be recorded using neutron transmutation doped (NTD) germanium thermistors. These devices were developed and produced by the Lawrence Berkeley National Laboratory (LBNL) and UC Berkeley Department of Materials Science. These sensors have been made unique in their uniformity of response and sensitivity by neutron

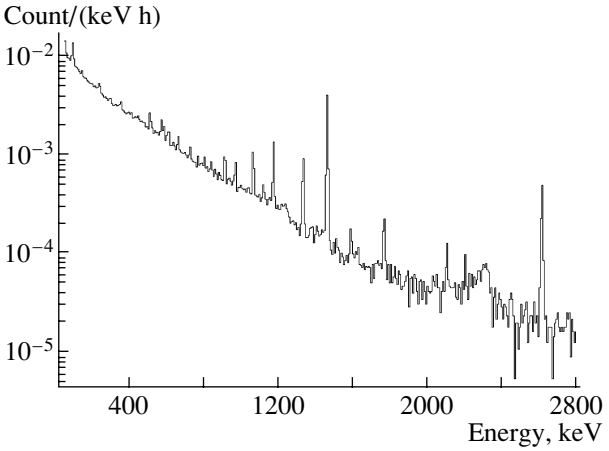

Fig. 1. Final spectrum of the MIBETA experiment.

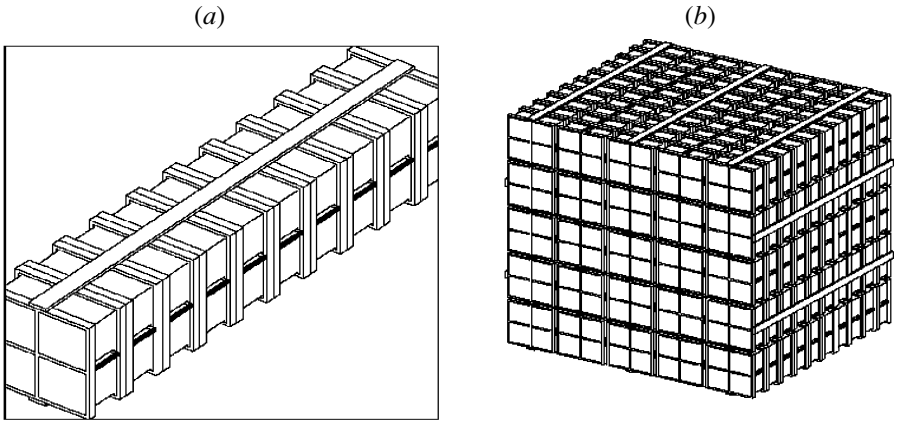

Fig. 2. (*a*) A single tower of CUORE. (*b*) The CUORE detector.

exposure control with neutron absorbing foils accompanying the germanium in the reactor [28].

The TeO_2 crystals are produced by the Shanghai Quinhua Material Company (SQM) in Shanghai, China. Crystals produced by other organizations have proven to be inferior. A search of potential suppliers in the United States revealed that the only dealers found sold crystals produced by SQM or other companies outside of the United States.

Long periods of operation suffer small excursions in temperature of the crystal array, which deteriorates energy resolution. A stabilization technique proven to be successful in the MIBETA 20-crystal array experiment will be employed. A periodic injection is made of precisely known Joule power directly into the crystals through heavily doped meanders in Si chips glued to the surface [17].

The single tower of 40 crystals is presently under construction. It will be attached to the mixing chamber of the same dilution refrigerator (DR) used in the MIBETA experiment [17] and run as a test. It will also be run as an experiment called CUORICINO, which is designed also to improve on the present sensitivity to $\langle m_\nu \rangle$ obtained with isotopically enriched Ge detectors [7, 8]. By the time significant funding from this proposal could be spent on CUORE, CUORICINO will have proven the feasibility of the extension of the MIBETA technology to large arrays. This, plus the fact that CUORE requires no isotopic enrichment, puts CUORE well ahead of all the other options of a truly next-generation $0\nu\beta\beta$ experiment. The technology, novel though it is, is developed and to a large degree proven.

5. CONCLUSION

The CUORE array will have 9.5×10^{25} nuclei of ^{130}Te. If the background is conservatively reduced to 0.01 count/(keV kg yr), then, in one year of running, the sensitivity of CUORE would be $T^{0\nu}_{1/2} > 1.1 \times 10^{26}$ yr. This corresponds to $\langle m_\nu \rangle < 0.05$ eV. If, eventually, the background were reduced to 0.001 count/(keV kg yr), the sensitivity with one year of counting would be $T^{0\nu}_{1/2} > 3.6 \times 10^{26}$ yr, corresponding to $\langle m_\nu \rangle < 0.03$ eV. If, in the two cases mentioned above, the detector were operated for a decade, the bounds on $\langle m_\nu \rangle$ would be <0.028 and <0.017 eV, respectively.

If CUORE fulfills these expectations, it could be replicated by a factor 6 for a similar cost (conservatively speaking) as any of the experiments requiring isotopic enrichment.

The detector will also be used to search for cold dark matter (CDM). The present thresholds of 5 keV are equivalent to 1.25 keV in ordinary Ge detectors, because ionization is 0.26 times as effective in converting nuclear recoil energy into a signal pulse as it is in converting photon energy. Such a large array could efficiently search for a seasonal variation in the CDM interaction rate. The large mass of Te theoretically enhances the interaction rate of many CDM candidates.

The CUORE crystals will be placed in known crystalline orientations that will allow a sensitive search for solar axions using the technique introduced by Creswick *et al.* [29] and demonstrated by the experiment of Avignone III *et al.* [30].

It should also be recognized that the highly granular configuration of CUORE, equivalent to ten layers of 100 crystals each, approximately forms a cube with 512 crystals in an inner cube with significant protection from a layer all around of 488 crystals. The coverage is not perfect because of necessary small spaces between crystals; however, it will significantly reduce background from gamma rays coming from outside of the configuration.

Finally, while the main emphasis is on building an array of TeO_2 crystals, CUORE or the CUORE technique can accommodate any material that can be made into bolometers. The most promising competing experiments are the two proposed large ^{76}Ge experiments GENIUS [15] and MAJORANA [31]. The direct observation of neutrinoless double beta decay absolutely requires at least two different experiments with different parent nuclei, if for no other reason than the uncertainties in nuclear matrix elements. In ^{76}Ge, for example, this results in a factor of 4.3 in the value of $\langle m_\nu \rangle$ and a factor of 2.4 in the case of ^{130}Te. These uncertainties should be carefully considered when comparing different proposals. For example, the present bounds on $\langle m_\nu \rangle$ from ^{76}Ge experiments range from 0.3 to 1.3 eV, while they range from 1.1 to 2.6 eV from the small MIBETA experiment recently completed [17]. CUORICINO should reach a comparable sensitivity during its test period. Which bound would be actually more restrictive? The answer lies in the uncertainties in the nuclear physics.

REFERENCES

1. W. H. Furry, Phys. Rev. **56**, 1184 (1939).
2. H. Primakoff and S. P. Rosen, Rep. Prog. Phys. **22**, 121 (1959); Phys. Rev. **184**, 1925 (1969).
3. W. C. Haxton and G. J. Stevenson, Jr., Prog. Part. Nucl. Phys. **12**, 409 (1984); F. T. Avignone III and R. L. Brodzinski, Prog. Part. Nucl. Phys. **21**, 99 (1988); M. Moe and P. Vogel, Annu. Rev. Nucl. Part. Sci. **44**, 247 (1994).
4. A. Morales, Nucl. Phys. B (Proc. Suppl.) **77**, 335 (1999); H. Ejiri, Int. J. Mod. Phys. E **6**, 1 (1997); V. Tretyak and Y. Zdesenko, At. Data Nucl. Data Tables **61**, 43 (1995).
5. E. Fiorini *et al.*, Phys. Lett. B **25B**, 602 (1967); Lett. Nuovo Cimento **3**, 149 (1970).
6. A. A. Vasenko *et al.*, Mod. Phys. Lett. A **5**, 1299 (1990); F. T. Avignone III *et al.*, Phys. Lett. B **256**, 559 (1991).
7. L. Baudis *et al.*, Phys. Rev. Lett. **83**, 41 (1999).
8. C. E. Aalseth *et al.*, Phys. Rev. D **65**, 092007 (2002); Yad. Fiz. **63**, 1299, 1341 (2000) [Phys. At. Nucl. **63**, 1225, 1268 (2000)].
9. E. Cauries *et al.*, Phys. Rev. Lett. **77**, 1954 (1996); P. B. Racha *et al.*, Phys. Rev. Lett. **76**, 2642 (1996).
10. Y. Fukuda *et al.*, Phys. Rev. Lett. **82**, 1810, 2430, 2644 (1999).
11. Q. R. Ahmad *et al.*, Phys. Rev. Lett. **89**, 011301 (2002); S. Fukuda *et al.*, Phys. Lett. B **539**, 179 (2002); GALLEX Collab. (W. Hampel *et al.*), Phys. Lett. B **388**, 384 (1996); SAGE Collab. (G. N. Abdurashitov *et al.*), Phys. Rev. Lett. **77**, 4708 (1996); B. T. Cleveland *et al.*, Astrophys. J. **496**, 505 (1998); R. Davis, Prog. Part. Nucl. Phys. **32**, 13 (1994).
12. H. Georgi and S. L. Glashow, Phys. Rev. D **61**, 097301 (2000).
13. G. Bellini *et al.*, nucl-ex/0007012.
14. M. Danilov *et al.*, Phys. Lett. B **480**, 12 (2000).
15. H. V. Klapdor-Kleingrothaus, J. Hellnig, and M. Hirsch, J. Phys. G **24**, 483 (1998).
16. H. Ejiri *et al.*, Phys. Rev. Lett. **85**, 2917 (2000).
17. A. Alessandrello *et al.*, Phys. Lett. B **486**, 13 (2000).
18. A. Alessandrello *et al.*, Nucl. Phys. B (Proc. Suppl.) **87**, 78 (2000).
19. M. Moe and P. Vogel, Annu. Rev. Nucl. Part. Sci. **44**, 247 (1994).
20. J. Engel *et al.*, Phys. Lett. B **225**, 5 (1989).
21. P. Vogel and M. R. Zirnbauer, Phys. Rev. Lett. **57**, 3148 (1986); J. Engel, P. Vogel, and M. R. Zirnbauer, Phys. Rev. C **37**, 731 (1988).
22. T. Tomoda, Rep. Prog. Phys. **54**, 53 (1991).
23. A. Staudt, K. Muto, and H. V. Klapdor-Kleingrothaus, Europhys. Lett. **13**, 31 (1990); K. Muto, E. Bender, and H. V. Klapdor-Kleingrothaus, Z. Phys. A **334**, 177, 187 (1989).
24. J. Suhonen and O. Civitarese, Phys. Rep. **300**, 123 (1998).
25. A. Faessler *et al.*, J. Phys. G **24**, 2139 (1998).
26. C. Barbero, J. M. Krmpotic, and D. Tadic, Nucl. Phys. A **650**, 485 (1999).
27. D. Twerenbold, Rep. Prog. Phys. **59**, 349 (1996); N. Booth, B. Cabrera, and E. Fiorini, Annu. Rev. Nucl. Sci. **46**, 471 (1996).
28. E. Norman and R. J. McDonald, *Presentation Made to the CUORE Collaboration, Milan, Italy, 2000.*
29. R. J. Creswick *et al.*, Phys. Lett. B **427**, 235 (1998).
30. F. T. Avignone III *et al.*, Phys. Rev. Lett. **81**, 5068 (1998).
31. C. E. Aalseth *et al.*, in *Proceedings of the 5th International Symposium on Sources and Detection of Dark Matter and Dark Energy in the Universe, Marina Beach, California, Febr. 20–22, 2002* (World Sci., Singapore) (in press).

Physics of Atomic Nuclei, Vol. 66, No. 3, 2003, pp. 458–461. From Yadernaya Fizika, Vol. 66, No. 3, 2003, pp. 486–489.

Double-Beta Decay of ^{100}Mo to 0^+ Excited States in ^{100}Ru*

A. S. Barabash**

Institute of Theoretical and Experimental Physics,
Bol'shaya Cheremushkinskaya ul. 25, Moscow, 117259 Russia

Received February 13, 2002

Abstract—A brief review on the $2\nu\beta\beta$ decay of ^{100}Mo to the 0^+ excited state in ^{100}Ru is performed. A weighted-average half-life value for the decay has been obtained, $T_{1/2} = (6.8 \pm 1.2) \times 10^{20}$ yr. The corresponding average value for the nuclear matrix element was extracted, 0.095 ± 0.009. © *2003 MAIK "Nauka/Interperiodica".*

1. INTRODUCTION

Although the main interest in studies of double-beta ($\beta\beta$) decay is currently related to the neutrinoless mode ($0\nu\beta\beta$), considerable efforts are under way to investigate the ordinary allowed second-order weak decay ($2\nu\beta\beta$). Accumulation of experimental information on the $2\nu\beta\beta$ processes (transitions to the ground and excited states) promotes a better understanding of the nuclear part of double-beta decay and allows one to check theoretical schemes of nuclear matrix element (NME) calculations for the two-neutrino mode as well as for the neutrinoless one. It is important to note that, in the framework of quasiparticle random-phase approximation (QRPA) models, the dependence of NMEs with the particle–particle strength parameter g_{pp} is completely different for ground-state transitions and transitions to excited states [1, 2]. Therefore, the decay to excited states probes different aspects of the calculational method.

Due to the strong energy dependence of $\beta\beta$-decay probabilities, experimental investigations were mainly concentrated on $\beta\beta$ transitions to the ground state of a daughter nucleus. Analysis of isotopes with high $Q_{\beta\beta}$ values showed that the half-lives of the $2\nu\beta\beta$ decay to the 0_1^+ level in the daughter nucleus for such nuclei as ^{100}Mo, ^{96}Zr, and ^{150}Nd could be detected by using available low-background HPGe detectors [3]. A set of experiments to search for such a transition in ^{100}Mo, ^{96}Zr, and ^{150}Nd were established [4–14]. Recently, the additional isotopes ^{82}Se, ^{130}Te, ^{116}Cd, and ^{76}Ge have become of interest to studies of the $2\nu\beta\beta$ decay to the 0_1^+ level too [2, 15–18].

The idea to detect the $2\nu\beta\beta(0^+ \to 0_1^+)$ decay of ^{100}Mo [3] initiated a few experiments to search for this decay using enriched Mo samples. Seven experiments were done to search for $\beta\beta$ decay of ^{100}Mo to the 0^+ excited state in ^{100}Ru [4–10], and in three of them, $\beta\beta$ decay of ^{100}Mo to the 0^+ excited state in ^{100}Ru was detected [7, 9, 10]. Here, we present all "positive" results for this type of $2\nu\beta\beta$ decay of ^{100}Mo and calculate the weighted-average value for the half-life and NME of this transition. The decay scheme of ^{100}Mo is presented in Fig. 1.

2. "POSITIVE" RESULTS WITH ^{100}Mo

Let us consider the experiments with positive results [7, 9, 10]. Two of them [7, 9] were performed using low-background HPGe detectors located in underground laboratories. The method with two HPGe detectors in a coincidence scheme was used in the last experiment [10].

2.1. Soudan Experiment

The counting facility used in this experiment is located in the Soudan mine in Minnesota at a depth

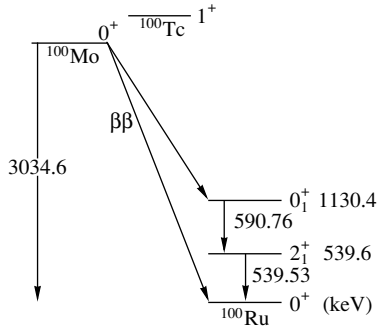

Fig. 1. $\beta\beta$-decay and γ-decay schemes for ^{100}Mo.

*This article was submitted by the author in English.

** e-mail: barabash@heron.itep.ru

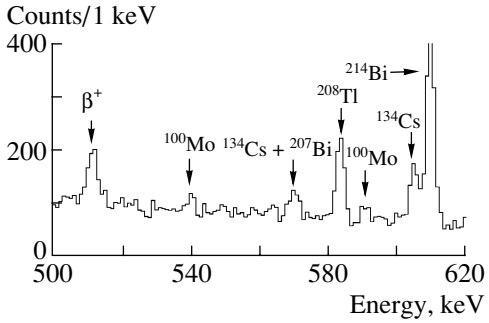

Fig. 2. Total γ-ray spectrum in the energy range corresponding to the $2\nu\beta\beta$ decay of ^{100}Mo to the first 0^+ excited state which is accompanied by two, 539.53- and 590.76-keV, γ quanta (from [7]).

of 2090 m w.e. [7]. The system consists of an intrinsic germanium detector having a volume of 114 cm^3 and an energy resolution of 2.4 keV FWHM at 1333 keV assembled in a cryostat of low-background copper components housed in a large bulk shield of ordinary lead having an inner liner 5 cm thick (150-yr-old lead recovered from a German ship that sank in the North Sea). The sample consisted of 956 g of powdered molybdenum metal enriched to 98.4% ^{100}Mo contained in a lucite Marinelli beaker.

The energy spectrum obtained in 415.43 d of counting is shown in the region of interest at 1 keV per channel in Fig. 2. The energy regions of the spectrum corresponding to the expected peaks from the $\beta\beta$-decay deexcitation gamma rays were analyzed by multiple independent techniques. The results are 66 ± 22 counts for the net area under the 539.53-keV peak and 67 ± 19 counts for the 590.76-keV peak. Both gamma rays of interest are from pure electric quadrupole transitions with very nearly the same internal conversion coefficients; hence, they have almost identical intensities. Summing these two energy regions of the spectrum improves the statistical accuracy of the data, and dividing the net area under the combined photopeak by the average efficiency (0.97%) leads to a precise value of the half-life: $T_{1/2} = (6.1^{+1.8}_{-1.1}) \times 10^{20}$ yr.

2.2. Modane Experiment

The experimental work has been performed in the Modane Underground Laboratory (depth of 4800 m w.e.) [9]. A set of ^{100}Mo-enriched metal powder samples were measured by using low-background HPGe detectors with volumes of 100, 120, 380 and 400 cm^3. Data of 17 measurements were analyzed and the total spectrum was obtained. The product $P = \sum m_i \eta_i t_i \varepsilon_i$ is equal to 154.85 kg h for the γ line at 539.53 keV. Here, summation is performed on 17 measurements, m_i is the mass of a sample, η_i is its enrichment, t_i is the counting time, and ε_i is the detection efficiency. Small peaks were found in places of interest (Fig. 3*a*).

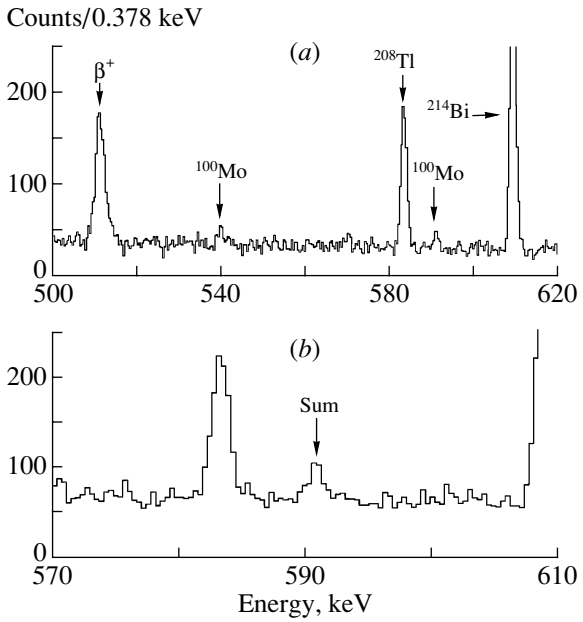

Fig. 3. (*a*) Total γ-ray spectrum [9] in the energy range corresponding to the $2\nu\beta\beta$ decay of ^{100}Mo to the first 0^+ excited state. (*b*) The sum of two peaks, 539.53 and 590.76 keV, with surrounding channels is shown.

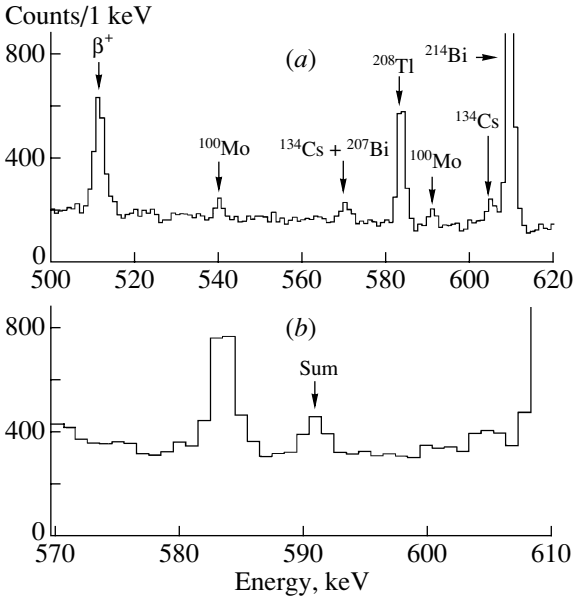

Fig. 4. (*a*) Sum of the Modane γ-ray spectrum [9] and the spectrum of reference [7] in the energy range corresponding to the $2\nu\beta\beta$ decay of ^{100}Mo to the first 0^+ excited state. (*b*) The sum of two peaks, 539.53 and 590.76 keV, with surrounding channels is shown.

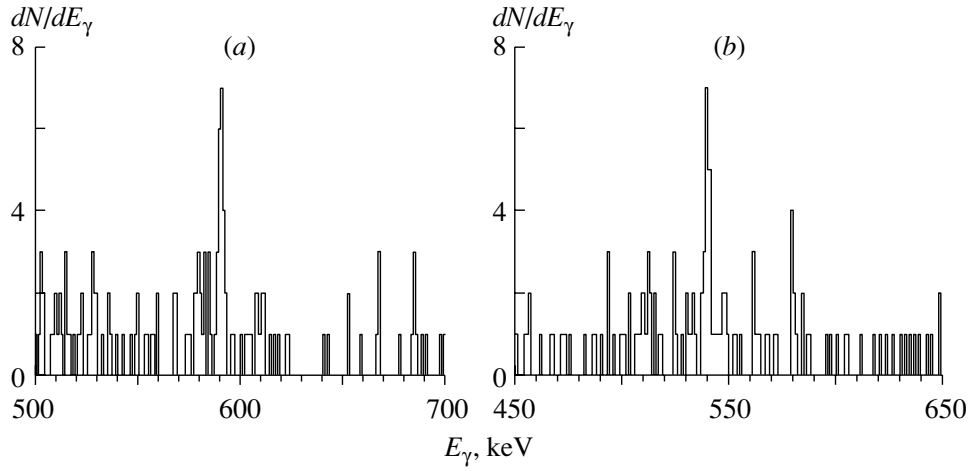

Fig. 5. The γ-ray spectra in coincidence (a) with 540 ± 2.5 keV and (b) with 591 ± 2.5 keV. Note the 22 coincidence events (591−540 keV) in 440 d of measuring time.

They are equal to 86 ± 25 events at 539.53 keV and 67 ± 23 events at 590.76 keV. To increase the effect one can sum the two peaks. The peak at 539.53 keV and surrounding channels were shifted to 590.73 keV and summed (Fig. 3*b*). The total peak is estimated at 153 ± 35 counts. The calculated value for the half-life is $(9.3^{+2.8}_{-1.7}) \times 10^{20}$ yr. The systematic error is estimated at 15%.

If the spectrum of [7] is used additively, one can produce an estimate with greater statistics. Figure 4*a* shows the summed spectrum. The peak at 539.53 keV is 165 ± 37, and the peak at 590.76 keV is 135 ± 34. The sum of the two peaks, 539 and 590 keV, is shown in Fig. 4*b* and is equal to 300 ± 51, which leads to $T_{1/2} = (7.6^{+1.6}_{-1.1}) \times 10^{20}$ yr. This value has a considerably smaller statistical error due to the peak estimation but retains an uncertainty on the order of 15% connected with systematic errors in the efficiencies calculated.

2.3. TUNL–ITEP Experiment

This experiment [10] is being performed in a well-shielded room located in the basement of the Physics Department of Duke University (USA). A disk of enriched Mo 106 mm in diameter and 11 mm thick (full weight is 1050 g; enrichment is 98.4%) is sandwiched between the front faces of two large HPGe detectors that work in the coincidence regime. The detectors, 87 mm in diameter by 50 mm in length, are inserted in a NaI(Te) annulus used as an active veto. The entire apparatus is inserted in a passive shielding made of lead bricks. Transition to the 0^+_1 excited state was investigated by detecting cascade of two, 539.53- and 590.76-keV, γ quanta. After 440 d of measurements, 22 coincidence events were detected using an interval of ± 2.5 keV at the aforementioned γ-quanta energies. The background was estimated from experimental data to be 2.5 events (Fig. 5). The efficiency ($\varepsilon = 0.22\%$) was estimated using Monte Carlo simulations and calibration with a ^{102m}Rh source. As a result $T_{1/2} = (5.9^{+1.7}_{-1.1}(\text{stat.}) \pm 0.6(\text{syst.})) \times 10^{20}$ yr was obtained for transition to 0^+_1 excited states in ^{100}Ru.

3. DISCUSSION

All "positive" experimental results, together with the number of useful events and the signal/background ratio, are presented in the table. One can see that the results are in good agreement. The weighted-average half-life value (using a standard procedure recommended by the Particle Data Group [19]) is $T_{1/2} = (6.8 \pm 1.2) \times 10^{20}$ yr.

These experiments do not distinguish between 2ν and 0ν modes of $\beta\beta$ decay. However, Ejiri *et al.* [20] have reported $T_{1/2}(0\nu) > 5.5 \times 10^{22}$ yr (90% C.L.) for neutrinoless $\beta\beta$ decay of ^{100}Mo to the ground state of ^{100}Ru, and it is reasonable to assume a negligible contribution of 0ν events in the data presented here. One can compare the derived value with theoretical predictions that were obtained using the QRPA-based models (1.3×10^{20} yr [2], 2.1×10^{21} yr [15], and 10^{21} yr [21]) and Pseudo-$SU(3)$ model (1.5×10^{21} yr [22]). Using the $2\nu\beta\beta$ half-life value presented here and the phase-space factor $G = 1.64 \times 10^{-19}$ yr^{-1} (for the bare axial-vector coupling constant $g_A = 1.254$), one obtains the nuclear matrix element $M_{2\nu}(0^+_1) = 0.095 \pm 0.009$ (scaled by the electron rest mass).

Present "positive" results on $\beta\beta$ decay of ^{100}Mo to the first 0^+ excited state in ^{100}Ru (the last line gives the weighted-average half-life value for this transition; N is the number of useful events, and S/B is the signal/background ratio)

Transition	$T_{1/2}$, yr	N	S/B	Reference
^{100}Mo–^{100}Ru	$6.1^{+1.8}_{-1.1} \times 10^{20}$	133	$\sim 1/3$	[7]
0^+_1; 1130.29 keV	$[9.3^{+2.8}_{-1.7}(\text{stat.}) \pm 1.4(\text{syst.})] \times 10^{20}$	153	$\sim 1/3$	[9]
	$[5.9^{+1.7}_{-1.1}(\text{stat.}) \pm 0.6(\text{syst.})] \times 10^{20}$	19.5	8/1	[10]
	Average value: $(6.8 \pm 1.2) \times 10^{20}$			

4. CONCLUSION

The existence of the $\beta\beta$ decay of ^{100}Mo to the excited state in ^{100}Ru (0^+_1; 1130.29 keV) has been confirmed in three independent experiments. The average value for the half-life is estimated as $T_{1/2} = (6.8 \pm 1.2) \times 10^{20}$ yr. The average value for the nuclear matrix element is 0.095 ± 0.009.

ACKNOWLEDGMENTS

I would like to thank M. Hornish (TUNL, USA) for his remarks.

REFERENCES

1. J. Suhonen and O. Civitarese, Phys. Rep. **300**, 123 (1998).
2. M. Aunola and J. Suhonen, Nucl. Phys. A **602**, 133 (1996).
3. A. S. Barabash, JETP Lett. **51**, 207 (1990).
4. A. S. Barabash *et al.*, Phys. Lett. B **249**, 186 (1990).
5. D. Blum *et al.*, Phys. Lett. B **275**, 506 (1992).
6. N. Kudomi *et al.*, Phys. Rev. C **46**, R2132 (1992).
7. A. S. Barabash *et al.*, Phys. Lett. B **345**, 408 (1995).
8. D. Dassie *et al.*, Phys. Rev. D **51**, 2090 (1995).
9. A. S. Barabash *et al.*, Phys. At. Nucl. **62**, 2039 (1999).
10. L. De Braeckeleer *et al.*, Phys. Rev. Lett. **86**, 3510 (2001).
11. C. Arpesella *et al.*, Europhys. Lett. **27**, 29 (1994).
12. A. S. Barabash *et al.*, J. Phys. G **22**, 487 (1996).
13. C. Arpesella *et al.*, Nucl. Phys. B (Proc. Suppl.) **48**, 247 (1996).
14. S. Vasiliev *et al.*, Pis'ma Zh. Éksp. Teor. Fiz. **61**, 353 (1995) [JETP Lett. **61**, 358 (1995)].
15. S. Stoica and I. Mihut, Nucl. Phys. A **602**, 197 (1996).
16. J. Suhonen *et al.*, Z. Phys. A **358**, 297 (1997).
17. A. Piepke *et al.*, Nucl. Phys. A **577**, 493 (1994).
18. A. S. Barabash *et al.*, Z. Phys. A **352**, 231 (1995).
19. D. E. Groom *et al.*, Eur. Phys. J. C **15**, 10 (2000).
20. H. Ejiri *et al.*, Phys. Rev. C **63**, 065501 (2001).
21. A. Griffiths and P. Vogel, Phys. Rev. C **46**, 181 (1992).
22. J. G. Hirsch *et al.*, Phys. Rev. C **51**, 2252 (1995).

Physics of Atomic Nuclei, Vol. 66, No. 3, 2003, pp. 462–465. From Yadernaya Fizika, Vol. 66, No. 3, 2003, pp. 490–493.

Ion-Pulse Ionization Chamber for Direct Measurement of Radon Concentration in the Air*

V. V. Kuzminov**

Institute for Nuclear Research, Russian Academy of Sciences, pr. Shestidesyatiletiya Oktyabrya 7a, Moscow, 117312 Russia

Received April 17, 2002

Abstract—A large-volume (24.8 l in total volume, 16.8 l in fiducial volume) multiwire pulse ion collection ionization chamber was examined as a detector of α particles from radon decays in the air inside the chamber. The possibility of obtaining spectrometric information from slow ion pulses was tested. An energy resolution of 3.9% for 5.49-MeV α particles was obtained in preliminary measurements. It was shown that a detector of this kind could be used for direct measurements of radon activities in flowing air at a level less than 1 Bq/m^3. A radon concentration at a level of 10 Bq/m^3 can be measured with an accuracy better than 10% for a counting time of 10^3 s. The detector will be used for continuous accurate monitoring of the ^{222}Rn concentration in the air of low-background laboratories. © *2003 MAIK "Nauka/Interperiodica".*

1. INTRODUCTION

The influence of radon radioactivity in the air on the results of low-background experiments is well known. Blowing off liquid nitrogen vapor through the inner volume of a low-background shield with the detector inside and using a hermetically sealed shield are the usual ways to reduce radon and daughter decay background. But these ways are not so simple in the case of a large-volume shield and detector. The outer air may penetrate partially into the detector region in this case. Direct measurement of the radon concentration in the laboratory air or in the outgoing gas is the way to obtain information about the radon and daughter decay contribution to the detector background.

Different methods for monitoring the radon concentration in the air are well known (see, e.g., [1]). Some of them are too complicated, while others are of low efficiency. We have examined the possibility of eliminating the shortcomings by using a large-volume multiwire ion-pulse ionization chamber (IPIC) as a detector of α particles from radon decays in the air inside the chamber. Since electrons in the air are captured very fast by electronegative oxygen molecules, the ionization charge is carried by positive and negative ions. The time of charge collection from a distance of 10 mm in an axial electric field with a potential of 1000 V on the central electrode 0.05 mm in diameter is 3.8 ms. It lies in the frequency region of environmental and industrial noise and 50-Hz stray pickups, so the chamber should be shielded against them.

2. CHAMBER CHARACTERISTICS

A cross-sectional view of the IPIC is shown in Fig. 1. The size of the fiducial volume is 243 × 243 × 420 mm (24.84 l), and the size of one cell is 20 × 20 × 420 mm. The anode and cathode grids are made of Ni–Cr alloy wires 0.05 mm in diameter. Supporting insulators of the anode wires are surrounded at both ends by guard electrodes. The outer cathode planes are made of double-sided copper-foil-coated glass-cloth-base laminate. The copper foils are electrically connected to the supporting construction. The load-carrying structure with the multiwire system is fixed inside the bottom section of the stainless-steel rectangular case by means of insulators. The top section of the case is used for electronic units. The fiducial volume of the IPIC is divided into two parts. The first one is the central-region cells (420-pF capacity, 100 cells, 16.8 l in volume). This part (CIPIC) is used for radon decay measurements. The second part (GIPIC) is a layer of cells along the walls (232-pF capacity, 8 l in volume). It protects the central part against wall α particles and wall effects and could be used as an active anticoincidence shield or as a passive gas filter with a cleaning electric field. In this paper, we present the results obtained for the latter case.

*This article was submitted by the author in English.

**e-mail: kuzminov@neutr.novoch.ru

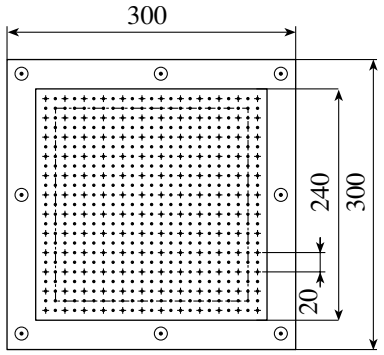

Fig. 1. Cross-sectional view of the ion-pulse ionization chamber: (·) cathode, (+) anode, and (dash-dotted line) boundary.

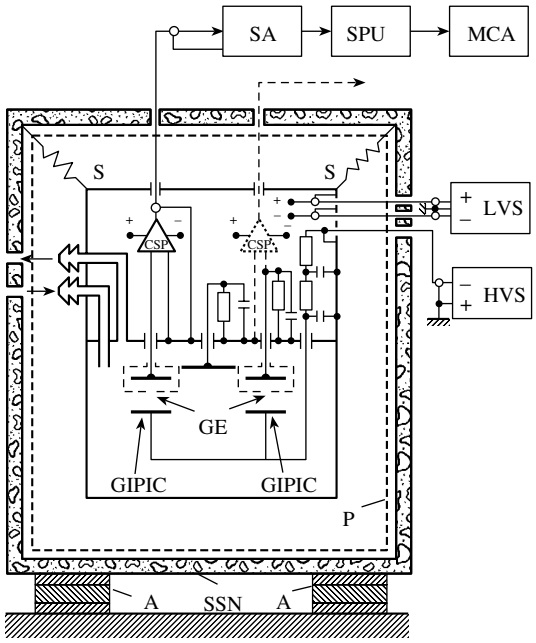

Fig. 2. Schematic diagram of the electronic system: CSP is charge-sensitive preamplifier, SA is shaping amplifier, SPU is shortening pulse unit, MCA is multichannel analyzer, LVS is low-voltage supply, HVS is high-voltage supply, GIPIC is central ion-pulse ionization chamber, GIPIC is guard ion-pulse ionization chamber, GE is guard electrode, P is permalloy screen, S is suspension, A is shock absorber, and SSN is shield against sound noise.

3. EXPERIMENTAL CONDITIONS

A schematic diagram of the IPIC electronic system and some details of the measuring installation are shown in Fig. 2. A negative high voltage is applied to the cathode. The optic feedback charge-sensitive preamplifier (CSP), shaping amplifier (SA), and shortening pulse unit (SPU) were specially designed for this work. The CSP has a decay time of 20–50 ms. The SA has an amplification of 800 and differentiation and integration shaping time in the 1–11 ms region.

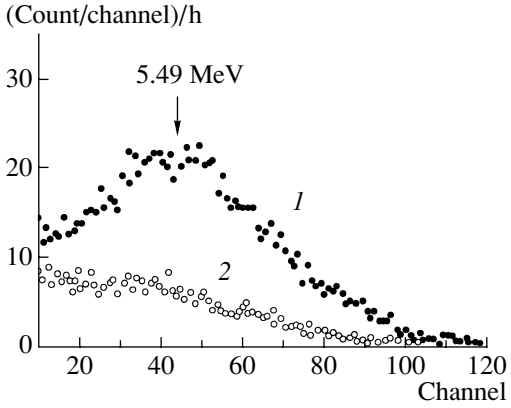

Fig. 3. ^{222}Ra decay α-particle spectrum from the CIPIC (first measurement): (*1*) collection time $t = 0$–12.2 h; (*2*) collection time $t = 381.2$–396.1 h.

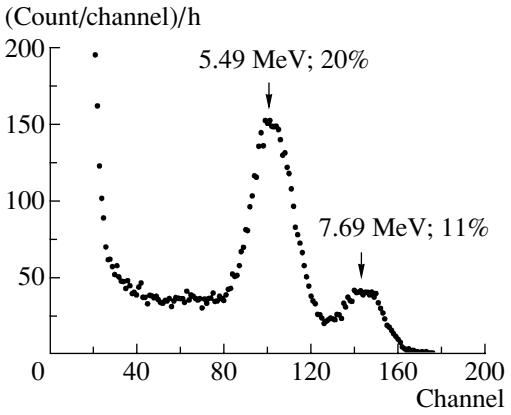

Fig. 4. ^{222}Ra decay α-particle spectrum from the CIPIC (low-noise shield). $\Delta t = 9.7$ h.

The SPU produces short pulses of 10 μs duration from ~10-ms SA output signals with the same amplitude. Short pulses allow a usual multichannel analyzer (MCA) to be used for amplitude spectra recording.

It was found after a number of preliminary investigations that a complete measuring installation should include a shield against sound noise (SSN), suspensions (S), and shock absorbers (A) against floor shake and a permalloy screen against 50-Hz stray pickups. We used laboratory air for the chamber filling. The normal air pressure at the elevation where the Baksan Neutrino Observatory is located is around 620 torr. In this air, the paths of α particles with energies of 5.49 MeV (^{222}Rn, $T_{1/2} = 3.82$ d), 6.00 MeV (^{218}Po, $T_{1/2} = 3.05$ min), and 7.69 MeV (^{214}Po, $T_{1/2} = 1.64$ to 10^{-4} s) are equal to 4.8, 5.6, and 8.1 cm, respectively [2]. Two bags made of metallic mash with silica gel (~100 cm^3) were soldered

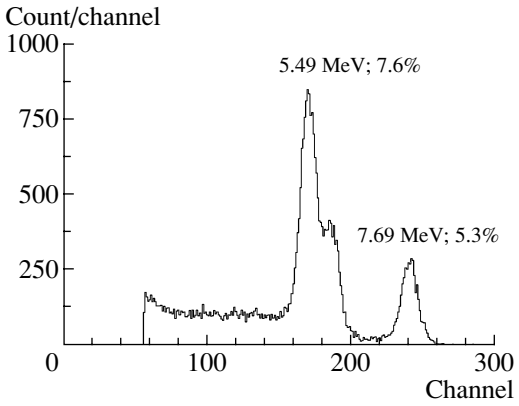

Fig. 5. ^{222}Rn decay α-particle spectrum. Improved sound noise shield.

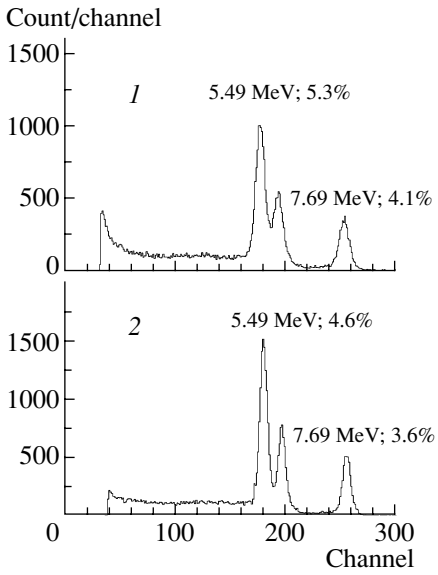

Fig. 6. ^{222}Rn decay α spectra from the IPIC with a 50-Hz stray pickup compensator. Spectra *1* and *2* differ in compensator conditions ($\Delta t_1 = 12$ h, $\Delta t_2 = 11$ h 49 min).

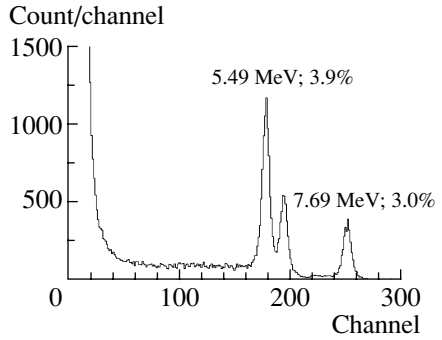

Fig. 7. ^{222}Rn decay α-particle spectrum (permalloy screen).

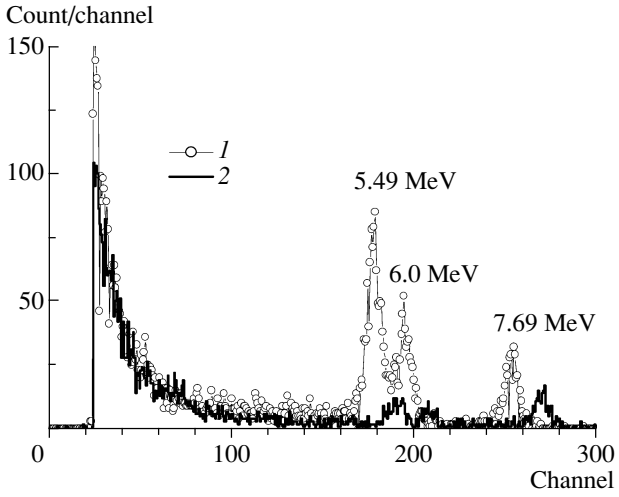

Fig. 8. ^{222}Rn decay α-particle spectra: (*1*) air (66 min); (*2*) nitrogen (66 min).

onto the outer surfaces of the cathode planes to dry the air inside the chamber. As was measured, silica gel generates radon with an equilibrium volume activity of 12 Bq/m^3. In the first measurements, we used as a calibration source the air enriched with radon by preliminarily blowing it through a vessel with a uranium salt.

4. RESULTS

The spectra of radon and daughter decay α particles obtained in the first measurement with IPIC without any shield are shown in Fig. 3. Spectrum *1* was collected during the time interval from 0 to 12.2 h. Spectrum *2* was collected during the time interval from 381.2 to 396.1 h. The ratio of an averaged signal amplitude to an averaged amplitude of a microphone effect noise was equal to 2 in this measurement. A confirmation of radon decay α-particle detection could be obtained only from comparison of the change in the spectrum count rate time and the radon decay time curve. The spectrum in Fig. 4 was obtained from the IPIC suspended inside the SSN with shock absorbers. The spectrum in Fig. 5 was obtained under the same conditions but with an improved sound noise shield. It was found that the microphone effect (ME) on the IPIC has two components. The first one is ME that occurs without a high voltage applied to the IPIC. The second one is connected with the IPIC capacity modulation during wire vibrations that produce signals when a high voltage is applied. As was found, the first component of ME is caused by a charge induced on the anode and cathode wires when they oscillate above the charged insulator surface. This component was decreased after the anode and cathode wires had been stuck to the insulator surface with melted paraffin.

Spectra *1* and *2* in Fig. 6 were obtained with the radon produced by the inner silica gel after the IPIC improvement. They differ in the 50-Hz stray pickup levels. A special compensator of 50-Hz pickups was made for this stage of measurement. A signal from its output was mixed with the CSP output signal at the SA input. Compensation was achieved by adjusting the phase and amplitude of the compensator signal. During measurement, this compensation could be destroyed due to time change of the 50-Hz stray pickup amplitude and phase. These shortcomings were avoided by using a permalloy screen. The spectrum measured with the screen is shown in Fig. 7. The energy resolution of the 5.49-MeV α peak equals 3.9%. The pulse-generator peak has the same resolution when a high voltage is applied to the chamber and a 1.2% resolution when the high voltage is switched off. The latter value can be compared with the 0.6% statistical energy resolution for the 5.49-MeV α peak calculated without taking into account charge recombination in α tracks. We assume two possible reasons for the pulse-generation peak resolution worsening when a high voltage is switched on. The first one is noise of the leakage current of the chamber insulators. The second one is noise of ionization pulses created by Compton electrons and cosmic rays. This component could be decreased by placing the chamber in an underground low-background shield. We tested the fitness of the chamber for radon concentration measurement in liquid nitrogen vapor. First, the α spectrum of equilibrium activity of radon produced by silica gel was measured for 66 min (Fig. 8, spectrum *1*). For 60 min after that, 100 l of liquid nitrogen vapor was blown through the chamber. The measurement was started just after the blowing. The spectrum collected for 66 min is shown in Fig. 8 (spectrum 2). The amplitude of α pulses in the nitrogen vapor ($\sim$0.5% O_2) increased by $\sim$4% in comparison with the air under the same conditions. This increase could be connected with lower track ion density due to a longer path of electrons before they are captured by oxygen molecules. The 7.69-MeV α peak in spectrum *2* has an abnormal amplitude because part of it is related to decays of ^{214}Po atoms that are left on the chamber electrodes after the measurements with the air.

We estimated the sensitivity of the chamber for radon volume activity to be of 10% standard deviation at 10 Bq/m^3 measured for 10^3 s. This value is 30 times higher than the sensitivity of a standard radon monitor [3]. A sufficiently good energy resolution allows one to measure the real radon activity in the air by analyzing only the 5.49-MeV α peak in comparison with methods giving values of radon activity on the basis of ^{218}Po and ^{214}Po activity measurements.

ACKNOWLEDGMENTS

I express sincere thanks to G.D. Korotky for his fruitful work in the design and preparation of the electronic units.

Part of this work was done through the financial support of the Russian Foundation for Basic Research (project no. 97-02-16051).

REFERENCES

1. *Proceedings of "Natural Radiation Environment III," Houston, Apr. 1978,* CONF-780422 (Technical Information Center/U. S. Department of Energy, 1980).
2. L. R. Kimel and V. P. Mashkovich, *Protection against Ionizing Radiation* (Atomizdat, Moscow, 1972), p. 226.
3. Description of the Radon Gas Monitor "ATMOS-10," The "GAMMA-DATA/MÄTTEKNIK AB" firm production, Uppsala, Sweden.

Physics of Atomic Nuclei, Vol. 66, No. 3, 2003, pp. 466–468. From Yadernaya Fizika, Vol. 66, No. 3, 2003, pp. 494–496.

NEUTRINO OSCILLATIONS AND MIXINGS, NEUTRINOS FROM THE SUN, REACTORS, AND ACCELERATORS

Neutrino-Driven Streaming Instability of Spin Waves in Dense Magnetized Plasma*

V. N. Oraevsky and V. B. Semikoz**

The Institute of Terrestrial Magnetism, Ionosphere, and Radio-Wave Propagation, Russian Academy of Sciences (IZMIRAN), Troitsk, Moscow oblast, 142092 Russia

Received February 13, 2002

Abstract—The spin effects on electromagnetic waves in a strongly magnetized plasma with rare collisions are considered with the help of relativistic kinetic equations, which take into account the electron spin dynamics in self-consistent electric and magnetic fields. The growth rate of the electromagnetic spin waves in the presence of intense quasi-monoenergetic fluxes of neutrinos is determined. © *2003 MAIK "Nauka/Interperiodica".*

Considering the spin wave propagation in a dense plasma with the strong magnetic field $\mathbf{B}_0 = (0, 0, B_0)$, one finds, in the case of quasi-perpendicular wave propagation in a cold magnetized electron gas, $k_z \ll k_\perp$, a new eigenmode with the spectrum given by the paramagnetic spin resonance of electrons, $\omega \approx \Omega_e$ [1]. The excitation of spin waves in solids (ferromagnets) by an electron beam is well known in the literature [2]. It should be kept in mind that we consider here the Fermi gas of free electrons in contrast to the quasiparticle approach in condensed matter and also neglect the exchange interaction of electrons since the long-range forces are dominant in a plasma. A suitable object for the appearance of spin waves in a plasma would be a polarized electron gas of a magnetized supernova (SN). A powerful neutrino flux can excite spin waves there analogously to the possible excitation of plasma waves in an isotropic SN plasma [3].

The system of self-consistent kinetic equations for the electron number density distribution $f^{(e)} = f^{(e)}(\mathbf{p}, \mathbf{x}, t)$ and the electron spin density distribution $\mathbf{S}^{(e)} = \mathbf{S}^{(e)}(\mathbf{p}, \mathbf{x}, t)$,

$$\left(\frac{\partial}{\partial t} + (\mathbf{v}\nabla)\right) f^{(e)} = e\left(\mathbf{E} + \frac{1}{c}[\mathbf{v}, \mathbf{B}]\right)\frac{\partial f^{(e)}}{\partial \mathbf{p}}, \quad (1)$$

$$\left(\frac{\partial}{\partial t} + (\mathbf{v}\nabla)\right) \mathbf{S}^{(e)} \quad (2)$$
$$= \left[e\left(\mathbf{E} + \frac{1}{c}[\mathbf{v}, \mathbf{B}]\right)\frac{\partial}{\partial \mathbf{p}}\right] \mathbf{S}^{(e)} + \frac{2\mu_\mathrm{B}}{\hbar}\left[\mathbf{S}^{(e)}, \mathbf{B}\right]$$
$$+ \frac{G_\mathrm{F}\sqrt{2}c_A f_0^{(e)}(\varepsilon_p)}{m_e}\int \frac{d^3q}{(2\pi)^3}\nabla\delta f^{(\nu)}(\mathbf{q}, \mathbf{x}, t),$$

is completed [4] by the neutrino kinetic equation for the total number density distribution $f^{(\nu)}(\mathbf{q}, \mathbf{x}, t) = f_0^{(\nu)}(\mathbf{q}) + \delta f^{(\nu)}(\mathbf{q}, \mathbf{x}, t)$,

$$\frac{\partial \delta f^{(\nu)}(\mathbf{q}, \mathbf{x}, t)}{\partial t} + \mathbf{n}\frac{\partial \delta f^{(\nu)}(\mathbf{q}, \mathbf{x}, t)}{\partial \mathbf{x}} \quad (3)$$
$$+ F_{j\mu}^{(V)}(\mathbf{x}, t)\frac{q^\mu}{\varepsilon_q}\frac{\partial f_0^{(\nu)}(\mathbf{q})}{\partial_{q_j}}$$
$$+ F_{j\mu}^{(A)}(\mathbf{x}, t)\frac{q^\mu}{\varepsilon_q}\frac{\partial f_0^{(\nu)}(\mathbf{q})}{\partial q_j} = 0,$$

and by the Maxwell equations

$$\frac{\partial \mathbf{B}}{c\partial t} = [\nabla, \mathbf{E}], \qquad c[\nabla, \mathbf{B}] + \frac{\partial \mathbf{E}}{\partial t} = 4\pi\mathbf{j}, \quad (4)$$

where the total electron current $\mathbf{j}(\mathbf{x}, t) = \mathbf{j}^{\mathrm{conv}}(\mathbf{x}, t) + \mathbf{j}^{\mathrm{mag}}(\mathbf{x}, t)$ consists of the convection current of electrons $\mathbf{j}^{\mathrm{conv}}(\mathbf{x}, t) = -e\int d^3p\,\mathbf{v}f^{(e)}(\mathbf{p}, \mathbf{x}, t)$ and the magnetization current

$$\mathbf{j}^{\mathrm{mag}}(\mathbf{x}, t) = \mu_\mathrm{B}\int \frac{d^3p_e}{(2\pi)^3}[\nabla, \mathbf{S}^e].$$

In the system above, $e = |e|$ is the electric (proton) charge, $\gamma = \varepsilon_p/m_e c^2$ is the electron gamma factor, $\mu_\mathrm{B} = e\hbar/2m_e c = 5.79 \times 10^{-5}$ eV/T is the Bohr magneton, and $\mathbf{B} \to \mathbf{B}_0 + \mathbf{B}$ is the total magnetic field. The system is linearized with respect to equilibrium distributions, $f^{(e)}(\mathbf{p}, \mathbf{x}, t) = f_0^{(e)}(\varepsilon_p) + \delta f^{(e)}(\mathbf{p}, \mathbf{x}, t)$, $\mathbf{S}^{(e)}(\mathbf{p}, \mathbf{x}, t) = \mathbf{S}_0^{(e)}(\varepsilon_p) + \delta\mathbf{S}^{(e)}(\mathbf{p}, \mathbf{x}, t)$,

*This article was submitted by the authors in English.

** e-mail: semikoz@orc.ru

1063-7788/03/6603-0466$24.00

where the Fermi distribution $f_0^{(e)}(\varepsilon_p)$ and the electron density n_{0e} are given by

$$f_0^{(e)}(\varepsilon_p) = \frac{2\hbar^{-3}}{\exp[(\varepsilon_p - \varepsilon_{\rm F})/T] + 1},$$
$$n_{0e} = \int \frac{d^3p}{(2\pi)^3} f_0^{(e)}(\varepsilon_p),$$

and the mean spin polarization

$$\mathbf{S}_0^{(e)}(\varepsilon_p) = -\mu_{\rm B}\frac{df_0^{(e)}(\varepsilon_p)}{d\varepsilon_p}\mathbf{B}_0. \qquad (5)$$

The weak forces in the neutrino kinetic equation (3) are given by the antisymmetric tensors $F_{j\mu}^{(V,A)}(\mathbf{x},t)$,

$$F_{j0}^{(V)}(\mathbf{x},t)/G_F\sqrt{2}c_V = -\nabla_j\delta n^{(e)}(\mathbf{x},t) \qquad (6)$$
$$-\frac{\partial\delta j_j^{(e)}(\mathbf{x},t)}{\partial t},$$
$$F_{jk}^{(V)}(\mathbf{x},t)/G_F\sqrt{2}c_V = e_{jkl}(\nabla\times\delta\mathbf{j}^{(e)}(\mathbf{x},t))_l,$$
$$\sqrt{2}F_{j0}^{(A)}(\mathbf{x},t)/G_F c_A = -\nabla_j\delta A_0^{(e)}(\mathbf{x},t)$$
$$-\frac{\partial\delta A_j^{(e)}(\mathbf{x},t)}{\partial t},$$
$$\sqrt{2}F_{jk}^{(A)}(\mathbf{x},t)/G_F c_A = e_{jkl}(\nabla\times\delta\mathbf{A}^{(e)}(\mathbf{x},t))_l,$$

where

$$j_\mu^{(\nu)}(\mathbf{x},t) = \int (q_\mu/\varepsilon_q) f^{(\nu)}(\mathbf{q},\mathbf{x},t)d^3q/(2\pi)^3,$$

$$\delta j_\mu^{(e)}(\mathbf{x},t) = \int (p_\mu/\varepsilon_p)\delta f^{(e)}(\mathbf{p},\mathbf{x},t)d^3p/(2\pi)^3$$

are four-vectors of the neutrino current density and the electron current density perturbation, respectively, and $\delta A_\mu^{(e)}(\mathbf{x},t) = m_e\int(d^3p/(2\pi)^3)\delta a_\mu^{(e)}\times(\mathbf{p},\mathbf{x},t)$ is the axial four-vector of the spin density perturbation, where the axial four-vector $\delta a_\mu^{(e)}(\mathbf{p},\mathbf{x},t)$ has the components

$$\delta a_\mu^{(e)}(\mathbf{p},\mathbf{x},t) = \left[\frac{\mathbf{p}\delta\mathbf{S}^{(e)}(\mathbf{p},\mathbf{x},t)}{m_e};\delta\mathbf{S}^{(e)}(\mathbf{p},\mathbf{x},t)\right. \qquad (7)$$
$$\left.+\frac{\mathbf{p}(\mathbf{p}\delta\mathbf{S}^{(e)}(\mathbf{p},\mathbf{x},t))}{m_e(\varepsilon_e+m_e)}\right].$$

The latter is the statistical generalization of the Pauli–Lubański four-vector a_μ [5],

$$a_\mu(\mathbf{p}) = \left[\frac{\mathbf{p}\varsigma}{m_e};\varsigma + \frac{\mathbf{p}(\mathbf{p}\varsigma)}{m_e(\varepsilon_e+m_e)}\right].$$

Note that the neutrino relativistic kinetic equation (RKE) (3) differs from the result of [3] by the last term, which is stipulated by the parity violation through the contribution of the axial vector currents to weak interactions.

Substituting the solution to the neutrino RKE (3) and properly solving the modified spin RKE (2), we find the increment of the neutrino-driven streaming instability for the spin waves. Such an increment arises due to the Cherenkov resonance $\omega = \mathbf{k}\cdot\mathbf{n}_0 c + i\delta = \Omega_e + i\delta$ and has the form

$$\delta = \Omega_e\frac{\sqrt{3}}{4}(\Delta^{(\nu)})^{1/3}(\sqrt{2}\mid c_A\mid\sin\theta_{q_0})^{2/3}, \qquad (8)$$

where θ_{q_0} is the angle between the neutrino beam direction $\mathbf{n}_0$ and the wave vector $\mathbf{k}$, and the dimensionless parameter $\Delta^{(\nu)} = 2G_{\rm F}^2\, n_{e0}\, n_{\nu 0}/m_e\, q_0$ is given by the mean densities of the electrons and neutrinos n_{e0} and $n_{\nu 0}$. We neglected here the vector current terms ($\sim c_V$) entering the neutrino RKE (3), which give a negligible contribution ($\sim c_A c_V$) in the spin RKE for long wavelengths exceeding the Compton one, $2\pi/k \gg \hbar/m_e c$, a reasonable approximation in nonrelativistic (NR) plasma.

For the mean neutrino energy in a magnetized supernova (SN) $q_0 \sim 10$ MeV and for the NR plasma outside the neutrinosphere and behind the shock with the densities $n_{e0} \simeq 10^{29}$ cm^{-3} and $n_{\nu 0} \simeq 10^{32}$ cm^{-3}, the parameter is very small, $\Delta^{(\nu)} \sim 10^{-25}$, while the increment (8) would be big enough; e.g., for the strong magnetic field $B_0 = 10^{12}$ G and the corresponding gyrofrequency $\Omega_e = 1.7\times 10^7 B_0 = 1.7\times 10^{19}$ s^{-1}, it reaches the value $\delta \sim 10^{10}$ s^{-1}. One can see that the spin wave amplitude increases faster than a neutrino passes through the SN envelope ($\sim 10^{-3}$ s). Thus, the energy exchange between the plasma and neutrino fluxes by their interaction with spin waves probably could lead to a shock revival during the neutrino burst ($\sim$ 10–20 s) through the heating of the surrounding plasma. In reality, these spin waves are generally coupled to the magnetosonic ones analogously to the spin waves in ferromagnets [2], or their energy can be transferred to the electromagnetic and plasma waves at the cross of spectra.

Note that, in a strong magnetic field, $\Omega_e \geq \omega_{pe}$, the increment (8) is less suppressed for small angles $\theta_{q_0} \leq \arccos(\langle v\rangle/c)$ than the corresponding one for plasma waves in an isotropic plasma [3],

$$\delta = \omega_p\frac{\sqrt{3}}{2}(\Delta^{(\nu)})^{1/3}\left(\sqrt{2}c_V\frac{\sin^3\theta_{q_0}}{\cos^2\theta_{q_0}}\right)^{2/3},$$

which allows one to decrease the inevitable Landau damping of collective modes excited by the neutrino beam when spin waves propagate through a relativistic plasma with the mean electron velocity

$\langle v \rangle \sim c$. There is the second advantage of spin waves enhanced via the weak axial vector currents ($c_A \simeq \mp 0.5$) instead of the case of plasma waves excited via the weak vector currents with the small vector coupling in the case of muon and tau neutrinos (choosing the lower sign in $c_V = 2\xi \pm 0.5$, where $\xi \simeq 0.23$ is the Weinberg parameter). This is the reason why the authors in [3] considered the case of electron neutrinos only and put for them $c_V \longrightarrow 1$. Note that, during the main neutrino burst in SN, all neutrino species are produced in the hot SN core via the pair annihilation $e^+e^- \to \nu_a\bar{\nu}_a$, $a = e, \mu, \tau$.

Thus, we conclude that spin waves can be efficiently excited, e.g., in a magnetized SN by a powerful neutrino flux that could be an effective collective mechanism to revive the shock with the following burst of the SN envelope. There remain questions about (i) a collision influence on the spin wave enhancement, (ii) the spin collision integral in the spin RKE, etc. Discussion of these problems will be done in detail elsewhere.

ACKNOWLEDGMENTS

This work was partially supported by the Russian Foundation for Basic Research, project no. 00-02-16271.

REFERENCES

1. V. N. Oraevsky, V. B. Semikoz, and A. S. Volokitin, hep-ph/0203020; V. N. Oraevsky and V. B. Semikoz, Astropart. Phys. **18**, 261 (2002).
2. A. I. Akhiezer, V. G. Bar'yakhtar, and S. V. Peletminskii, *Spin Waves* (Nauka, Moscow, 1967; North-Holland, Amsterdam, 1968).
3. L. O. Silva *et al.*, Phys. Rev. Lett. **83**, 2703 (1999).
4. V. B. Semikoz, Physica A **142**, 157 (1987).
5. V. B. Berestetskiĭ, E. M. Lifshits, and L. P. Pitaevskiĭ, *Quantum Electrodynamics*, 2nd ed. (Pergamon Press, Oxford, 1982).

Physics of Atomic Nuclei, Vol. 66, No. 3, 2003, pp. 469–471. From Yadernaya Fizika, Vol. 66, No. 3, 2003, pp. 497–499.

NEUTRINO OSCILLATIONS AND MIXINGS, NEUTRINOS FROM THE SUN, REACTORS, AND ACCELERATORS

Two-Detector Reactor Neutrino Oscillation Experiment Kr2Det at Krasnoyarsk: Status Report*

Yu. V. Kozlov, L. A. Mikaelyan, and V. V. Sinev**

Russian Research Centre Kurchatov Institute, pl. Kurchatova 1, Moscow, 123182 Russia

Received February 13, 2002

Abstract—We consider the status of the Kr2Det project aimed at sensitive searches for neutrino oscillations in the atmospheric neutrino mass parameter region around $\Delta m^2 \sim 3 \times 10^{-3}$ eV^2 and at obtaining new information on the electron neutrino mass structure (U_{e3}). © *2003 MAIK "Nauka/Interperiodica".*

1. INTRODUCTION

The CHOOZ experiment [1] conclusively showed that oscillations of electron neutrinos do not play the dominant role in the atmospheric neutrino anomaly:

$$\sin^2 2\theta_{\mathrm{CHOOZ}} \leq 0.1 \quad (\text{at } \Delta m^2 = 3 \times 10^{-3}\ \mathrm{eV}^2). \tag{1}$$

In the three-active-neutrino-mixing scheme, $\sin^2 2\theta_{\mathrm{CHOOZ}} = 4U_{e3}^2(1 - U_{e3}^2)$, where U_{e3} is the contribution of the mass-3 eigenstate to the ν_e flavor state. Thus, the CHOOZ result indicates that this contribution is not large: $U_{e3}^2 \leq 2.4 \times 10^{-2}$.

The main physical goals of the Kr2Det project [2] are (i) to look for much smaller mixing angles and to find the element U_{e3} or to set stronger constraints on its value, (ii) to provide normalization for future long-baseline experiments at accelerators, and (iii) to reach a better understanding of the role that ν_e can play in the atmospheric neutrino anomaly. We also mention that new information on U_{e3} can help to choose between possible solar neutrino oscillation solutions [3].

The main practical goal of the project is to decrease, relative to the CHOOZ, the systematic and statistic errors as much as possible. This can be achieved (i) by using a two(far and near)-detector scheme of the experiment, which eliminates systematic uncertainties associated with the reactor neutrino flux and spectrum and (ii) by considerably increasing the number of detected neutrinos.

2. THE Kr2Det PROJECT

2.1. Detectors

Two identical liquid scintillation spectrometers stationed at distances $R_1 = 1100$ m (far position) and $R_2 = 150$ m (near position) from the Krasnoyarsk underground (600 m w.e.) reactor detect (e^+, n) pairs produced in the $\bar{\nu}_e + p \to n + e^+$ reaction. A miniature version of the KamLAND and BOREXINO [4] three-concentric-zone detector composition is chosen for the design of the spectrometers (Fig. 1.) The neutrino targets have 46 t of liquid scintillator enclosed in transparent balloons. The target is viewed by 500 8-inch EMI-9350 PMTs [5] through a 90-cm layer of zone-2 isoparaffin. PMTs of the same type were successfully used in the CHOOZ experiment and are used now in the SNO and BOREXINO detectors. A 120-photoelectron signal is expected for 1-MeV energy deposit in the detector center. The PMTs are mounted on a stainless steel screen, which optically separates external zone 3 from two central zones. The 75-cm-thick zone 3 is filled with mineral oil and serves as active (muons) and passive shielding against external radioactivity.

2.2. Neutrino Rates and Backgrounds

The neutrino event satisfies the following requirements: (i) a time window on the delay between e^+ and

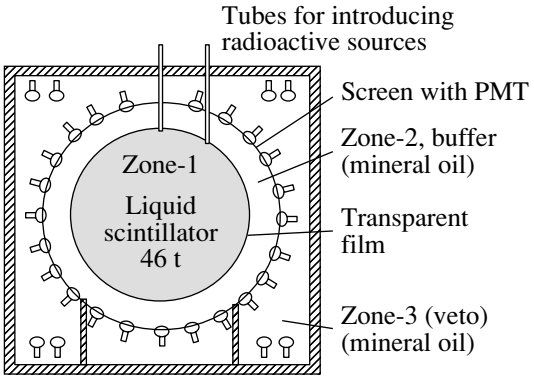

Fig. 1. The detector.

*This article was submitted by the authors in English.

** e-mail: sinev@polyn.kiae.su

Table 1. Single background rates due to natural radioactivity of detector materials

Material mass, t	Isotope	Purity, g/g	Background, Hz		
			>1.0 MeV	>1.2 MeV	>1.7 MeV
Scintillator, 45 t	^{238}U	10^{-13}	0.078	0.051	0.045
	^{232}Th	10^{-13}	0.033	0.022	0.017
	^{40}K	10^{-13}	0.020	0.005	0.001
	^{222}Rn	1 mBq/m^3	0.050	0.040	0.040
$\sum$ Scintillator			0.081	0.118	0.103
Zone-2 oil, 76 t	^{238}U	10^{-13}	0.0035	0.0019	0.0012
	^{232}Th	10^{-13}	0.0014	0.0008	0.0007
	^{40}K	10^{-13}	0.0097	0.0033	0.0007
	^{222}Rn	10 mBq/m^3	0.033	0.018	0.0116
$\sum$ zone-2 oil			0.0476	0.0240	0.0142
PMT, 500 kg	^{238}U	1×10^{-8}	0.028	0.013	0.008
	^{232}Th	2×10^{-8}	0.037	0.026	0.022
	^{40}K	7×10^{-9}	0.024	0.002	< 0.001
$\sum$ PMT			0.089	0.041	0.030
Screen stainless steel, 2 t	^{238}U	5×10^{-9}	0.056	0.27	0.016
	^{232}Th	1×10^{-8}	0.074	0.52	0.045
	^{40}K	2×10^{-9}	0.027	0.002	< 0.001
$\sum$ Screen			0.157	0.081	0.061
Zone-3 oil, 218 t	^{238}U	10^{-12}	<0.001		
	^{232}Th	10^{-12}			
	^{40}K	10^{-12}			
	^{222}Rn	10 mBq/m^3			
$\sum$ Zone-3 oil			0.0027	0.0016	0.0014
Total BKG rates			0.477	0.257	0.210

Table 2. Neutrino detection rates and backgrounds

Parameter	Distance, m	Depth, m w.e.	Target mass, t	Neutrino detection rates N_ν, d^{-1}	Background, d^{-1}	
					correlated	accidental
Far detector	1100	600	46	46	5	0.1
Near detector	150	600	46	2500	5	0.1

the neutron of 2–600 μs, (ii) an energy window for the neutron candidate of 1.7–3.0 MeV and for e^+ of 1.2–8.0 MeV, and (iii) the distance between e^+ and the neutron less than 100 cm. No pulse shape analysis is planned. Under these assumptions, the neutrino detection efficiency $\varepsilon = 77\%$ was found and the neutrino detection rate $N_\nu = 46$ d^{-1} was calculated for the detector at the 1100-m position.

The expected rate of the correlated background in the Kr2Det project [2], 0.1 per day per ton of the target mass, is about 3 times lower than was measured at CHOOZ, which reasonably agrees with the deeper position (600 vs. 300 m w.e.) of the Kr2Det detectors.

While the correlated background originates from

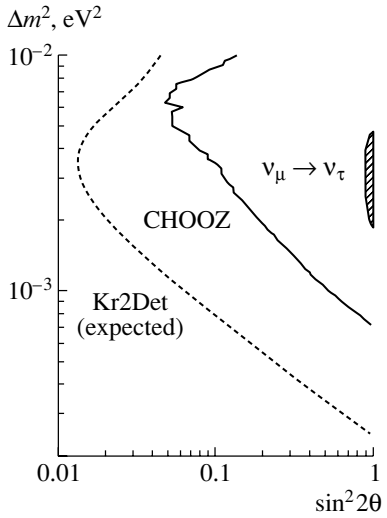

Fig. 2. Reactor neutrino 90% C.L. disappearance limits. Shaded is the atmospheric $\nu_\mu \to \nu_\tau$ allowed region.

cosmic muons, the accidentals come from natural radioactivity of materials. Table 1 summarizes radioactivity levels of the scintillator and other detector materials and calculated single rates, which define the rate of accidental coincidences. Backgrounds coming from U and Th contained in the surrounding rock are still under consideration.

The calculated accidental background rate is $N_{\mathrm{Acc}} \approx 0.1\ \mathrm{d}^{-1}$, which is a hundred times smaller than neutrino signal N_ν. We note that BOREXINO and KamLAND detectors intended for detecting solar neutrinos in the sub-MeV range will use scintillators with a level of radioactive impurities three to four orders of magnitude lower than the level sufficient for the present project. Calculated neutrino detection rates and backgrounds are summarized in Table 2.

2.3. Data Analysis and Expected Results

In the no oscillation case, the ratio of two simultaneously measured positron energy spectra $S_{\mathrm{FAR}}/S_{\mathrm{NEAR}}$ is energy-independent. Small deviations from the constant value of this ratio

$$\frac{S_{\mathrm{FAR}}}{S_{\mathrm{NEAR}}} = C\frac{(1-\sin^2 2\theta \sin^2\phi_F)}{(1-\sin^2 2\theta \sin^2\phi_N)} \qquad (2)$$

are the sought oscillations ($\phi_{F,N}$ stands for $1.27\Delta m^2 L_{F,N}/E_\nu$, and $L_{F,N}$ are the distances between the reactor and detectors). The results of the analysis do not depend on the exact knowledge of the neutrino flux and their energy spectrum, burnup effects, or the numbers of target protons. However, the possible relative difference of the detector energy scales should be strictly controlled. This can be done by a combination of different methods briefly mentioned in [2]. Expected 90% C.L. oscillation limits are presented in Fig. 2. It was assumed that 40 000 neutrinos are detected in the far detector and that detector response function differences are controlled down to 0.5%.

3. CONCLUSIONS

The mass structure of the electron neutrino can sensitively be explored using two-detector techniques in an underground laboratory. The project is relatively inexpensive when compared with modern neutrino experiments listed in the neutrino oscillation industry web sites. Effective international cooperation would be highly desirable to complete the project and start the experiment.

ACKNOWLEDGMENTS

We appreciate valuable discussions with E. Akhmedov, S. Bilenky, and A. Smirnov on the physics of neutrino oscillations. Discussions with our colleagues of the Kurchatov Institute's neutrino groups are of great help in developing this project. We are grateful to Yu. Kamyshkov and A. Piepke for valuable information on the KamLAND experiment.

This study is supported by the Russian Foundation for Basic Research, project nos. 00-02-16035 and 00-15-98708.

REFERENCES

1. M. Apollonio *et al.* (CHOOZ Collab.), Phys. Lett. B **446**, 415 (1999).
2. L. Mikaelyan, Nucl. Phys. B (Proc. Suppl.) **91**, 120 (2001); L. Mikaélyan and V. Sinev, Yad. Fiz. **63**, 1077 (2000) [Phys. At. Nucl. **63**, 1002 (2000)].
3. E. Akhmedov, G. Bianco, and M. Rebelo, Phys. Rev. Lett. **84**, 3535 (2000).
4. A. Piepke (KamLAND Collab.), Nucl. Phys. B (Proc. Suppl.) **91**, 99 (2001).
5. A. Baldini *et al.*, Nucl. Instrum. Methods Phys. Res. A **372**, 207 (1996).

Physics of Atomic Nuclei, Vol. 66, No. 3, 2003, pp. 472–475. From Yadernaya Fizika, Vol. 66, No. 3, 2003, pp. 500–503.

NEUTRINO OSCILLATIONS AND MIXINGS, NEUTRINOS FROM THE SUN, REACTORS, AND ACCELERATORS

The Search for New Physics in Nonequilibrium Reactor-Antineutrino Energy Spectrum*

V. I. Kopeikin**

Russian Research Centre Kurchatov Institute, pl. Kurchatova 1, Moscow, 123182 Russia

Received April 17, 2002

Abstract—The calculations of the time-dependent reactor-antineutrino energy spectrum are presented. Some problems associated with sensitive searches for the neutrino magnetic moment and neutrino oscillations in a reactor-antineutrino flux are considered. © *2003 MAIK "Nauka/Interperiodica".*

1. INTRODUCTION

The previous results from $\bar{\nu}_e e$ scattering reactor experiments were interpreted as an upper limit of $2 \times 10^{-10}\mu_B$ (μ_B is the electron Bohr magneton) on the neutrino magnetic moment μ_ν [1]. Direct measurements of the neutrino magnetic moment at a level of $10^{-11}\mu_B$ would have a serious impact on particle physics and astrophysics [2]. To achieve this sensitivity, the low-energy recoil electrons in $\bar{\nu}_e e$ scattering should be detected. Preparations for such experiments are under way [3]. As was discussed in [4], the soft part of the recoil-electron energy spectrum may be strongly time-dependent during the reactor cycle. In the present study, the time evolution of the $\bar{\nu}_e e$ scattering cross sections expected in reactor experiments for weak and magnetic interactions is calculated.

In any neutrino reaction, the cross section observed, σ_{fis}, is the reaction cross section for monoenergetic antineutrinos, $\sigma(E_\nu)\,(\text{cm}^2/\bar{\nu}_e)$, folded with the reactor-$\bar{\nu}_e$ spectrum $\rho(E_\nu, t)\,[\bar{\nu}_e/(\text{MeV fission})]$,

$$\sigma_{\text{fis}}(t) = \int \rho(E_\nu, t)\,\sigma(E_\nu)dE \quad [\text{cm}^2\ \text{fission}^{-1}]. \quad (1)$$

To interpret the data, one, therefore, must have accurate knowledge of the antineutrino spectrum. In this work, a typical thermal power reactor-$\bar{\nu}_e$ spectrum and its time evolution are calculated.

Oscillation experiments are based on the reaction

$$\bar{\nu}_e + p \to e^+ + n. \quad (2)$$

Any distortions of the positron energy spectrum or decrease in cross section (1) measured at the reactor would indicate oscillations. In a recent paper [5], we calculated corrections to the nonoscillation cross section for reaction (2) that had been precisely measured near the power reactor [6]. In the present study, we discuss the role of the residual $\bar{\nu}_e$ emission after reactor shutdown in measurement of the positron spectrum.

2. REACTOR-ANTINEUTRINO SPECTRUM

Here, we consider the antineutrino energy spectrum of a light water reactor (LWR). Reactors of this type are used in most neutrino experiments. They usually operate for 11 months, followed by a shutdown of one month for replacing one-third of the fuel elements. At the beginning of each annual reactor cycle, $\alpha_5 = 69\%$ of the fissions are from ^{235}U, $\alpha_9 = 21\%$ from ^{239}Pu, $\alpha_8 = 7\%$ from ^{238}U, and $\alpha_1 = 3\%$ from ^{241}Pu. During operation, ^{235}U burns up and ^{239}Pu and ^{241}Pu are accumulated from ^{238}U. The average ("standard") fuel composition is

$$\bar{\alpha}_5 = 58\%,\ \ \bar{\alpha}_9 = 30\%,\ \ \bar{\alpha}_8 = 7\%,\ \ \bar{\alpha}_1 = 5\%. \quad (3)$$

The present calculation of the time-dependent reactor-$\bar{\nu}_e$ spectrum during operation and shutdown periods include the following:

(a) Time-dependent $\bar{\nu}_e$ activity of the fission products, including possible isomeric states, effect of delayed neutrons, and transmutations of fission products by reactor neutrons. The time-dependent fission contributions $\alpha_i(t)$ $(i = 5, 9, 8, 1)$ in both the current and two previous annual reactor cycles are taken into account.

(b) Time-dependent $\bar{\nu}_e$ activity coming from the neutron captures by heavy elements. A dominant contribution comes from the captures by ^{238}U: $^{238}\text{U}(n,\gamma)^{239}\text{U} \to {}^{239}\text{Np} \to {}^{239}\text{Pu}$. The relative contribution of the other antineutrino sources in the reactor core is less than 0.5% [7].

*This article was submitted by the author in English.

**e-mail: kopeykin@polyn.kiae.su

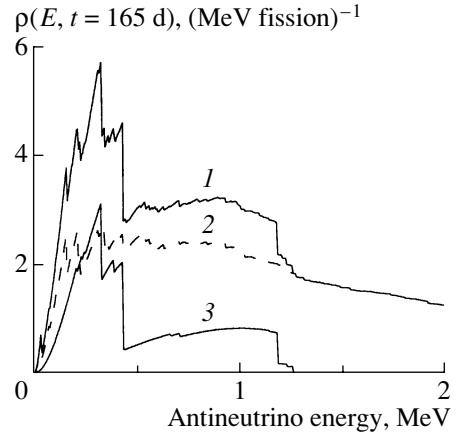

Fig. 1. Energy spectrum of antineutrinos from the LWR in the middle of the 330-d operating period: (*1*) all antineutrinos, (*2*) fission antineutrinos, and (*3*) antineutrinos associated with neutron captures in heavy elements.

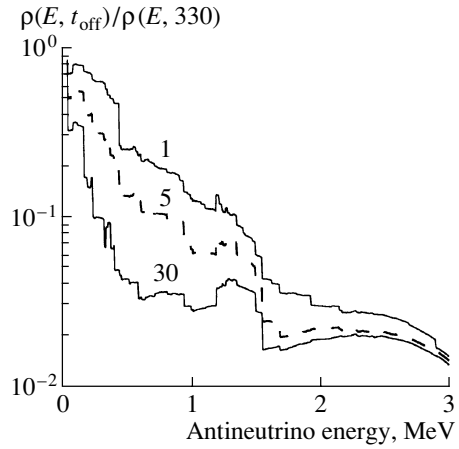

Fig. 2. Ratios of the current $\bar{\nu}_e$ spectra after the reactor is shut down to the spectrum at the end of the 330-d reactor operation period. The numbers by the lines indicate days after reactor shutdown.

The calculation of the $\bar{\nu}_e$ spectrum below 2 MeV (to which three-fourths of all emitted antineutrinos belong) and its components is presented in Fig. 1. The $\bar{\nu}_e$ spectrum in the energy range of $E_\nu = 2$–9 MeV was measured at the Rovno reactor [7]:

$$\rho(E_\nu) = 5.09\exp[-(E_\nu/1.54) - (E_\nu/6.05)^2 - (E_\nu/7.73)^{10}] \quad [\text{MeV}^{-1}\ \text{fission}^{-1}]. \quad (4)$$

The spectra, both calculated (Fig. 1) and measured (4), correspond to standard fuel composition (3). Typical time evolution of the antineutrino spectrum during an annual reactor cycle is shown in Figs. 2 and 3. This evolution during reactor operation is mainly caused by accumulation of nuclear beta activity (in the region $E < 2$ MeV) and changes in the reactor fuel composition (in the region $E > 2$ MeV).

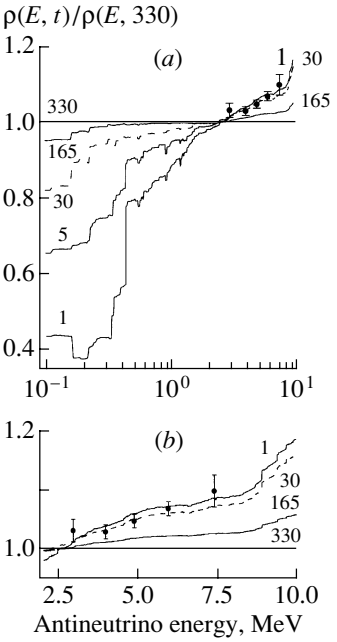

Fig. 3. Ratios of the current reactor-$\bar{\nu}_e$ spectra during reactor operation to that at the end of the 330-d reactor operating period: lines are the present calculation, and circles are the experiment at the Rovno reactor [7]. The numbers by the lines indicate days from the beginning of the operating period.

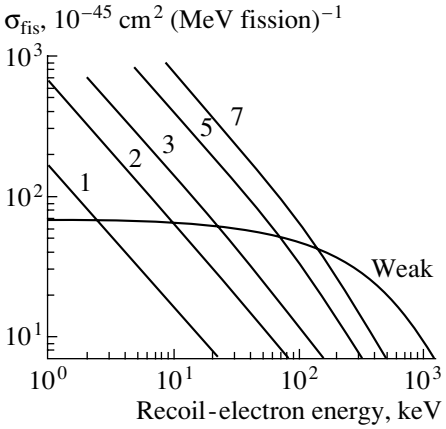

Fig. 4. Cross sections for weak and magnetic scattering of reactor antineutrinos on free electrons in the middle of the 330-d operating period. The numbers by the lines indicate the values of the moment μ_ν in $10^{-11}\ \mu_B$.

3. CROSS SECTIONS FOR SCATTERING OF REACTOR ANTINEUTRINOS ON ELECTRONS

The calculated weak and magnetic elastic cross sections σ_{fis} (1) for the $\bar{\nu}_e$e scattering reaction as a function of the recoil-electron energy are shown in Fig. 4. Corrections associated with the electron binding in atoms were considered in [8]. It should be

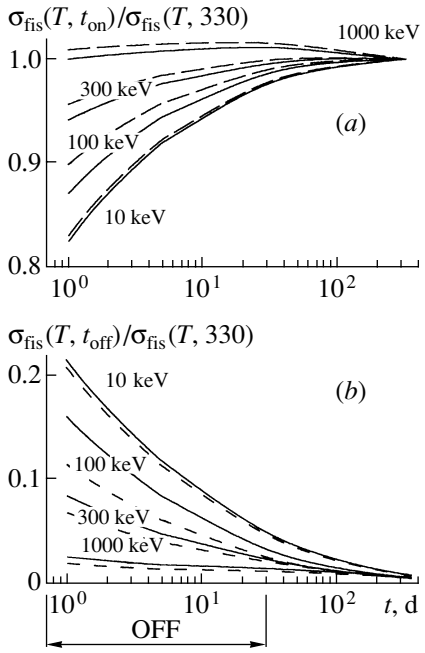

Fig. 5. Ratios of the current $\bar{\nu}_e e$ scattering cross sections expected in the experiment to those at the end of the 330-d reactor operation period for the reactor (a) operating and (b) shutdown (OFF) periods. The data are presented for four groups of recoil-electron energies. The solid (dashed) curves represent magnetic (weak) scattering.

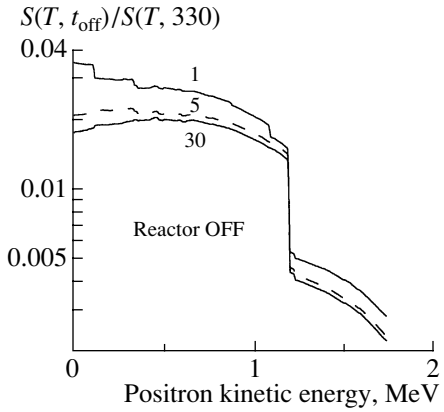

Fig. 6. Ratios of the current positron spectra for the reaction $\bar{\nu}_e + p \to e^+ + n$ associated with residual antineutrino emission after the reactor is shut down to the spectrum at the end of the 330-d reactor operation period. The numbers by the lines indicate days after reactor shutdown.

emphasized that weak $\bar{\nu}_e e$ scattering plays the role of a background, which must be calculated exactly and subtracted. In sensitive searches for μ_ν, the measured weak recoil-electron energy spectrum could be used as a tool for detector check and calibration. The calculated time variations of the folded cross sections (1) for weak and magnetic $\bar{\nu}_e e$ scattering during the reactor cycle are presented in Fig. 5.

4. PRECISION MEASUREMENT OF THE POSITRON SPECTRUM FOR THE REACTION $\bar{\nu}_e + p \to e^+ + n$

Radical improvements of the detector characteristics including a substantial decrease in the accidental and correlated backgrounds have been achieved in the latest long-baseline reactor oscillation experiments. In the present study, we discuss the third type of background which was not taken into account earlier in measurement of the positron spectrum. It is a reactor-correlated positron background, associated with residual $\bar{\nu}_e$ emission after reactor shutdown. This positron background is about 3% in the energy range $T_{e^+} < 1.2$ MeV, in regards to positron rate when the reactor is in operation (Fig. 6).

This effect may be more significant if the oscillation experiment is implemented by one detector positioned from the near (distance r) and far (distance R) reactors. Such an experimental setup was implemented, for example, in Bugey, $r = 15$ m and $R = 95$ m [9]. In this situation, the positron background signal from the near stopped reactor, $S^{\rm off}_{\rm near}$, for $T_{e^+} < 1.2$ MeV is approximately equal to the positron signal from the operating far reactor, $S^{\rm on}_{\rm far}$; that is,

$$\frac{S^{\rm off}_{\rm near}}{S^{\rm on}_{\rm far}} \sim 1 \quad \text{for} \quad T_{e^+} = 0\text{–}1.2\ \text{MeV}$$

and

$$\frac{S^{\rm off}_{\rm near}}{S^{\rm on}_{\rm far}} \sim 0.15 \quad \text{for} \quad T_{e^+} = 1.2\text{–}1.7\ \text{MeV}.$$

5. CONCLUSION

Searches for new physics in neutrino experiments at nuclear reactors require refining our knowledge of the reactor $\bar{\nu}_e$ spectrum. At the present level of experimental accuracy and sensitivity, a detailed and profound analysis of the reactor $\bar{\nu}_e$ spectrum for each particular experiment should be carried out.

ACKNOWLEDGMENTS

I would like to thank L.A. Mikaelyan and V.V. Sinev for helpful discussions.

This work was supported by the Russian Foundation for Basic Research (project nos. 00-15-06708 and 00-02-16035).

REFERENCES

1. A. V. Derbin, Yad. Fiz. **57**, 236 (1994) [Phys. At. Nucl. **57**, 222 (1994)].
2. M. B. Voloshin, M. I. Vysotskiĭ, and L. B. Okun, Zh. Éksp. Teor. Fiz. **91**, 754 (1986) [Sov. Phys. JETP **64**, 446 (1986)]; P. Vogel and J. Engel, Phys. Rev. D **39**, 3378 (1989).
3. L. A. Mikaelyan, Yad. Fiz. **65**, 1206 (2002) [Phys. At. Nucl. **65**, 1173 (2002)].
4. V. I. Kopeĭkin, L. A. Mikaélyan, and V. V. Sinev, Yad. Fiz. **63**, 1087 (2000) [Phys. At. Nucl. **63**, 1012 (2000)].
5. V. I. Kopeikin, L. A. Mikaelyan, and V. V. Sinev, Yad. Fiz. **64**, 914 (2001) [Phys. At. Nucl. **64**, 849 (2001)].
6. V. N. Vyrodov, Y. Declais, H. de Kerret, *et al.*, Pis'ma Zh. Éksp. Teor. Fiz. **61**, 161 (1995) [JETP Lett. **61**, 163 (1995)].
7. V. I. Kopeikin, L. A. Mikaelyan, and V. V. Sinev, Yad. Fiz. **60**, 230 (1997) [Phys. At. Nucl. **60**, 172 (1997)].
8. V. I. Kopeikin, L. A. Mikaelyan, V. V. Sinev, and S. A. Fayans, Yad. Fiz. **60**, 2032 (1997) [Phys. At. Nucl. **60**, 1859 (1997)].
9. B. Achkar, R. Aleksan, M. Avenier, *et al.*, Nucl. Phys. B **434**, 503 (1995).

Physics of Atomic Nuclei, Vol. 66, No. 3, 2003, pp. 476–480. From Yadernaya Fizika, Vol. 66, No. 3, 2003, pp. 504–508.

COSMOLOGY AND ASTROPHYSICS. DARK MATTER

Baryon Asymmetry of the Universe from Evaporation of Primordial Black Holes*

E. V. Bugaev, M. G. Elbakidze, and K. V. Konishchev**

Institute for Nuclear Research, Russian Academy of Sciences, pr. Shestidesyatiletiya Oktyabrya 7a, Moscow, 117312 Russia

Received April 17, 2002

Abstract—The process of baryogenesis through evaporation of black holes formed at the end of the inflation phase is considered. The increase in black hole mass due to accretion from the surrounding radiation after reheating is taken into account. It is shown that the influence of the accretion on the baryogenesis is important only in the case where the initial values of black hole mass are larger than $\sim 10^4$ g. The behavior of the calculated baryon asymmetry as a function of model parameters is studied.

1. INTRODUCTION

The first discussions about a possible connection between baryon asymmetry and primordial black hole evaporations appeared in the middle 1970s, just after discovery of the phenomenon of black hole evaporation. The possibility of the excess of baryons over antibaryons appearing in the process of evaporation of primordial black holes was noted in [1, 2]. The mechanism discussed in [1, 2] does not require nonconservation of the baryon number in an underlying microscopic theory. Detailed calculations using this mechanism were done in [3].

Later, this question was studied [4, 5] in the context of grand unified theories (GUTs) (i.e., theories in which the baryon number is not conserved). The idea is simple: when black holes decay by emission of Hawking radiation, they may emit baryon-number-violating Higgs particles (and/or leptoquarks) whose decays naturally generate baryon asymmetry.

In [6], baryogenesis via primordial black holes was considered using GUT and the extended inflation scenario. The formation of very light primordial black holes (which disappear, as a result of evaporation, before nucleosynthesis without any trace, except for the net baryon asymmetry) seemed to be most probable in inflationary models with the first-order phase transition. Recently, however, it has been shown that, in some modern variants of second-order inflation models [7, 8], the formation of small black holes (and, consequently, baryon asymmetry production via black hole evaporation) is also quite possible.

Recently [9, 10], the baryogenesis through evaporation of primordial black holes was studied quantitatively. It was argued that this scenario of baryogenesis can, in principle, explain the observed baryon number of the Universe (which is constrained by primordial nucleosynthesis data to be in the range $(1.55–8.10) \times 10^{-11}$). However, the distinct conclusion of [9, 10] is that a sufficient number of black holes can survive beyond the electroweak phase transition and, therefore, the baryon excess produced is not washed out by sphaleron transitions. These conclusions are in contradiction with the qualitative statements of the pioneering paper [6]. It was claimed in [9, 10] that the difference can be explained by taking into account the accretion (the accretion term was omitted in formulas of [6]).

Aside from the problem of the possible erasure of produced baryon asymmetry by sphaleron transitions, it is important to have a definite answer to the following question: Is it possible to obtain the cosmologically interesting value of baryon asymmetry by such a mechanism (i.e., by primordial black hole evaporations)?

In the present work, we try to answer this question. We calculate the baryon asymmetry using the same assumptions as in [6]. Most attention is paid to rigorous solution of kinetic equations (containing an accretion term) and to comparison of exact results with predictions based on approximate formulas derived in [6].

2. BASIC ASSUMPTIONS

1. Generation of black holes in the early Universe may take place in many inflationary scenarios. The

*This article was submitted by the authors in English.

**e-mail: bugaev@pcbai10.inr.ruhep.ru

main assumption is that, in the early Universe, there was the period of inflationary expansion and the inflation was completed by a symmetry-breaking phase transition. The energy scale of symmetry breaking is $\sigma_0 \sim 10^{16}$ GeV (GUT scale).

Clearly, concrete mechanisms of black hole production are not the same in different inflationary models.

1a. Inflation of "old" type (extended inflation, first-order inflation): the Universe gets out of the false-vacuum state by bubble nucleation. Reheating and thermalization of the Universe proceeds through bubble collisions at the end of inflation [5]. The false-vacuum energy density is $\rho_v \sim \xi\sigma_0^4$ ($\xi \sim 10^{-4}$), so $\rho_v \sim 10^{60}$ GeV$^4 \equiv M^4$. The Hubble parameter at the end of inflation is

$$H_{\rm end} = \sqrt{\frac{8\pi}{3}\frac{\rho_v}{m_{\rm Pl}^2}} \sim 10^{12}\ {\rm GeV}, \qquad (1)$$

so the time of the end of inflation is

$$t_{\rm end} \sim \frac{1}{H_{\rm end}} \sim 10^{-35}\ {\rm s}. \qquad (2)$$

One usually supposes that $t_{\rm rh} \approx t_{\rm end} \approx t_f \ll \tau_h$, where $t_{\rm rh}$ is the time of reheating, t_f is the time of formation of black holes, and τ_h is the lifetime of the black hole.

Black hole production proceeds (i) via gravitational instability of inhomogeneities formed during the thermalization phase (i.e., during the bubble wall collisions) or (ii) via the appearance of trapped regions of false vacuum caught between bubbles of true vacuum.

1b. "New" or "slow-rollover" inflation: in this case, black holes are produced through collapses of the overdense regions in space. Thus, for a large probability of primordial black hole (PBH) production, there must exist large amplitudes of primordial density fluctuations at small scales. Such fluctuations appear during inflation. The overdense region of mass M can produce a black hole when this fluctuation crosses the horizon inside. At this time, M is equal to the horizon mass M_h, and the black hole produced has a mass $M_{\rm BH}$ that is close to M_h,

$$M_{\rm BH} \sim 0.1 M_h. \qquad (3)$$

The time of PBH formation is

$$t_f \sim \frac{8M_h}{m_{\rm Pl}} \sim 10^2 \frac{M_{\rm BH}}{m_{\rm Pl}} t_{\rm Pl}. \qquad (4)$$

If, for example, $M_{\rm BH}$ is about 10^3 g, then $t_f \sim 10^{-33}$ s. At this time, the corresponding scale factor is

$$a_f \sim (H_0^{3/2}(2.4\times 10^4)^{-3/4} t_f^{3/2})^{1/3} \sim 10^{-27} \qquad (5)$$

and the comoving length scale of the perturbation is

$$\lambda_f \sim \frac{ct_f}{a_f} \sim 10^{-14}\ {\rm pc}. \qquad (6)$$

Further, we use the known formula

$$N_{\lambda_f} = 45 + \ln\frac{\lambda_f}{1\ {\rm Mpc}} + \frac{2}{3}\ln\frac{M}{10^{14}\ {\rm GeV}} + \frac{1}{3}\ln\frac{T_{\rm rh}}{10^{10}\ {\rm GeV}}. \qquad (7)$$

Here, $M \sim 10^{15}$ GeV (it is $\sqrt[4]{\rho_v}$), $T_{\rm rh}$ is the reheating temperature, and N_{λ_f} is the number of e-folds before the end of inflation beginning at the moment when the scale crosses the horizon outside.

If, for example, $T_{\rm rh} \sim 10^{11}$ GeV, one has $N_{\lambda_f} \sim 1$. Now, it is clear that the fluctuations responsible for $M_{\rm BH} \sim 10^3$ g are formed just near the end of inflation. So, in this sense, black holes with $M_{\rm BH} \sim 10^2$–10^3 g are the lightest ones.

The large amplitudes of density perturbations at small scales corresponding to $N_{\lambda_f} \sim 1$ are naturally obtained in the hybrid inflation model [7, 8].

If $T_{\rm rh} \sim 10^{11}$ GeV, the reheating time is

$$t_{\rm rh} = 0.3\frac{1}{\sqrt{g_*}}\frac{m_{\rm Pl}}{T_{\rm rh}^2} \sim 10^{-29}\ {\rm s}. \qquad (8)$$

Thus, black holes can be produced even at a time before reheating, when the Universe is dominated by oscillations of the inflation field.

2. We assume that all produced PBHs have the same mass. It will be approximately so in hybrid inflation-type models, where the sharp maximum of the density fluctuation amplitude exists at some definite scale.

3. We assume that, at $t_{\rm rh}$, part of the energy density is in black holes:

$$\rho(t_{\rm rh}) = \rho_R(t_{\rm rh}) + \rho_{\rm BH}(t_{\rm rh}), \qquad (9)$$
$$\rho_{\rm BH}(t_{\rm rh}) = \beta\rho(t_{\rm rh})$$

where β is the free parameter of our model and ρ_R is the energy density of the radiation.

In the following, we will consider only black holes having a lifetime τ_h that is much larger than $t_{\rm rh}$, $\tau_h \gg t_{\rm rh}$.

We will see that the most interesting predictions for baryon asymmetry do not depend on $t_{\rm rh}$ and are the same for both inflation scenarios provided we use the parameter β in both cases.

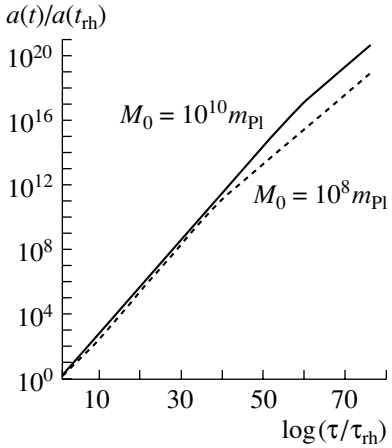

Fig. 1. The time evolution of the scale factor parameter α for $\beta = 0.1$ and for two values of M_0.

3. KINETIC EQUATIONS

Evolution of the black hole mass is described by the equation

$$\dot{M}_{\rm BH} = AM_{\rm BH}^2 - \frac{\alpha(M_{\rm BH})}{M_{\rm BH}^2}. \qquad (10)$$

The accretion term $AM_{\rm BH}^2$ is equal to $\sigma_{\rm abs}\rho_R c$, where $\sigma_{\rm abs}$ is the cross section of absorption of relativistic particles by a black hole,

$$\sigma_{\rm abs} = 27\pi M_{\rm BH}^2 \frac{G^2}{c^4}. \qquad (11)$$

The evaporation term is $-\alpha(m)/m^2$, where $\alpha(m)$ counts the degrees of freedom of the black hole radiation (m is the instantaneous value of the black hole mass).

In the following, we will use the value [11, 12]

$$\alpha(m) = 80 \times 10^{25}\ {\rm g}^3/{\rm s} = {\rm const}. \qquad (12)$$

Evolution of the radiation energy density is given by the equation

$$\dot{\rho}_R = -4\frac{\dot{a}}{a}\rho_R - \dot{M}_{\rm BH} n_{\rm BH} \qquad (13)$$

with

$$n_{\rm BH}(t) = \frac{\rho_{\rm BH}(t_{\rm rh})}{M_0}\frac{a^3(t_{\rm rh})}{a^3(t)}.$$

Here, $n_{\rm BH}$ is the number density of PBHs, M_0 is the initial value of the black hole mass, and $a(t)$ is the scale factor.

Evolution of the scale factor is given by the Friedmann–Einstein equation:

$$\left(\frac{\dot{a}}{a}\right)^2 = \frac{8\pi G}{3}(\rho_R + M_{\rm BH} n_{\rm BH}). \qquad (14)$$

In this paper, we use, for simplicity, the Einstein–de Sitter model.

The equation for evolution of the baryon number is

$$\dot{n}_B = -\frac{\dot{M}_{\rm BH}c^2}{3kT_{\rm BH}} n_{\rm BH}\varepsilon f_H - 3\frac{\dot{a}}{a}n_B. \qquad (15)$$

We assume here that, for the change in black hole mass $dM_{\rm BH}$, we have $dM_{\rm BH}\cdot c^2/3kT_{\rm BH}$ particles produced ($T_{\rm BH}$ is the temperature of the black hole connected with $M_{\rm BH}$ by the Hawking relation $kT_{\rm BH} = \hbar c^3/8\pi G M_{\rm BH}$); f_H is the fraction of X particles decaying with violation of B. Typically, $f_H \sim 1/g_* \sim 10^{-2}$. The baryon number is obtained by introducing the factor ε, which is given by the relation

$$\varepsilon \equiv \sum_i B_i \frac{\Gamma(X \to f_i) - \Gamma(\bar{X} \to \bar{f}_i)}{\Gamma_X}; \qquad (16)$$

$\varepsilon \neq 0$ if C, CP are not conserved. For obtaining the baryon asymmetry, one must divide n_B by entropy s, which is given by

$$s(t) = \frac{2\pi^2}{45} g_* T^3(t) \left(\frac{k}{\hbar c}\right)^3, \qquad (17)$$

$$T \sim \rho_R^{1/4}. \qquad (18)$$

It is very convenient [6, 9] to use dimensionless variables:

$$m = \frac{M_{\rm BH}}{M_0}, \quad \alpha \equiv \frac{a(t)}{a(t_{\rm rh})}, \quad R = \frac{\rho_R \alpha^4}{(1-\beta)\rho(t_{\rm rh})};$$
$$\tau = \sqrt{G\rho(t_{\rm RH})}\,t,$$

for which we have simple initial conditions

$$m(\tau = \tau_{\rm rh}) = \alpha(\tau = \tau_{\rm rh}) = R(\tau = \tau_{\rm rh}) = 1;$$
$$\tau_{\rm rh} = \sqrt{G\rho(t_{\rm rh})}\,t_{\rm rh}.$$

We assume that X particles are evaporated when the following condition holds:

$$3kT_{\rm BH} = 3k\frac{\hbar c^3}{8\pi G M_{\rm BH}} \geq M_X c^2, \qquad (19)$$

$$M_{\rm BH}^{\rm thr} = \frac{3m_{\rm Pl}^2}{8\pi M_X}.$$

Here, M_X is the mass of X particles. Finally, we have the following free parameters: M_0, $\rho(t_{\rm rh})$, β, M_X, and ε.

Some results of the solution to the system of kinetic equations (10), (13), (14), and (15) are presented in Figs. 1–4. All calculations are carried out with $\rho(t_{\rm rh}) = 10^{55}$ GeV^4. This value of $\rho(t_{\rm rh})$ corresponds to $t_{\rm rh} \sim 10^{-33}$ s and reheating temperature $T_{\rm rh} \sim 10^{13}$ GeV.

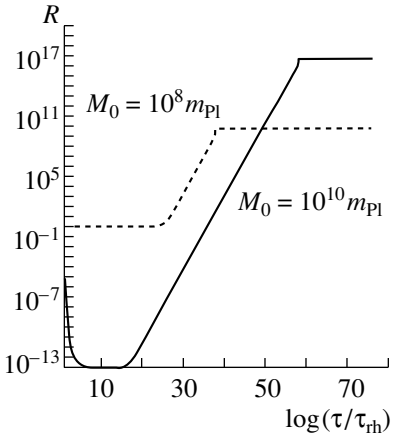

Fig. 2. The dependence of the function R on τ for $\beta = 0.1$ and for two values of M_0.

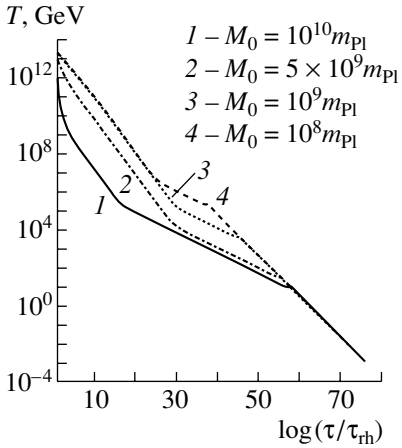

Fig. 3. The τ dependence of the temperature of radiation in the Universe for $\beta = 0.1$ and for several values of M_0.

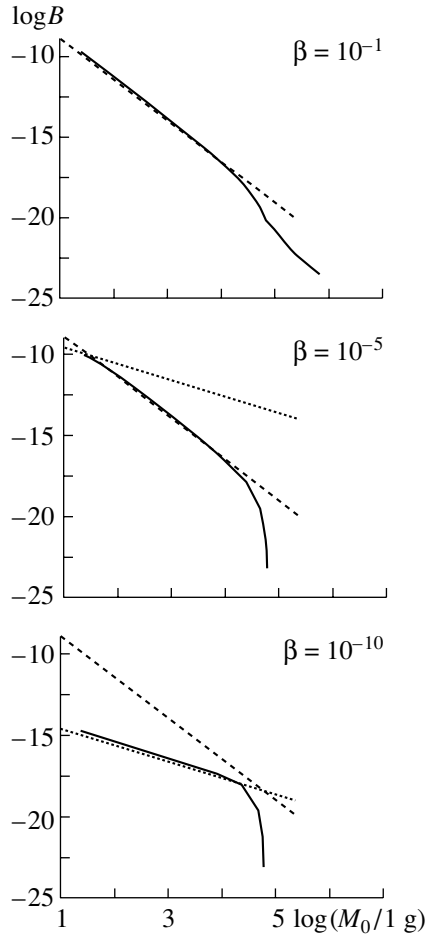

Fig. 4. Baryon asymmetry parameters as a function of M_0 for three values of β (solid lines). Dashed lines represent calculation by approximate formula (21). Dotted lines represent calculation by formula (21) with substitution (28).

4. APPROXIMATE FORMULAS FOR B

One can easily show [6] that, for the practically important case when

$$\beta \gg \sqrt{\frac{t_{rh}}{\tau_h}} \tag{20}$$

and when accretion is not important ($M_0 \leq 10^3$ g), there is an approximate solution to the kinetic equations for B which is given by the formula

$$B = \left(\frac{30}{g_*}\right)^{1/4} \sqrt{\pi} \left(\frac{\hbar}{c}\right)^{3/4} \times \rho^{1/4}(t_{rh}) \frac{(M_{BH}^{thr})^2}{m_{Pl}^2 M_0} \frac{\varepsilon}{g_*} \left(\frac{t_{rh}}{\tau_h}\right)^{1/2}. \tag{21}$$

Using the relation

$$\rho(t_{rh}) = \frac{3}{32} \frac{m_{Pl}^2}{t_{rh}^2} \sim \frac{1}{t_{rh}^2}, \tag{22}$$

one can see that B does not depend on $\rho(t_{rh})$ or t_{rh}.

The expression for τ_h is obtained from the equation

$$\dot{M}_{BH} = -\alpha / M_{BH}^2 \tag{23}$$

and is given by

$$\tau_h = M_0^3 / 3\alpha. \tag{24}$$

For $M_0 \sim 10^2$–10^3 g, one has $\tau_h \sim 10^{-21}$–10^{-18} s. In our numerical calculations, we used $t_{rh} = 10^{-33}$ s. Thus, one has $t_{rh} \ll \tau_h$. From here, one has the condition for the parameter β:

$$\beta \gg \sqrt{t_{rh}/\tau_h} \sim (10^{-6}\text{–}10^{-7}). \tag{25}$$

For these values of β, t_{rh}, and τ_h, one has the final formula

$$B \cong 10^{-14} \left(\frac{M_0}{10^3\ \text{g}}\right)^{-5/2} \left(\frac{M_X}{10^{14}\ \text{GeV}}\right)^{-2} \left(\frac{\varepsilon}{1}\right). \tag{26}$$

Condition (20) means [6] that the black hole energy density dominates at the time of evaporation. If the value of the parameter β is such that

$$\beta \ll \sqrt{t_{\rm rh}/\tau_h}, \tag{27}$$

evaporation occurs while background radiation dominates the energy density of the Universe (with the entropy arising mainly from the radiation). In this case, the approximate formula for B [6] can be obtained from (21) by the following substitution of the last factor:

$$\left(\frac{t_{\rm rh}}{\tau_h}\right)^{1/2} \to \frac{\beta}{(1-\beta)^{3/4}}. \tag{28}$$

5. CONCLUSION

The main conclusion of our work is the following: the predicted baryon asymmetry in the region $M_0 \lesssim 10^4$ g is well described by approximate formulas (21) and (21) with substitution of (28). These formulas were obtained without taking into account the accretion, and it means that the accretion process is not important for small values of initial black hole masses. At larger masses, accretion becomes important (the same was argued in [10]). One can see from Fig. 4 that the accretion leads to a significant decrease in B (this decrease is a consequence of a significant growth of entropy after evaporation of black holes enlarged due to accretion).

The resulting formula for B (21) does not depend on $\rho(t_{\rm rh})$ and $t_{\rm rh}$ and, therefore, is valid for both variants of the inflationary scenario mentioned in Section 4 (as far as condition (20) is fulfilled). It is seen that, if $M_0 \sim 10^3$ g and $M_X \sim 10^{14}$ GeV, the predicted asymmetry is quite small (even for $\varepsilon \sim 1$). This calculation of ours strongly disagrees with the corresponding results of [10]. The effect (baryon asymmetry) can be large if $M_0 < 10^3$ g and/or $M_X \ll 10^{14}$ GeV (e.g., if $M_X \sim 10^{11}$ GeV).

It follows from Fig. 3 that the temperature of the Universe at the moment of evaporation is smaller than $\sim$100 GeV only when $M_0 \gtrsim 10^5$ g. For smaller values of M_0 (for which the value of B can be acceptably large), one has $T_{\rm ev} > 100$ GeV, and the problem connected with the sphaleron transitions exists. Evidently, the baryon asymmetry produced by primordial black hole evaporations can survive only if the nonzero $(B-L)$ value is generated in decays of Higgs particles of GUT.

REFERENCES

1. S. W. Hawking, Nature **248**, 30 (1974).
2. Ya. B. Zel'dovich, Pis'ma Zh. Éksp. Teor. Fiz. **24**, 29 (1976) [JETP Lett. **24**, 25 (1976)].
3. A. D. Dolgov, Zh. Éksp. Teor. Fiz. **79**, 337 (1980) [Sov. Phys. JETP **52**, 169 (1980)]; Phys. Rev. D **24**, 1042 (1981).
4. J. D. Barrow and F. Tipler, Nature **276**, 453 (1978); D. Toussaint *et al.*, Phys. Rev. D **19**, 1036 (1979); M. Turner, Phys. Lett. B **89B**, 155 (1979).
5. S. W. Hawking, I. G. Moss, and J. M. Stewart, Phys. Rev. D **26**, 2681 (1982).
6. J. D. Barrow *et al.*, Phys. Rev. D **43**, 984 (1991).
7. L. Randall *et al.*, Nucl. Phys. B **472**, 377 (1996).
8. J. García-Bellido *et al.*, Phys. Rev. D **54**, 6040 (1996).
9. A. S. Majumdar *et al.*, Int. J. Mod. Phys. D **4**, 517 (1995).
10. N. Upadhyay *et al.*, Phys. Rev. D **60**, 063513 (1999).
11. J. H. MacGibbon, Phys. Rev. D **44**, 376 (1991).
12. E. V. Bugaev and K. V. Konishchev, Phys. Rev. D **65**, 123005 (2002).

Physics of Atomic Nuclei, Vol. 66, No. 3, 2003, pp. 481–489. From Yadernaya Fizika, Vol. 66, No. 3, 2003, pp. 509–517.

COSMOLOGY AND ASTROPHYSICS. DARK MATTER

SUSY Dark Matter in the Universe—Theoretical Direct Detection Rates*

J. D. Vergados**

Theoretical Physics Section, University of Ioannina, Greece

Received February 13, 2002

Abstract—Exotic dark matter, together with the vacuum energy (associated with the cosmological constant), seems to dominate in the Universe. An even higher density of such matter seems to be gravitationally trapped in the Universe. Thus, its direct detection is central to particle physics and cosmology. Currently fashionable supersymmetric models provide a natural dark matter candidate that is the lightest supersymmetric particle (LSP). Such models, combined with fairly well understood physics like the quark substructure of the nucleon and the nuclear structure (form factor and/or spin response function) permit the evaluation of the event rate for LSP–nucleus elastic scattering. The thus obtained event rates are, however, very low or even undetectable. Therefore, it is imperative to exploit the modulation effect, i.e., the dependence of the event rate on the Earth's annual motion. Also, it is useful to consider the directional rate, i.e., its dependence on the direction of the recoiling nucleus. In this paper, we study such a modulation effect in both nondirectional and directional experiments. We calculate both the differential and the total rates using both isothermal, symmetric as well as only axially asymmetric, and nonisothermal, due to caustic rings, velocity distributions. We find that, in the symmetric case, the modulation amplitude is small. The same is true for the case of caustic rings. The inclusion of asymmetry, with a realistic enhanced velocity dispersion in the galactocentric direction, yields an enhanced modulation effect, especially in directional experiments. © *2003 MAIK "Nauka/Interperiodica"*.

1. INTRODUCTION

In recent years, the consideration of exotic dark matter has become necessary in order to close the Universe [1]. Furthermore, in order to understand the large-scale structure of the Universe, it has become necessary to consider matter made up of particles that were nonrelativistic at the time of freeze-out. This is the cold-dark-matter (CDM) component. The COBE data [2] suggest that CDM is at least 60% [3]. On the other hand, during the last few years, evidence has appeared from two different teams, the High-z Supernova Search Team [4] and the Supernova Cosmology Project [5, 6], which suggests that the Universe may be dominated by the cosmological constant Λ. As a matter of fact, the situation can be adequately described by a baryonic component $\Omega_B = 0.1$ along with the exotic components $\Omega_{\rm CDM} = 0.3$ and $\Omega_\Lambda = 0.6$ (see the next section for the definitions). In another analysis, Turner [7] gives $\Omega_m = \Omega_{\rm CDM} + \Omega_B = 0.4$. Since the nonexotic component cannot exceed 40% of the CDM [1, 8], there is room for exotic weakly interacting massive particles (WIMPs). In fact, the DAMA experiment [9] has claimed the observation of one signal in direct detection of a WIMP, which with better statistics has subsequently been interpreted as a modulation signal [10].

The above developments are in line with particle physics considerations. Thus, in the currently favored supersymmetric (SUSY) extensions of the Standard Model, the most natural WIMP candidate is the lightest supersymmetric particle (LSP). In the most favored scenarios, the LSP can be simply described as a Majorana fermion, a linear combination of the neutral components of the gauginos and Higgsinos [1, 11–13].

2. DENSITY VERSUS COSMOLOGICAL CONSTANT

The evolution of the Universe is governed by the general theory of relativity. The most commonly used model is that of Friedman, which utilizes the Robertson–Walker metric

$$(ds)^2 = (dt)^2 - R^2(t)\left[\frac{(dr)^2}{1-\kappa r^2} + r^2\left((d\theta)^2 + \sin^2\theta(d\phi)^2\right)\right]. \quad (1)$$

The resulting Einstein equations are

$$R_{\mu\nu} - \frac{g_{\mu\nu}}{2}R = -8\pi G_{\rm N} T_{\mu\nu} + \Lambda g_{\mu\nu}, \quad (2)$$

*This article was submitted by the author in English.

** e-mail: Vergados@cc.uoi.gr

where G_N is Newton's constant and Λ is the cosmological constant. The equation for the scale factor $R(t)$ becomes

$$\frac{d^2R}{dt^2} = -\frac{4\pi}{3}G_N(\rho + 3p)R = -\frac{4\pi G_N\rho}{3}R + \frac{\Lambda}{3}, \quad (3)$$

where ρ is the mass density. Then, the energy is

$$E = \frac{m}{2}\left(\frac{dr}{dt}\right)^2 - G_N\frac{m}{R}(4\pi\rho R^3) \quad (4)$$
$$+ \frac{\Lambda}{6}mR^2 = -\frac{\kappa}{2}m = \text{const}.$$

This can equivalently be written as

$$H^2 + \frac{\kappa}{R^2} = \frac{8\pi}{3}G_N\rho + \frac{\Lambda}{3}, \quad (5)$$

where the quantity H is Hubble's constant defined by

$$H = \frac{1}{R}\frac{dR}{dt}. \quad (6)$$

Hubble's constant is perhaps the most important parameter of cosmology. In fact, it is not a constant but changes with time. Its present-day value is given by

$$H_0 = 65 \pm 15 \text{ km/s Mpc}^{-1}. \quad (7)$$

In other words, $H_0^{-1} = (1.50 \pm 0.35) \times 10^{10}$ yr, which is roughly equal to the age of the Universe. Astrophysicists conventionally write it as

$$H_0 = 100h \text{ km/s Mpc}^{-1}, \quad 0.5 < h < 0.8. \quad (8)$$

Equations (3)–(5) coincide with those of the Newtonian theory with the following two types of forces. An attractive force decreasing in absolute value with the scale factor (Newton) and a repulsive force increasing with the scale factor (Einstein),

$$F = -G_N\frac{mM}{R^2} \quad \text{(Newton)}, \quad (9)$$
$$F = \frac{1}{3}\Lambda mR \quad \text{(Einstein)}.$$

Historically, the cosmological constant was introduced by Einstein so that general relativity yields a stationary Universe, i.e., one which satisfies the conditions

$$\frac{dR}{dt} = 0, \qquad \frac{d^2R}{dt^2} = 0. \quad (10)$$

Indeed, for $\kappa > 0$, the above equations lead to $R = R_c = \text{const}$ provided that

$$\frac{1}{3}\Lambda R_c - \frac{4\pi}{3}G_N\rho R_c = 0, \quad (11)$$
$$\frac{1}{3}\Lambda R_c^2 - \frac{4\pi}{3}G_N\rho R_c^2 = \kappa.$$

These equations have a nontrivial solution provided that the density ρ and the cosmological constant Λ are related, i.e.,

$$\Lambda = 4\pi G_N\rho. \quad (12)$$

The radius of the Universe is then given by

$$R_c = \left(\frac{\kappa}{4\pi G_N\rho}\right)^{1/2}. \quad (13)$$

Define now

$$\Omega_m = \frac{\rho}{\rho_c}, \quad \Omega_\Lambda = \frac{\rho_v}{\rho_c}, \quad \rho_v = \frac{\Lambda}{8\pi G_N} \quad (14)$$
("vacuum" density).

The critical density is

$$\rho_c = 1.8 \times 10^{-23}h^2\frac{\text{g}}{\text{cm}^3} = 10h^2\frac{\text{nucleons}}{\text{m}^3}. \quad (15)$$

With these definitions, Friedman's equation (4) takes the form

$$\frac{\kappa}{R^2} = (\Omega_m + \Omega_\Lambda - 1)H^2. \quad (16)$$

Therefore, we distinguish the following special cases:

$$\kappa > 0 \quad \Leftrightarrow \quad \Omega_m + \Omega_\Lambda > 1 \quad \Leftrightarrow \quad \text{closed curved Universe};$$
$$\kappa = 0 \quad \Leftrightarrow \quad \Omega_m + \Omega_\Lambda = 1 \quad \Leftrightarrow \quad \text{open flat Universe};$$
$$\kappa < 0 \quad \Leftrightarrow \quad \Omega_m + \Omega_\Lambda < 1 \quad \Leftrightarrow \quad \text{open curved Universe}.$$

In other words, it is the combination of matter and "vacuum" energy that determines the fate of the Universe.

Before concluding this section, we remark that the above equations do not suffice to yield a solution since the density is a function of the scale factor. An equation of state is needed in addition, but we are not going to elaborate further.

3. AN OVERVIEW OF DIRECT DETECTION—THE ALLOWED SUSY PARAMETER SPACE

Since this particle is expected to be very massive, $m_\chi \geq 30$ GeV, and extremely nonrelativistic with average kinetic energy $T \leq 100$ KeV, it can be directly detected [14, 15] mainly via the recoiling of a nucleus

(A, Z) in the elastic scattering process:

$$\chi + (A, Z) \to \chi + (A, Z)^* \qquad (17)$$

(χ denotes the LSP). In order to compute the event rate, one needs the following ingredients:

(i) An effective Lagrangian at the elementary particle (quark) level obtained in the framework of supersymmetry as described, e.g., in [1, 13].

(ii) A procedure in going from the quark to the nucleon level, i.e., a quark model for the nucleon. The results depend crucially on the content of the nucleon in quarks other than u and d. This is particularly true for the scalar couplings as well as the isoscalar axial coupling [16–19].

(iii) Computation of the relevant nuclear matrix elements [10, 21] using as reliable as possible many-body nuclear wave functions. By putting as accurate a nuclear-physics input as possible, one will be able to constrain the SUSY parameters as much as possible. The situation is a bit simpler in the case of scalar coupling, in which case one only needs the nuclear form factor.

Since the obtained rates are very low, one would like to be able to exploit the modulation of the event rates due to the Earth's revolution around the Sun [22–25]. To this end, one adopts a folding procedure assuming some distribution [1, 23, 25] of velocities for the LSP. One also would like to know the directional rates, by observing the nucleus in a certain direction, which correlate with the motion of the Sun around the center of the Galaxy and the motion of the Earth [11, 26].

The calculation of this cross section has become pretty standard. One starts with a representative input in the restricted SUSY parameter space as described in the literature [12, 13]. We will adopt a phenomenogical procedure taking universal soft SUSY-breaking terms at $M_{\rm GUT}$, i.e., a common mass for all scalar fields m_0; a common gaugino mass $M_{1/2}$; and a common trilinear scalar coupling A_0, which we set equal to zero (we will discuss later the influence of nonzero A_0). Our effective theory below $M_{\rm GUT}$ then depends on the parameters [12]

$$m_0,\ M_{1/2},\ \mu_0,\ \alpha_G,\ M_{\rm GUT},\ h_t,\ h_b,\ h_\tau,\ \tan\beta,$$

where $\alpha_G = g_G^2/4\pi$ (g_G being the GUT gauge coupling constant) and h_t, h_b, and h_τ are, respectively, the top, bottom, and tau Yukawa coupling constants at $M_{\rm GUT}$. The values of α_G and $M_{\rm GUT}$ are obtained as described in [12]. For a specified value of $\tan\beta$ at M_S, we determine h_t at $M_{\rm GUT}$ by fixing the top-quark mass at the center of its experimental range, $m_t(m_t) = 166$ GeV. The value of h_τ at $M_{\rm GUT}$ is fixed by using the running tau-lepton mass at m_Z, $m_\tau(m_Z) = 1.746$ GeV. The value of h_b at $M_{\rm GUT}$ used is such that

$$m_b(m_Z)^{\overline{\rm DR}}_{\rm SM} = 2.90 \pm 0.14\ {\rm GeV}$$

after including the SUSY threshold correction. The SUSY parameter space is subject to the following constraints:

(i) The LSP relic abundance will satisfy the cosmological constraint

$$0.09 \le \Omega_{\rm LSP} h^2 \le 0.22. \qquad (18)$$

(ii) The Higgs bound obtained from recent CDF [27] and LEP2 [28], i.e., $m_h > 113$ GeV.

(iii) We will limit ourselves to LSP–nucleon cross sections for the scalar coupling, which gives detectable rates

$$4 \times 10^{-7} \le \sigma^{\rm nucl}_{\rm scal} \le 2 \times 10^{-5}\ {\rm pb}. \qquad (19)$$

We should remember that the event rate does not depend only on the nucleon cross section, but on other parameters also, mainly on the LSP mass and the nucleus used in the target. The condition on the nucleon cross section imposes severe constraints on the acceptable parameter space. In particular, in our model, it restricts $\tan\beta$ to values $\tan\beta \simeq 50$. We will not elaborate further on this point, since it has already appeared [29].

4. EXPRESSIONS FOR THE DIFFERENTIAL CROSS SECTION

The effective Lagrangian describing the LSP nucleus cross section can be cast in the form [14]

$$\mathcal{L}_{\rm eff} = -\frac{G_{\rm F}}{\sqrt{2}}\left\{(\bar\chi_1\gamma^\lambda\gamma_5\chi_1)J_\lambda + (\bar\chi_1\chi_1)J\right\}, \qquad (20)$$

where

$$J_\lambda = \bar N\gamma_\lambda(f_V^0 + f_V^1\tau_3 + f_A^0\gamma_5 + f_A^1\gamma_5\tau_3)N, \qquad (21)$$
$$J = \bar N(f_S^0 + f_S^1\tau_3)N.$$

We have neglected the uninteresting pseudoscalar and tensor currents. Note that, due to the Majorana nature of the LSP, $\bar\chi_1\gamma^\lambda\chi_1 = 0$ (identically). With the above ingredients, the differential cross section can be cast in the form [11, 22, 23]

$$d\sigma(u, v) = \frac{du}{2(\mu_r b v)^2}\left[\left(\bar\Sigma_S + \bar\Sigma_V\frac{v^2}{c^2}\right)F^2(u) + \bar\Sigma_{\rm spin}F_{11}(u)\right], \qquad (22)$$

$$\bar\Sigma_S = \sigma_0\left(\frac{\mu_r(A)}{\mu_r(N)}\right)^2 A^2\left(f_S^0 - f_S^1\frac{A-2Z}{A}\right)^2 \qquad (23)$$

The static spin matrix elements for the light nuclei considered here (for comparison, we also quote the results for the medium-heavy nucleus ^{73}Ge [30] and the heavy nucleus ^{207}Pb [15])

Nucleus	$[\Omega_0(0)]^2$	$[\Omega_1(0)]^2$	$\Omega_0(0)\Omega_1(0)$	$\mu_{\rm th}$	$\mu_{\rm exp}$	$\mu_{\rm th}({\rm spin})/\mu_{\rm exp}({\rm spin})$
^{19}F	2.610	2.807	2.707	2.91	2.62	0.91
^{29}Si	0.207	0.219	−0.213	−0.50	−0.56	0.99
^{23}Na	0.477	0.346	0.406	2.22	2.22	0.57
^{73}Ge	1.157	1.005	−1.078			
^{207}Pb	0.305	0.231	−0.266			

$$\simeq \sigma^S_{p,\chi^0} A^2 \left(\frac{\mu_r(A)}{\mu_r(N)}\right)^2,$$

$$\bar{\Sigma}_{\rm spin} = \sigma^{\rm spin}_{p,\chi^0}\,\zeta_{\rm spin}, \tag{24}$$

$$\zeta_{\rm spin} = \frac{(\mu_r(A)/\mu_r(N))^2}{3\left(1+\dfrac{f^0_A}{f^1_A}\right)^2} S(u),$$

$$S(u) = \left(\frac{f^0_A}{f^1_A}\Omega_0(0)\right)^2 \frac{F_{00}(u)}{F_{11}(u)} \tag{25}$$

$$+ 2\frac{f^0_A}{f^1_A}\Omega_0(0)\Omega_1(0)\frac{F_{01}(u)}{F_{11}(u)} + \Omega_1(0)^2,$$

$$\bar{\Sigma}_V = \sigma^V_{p,\chi^0}\zeta_V, \tag{26}$$

$$\zeta_V = \frac{(\mu_r(A)/\mu_r(N))^2}{(1+\dfrac{f^1_V}{f^0_V})^2} A^2 \left(1 - \frac{f^1_V}{f^0_V}\,\frac{A-2Z}{A}\right)^2 \tag{27}$$

$$\times \left(\frac{v_0}{c}\right)^2 \left[1 - \frac{1}{(2\mu_r b)^2}\frac{2\eta+1}{(1+\eta)^2}\frac{\langle 2u\rangle}{\langle v^2\rangle}\right].$$

The proton–neutralino cross sections are given by

$$\sigma^S_{p,\chi^0} = \sigma_0 (f^0_S)^2 \frac{\mu^2_r(N)}{m^2_N},$$

$$\sigma^{\rm spin}_{p,\chi^0} = 3\sigma_0 (f^0_A + f^1_A)^2 \frac{\mu^2_r(N)}{m^2_N},$$

$$\sigma^V_{p,\chi^0} = \sigma_0 (f^0_V + f^1_V)^2 \frac{\mu^2_r(N)}{m^2_N}$$

for scalar, spin, and vector, respectively (the isovector scalar is negligible, i.e., $\sigma^S_p = \sigma^S_n$). Here, m_N is the nucleon mass, $\eta = m_x/m_N A$, $\mu_r(A)$ is the LSP–nucleus reduced mass, $\mu_r(N)$ is the LSP–nucleon reduced mass, and

$$\sigma_0 = \frac{(G_{\rm F} m_N)^2}{2\pi} \simeq 0.77\times 10^{-38}\ {\rm cm}^2, \tag{28}$$

$$Q = Q_0 u, \quad Q_0 = \frac{1}{A m_N b^2} = 4.1\times 10^4 A^{-4/3}\ {\rm keV}, \tag{29}$$

where Q is the energy transfer to the nucleus, $F(u)$ is the nuclear form factor, and

$$F_{\rho\rho'}(u) = \sum_{\lambda,\kappa} \frac{\Omega^{(\lambda,\kappa)}_\rho(u)}{\Omega_\rho(0)} \frac{\Omega^{(\lambda,\kappa)}_{\rho'}(u)}{\Omega_{\rho'}(0)}, \quad \rho,\rho' = 0,1 \tag{30}$$

are the spin form factors [15] (ρ,ρ' are isospin indices) normalized to one at $u=0$; Ω_0 (Ω_1) are the static isoscalar (isovector) spin matrix elements. Note that the quantity $S(u)$ is essentially independent of u. Thus, the energy-transfer dependence is contained in the function $F_{11}(u)$. Note also that $S(u)$ depends on the ratio of the isoscalar to isovector axial current couplings. These individual couplings can vary a lot within the SUSY parameter space.

Their ratio, however, does not change very much. In fact, actual calculations [21] show that $3.0 \le S(0) \le 7.5$ for ^{19}F, $0.03 \le S(0) \le 0.2$ for ^{29}Si, and $0.4 \le S(0) \le 1.1$ for ^{23}Na. The quantity $S(u)$ depends very sensitively on nuclear physics via the static spin matrix element (table). As we can see from the table, the spin matrix elements are very accurate. This is evident by comparing the obtained magnetic dipole moments to experiment and noting that the magnetic moments, with the exception of ^{23}Na, are dominated by the spin. From the same table, we see that ^{19}F is favored from the point of view of the spin matrix element. This advantage may be partially lost if the LSP is very heavy, due to the kinematic factor $\mu_r(A)$, which tends to favor a heavy target. The energy-transfer dependence of the differential cross section for the coherent mode is given by the square of the form factor, i.e., $|F(u)|^2$. These form factors for the isotopes ^{19}F, ^{23}Na, and ^{29}Si were calculated in [21] and are shown in Fig. 1. The energy-transfer dependence of the differential cross section due to spin is essentially given by $F_{11}(u)$. These functions

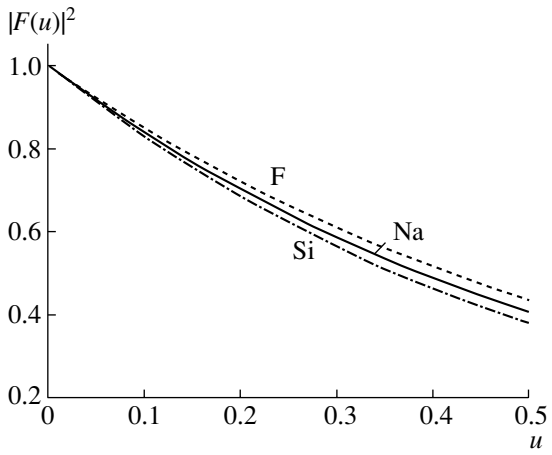

Fig. 1. The energy dependence of the coherent process, i.e., the square of the form factor, $|F(u)|^2$, for the isotopes ^{19}F, ^{23}Na, and ^{29}Si. The allowed range of u for the above isotopes is $0.011 \le u \le 0.17$, $0.015 \le u \le 0.30$, and $0.021 \le u \le 0.50$, respectively. This corresponds to energy transfers $8.9 \le Q \le 140$, $9.5 \le Q \le 190$, and $9.7 \le Q \le 230$ keV, respectively.

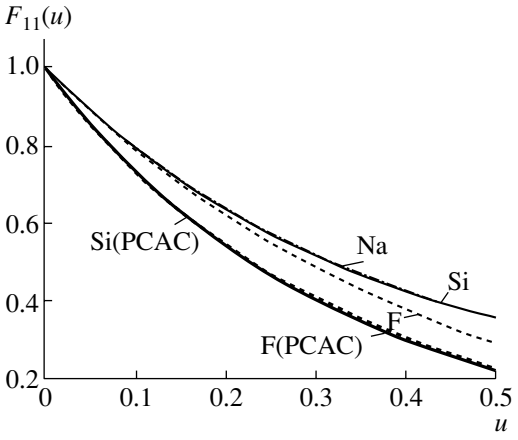

Fig. 2. The energy dependence of the spin contribution (spin response function $F_{11}(u)$) for the isotopes ^{19}F, ^{23}Na and ^{29}Si. The allowed range of energy transfers is the same as in the table. In this figure, we also plot $F_{11}(u)$ when the PCAC effect is considered.

for the isotopes ^{19}F, ^{23}Na, and ^{29}Si were calculated in [21] and are shown in Fig. 2. Note that the energy dependences of the coherent and the spin modes for light systems are not very different, especially if the PCAC corrections on the spin response function are ignored.

5. EXPRESSIONS FOR THE RATES

The total nondirectional event rate is given by

$$R = R_{\rm nondir} = \frac{dN}{dt} = \frac{\rho(0)}{m_\chi}\frac{m}{Am_N}\sigma(u,v)|v|, \quad (31)$$

where $\rho(0) = 0.3$ GeV/cm^3 is the LSP density in our vicinity and m is the detector mass. The differential nondirectional rate can be written as

$$dR = dR_{\rm nondir} = \frac{\rho(0)}{m_\chi}\frac{m}{Am_N}d\sigma(u,v)|v|. \quad (32)$$

The directional differential rate [11, 25] in the direction $\hat{\mathbf{e}}$ is given by

$$dR_{\rm dir} = \frac{\rho(0)}{m_\chi}\frac{m}{Am_N}\mathbf{v}\cdot\hat{\mathbf{e}}\,H(\mathbf{v}\cdot\hat{\mathbf{e}})\frac{1}{2\pi}d\sigma(u,v), \quad (33)$$

where H the Heaviside step function. The factor of $1/2\pi$ is introduced since the differential cross section of the last equation is the same as that entering the nondirectional rate, i.e., after an integration over the azimuthal angle around the nuclear momentum has been performed. In other words, crudely speaking, $1/2\pi$ is the suppression factor that we expect in the directional rate compared to the usual one. The precise suppression factor depends, of course, on the direction of observation. In spite of their very interesting experimental signatures, we will not be concerned here with directional rates. The mean value of the nondirectional event rate of (32) is obtained by convoluting the above expressions with the LSP velocity distribution $f(\mathbf{v},\mathbf{v}_E)$ with respect to the Earth:

$$\left\langle\frac{dR}{du}\right\rangle = \frac{\rho(0)}{m_\chi}\frac{m}{Am_N}\int f(\mathbf{v},\mathbf{v}_E)|\mathbf{v}|\frac{d\sigma(u,v)}{du}d^3\mathbf{v}. \quad (34)$$

The above expression can be more conveniently written as

$$\left\langle\frac{dR}{du}\right\rangle = \frac{\rho(0)}{m_\chi}\frac{m}{Am_N}\sqrt{\langle v^2\rangle}\left\langle\frac{d\Sigma}{du}\right\rangle, \quad (35)$$

where

$$\left\langle\frac{d\Sigma}{du}\right\rangle = \int\frac{|\mathbf{v}|}{\sqrt{\langle v^2\rangle}}f(\mathbf{v},\mathbf{v}_E)\frac{d\sigma(u,v)}{du}d^3\mathbf{v}. \quad (36)$$

After performing the integrations over the velocity distribution, to first order in the Earth's velocity, and over the energy transfer u, the last expression takes the form

$$R = \bar{R}t[1 + h(a,Q_{\rm min})\cos\alpha], \quad (37)$$

where α is the phase of the Earth ($\alpha = 0$ around June 2) and $Q_{\rm min}$ is the energy transfer cutoff imposed by the detector. In the above expressions, $\bar{R}$ is the rate obtained in the conventional approach [14] by neglecting the folding with the LSP velocity and the momentum transfer dependence of the differential

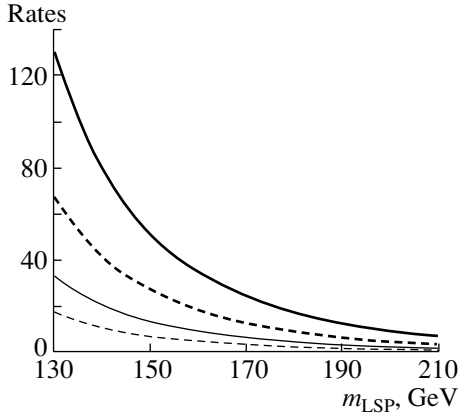

Fig. 3. The total detection rate per kg target yr vs. the LSP mass for a typical solution in our parameter space in the case of ^{127}I corresponding to model B (thick line) and model C (fine line). For the definitions, see the text.

cross section:

$$\bar{R} = \frac{\rho(0)}{m_\chi}\frac{m}{Am_N}\sqrt{\langle v^2\rangle}\left[\bar{\Sigma}_S + \bar{\Sigma}_{\mathrm{spin}} + \frac{\langle v^2\rangle}{c^2}\bar{\Sigma}_V\right], \tag{38}$$

where $\bar{\Sigma}_i$ are defined by (23)–(26). It contains all the parameters of the SUSY models. The modulation is described by the parameter h. Once the rate is known, as well as the parameters t and h, which depend only on the LSP mass, the nuclear form factor, and the velocity distribution, the nucleon cross section can be extracted and compared to experiment. The total directional event rates can be obtained in a similar fashion by integrating (33) with respect to the velocity as well as the energy transfer u. We find

$$R_{\mathrm{dir}} = \bar{R}\frac{t_0}{4\pi}\big|(1 + h_1(a, Q_{\min})\cos\alpha)\mathbf{e}_z\cdot\mathbf{e} \tag{39}$$
$$- h_2(a, Q_{\min})\cos\alpha\,\mathbf{e}_y\cdot\mathbf{e} + h_3(a, Q_{\min})\sin\alpha\,\mathbf{e}_x\cdot\mathbf{e}\big|.$$

We recall that the z axis is in the direction of the Sun's motion, the y axis is perpendicular to the plane of the Galaxy, and the x axis is in the galactocentric direction. The effect of folding with LSP velocity on the total rate is taken into account via the quantity t_0, which depends on the LSP mass. All other SUSY parameters have been absorbed in $\bar{R}$. We see that the modulation of the directional total event rate can be described in terms of three parameters h_l, $l = 1, 2, 3$. In the special case of $\lambda = 0$, we essentially have one parameter, namely h_1, since then we have $h_2 = 0.117$ and $h_3 = 0.135$. Given the functions $h_l(a, Q_{\min})$, one can plot the expression in (39) as a function of the phase of the Earth, α.

6. THE SCALAR CONTRIBUTION—THE ROLE OF HEAVY QUARKS

The coherent scattering can be mediated via the neutral intermediate Higgs particles (h and H), which survive as physical particles. It can also be mediated via squarks, via the mixing of the isodoublet and isosinglet squarks of the same charge. In our model, we find that the Higgs contribution becomes dominant, and, as a matter of fact, the heavy Higgs H is more important (the Higgs particle A couples in a pseudoscalar way, which does not lead to coherence). It is well known that all quark flavors contribute [17], since the relevant couplings are proportional to the quark masses. One encounters in the nucleon not only the usual sea quarks ($u\bar{u}$, $d\bar{d}$, and $s\bar{s}$) but also the heavier quarks c, b, and t which couple to the nucleon via two-gluon exchange (see [18] and references therein). As a result, one obtains an effective scalar Higgs–nucleon coupling by using effective quark masses as follows:

$$m_u \to f_u m_N, \quad m_d \to f_d m_N, \quad m_s \to f_s m_N,$$
$$m_Q \to f_Q m_N \quad (\text{for heavy quarks } (c, b, t)),$$

where m_N is the nucleon mass. The isovector contribution is now negligible. The parameters f_q ($q = u, d, s$) can be obtained by chiral-symmetry-breaking terms in relation to phase-shift and dispersion analysis. Following [19], we obtain

$$f_u = 0.021, \quad f_d = 0.037, \quad f_s = 0.140 \text{ (model B)};$$
$$f_u = 0.023, \quad f_d = 0.034, \quad f_s = 0.400 \text{ (model C)}.$$

In both models, the s quark is dominant. To leading order via quark loops and gluon exchange with the nucleon, one finds

$$f_Q = \frac{2}{27}\left(1 - \sum_q f_q\right).$$

This yields $f_Q = 0.060$ (model B) and $f_Q = 0.040$ (model C). There is a correction to the above parameters coming from loops involving s quarks [18] and due to QCD effects. Thus, for large $\tan\beta$, we find [11] (see also [17, 18]) in models B and C, respectively,

$$f_c = 0.060 \cdot 1.068 = 0.064,$$
$$f_t = 0.060 \cdot 2.048 = 0.123,$$
$$f_b = 0.060 \cdot 1.174 = 0.070;$$
$$f_c = 0.040 \cdot 1.068 = 0.043,$$
$$f_t = 0.040 \cdot 2.048 = 0.082,$$
$$f_b = 0.040 \cdot 1.174 = 0.047.$$

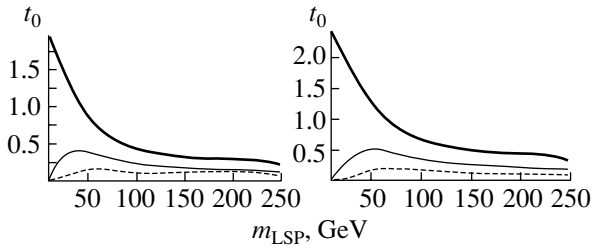

Fig. 4. The dependence of the quantity t_0 on the LSP mass for the symmetric case ($\lambda = 0$, left) as well as for the maximum axial asymmetry ($\lambda = 1$, right) in the case of the target ^{127}I. For orientation purposes, three detection cutoff energies are exhibited, $Q_{\min} = 0$ (thick solid line), $Q_{\min} = 10$ keV (thin solid line), and $Q_{\min} = 20$ keV (dashed line). As expected, t_0 decreases as the cutoff energy increases.

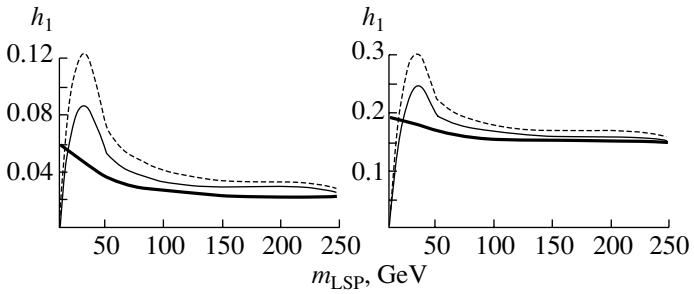

Fig. 5. The same as in the previous figure, but for the modulation amplitude h_1.

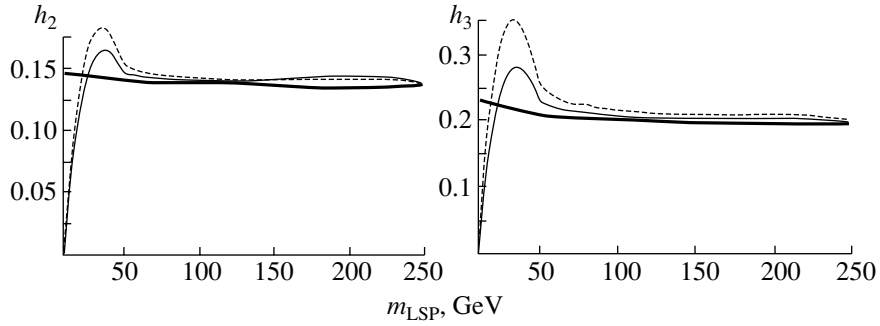

Fig. 6. The same as in Fig. 4, but for the modulation amplitudes h_2 and h_3 for $\lambda = 1$.

7. RESULTS AND DISCUSSION

The three basic ingredients of our calculation were the input SUSY parameters, a quark model for the nucleon, and the velocity distribution combined with the structure of the nuclei involved. We will focus our attention on the coherent scattering and present results for the popular target ^{127}I. We have utilized two nucleon models, indicated by B and C, that take into account the presence of heavy quarks in the nucleon. We also considered energy cutoffs imposed by the detector, by considering two typical cases $Q_{\min} = 10$, 20 keV. The thus obtained results for the unmodulated total nondirectional event rates $\bar{R}t$ in the case of the symmetric isothermal model for a typical SUSY parameter choice [12] are shown in Fig. 3. Special attention was paid to the directional rate and its modulation due to the annual motion of the Earth in the case of isothermal models. The case of nonisothermal models, e.g., caustic rings, is more complicated [25] and will not be further discussed here. As expected, the parameter t_0, which contains the effect of the nuclear form factor and the LSP velocity dependence, decreases as the reduced mass increases.

We will focus on discussion of the directional rates described in terms of t_0 and h_i, $i = 1, 2, 3$ [see (39)], and limit ourselves to directions of observation close to the coordinate axes. As expected, the parameter t_0 decreases as the reduced mass increases. The quantity t_0 is shown in Fig. 4 for three values of the detector energy cutoff, $Q_{\min} = 0$, 10, and 20 KeV. Similarly,

we show the quantity h_1 in Fig. 5. The quantities h_2 and h_3 are shown in Fig. 6 for $\lambda = 1$. For $\lambda = 0$, they are not shown since they are essentially constant and equal to 0.117 and 0.135, respectively. As expected, the parameter t_0 decreases as the reduced mass increases. It also decreases as the cutoff energy $Q_{\min}$ increases. We notice that t_0 is little affected by the presence of asymmetry. On the other hand, h_1, h_2, and h_3 substantially increase in the presence of asymmetry. Sometimes, they increase as the cutoff energy increases (at the expense, of course, of the total number of counts). For the differential rate, the reader is referred to our previous works [23, 24].

8. CONCLUSIONS

We have discussed the parameters that describe the event rates for direct detection of SUSY dark matter. Only in a small segment of the allowed parameter space are the rates above the present experimental goals. We thus looked for characteristic experimental signatures for background reduction, i.e., (a) correlation of the event rates with the motion of the Earth (modulation effect) and (b) the directional rates (their correlation both with the velocity of the Sun and that of the Earth).

A typical graph for the total unmodulated rate is shown in Fig. 3. We will concentrate here on the directional rates, described in terms of the parameters t_0, h_1, h_2, and h_3. For simplicity, these parameters are given in Figs. 4–6 for directions of observation close to the three axes x, y, z. We see that the unmodulated rate scales by $\cos\theta_S$ with θ_S being the angle between the direction of observation and the velocity of the Sun. The reduction factor, $f_{\rm red} = t_0/(4\pi\, t_0) = \kappa/(2\pi)$, of the total directional rate, along the Sun's direction of motion, compared to the total nondirectional rate depends on the nuclear parameters, the reduced mass, and the asymmetry parameter λ [24]. We find that κ is around 0.6 (no asymmetry) and around 0.7 (maximum asymmetry, $\lambda = 1.0$), i.e., not very different from the naively expected $f_{\rm red} = 1/(2\pi)$ (i.e., $\kappa = 1$). The modulation of the directional rate increases with the asymmetry parameter λ, and it also depends on the direction of observation. For $Q_{\min} = 0$, it can reach values up to 23%. Values up to 35% are possible for large values of $Q_{\min}$, but they occur at the expense of the total number of counts.

ACKNOWLEDGMENTS

This work was supported by the European Union under the contracts RTN no. HPRN-CT-2000-00148 and TMR no. ERBFMRX-CT96-0090 and ΠΕΝΕΔ95 of the Greek Secretariat for Research.

REFERENCES

1. G. Jungman *et al.*, Phys. Rep. **267**, 195 (1996).
2. G. F. Smoot *et al.* (COBE data), Astrophys. J. **396**, L1 (1992).
3. E. Gawiser and J. Silk, Science **280**, 1405 (1988); M. A. K. Gross *et al.*, Mon. Not. R. Astron. Soc. **301**, 81 (1998).
4. A. G. Riess *et al.*, Astron. J. **116**, 1009 (1998).
5. R. S. Somerville, J. R. Primack, and S. M. Faber, astro-ph/9806228.
6. S. Perlmutter *et al.*, Astrophys. J. **517**, 565 (1999); **483**, 565 (1997); astro-ph/9812133; S. Perlmutter, M. S. Turner, and M. White, Phys. Rev. Lett. **83**, 670 (1999).
7. M. S. Turner, astro-ph/9904051; Phys. Rep. **333–334**, 619 (2000).
8. D. P. Bennett *et al.* (MACHO Collab.), in *Proceedings of the 5th Annual Maryland Conference, 1995,* Ed. by S. Holt; C. Alcock *et al.* (MACHO Collab.), Phys. Rev. Lett. **74**, 2867 (1995).
9. R. Bernabei *et al.*, INFN/AE-98/34 (1998); Phys. Lett. B **389**, 757 (1996).
10. R. Bernabei *et al.*, Phys. Lett. B **424**, 195 (1998); **450**, 448 (1999).
11. J. D. Vergados, hep-ph/0010151.
12. M. E. Gómez and J. D. Vergados, hep-ph/0012020; M. E. Gómez, G. Lazarides, and C. Pallis, Phys. Rev. D **61**, 123512 (2000); Phys. Lett. B **487**, 313 (2000).
13. A. Bottino *et al.*, Phys. Lett. B **402**, 113 (1997); R. Arnowitt and P. Nath, Phys. Rev. Lett. **74**, 4592 (1995); Phys. Rev. D **54**, 2374 (1996); hep-ph/9902237; V. A. Bednyakov, H. V. Klapdor-Kleingrothaus, and S. G. Kovalenko, Phys. Lett. B **329**, 5 (1994).
14. J. D. Vergados, J. Phys. G **22**, 253 (1996).
15. T. S. Kosmas and J. D. Vergados, Phys. Rev. D **55**, 1752 (1997).
16. M. Drees and M. M. Nojiri, Phys. Rev. D **47**, 376 (1993).
17. M. Drees and M. M. Nojiri, Phys. Rev. D **48**, 3483 (1993); **47**, 4226 (1993).
18. A. Djouadi and M. Drees, Phys. Lett. B **484**, 183 (2000); S. Dawson, Nucl. Phys. B **359**, 283 (1991); M. Spira *et al.*, Nucl. Phys. B **453**, 17 (1995).
19. T. P. Cheng, Phys. Rev. D **38**, 2869 (1988); H.-Y. Cheng, Phys. Lett. B **219**, 347 (1989).
20. J. D. Vergados and T. S. Kosmas, Yad. Fiz. **61**, 1166 (1998) [Phys. At. Nucl. **61**, 1066 (1998)].
21. P. C. Divari, T. S. Kosmas, J. D. Vergados, and L. D. Skouras, Phys. Rev. C **61**, 054612 (2000).
22. J. D. Vergados, Phys. Rev. D **58**, 103001 (1998).
23. J. D. Vergados, Phys. Rev. Lett. **83**, 3597 (1999).
24. J. D. Vergados, Phys. Rev. D **62**, 023519 (2000).
25. J. D. Vergados, Phys. Rev. D **63**, 063511 (2001).

26. K. N. Buckland, M. J. Lehner, G. E. Masek, in *Proceedings of the 3rd International Conference on Dark Matter in Astro- and Particle Physics (Dark 2000),* Ed. by H. V. Klapdor-Kleingrothaus, (Springer-Verlag, Berlin, 2000).
27. CDF Collab., FERMILAB-Conf-99/263-E CDF; http://fnalpubs.fnal.gov/archive/1999/conf/Conf-99-263-E.html
28. P. J. Dorman (ALEPH Collab.), http://alephwww.cern.ch/ALPUB/seminar/lepcmar200/lepc2000.pdf
29. M. E. Gómez and J. D. Vergados, hep-ph/0105115.
30. M. T. Ressell *et al.*, Phys. Rev. D **48**, 5519 (1993).

Physics of Atomic Nuclei, Vol. 66, No. 3, 2003, pp. 490–493. From Yadernaya Fizika, Vol. 66, No. 3, 2003, pp. 518–520.

COSMOLOGY AND ASTROPHYSICS. DARK MATTER

Possible Lower Bounds for the Direct Detection Rate of SUSY Dark Matter*

V. A. Bednyakov**

Joint Institute for Nuclear Research, Dubna, Moscow oblast, 141980 Russia

Received February 13, 2002

Abstract—One can expect accessible lower bounds for the dark matter detection rate due to restrictions on masses of the SUSY partners. To explore this correlation, one needs a new-generation large-mass detector. The absolute lower bound for the detection rate can naturally be due to spin-dependent interaction. Aimed at detecting dark matter with sensitivity higher than 10^{-5} event/kg/d, an experiment should have a nonzero-spin target. Perhaps, it is best to create a GENIUS-like detector with both ^{73}Ge (high spin) and ^{76}Ge nuclei. © *2003 MAIK "Nauka/Interperiodica"*.

A new generation of high-sensitivity dark matter detectors, in particular, aimed at searching for neutralinos, the lightest SUSY particles (LSP), has been proposed (see, for example, proposals GENIUS [1], GENIUS-TF [2], CRESST [3], and CDMS [4]). The question naturally arises of how small the expected event rate, R, of the LSP direct detection can be, provided the LSP is a cold dark matter particle (or so-called weakly interacting massive particle—WIMP). The upper and lower bounds for the neutralino–nucleon cross section were considered in various SUSY models [5–8]. The main goal of this paper is to attract extra attention to possible lower bounds for R, which is to be measured directly.

To this end, the exploration of the SUSY parameter space is performed at the weak scale (without any unification assumptions). The parameter space is determined by entries of the mass matrices of neutralinos, charginos, Higgs bosons, sleptons, and squarks. Available restrictions from cosmology ($0.1 < \Omega_\chi h_0^2 < 0.3$), rare $b \to s\gamma$ decay ($1.0 \times 10^{-4} < \mathrm{Br}(b \to s\gamma) < 4.2 \times 10^{-4}$), accelerator SUSY searches, etc., were taken into account [7, 8].

Scatter plots with individual cross sections of spin-dependent and spin-independent (scalar) interactions of LSP with the proton and the neutron are given in Fig. 1 as functions of the LSP mass. The different behavior of these cross sections with the mass of the LSP can be seen from the plots. There is a lower bound for the spin-dependent cross section. Due to the absence of a clear lower bound for the scalar cross section of the WIMP–nucleon interaction, one can expect that the lower bound for the rate can be established by the spin-dependent interaction, which, in contrast to the scalar interaction, is associated with WIMP–nucleon cross sections that are about three orders of magnitude larger.

The existence of the absolute lower bound for the event rate (thick curve in Fig. 2) and the variation of the bound with the parameters and masses of the SUSY particles [7] allow one to consider prospects for searching for dark matter under special assumptions about restricted values for the SUSY parameters and masses.

Figure 2 gives different lower bounds for R obtained with extra limitations on SUSY-particle masses [7]. A restriction for the single (light) squark mass to be quite small ($M_{\mathrm{sq}} < 230$ GeV), as well as another assumption that all sfermion masses do not exceed 300–400 GeV, sets upper limits on the mass of the LSP and, therefore, does not permit R to drop very deeply with increasing LSP mass. Furthermore, in both cases, the lower bound for the rate is established for all allowed masses of the LSP at a level of 10^{-3} event/kg/d. This value is considered as an optimistic sensitivity expectation for future high-accuracy detectors of dark matter, such as GENIUS [1]. One can see that the mass of the light neutral CP-even Higgs boson, M_{H^0}, unfortunately has a very poor restrictive potential. The situation looks most promising when one limits the mass of the charged Higgs boson. If it happened, for instance, that either the SUSY spectrum is indeed light or $M_{H^+} < 200$ GeV, in both cases at least the GENIUS experiment should detect a dark matter signal.

Therefore, the prospects could be very promising if from collider searches one restricted M_{H^+} at a level of about 200 GeV. The observation, due to its

*This article was submitted by the author in English.

**e-mail: bedny@nusun.jinr.ru

1063-7788/03/6603-0490$24.00

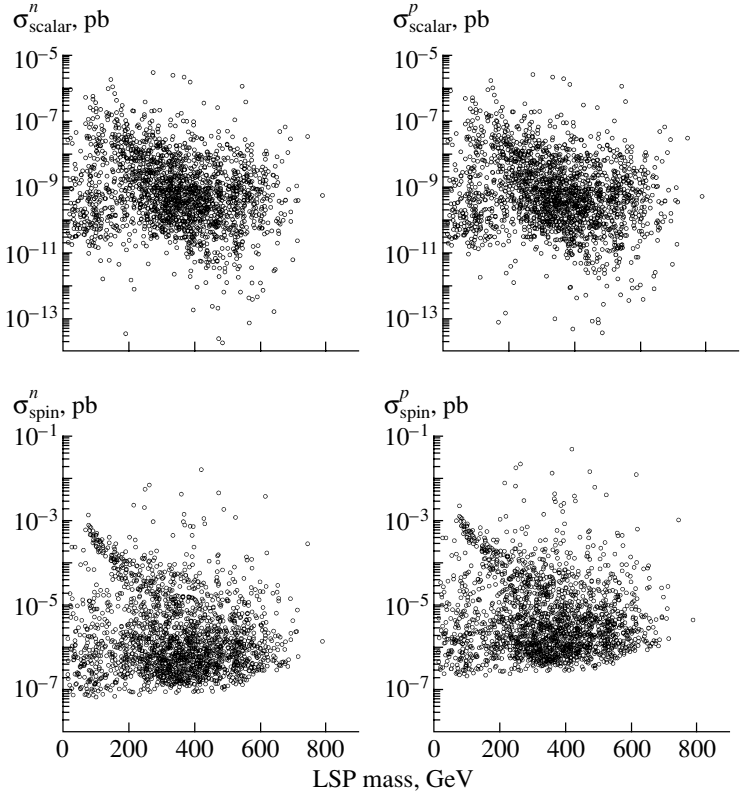

Fig. 1. Cross sections of spin-dependent and spin-independent interactions of WIMPs with the proton and the neutron.

importance for dark matter detection, could serve as a source for extra efforts in searching for the charged Higgs boson with colliders. Otherwise, nonobservation of any dark matter signal with very sensitive dark matter detectors would exclude, for example, a SUSY spectrum with masses lighter than 300–400 GeV, charginos with masses smaller than 250 GeV (Fig. 2), and the charged Higgs bosons with $M_{H^+} < 200$ GeV.

It was claimed that nuclear spin is not important for detection of dark matter particles, provided the detection sensitivity does not exceed 0.01 event/kg/d, which was considered unattainable in 1994 [9]. Now, with new-generation detectors, the situation has changed and targets with nonzero-spin nuclei should again be taken into account.

For any mass of the LSP, one can find very large and very small values for the spin-dependent to spin-independent cross-section (or rate) ratio. The spin-independent (scalar) contribution obviously dominates in the domain of large expected rates (Fig. 3) in the nonzero-spin germanium detector ($R > 0.1$ event/kg/d). But as soon as the total rate drops down to $R < 0.01$ event/kg/d or, equivalently, the scalar neutralino–proton cross section becomes smaller than 10^{-9}–10^{-10} pb, the spin-dependent

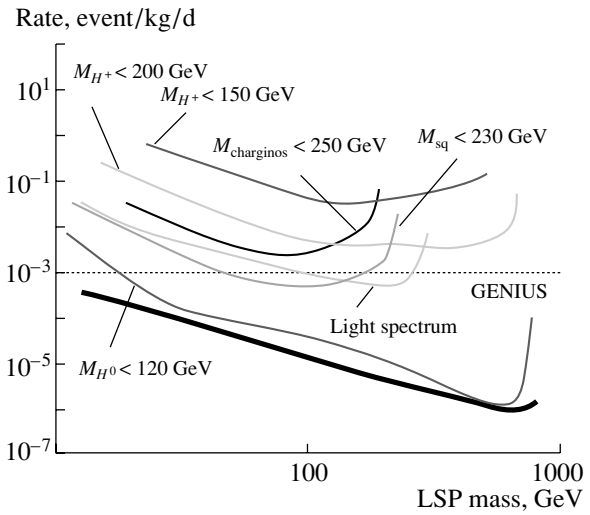

Fig. 2. Different lower bounds for the total event rate in ^{73}Ge. Here, M_{sq}, M_{H^+}, and M_{H^0} denote masses of the squark, the charged Higgs boson, and the light neutral CP-even Higgs boson, respectively. The heavy chargino mass is denoted as $M_{\text{charginos}}$. The thick curve corresponds to the absolute lower bound. "Light spectrum" denotes the lower bound for the rate, obtained when all sfermion masses are lighter than 300–400 GeV. The dotted line represents the expected sensitivity for the direct dark matter detection with GENIUS.

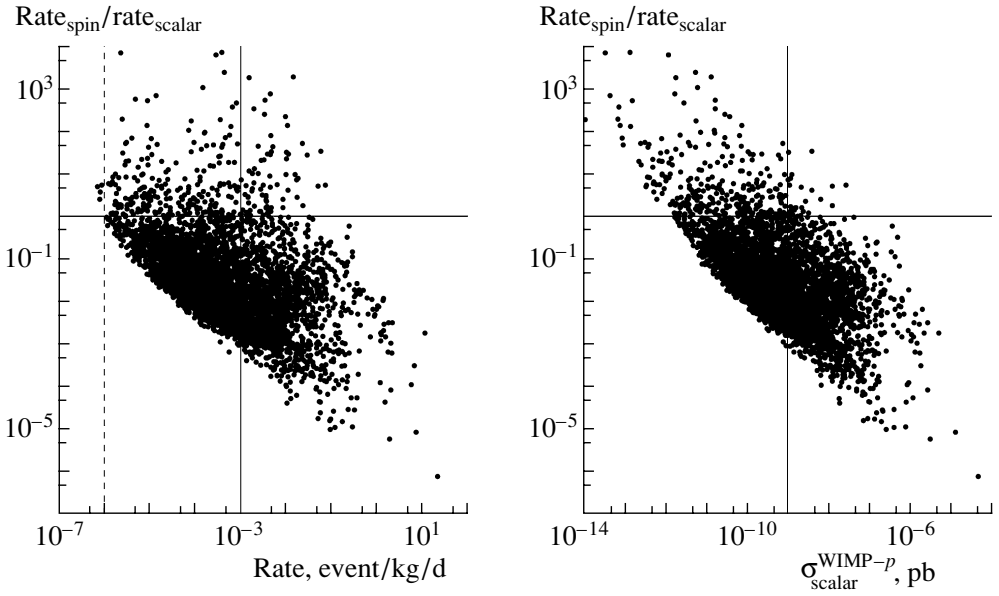

Fig. 3. Ratio of the spin-dependent event rate to the spin-independent event rate in the ^{73}Ge isotope (spin $= 9/2$) as a function of the total (spin-dependent plus spin-independent) event rate (left) and the scalar cross section of the neutralino–proton interaction (right). The solid vertical lines give the expected sensitivity of GENIUS [1]. In the region above the horizontal line, the spin contribution dominates.

interaction may produce a rather nonnegligible contribution to the total event rate. Moreover, if the scalar cross section further decreases ($\sigma < 10^{-12}$ pb), it becomes obvious that the spin contribution alone saturates the total rate and protects it from decreasing below $R \approx 10^{-6}$–10^{-7} event/kg/d [7]. With only a spinless detector, one can miss a signal caused by spin-dependent interaction. Aimed at detecting dark matter with sensitivity higher than 10^{-5} event/kg/d, an experiment should have a nonzero-spin target. Indeed, while the scalar cross sections governed mostly by Higgs exchange can be rather small, the spin cross section cannot be arbitrarily small, because the mass of the Z boson, which gives the dominant contribution, is well defined, provided one ignores any possible fine-tuning cancellations [6].

Therefore, if an experiment with a sensitivity of 10^{-5}–10^{-6} event/kg/d fails to detect a dark matter signal, an experiment with higher sensitivity should have a nonzero-spin target and will be able to detect dark matter particles only due to the spin neutralino–quark interaction. In this situation, it seems the best to create a huge GENIUS-like detector with both ^{73}Ge (high spin) and ^{76}Ge (spinless) isotopes.

ACKNOWLEDGMENTS

I thank Prof. H.V. Klapdor-Kleingrothaus and the Russian Foundation for Basic Research (project no. 00-02-17587) for support.

REFERENCES

1. H. V. Klapdor-Kleingrothaus, Yad. Fiz. **61**, 967 (1998) [Phys. At. Nucl. **61**, 875 (1998)]; J. Mod. Phys. A **13**, 3953 (1998); H. V. Klapdor-Kleingrothaus and Y. Ramachers, Eur. Phys. J. A **3**, 85 (1998); H. V. Klapdor-Kleingrothaus *et al.*, hep-ph/9910205.
2. H. V. Klapdor-Kleingrothaus *et al.*, http://www.mpi-hd.mpg.de/non_acc/
3. M. Altmann *et al.*, astro-ph/0106314; W. Seidel *et al.* (CRESST Collab.), Phys. At. Nucl. **63**, 1242 (2000).
4. M. Bravin *et al.*, Astropart. Phys. **12**, 107 (1999); J. Hellmig *et al.*, Nucl. Instrum. Methods Phys. Res. A **444**, 308 (2000).
5. R. Arnowitt and P. Nath, Phys. Rev. D **54**, 2374 (1996); **56**, 2820 (1997); Phys. Lett. B **437**, 344 (1998); R. Arnowitt, Phys. At. Nucl. **61**, 1098 (1998); V. Mandic, A. T. Pierce, P. Gondolo, and H. Murayama, hep-ph/0008022; R. Arnowitt, B. Dutta, and Y. Santoso, hep-ph/0008336; hep-ph/0005154; A. B. Lahanas, D. V. Nanopoulos, and V. C. Spanos, Mod. Phys. Lett. A **16**, 1229 (2001); A. Bottino, F. Donato, N. Fornengo, and S. Scopel, Phys. Rev. D **59**, 095004 (1999); V. Berezinsky *et al.*, Astropart. Phys. **5**, 1 (1996); A. Bottino, F. Donato, N. Fornengo, and S. Scopel, Phys. Rev. D **63**, 125003 (2001); H. Baer and M. Brhlik, Phys. Rev. D **57**, 567 (1998); J. L. Feng, K. T. Matchev, and F. Wilczek, Phys. Lett. B **482**, 388 (2000); E. Gabrielli, S. Khalil, C. Munoz, and E. Torrente-Lujan, Phys. Rev. D **63**, 025008 (2001); E. Accomando, R. Arnowitt, B. Dutta, and Y. Santoso, Nucl. Phys. B **585**, 124 (2000); L. Bergström and

P. Gondolo, Astropart. Phys. **6**, 263 (1996); J. D. Vergados, Phys. Rev. Lett. **83**, 3597 (1999); Phys. Rev. D **62**, 023519 (2000); Part. Nucl. Lett. **106**, 74 (2001).
6. J. R. Ellis, A. Ferstl, and K. A. Olive, Phys. Lett. B **481**, 304 (2000); Phys. Rev. D **63**, 065016 (2001).
7. V. A. Bednyakov and H. V. Klapdor-Kleingrothaus, Phys. Rev. D **62**, 043524 (2000).
8. V. A. Bednyakov and H. V. Klapdor-Kleingrothaus, Phys. Rev. D **63**, 095005 (2001); V. A. Bednyakov, H. V. Klapdor-Kleingrothaus, and H. Tu, Phys. Rev. D **64**, 075004 (2001).
9. V. A. Bednyakov, H. V. Klapdor-Kleingrothaus, and S. G. Kovalenko, Phys. Rev. D **50**, 7128 (1994).

Physics of Atomic Nuclei, Vol. 66, No. 3, 2003, pp. 494–496. From Yadernaya Fizika, Vol. 66, No. 3, 2003, pp. 521–523.

Dark Matter Search with CRESST Cryogenic Detectors*

G. Angloher, M. Altmann[1], M. Bruckmayer[1], C. Bucci[2], S. Cooper, C. Cozzini[1], P. Di Stefano[1], F. von Feilitzsch[3], T. Frank[1], D. Hauff[1], Th. Jagemann[3], J. Jochum[3], R. Keeling, H. Kraus, J. Macallister, F. Pröbst[1], Y. Ramachers, J. Schnagl[3], W. Seidel[1], I. Sergeyev[1], M. Stark[3], L. Stodolsky[1], and H. Wulandari[3]**

Physics Department, University of Oxford, Oxford, UK

Received February 13, 2002

Abstract—Results of the CRESST experiment at Gran Sasso using 262-g sapphire calorimeters with tungsten phase transition thermometers are presented. Calibration and analysis methods are described. Data taken in 2000 have been used to place limits on WIMP dark matter particles in the Galactic halo. The sapphire detectors are especially sensitive to low-mass WIMPs with spin-dependent interaction and improve on existing limits in this region. © *2003 MAIK "Nauka/Interperiodica".*

The CRESST collaboration has installed a low-background facility [1] in the Gran Sasso Underground Laboratory (LNGS) and in phase I of the project has used 262-g sapphire cryogenic calorimeters with W superconducting phase transition thermometers [2]. More details are given in those references. This paper presents the resulting dark matter limits.

The data used to set dark matter limits were taken during a week in October 2000, with a few short interruptions to refill the cryostat with liquid helium. The data consist of a 10-h calibration run with an external ^{57}Co source, 138.8 h of data without the source (of which 0.6 h is dead time following triggers), and finally another calibration run. The data from detector 8, which had the lowest threshold, is used to set our dark matter limits. A second detector was used to eliminate coincident events.

The performance of each detector was monitored by injecting heater pulses into a small heater wire bonded to the W thermometer. Their shape was adjusted to create a detector response similar to that of a particle interaction. A pulse was sent every 30 s throughout both dark matter and calibration runs. The height of the pulses was varied to cover the whole dynamic range, with more pulses in the low-energy region. This method provides a monitor of the stability of the detectors, an extrapolation of the energy calibration over the whole dynamic range, and a measure of their trigger efficiency as a function of deposited energy.

The amplitude of each pulse was determined by fitting it with a template. This avoids the bias of picking the highest point of suitably filtered pulses, which is systematically pulled by noise fluctuations to larger values. The absence of any bias is important for a precise definition of the threshold. It was therefore checked by fitting randomly sampled baseline noise. The resulting distribution peaked with no significant bias at -0.0019 ± 0.003 keV.

To calibrate the energy scale, a ^{57}Co source (122- and 136-keV γ lines) was inserted inside the shielding via a removable plug, illuminating the cold box from below. Data were taken with this source along with the heater pulses. A comparison of heater pulse amplitudes with those from the 122-keV γ line of the calibration source provides an absolute calibration of the heater pulses in terms of equivalent γ energy.

A separate heater pulse template was made for each amplitude of heater pulses by averaging many pulses from that heater pulse voltage. To extrapolate the energy calibration over the whole dynamic range, we used the heater pulses and plotted their fitted amplitude versus the injected energy. These data were fit with a polynomial function to give the detector response as a function of the deposited energy.

For the dark matter data, the response function determined above was used to convert each recorded event pulse to energy in each time bin. A template was made from similarly converted calibration-source pulses around the Compton edge (30–35 keV). This

*This article was submitted by the authors in English.

[1]Max-Planck-Institut für Physik, Munich, Germany.
[2]Laboratori Nazionali del Gran Sasso, Assergi, Italy.
[3]Technische Universität München, Physik Department, Germany.
**e-mail: angloher@mppmu.mpg.de

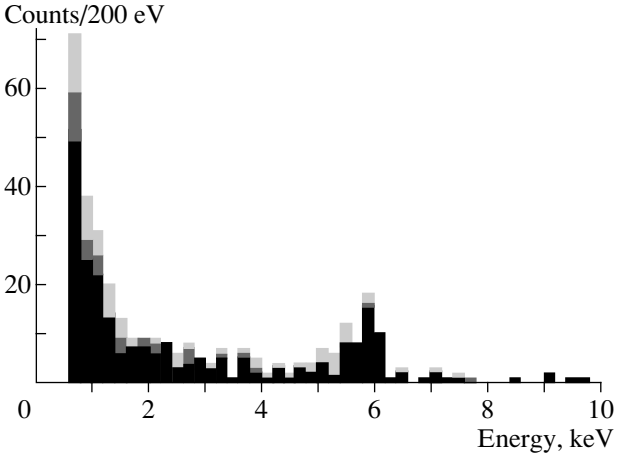

Fig. 1. Energy spectrum of events in detector 8 in the dark matter run (without source) in 200-eV bins. The upper histogram shows the uncut data, the middle histogram the data after coincident events are rejected, and the lower histogram after the pulse-shape cut.

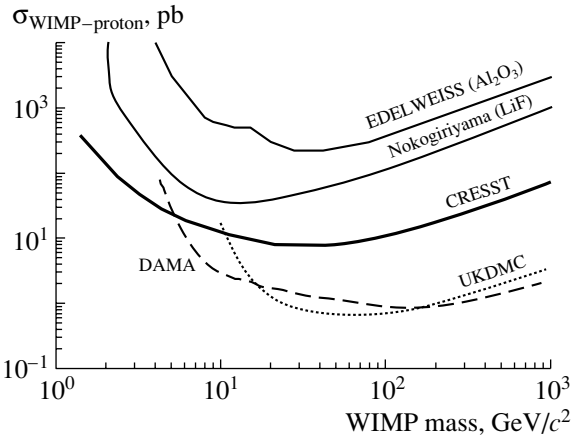

Fig. 2. Equivalent WIMP–proton cross section limits (90% C.L.) for a spin-dependent interaction as a function of the WIMP mass from a 1.51-(kg d) exposure of a 262-g sapphire detector. For comparison, we show limits from the EDELWEISS dark matter search with cryogenic sapphire detectors [5] and from DAMA [6] and UKDMC [7] with NaI detectors.

template could be used to fit the pulse height, but it was found that an optimal filter gave a slightly better resolution. The optimal filter was calculated using the template and randomly sampled baseline noise. A comparison to the template fit showed that the optimal filter applied did not introduce an energy bias.

The reliability of the energy calibration method to low energy was later checked in a dedicated run, where a low-activity ^{57}Co source was mounted inside the cryostat directly facing the crystals. Besides the 122- and 136-keV γ lines, this source gave a 14.4-keV γ line and a 6.4-keV Fe X-ray line. The source was chosen to be very weak to reduce the chance of contamination, with the result that the one-week run gave low statistics in the 14.4- and 6.4-keV lines. After applying the standard calibration method of extrapolation from the 122-keV line as described above, the measured energies for the 14.4- and 6.4-keV lines were $15.16^{+0.09}_{-0.09}$ and $6.70^{+0.07}_{-0.05}$ keV, respectively, with the fit errors corresponding to a 90% C.L. Our calibration procedure puts the 14.4- and the 6.4-keV lines 5.3% and 5.4% too high. Since it is the lower energies that most affect our dark matter limits, this tendency to shift events up in energy puts our limits on the conservative side.

For the analysis of the dark matter data, a software threshold of 600 eV was used, above which the trigger efficiency was 100%, as measured with the heater pulses. The spectrum for detector 8 is shown as the upper histogram in Fig. 1. There are 446 events from the software threshold to 120 keV. Events in coincidence in two or more detectors cannot be due to WIMP interactions and thus can be discarded. The coincidence cut was set at ± 4 ms, removing 76 events and introducing negligible dead time. Considering that only two detectors were active in this run, the coincidence rate of about 17% is consistent with the solid angle for detecting coincidence and thus with all events being background. This shows that the coincidence cut could be very useful in reducing background in a larger segmented detector.

The pulse shape of the remaining 370 events was then examined. Some of the events were spurious, induced by mechanical vibration or electronic noise, with an abnormal pulse shape. To judge the correctness of the pulse shape, each event was fitted with a template and the rms deviation was calculated. A cut on this deviation was chosen to be conservative and have a retention efficiency of 100% at all energies for good events.

The effect of these cuts are shown in Fig. 1. After the pulse-shape cut, 320 events remain. In the energy range from 15 to 25 keV, the background is 0.73 ± 0.22 count/(kg keV d) and drops to about 0.3 count/(kg keV d) at 100 keV. The spectrum shows a peak at about 5.9 keV with 7.0 ± 1.2 count/d. The position of the peak suggests a contamination with ^{55}Fe in the vicinity of the crystal. However, the peak is wider than expected, 572 ± 90 eV FWHM compared to 200 ± 50 eV of the 6.4-keV line from the internal calibration source, so that it may be due to more than a single X-ray line.

To extract upper limits for the WIMP interaction cross section, we tried the optimal-interval method used by some other groups, but found that it was biased to lower cross sections from picking a "lucky" downward fluctuation. For example, for

WIMP masses between 30 and 1000 GeV, the relatively small interval of 22.6–26.4 keV with no counts was selected. Instead we used fit and Monte Carlo methods, as described in [3]. For comparison with other experiments, our limits for spin-dependent WIMP interactions were converted to the equivalent WIMP–proton cross section using the $\lambda^2 J(J+1)$ factors for the odd-group model as given in [4]. The result is shown in Fig. 2. Using the spin factor from [8] would shift the whole CRESST exclusion curve down by a factor of 1/1.9 to lower cross sections, if one neglects the possible neutron contribution. In either case, we improve existing limits for low-mass WIMPs, which is due to our low threshold and was the goal of the first phase of CRESST.

The second phase of the experiment is now being prepared. It will use cryogenic scintillators [9, 10], with simultaneous measurement of the phonon and scintillation light to reduce the background from local radioactivity and provide improved sensitivity for high-mass WIMPs.

ACKNOWLEDGMENTS

This work was supported by the DFG SFB 375 "Particle Astrophysics," the EU Network "Cryogenic Detectors" (contract no. ERBFMRXCT980167), BMBF, PPARC, and two EU Marie Curie Fellowships.

REFERENCES

1. CRESST Collab. (M. Bühler *et al.*), Nucl. Instrum. Methods Phys. Res. A **370**, 237 (1996).
2. CRESST Collab. (M. Sisti, O. Meier, *et al.*), Nucl. Instrum. Methods Phys. Res. A **466**, 499 (2001).
3. CRESST Collab. (M. Altmann *et al.*), astro-ph/0106314.
4. J. Ellis and R. A. Flores, Phys. Lett. B **263**, 259 (1991).
5. EDELWEISS Collab. (A. de Bellefon *et al.*), Astropart. Phys. **6**, 35 (1996).
6. DAMA Collab. (R. Bernabei *et al.*), Phys. Lett. B **389**, 757 (1996).
7. UKDMC Collab. (N. Spooner *et al.*), Phys. Lett. B **473**, 330 (2000).
8. J. Engel *et al.*, Phys. Rev. C **52**, 2216 (1995).
9. P. Meunier *et al.*, Appl. Phys. Lett. **75**, 1335 (1999).
10. CRESST Collab. (M. Bravin *et al.*), Astropart. Phys. **12**, 107 (1999).

Physics of Atomic Nuclei, Vol. 66, No. 3, 2003, pp. 497–499. From Yadernaya Fizika, Vol. 66, No. 3, 2003, pp. 524–526.

Development of a Two-Phase Xenon Dark Matter Detector*

D. Yu. Akimov**, **A. Bewick**[1], **M. V. Danilov**, **D. C. R. Davidge**[1], **J. V. Dawson**[1], **V. A. Ditlov**, **J. R. Gillespie**[1,2], **A. S. Howard**[1], **W. G. Jones**[1], **M. K. Joshi**[1], **A. G. Kovalenko**, **D. A. Kovalenko**, **V. N. Lebedenko**[3], **T. J. Sumner**[1], and **J. J. Quenby**[1]

Institute of Theoretical and Experimental Physics, Bol'shaya Cheremushkinskaya ul. 25, Moscow, 117259 Russia

Received April 17, 2002

Abstract—The current status of the development study focused on building a novel two-phase xenon detector for dark matter search is described. Discrimination of the radioactive background is based on particle identification that comes from the analysis of the scintillation-to-ionization ratio. Electroluminescence (proportional scintillation) is used for "amplification" of the ionization signal. © *2003 MAIK "Nauka/Interperiodica".*

1. INTRODUCTION

Worldwide efforts in searching for dark matter particles (WIMPs) by detection of low-energy nuclear/atomic recoils produced in detector targets are in progress now with the use of various kinds of detectors (see, for example, reviews [1, 2]). A two-phase xenon detector principle [3, 4] promises good gamma and electron (γ/e) background rejection. Discrimination between different kinds of particles is based on comparison of the fractions of energy deposition that go to the scintillation and ionization channels. Gammas and electrons produce a comparable number of scintillation photons and ionization electrons, while for the Xe recoils the ionization yield is strongly suppressed due to recombination. There are experimental data [5] showing that, for recoils from neutrons (which should be similar to those from WIMPs), the scintillation signal is more than one order of magnitude higher than the ionization one. Actually, no ionization signal was detected in the experiment [5], but the electric field was quite low (few hundred V/cm). The aim of the current study is to look for the ionization signal at a higher (~ 4 kV/cm) field.

2. WIMP DETECTION BY TWO-PHASE XENON

There are two ultraviolet (UV) signals recorded by photomultipliers in a two-phase (liquid/gas) xenon system. The first one (scintillation, SC) is directly produced by particles in liquid xenon (LXe). The second one is obtained by the following process: The ionization electrons drift towards the surface of the liquid, and there they are extracted to the gas phase. In the gas gap above the liquid, the region with a high electric field, these electrons produce electroluminescence (EL) (Fig. 1). EL produces hundreds of UV photons per electron of ionization and serves as a proportional measure of ionization.

In building the ZEPLIN III detector [6], we follow the conceptual design proposed in [3]. The basic principles are the thin-disk geometry of the sensitive volume (target) and immersion of photomultipliers (viewing upward) in liquid xenon. Both significantly increase the light collection, giving the low-energy threshold.

In order to set the final detector design parameters, two prototype/test chambers have been built. The inner part of the ITEP development chamber (Fig. 1) is a small prototype of a full-scale detection system. An array of seven compact photomultipliers (PMTs) [(*4*) in Fig. 1], HAMAMATSU R7400U-06, is used for UV light collection. The sensitive volume of the ITEP chamber is between the top electrode (*1*) (anode), which is a polished Al mirror, and the grid cathode (*2*). There is a screening grid electrode (*3*) with electrical potential equal to that of the photocathodes. An ^{241}Am radioactive source is placed in the center of the cathode (*2*). The LXe thickness between the

*This article was submitted by the authors in English.

[1]Physics Department, Imperial College of Science Technology and Medicine (ICSTM), London, UK.

[2]Department of Physics and Astronomy, Lehman College of CUNY, Bronx, NY, USA.

[3]Institute of Theoretical and Experimental Physics, Bol'shaya Cheremushkinskaya ul. 25, Moscow, 117259 Russia, and ICSTM, London, UK.

**e-mail: akimov_d@itep1.itep.ru

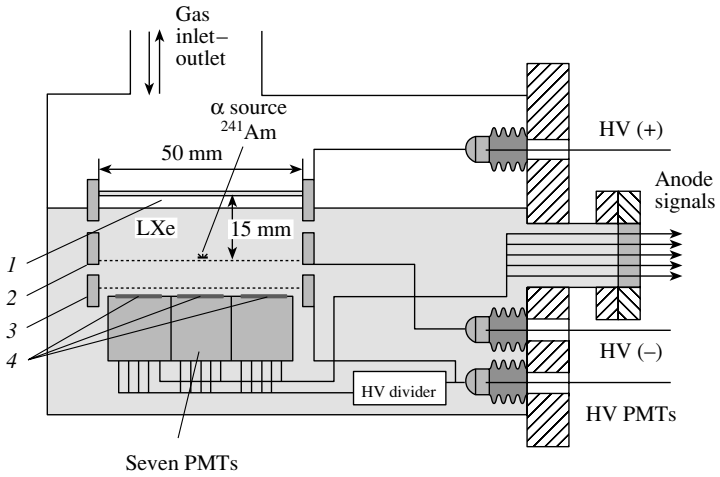

Fig. 1. ITEP two-phase Xe test chamber. For details see the text.

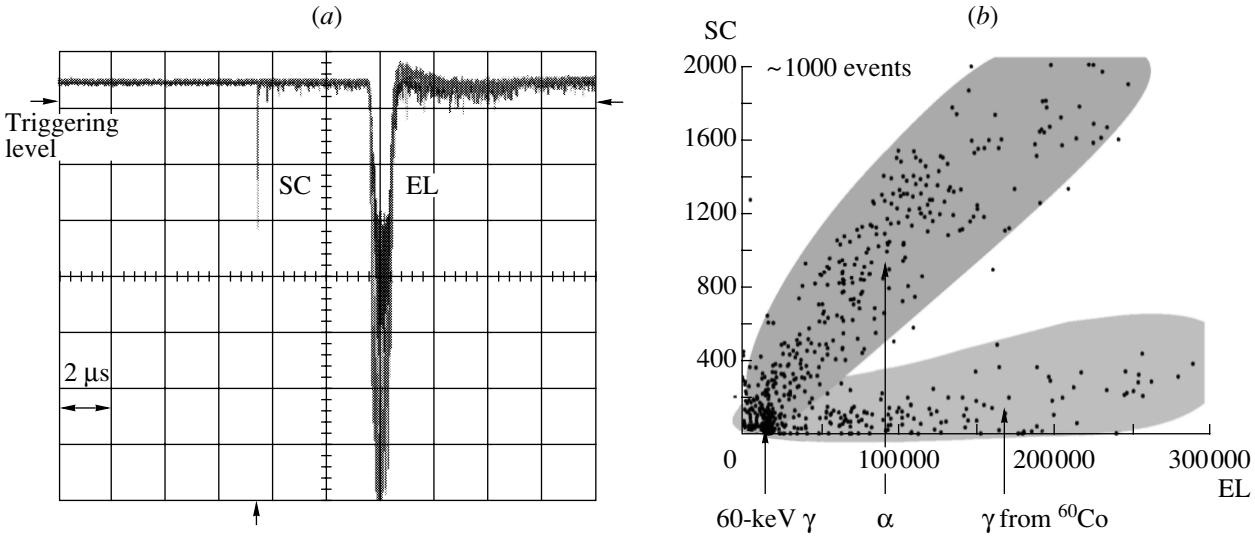

Fig. 2. (*a*) Combined signal from four channels of the LT344 oscilloscope and (*b*) the scatter plot for the SC and EL signals.

cathode and the anode is 10 mm, and the EL gap is 5 mm. A similar construction of electrodes with approximately the same size is utilized in the Imperial College chamber [7]. A single 2-in. ETL 9829QA quartz-windowed PMT located at the bottom is used for UV light detection.

The high voltage of up to ~10 kV is applied between electrodes (*1*) and (*2*) to ensure an electric field (~10 kV/cm in the gas phase) sufficient for extraction of the electrons from the LXe surface and for a high EL yield of ~200 UV photons per extracted electron.

The ITEP test chamber readout is based on a digital four-channel LeCroy LT344 oscilloscope (500 Ms/s). To match the number of PMTs (seven) to the number of oscilloscope inputs (four), the signals from the peripheral PMT pairs are summed, while the signal from the central one goes to an individual input.

Multichannel detection of light allows us to reconstruct a 3D position of the event. It helps to introduce additional criteria of background rejection in a low-background experiment, i.e., to exclude undesirable surface and near-wall events. Development of the reconstruction procedure for the two-phase xenon system is in progress now.

At ITEP, the purification system consists of Ca and Ti hot getters. At ICSTM, a slow distillation procedure and OXISORB purifier are used. Both purification systems provide LXe with electron drift length much greater than the distance between the electrode (*2*) and the LXe surface.

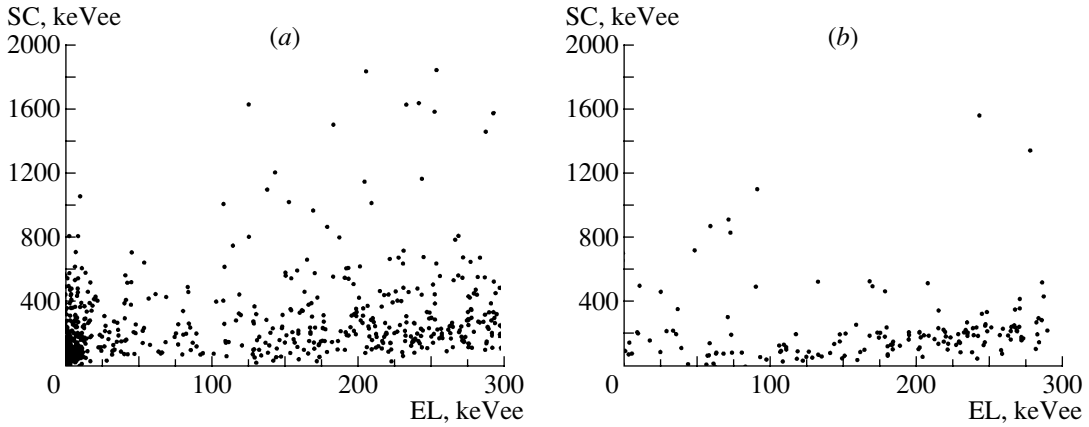

Fig. 3. Scatter plots of SC vs. EL: (*a*) neutron test and (*b*) control test with external ^{22}Na source (keVee is keV of electron equivalent).

3. EXPERIMENTAL TESTS

The typical recorded ^{241}Am alpha event is shown in Fig. 2*a*. The scintillation signal is followed by the intense electroluminescent one in 4.5 μs, the drift time from the location of the source to the LXe surface. A similar signal structure but with relatively small SC is obtained for gammas. A two-dimensional scatter plot of SC and EL signals shown in Fig. 2*b* demonstrates separation of particles with different ionization yield. Note that the real SC signal for alphas is significantly greater because the direct scintillation light from the ^{241}Am source is screened by the substrate.

The first laboratory test was carried out with a 14-MeV (d–t) neutron generator. To ensure a narrow beam, 1-m-thick water and 0.5-m-thick paraffin collimators were used. Such neutrons produce Xe recoils with a maximum energy of $\sim$ 420 keV. The angular distribution of elastically scattered neutrons has predominant wide peaks at 0° and $\sim$ 45° [8] (the latter corresponds to $\sim$ 60 keV of the recoils). Two 2D scatter plots of SC and EL signals are shown in Fig. 3*a* for the neutron test and in Fig. 3*b* for the control test with the external ^{22}Na source. It is important that the external triggering of the readout electronics was used in both cases for exclusion of any threshold effect. No additional angular selection of scattered neutrons was used. There is a clearly distinguishable population of events at low energies (below 20 keV on EL) in Fig. 3*a,* and this area is rather clean in Fig. 3*b*. It is clear that these events originate from the neutron source and indicate that recoil ionization may be occurring. The population corresponds to the 45° peak of scattered neutrons (five events recorded in the separate test in coincidences with scattered neutrons detected at 45° lie in this region). Zero-degree peak events are under the threshold: they have very low SC and, therefore, are not selected to the plot. The "visible" energy corresponding to the center of gravity of this distribution (in the one-dimensional projection on the EL axis) is approximately 5 keV e.e. Although the population is distinct, the primary scintillation signal is much larger than expected. Further investigation is going on to understand the origin of these events and carefully measure the level of recoil ionization.

ACKNOWLEDGMENTS

This work was supported by INTAS (grant no. 97-2082) and the Russian Foundation for Basic Research (project no. 01-02-17267). It was also supported by PPARC (the UK Particle Physics and Astronomy Research Council) and by the Royal Society (UK).

REFERENCES

1. L. Baudis and H. V. Klapdor-Kleingrothaus, astro-ph/0003434.
2. N. Smith and N. Spooner, Phys. World **13**, 23 (2000).
3. D. Akimov *et al.*, in *Sources and Detection of Dark Matter in the Universe*, Ed. by D. B. Cline (Elsevier, Berlin, 1998), p. 461.
4. H. Wang, Phys. Rep. **307**, 263 (1998).
5. D. Cline *et al.*, Astropart. Phys. **12**, 373 (2000).
6. T. J. Sumner *et al.*, in *Proceedings of the IDM2000, York, UK,* Ed. by N. J. C. Spooner and V. Kudryavtsev (World Sci., Singapore, 2000), p. 452.
7. A. S. Howard *et al.*, in *Proceedings of the IDM2000, York, UK,* Ed. by N. J. C. Spooner and V. Kudryavtsev (World Sci., Singapore, 2000), p. 457; T. J. Sumner *et al.*, in *Proceedings of the 26th International Cosmic Ray Conference (ICRC 99), Salt Lake City, Utah,* 1999, Vol. 2, p. 516.
8. *T-2 Nuclear Information Service,* http://t2.lanl.gov.

Physics of Atomic Nuclei, Vol. 66, No. 3, 2003, pp. 500–502. From Yadernaya Fizika, Vol. 66, No. 3, 2003, pp. 527–529.

Observation of Primary and Secondary (Proportional) Scintillation in Two-Phase Xenon Detector*

V. N. Afanasiev†, V. V. Barmin, A. A. Burenkov, V. I. Demekhin, A. G. Dolgolenko, A. S. Gerasimov, V. S. Goryachev, Yu. I. Povarov, V. A. Shebanov, G. N. Smirnov, L. I. Sokolov, A. P. Solovjev, G. K. Tumanov, and S. M. Zombkovsky**

Institute of Theoretical and Experimental Physics, Bol'shaya Cheremushkinskaya ul. 25, Moscow, 117259 Russia

Received April 17, 2002

Abstract—A half-liter two-phase xenon chamber was built and primary and secondary (proportional) scintillation signals were investigated by using α particles. The energy threshold in the chamber was less than 50 keV of electron equivalent and energy resolution was 18%. The value of the spatial (Z-coordinate) resolution achieved in the time projection chamber was about 0.4 mm. © *2003 MAIK "Nauka/Interperiodica".*

1. INTRODUCTION

We have recently proposed the use of a large-volume (0.25 m^3, 750 kg of Xe) two-phase xenon time projection chamber (TPC) for experimental study of $\bar{\nu}_e e^-$ scattering with the threshold of 0.1 MeV on the electron recoil energy at the nuclear power reactor [1]. The TPC will be started by fast scintillation light, abundantly produced by a particle in liquid xenon, and stopped by electroluminescent light, produced by ionization electrons extracted from liquid xenon in the gas phase. A matrix of photomultiplier tubes (PMTs) will determine the spatial coordinates and energy of each event by electroluminescent light.

The proposed parameters of the detector are as follows: energy threshold of 100 keV; energy resolution for 100-keV electrons about 15%; space localization of $\bar{\nu}_e e^-$-scattering events about 2–3 mm. The sensitivity to the magnetic moment $\mu_\nu = (3–5) \times 10^{-11}\,\mu_B$ can be achieved. A one-channel model of the proposed detector is tested.

2. EXPERIMENTAL APPARATUS

A schematic diagram of the setup used for the primary and secondary scintillation studies in liquid and gaseous xenon is shown in Fig. 1. The detector is composed of an electrode assembly and a UV-sensitive PMT (FEU-39 by MELZ) optically coupled to the chamber through a quartz window. The electrode assembly functionally consists of two parts: a drift assembly with a 66 (13 + 53) mm gap between the cathode and the anode and another electroluminescent gap formed by two grids placed in liquid–gas phases of xenon. They have a 1-mm square mesh made of 0.1-mm-diameter stainless steel wires. The diameter of the electroluminescent grids is 25 mm. The width of the electroluminescent gap is 6 mm.

The field in the drift region is made uniform by a series of stainless steel rings spaced 9 mm apart. A divider chain of 30-MΩ resistors gives the voltage to the rings. Two ^{241}Am α sources are located in the chamber. These α sources were embedded into

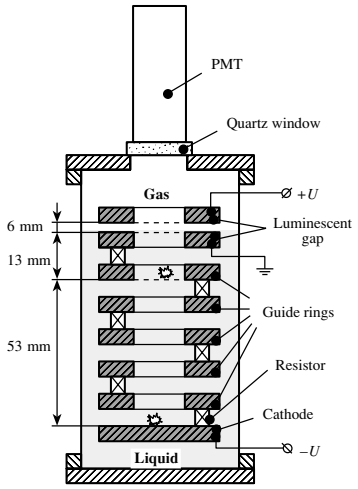

Fig. 1. Schematic view of the two-phase xenon chamber. Stars are ^{241}Am sources.

*This article was submitted by the authors in English.

†Deceased.

**e-mail: Alexander.Burenkov@itep.ru

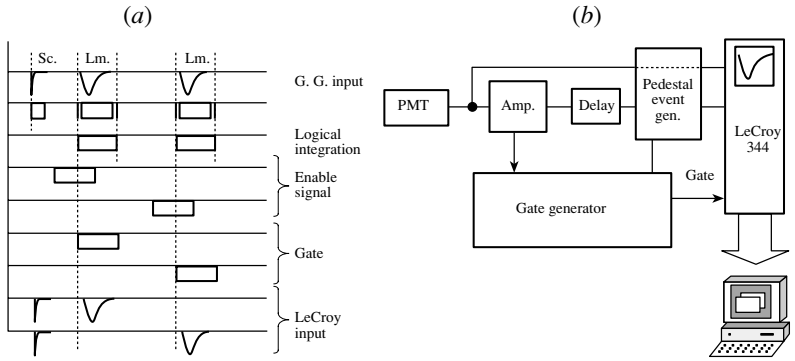

Fig. 2. (*a*) Diagram of signals. (*b*) Block diagram of electronic circuits.

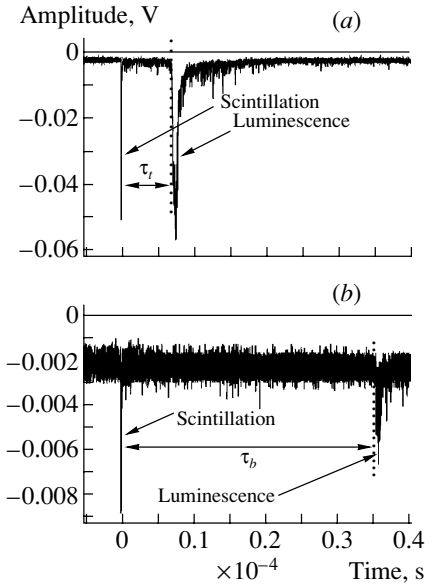

Fig. 3. Oscillograms of typical scintillation and electroluminescence pulses produced by (*a*) the top α source and (*b*) the bottom alpha source with an electric field of 1.2 kV/cm applied to the electron drift space.

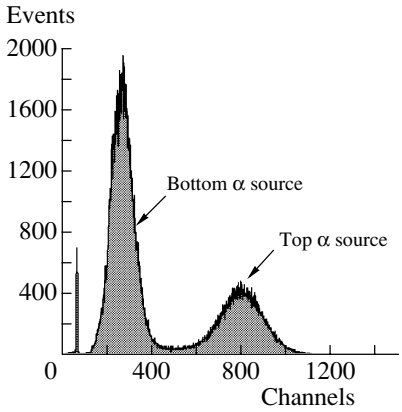

Fig. 4. ^{241}Am energy spectrum obtained from the scintillation in liquid xenon.

2×2 mm mylar film. The bottom α source (85 Bq) is placed on the central part of the cathode, and the top α source (65 Bq) is placed on the central part of the upper guide ring of the drift gap.

Before the chamber was filled with xenon, the gas filling system and the chamber were baked and pumped out to a pressure less than 10^{-6} torr. After that, the outgassing rate of the chamber was assured to be less than 5×10^{-10} torr l/s. The xenon was purified by an electrosparking titanium purifier.

Liquid nitrogen was used for liquefaction of gaseous xenon and kept the chamber at 186 K with a one-degree accuracy. The level of liquid xenon was determined by measuring the capacitance between the electroluminescent gap rings and was kept 1 mm above the bottom grid of the electroluminescent gap.

The anode pulse of the photomultiplier was fed to the amplifier and then to the gate generator, which formed a gate if the input analog signal coincided with the external enable signal in time. This signal was used as an external gate for the oscilloscope. The anode pulse of the photomultiplier was observed with a LeCroy 344 digital oscilloscope and stored on a PC hard disk. A block diagram of the electronic circuits is shown in Fig. 2.

3. RESULTS AND DISCUSSION

Figures 3*a* and 3*b* show the typical anode pulse of the PMT corresponding to the time dependence of scintillation and electroluminescence of xenon excited by an α particle from the top and bottom α sources, respectively. In both figures, the first pulses correspond to primary (direct) scintillation produced by the α particle in liquid xenon. The second pulses correspond to proportional scintillation (electroluminescence) produced by ionization electrons extracted by a strong electric field from the liquid phase into the gas phase.

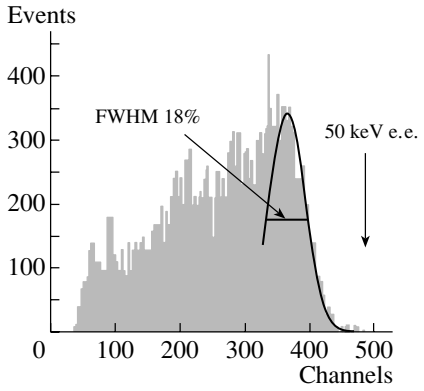

Fig. 5. ^{241}Am energy spectrum obtained from the electroluminescence in the gas phase of xenon.

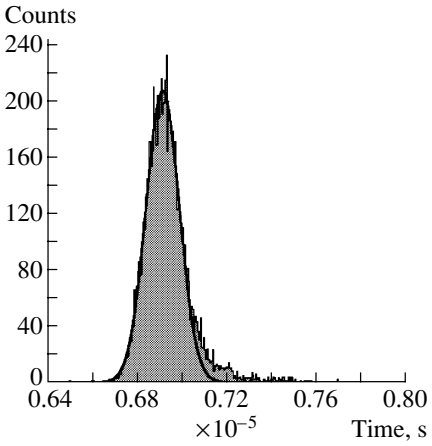

Fig. 6. Appearance time τ_t of electroluminescent signal from the top α source.

Figure 4 shows typical scintillation pulse-height spectra due to α particles. As can be seen from Fig. 4, the energy spectrum is well represented by two quasi-Gaussian distributions with FWHM of 24% for the top α source and 45% for the bottom α source. The quite bad resolution is connected with loss of light due to geometric factors, quantum efficiency of the photocathode of PMT, and transparency of the quartz window. In energy measurement by electron ionization, such kind of losses could be compensated on the whole by electroluminescent gain. The number of generated electroluminescence photons $N_{\rm ph}$ per ionization electron is described by a semiempirical equation [2]: $N_{\rm ph} = 70(E/p - 0.8)dp$, where E is the electric field strength in the electroluminescent gap in kV/cm, p is the gas pressure in bars, and d is the depth of the electroluminescent gap in centimeters. In our case ($E = 1.2$ kV/cm, $p = 3$ bar, $d = 0.5$ cm), the gain factor is about 400.

The energy spectrum obtained from the electroluminescent signal for the top α source is shown in Fig. 5, which represents the energy distribution at the applied electric field of 1.2 kV/cm. At this field strength, the electron yield from the α trace is 1.2% [3, 4]. In our case, this corresponds to energy deposition of about 50 keV electron equivalent (e.e.). As is shown in the figure, the sensitivity of the detector is better than 50 keV e.e. and the width of the distribution is determined almost completely by the energy spectra of α particles from ^{241}Am nuclei embedded in mylar. The figure also shows the energy resolution for ~40 keV e.e. defined on the right end. It should be noted that the result presented in the figure was obtained with not very good purity of xenon. We estimated the level of impurities to be ~10 ppb on O_2 (lifetime of drift electron was about 15 μs). It is obvious that improvement of xenon purity will result in a better energy resolution. From the width distribution for the appearance time of the electroluminescent signal (from top α source) shown in Fig. 6 and the electron drift velocity of 1.86×10^5 obtained from Fig. 3, we estimated the spatial resolution of our detector for the Z coordinate to be 0.4 mm.

4. CONCLUSION

A half-liter two-phase xenon chamber was built and primary and secondary (proportional) scintillation signals were investigated by using α particles. The energy threshold in the chamber was less than 50 keV e.e. and the energy resolution was 18%. The value of the spatial (Z-coordinate) resolution achieved in the TPC was about 0.4 mm.

The results confirm that it is possible to create a large-volume two-phase xenon detector for measurement of the neutrino magnetic moment with a sensitivity equal to $(3–5) \times 10^{-11}$ $\mu_{\rm B}$.

ACKNOWLEDGMENTS

The research work presented in this report was made possible in part by the Russian Foundation for Basic Research (project no. 00-02-16344) and by the International Science Foundation (grant N 81000).

REFERENCES

1. M. Baldo-Ceolin *et al.*, in *Proceedings of the III International Symposium on WEIN 92* (World Sci., Singapore, 1992), p. 735; Preprint No. 35, ITEP (Moscow, 1992).
2. A. Parsons *et al.*, IEEE Trans. Nucl. Sci. **37**, 541 (1990); H. Brauning *et al.*, Nucl. Instrum. Methods Phys. Res. A **348**, 223 (1994); A. Bolozdynya *et al.*, Nucl. Instrum. Methods Phys. Res. A **385**, 225 (1997).
3. B. A. Dolgoshein *et al.*, Fiz. Élem. Chastits At. Yadra **4**, 167 (1973).
4. E. Aprile *et al.*, IEEE Trans. Nucl. Sci. **37**, 553 (1990).

Physics of Atomic Nuclei, Vol. 66, No. 3, 2003, pp. 503–508. From Yadernaya Fizika, Vol. 66, No. 3, 2003, pp. 530–535.

HIGH ENERGY NEUTRINOS

The Lake Baikal Neutrino Experiment*

V. A. Balkanov, I. A. Belolaptikov[1], L. B. Bezrukov, N. M. Budnev[2], A. G. Chensky[2], I. A. Danilchenko, Zh.-A. M. Dzhilkibaev, G. V. Domogatsky, S. V. Fialkovsky[3], O. N. Gaponenko, O. A. Gress[2], T. I. Gress[2], R. V. Il'yasov, A. M. Klabukov, A. I. Klimov[4], S. I. Klimushin, A. P. Koshechkin, K. V. Konischev, V. F. Kulepov[3], L. A. Kuzmichev[5], Vy. E. Kuznetsov, B. K. Lubsandorzhiev, S. P. Micheev, M. B. Milenin[3], R. R. Mirgazov[2], N. I. Moseiko[5], E. A. Osipova[5], A. I. Panfilov, L. V. Pan'kov[2], Yu. V. Parfenov[2], A. A. Pavlov[2], E. N. Pliskovsky[1], P. G. Pokhil, V. A. Poleshuk, E. G. Popova[5], V. V. Prosin[5], M. I. Rosanov[6], V. Yu. Rubzov[2], Yu. A. Semenei[2], Ch. Spiering[7], O. Streicher[7], B. A. Tarashansky[2], R. V. Vasiliev, R. Wischnewski[7], I. V. Yashin[5], and V. A. Zhukov**

Institute for Nuclear Research, Russian Academy of Sciences, pr. Shestidesyatiletiya Oktyabrya 7a, Moscow, 117312 Russia

Received April 17, 2002

Abstract—We review the present status of the Baikal neutrino experiment. The structure and parameters of the neutrino telescope NT-200, which was put into operation in April 1998, are described. Selected methodological results are presented. Physics results cover separating up-going muons from atmospheric neutrinos, searches for neutrino events from WIMP annihilation, searches for magnetic monopoles, and high-energy neutrinos. © *2003 MAIK "Nauka/Interperiodica".*

1. INTRODUCTION

The idea to detect the Cherenkov light emitted by particles in neutrino interactions in big water basins was proposed in 1960 [1]. The scientific goals of underwater telescopes are manifold. Observation of high-energy neutrinos are of particular importance for neutrino astronomy to shed light on the physics of active galactic nuclei (AGN), binary star systems, and gamma ray bursts (GRB). Beyond the field of neutrino astronomy, the diverse scientific missions of underwater telescopes include the search for neutrinos emerging from annihilation of weakly interacting massive particles (WIMPs) in the center of the Earth or the Sun [2] and the search for bright objects like relativistic magnetic monopoles. They can contribute to such different fields like atmospheric muon physics, on one hand, and limnology, on the other hand. The possibility build a neutrino telescope at the Lake Baikal has been under investigation since 1980, with Chudakov's basic suggestion to use, instead of a ship, the winter ice cover of the lake as a platform for easy deployment and retrieval of detector components in late winter. The Baikal neutrino experiment spans almost two decades, from the first small experiment with a few photomultiplier tubes (PMTs) to the present large-scale neutrino telescope NT-200 [3], which was put into full operation in April 1998.

2. NEUTRINO TELESCOPE NT-200

2.1. Detector and Site

The neutrino telescope NT-200 [3] is located in the southern part of Lake Baikal (51.5° N and 104.2° E), 3.6 km from the shore and at the depth of 1 km. The optical parameters of water at the depth of the detector have been measured with special instruments over many years. The absorption length for wavelengths

*This article was submitted by the authors in English.

[1]Joint Institute for Nuclear Research, Dubna, Moscow oblast, 141980 Russia.
[2]Irkutsk State University, Irkutsk, Russia.
[3]Nizhni Novgorod State Technical University, ul. Lenina 24, Nizhni Novgorod, 603600 Russia.
[4]Russian Research Centre Kurchatov Institute, pl. Kurchatova 1, Moscow, 123182 Russia.
[5]Skobeltsyn Research Institute of Nuclear Physics, Moscow State University, Vorob'evy gory, Moscow, 119899 Russia.
[6]St. Petersburg State Marine Technical University, ul. Lotsmanskaya 3, St. Petersburg, 190008 Russia.
[7]DESY—Institut für Hochenergiephysik Zeuthen, Germany.
**e-mail: domogats@pcbai10.inr.ruhep.ru

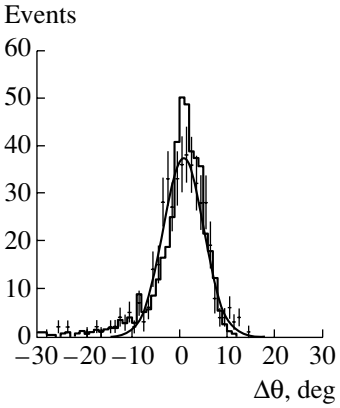

Fig. 1. Distribution of the difference of the zenith angles reconstructed by the EAS array and by the NT-200.

between 470 and 500 nm is about 20 m, and its seasonal variations are less than 20%. The light scattering is strongly anisotropic. The mean cosine of the scattering length is between 0.85–0.95. The typical scattering length is about 50 m, and it is strongly subjected to seasonal and annual variations. The water luminescence shows strong seasonal variation with typical values of 250 Hz on a 1-cm^2 phototube. The variations of the counting rates due to water luminescence allow investigation of limnological issues like the seasonal change in water currents.

The NT-200 consists of 192 optical modules (OMs) on eight strings arranged in an umbrella-like frame. Three underwater electrical cables and an optical cable connect the detector with the shore station. Pairs of OMs are switched in coincidence with a 15-ns time window and define a channel. The OM [4] consists of a Quasar-370 phototube [5, 6] enclosed in a transparent, nearly spherical pressure housing. Apart from the phototube, every OM contains two high-voltage (25 and 2 kV) power supplies, a voltage divider, two preamplifiers, a calibration light emitting diode (LED), and a vacuum probe. The Quasar-370 phototube has been developed specially for the Lake Baikal neutrino experiment by the Institute for Nuclear Research (Moscow) and the KATOD Company in Novosibirsk. The phototube is a hybrid one and has excellent time and amplitude resolutions. A muon trigger is formed by the requirement of more than N fired channels within 500 ns, where N is typically set to 3 or 4. For such events, the amplitude and time of all fired channels are digitized and sent to the shore. A separate monopole trigger system searches for clusters of sequential hits in individual channels, which are characteristic of the passage of slowly moving, bright objects like GUT monopoles. The calibration of the relative time shifts between all channels is performed with the help of a nitrogen laser positioned above the array. The light from this laser is guided by optical fibers of equal length separately to each OM pair. A special second laser emitting light directly through the water was mounted on the central string 20 m below the last layer of OMs. Measuring the arrival time of laser light pulses on the channels permits us to determine the group light velocity in water with a high accuracy at the depth of 1 km [7]. It is equal to $(2.178 \pm 0.014) \times 10^{10}$ cm/s and is in agreement with the calculation [8].

2.2. Study of Water Parameters

There is a separate hydrological string at a distance about 60 m from the main part of the NT-200 to study the water parameters of the lake on a permanent basis. Since good knowledge of these parameters is essential for underwater neutrino experiments, independent measurements of the NEMO group were performed during the last expedition. Preliminary results indicate that the two independent sets of optical data are compatible.

2.3. Technology Test String

A special string for diverse goals was operated in the course of the expedition in 2001. With instruments on this string, we measured the group velocity of light in water at two different wavelengths and tested the two-channel optical module [9] and the calibration light beacon [10].

3. SELECTED METHODOLOGICAL RESULTS

3.1. Study of Telescope Angular Resolution

During three winter seasons, starting in 1998, a Cherenkov array for registration of extensive atmospheric showers (EAS), consisting of four Quasar-370 phototubes, was deployed on the ice, just above the underwater telescope, with the aim to study the angular resolution of the latter. The angular resolution of the EAS array is better than 1°. The full statistics of coincidence events is nearly 600. The main part of these events have a zenith angle smaller than 15°. Due to the relatively high-energy threshold of the EAS array (200 TeV), nearly all these events are multimuon events. For such events, our standard track reconstruction procedure [11] does not work properly, but the zenith angles of nearly vertical multimuon events can be reconstructed under the assumption that OMs along a single string are mostly illuminated by only one of these muons. Figure 1 shows the distribution of the difference of the zenith angles reconstructed by the EAS array and by the underwater telescope (points) and the expected one from the MC calculation (histogram). The number of hit channels

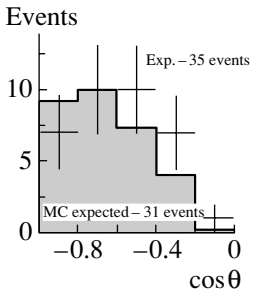

Fig. 2. Experimental angular distribution of reconstructed upward-going muons in the NT-200. The filled histogram is the MC expectation.

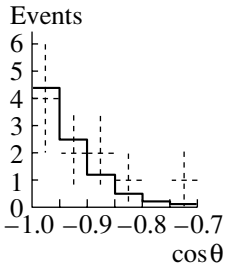

Fig. 3. Zenith angular distribution of nearly vertically upward neutrino candidates as well as MC expectation for atmospheric neutrino-induced muons (histogram).

was requested to be ≥ 5. The distribution can be fitted by a Gaussian distribution with $\sigma = 4.3°$. This value decreases slightly (to 3.8°) if only events with ≥ 6 hit channels at one string are used. From this analysis, we can conclude that the angular resolution of the underwater telescope for vertical muons is about 4°.

3.2. Study of Acoustic Signals from EAS

In 2000, we began to study the possibility of registration of acoustic signals from the EAS in water or ice at Baikal. For this purpose, the EAS scintillator array was used as a trigger system. The core of the EAS triggering the scintillator array is expected to lead to an acoustic signal in the ice or in the upper water slice. An acoustic hydrophone was placed 90 m away from the center of the EAS array at the depth of 5 m. A characteristic bipolar acoustic signal with a 150-μs duration and with a reasonable delay time compared to the EAS trigger was detected. A preliminary analysis shows that the amplitude of the acoustic signals is somewhat larger than would be expected from the standard thermoacoustic theory [12]. The source of this disagreement maybe lies in uncertaintes in hydrophone calibration and in high noise level. In winter 2001, we continued to study the feasibility of acoustic detection of EAS cores. The EAS array was deployed at a distance of 1.5 km from the main ice camp in order to decrease the electromagnetic and acoustic cross talks on the hydrophones. The EAS array consisted of seven scintillators with an area of 0.5 m^2 each. Six detectors were placed at the corners of a hexagon and one in the center. The distances between the central and the peripheral detectors were 80 m. Four hydrophones were placed 34 m away from the center of the EAS array at a depth of 5 m.[8)] During the EAS array lifetime of 154 h, nearly 2400 showers with energies above 5 PeV were recorded. The coincidence data of the EAS array and hydrophones are being analyzed.

[8)]The acoustic antenna was additionally installed by the ITEP team (Moscow) 20 m away from the center of the EAS array.

4. PHYSICS RESULTS

4.1. Separation of Fully Reconstructed Neutrino Events

The signature of neutrino-induced events is a muon crossing the detector from below. The reconstruction algorithm is based on the assumption that the light radiated by the muons is emitted under the Cherenkov angle with respect to the muon path. The algorithm uses a single-muon model to reconstruct events. We first reject hits that are likely to be due to dark current or water luminescence, as well as hits which are due to showers and have large time delays with respect to the expected hit times from single-muon Cherenkov light. The reconstruction yields a fraction of about 4.6×10^{-2} of triggered events that are reconstructed as upward going, with the trigger $\geq 6/3$ (at least six hits on at least three strings). This is still far from the suppression factor of 10^{-6} necessary for the depth of the NT-200. To reject most of the wrongly reconstructed events, we use a set of quality cuts [13]. If the event does not obey any of the chosen criteria, it is rejected as wrongly reconstructed. The efficiency of the procedure and correctness of the MC background estimation were tested with a sample of 2.8×10^6 MC-generated atmospheric muons and with MC-generated upward-going muons due to atmospheric neutrinos. For this MC sample, none of the MC background events passed all cuts. The data taken with the NT-200 between April 1998 and February 1999 cover the 234 days lifetime. For this period, we got 5.3×10^7 events with the trigger $\geq 6/3$. The set of the above criteria was applied to this sample, yielding 35 events that passed all of them. This number is in good agreement with 31 events expected from neutrino-induced muons for this period. The reconstructed angular distribution for upward-going muons from the experimental sample after all cuts is shown in Fig. 2.

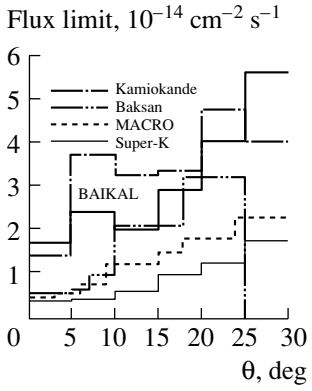

Fig. 4. Comparison of BAIKAL limits on nearly vertically upward muons with those from other experiments.

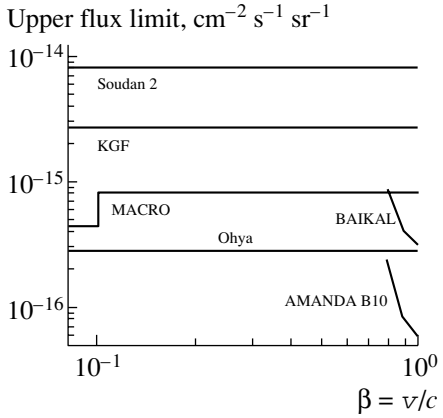

Fig. 5. Upper limits on the flux of fast monopoles obtained in different experiments.

4.2. Identification of Nearly Vertically Upward Moving Muons

The search for WIMPs with the Baikal neutrino telescope is based on the search for a statistically significant excess of neutrino-induced, nearly vertically upward going muons, compared to the expectation for atmospheric neutrinos. In contrast to the standard analysis described in the previous section, the method of event selection relies on the application of a series of cuts that are tailored to the response of the telescope to nearly vertically upward moving muons [14]. The candidates identified by the cuts are fitted afterward in order to determine their zenith angles. For the present analysis, we included all events with $\geq$6 hit channels, with at least one string containing $\geq$4 hits. A series of six cuts is applied to this sample. The effective area of the full-scale neutrino telescope NT-200 for muons with energy $E_\mu > 10$ GeV, which move close to the opposite zenith and fulfill all cuts, exceeds 2500 m^2. After applying all cuts, 10 events were selected as neutrino candidates, compared to 8.9 expected from atmospheric neutrinos. The reconstructed angular distribution for upward-going muons from the experimental sample after all cuts is shown in Fig. 3. Regarding the 10 detected events as being due to atmospheric neutrinos, one can derive an upper limit on the flux of muons from the center of the Earth due to annihilation of neutralinos—a candidate for cold dark matter.

The comparison of BAIKAL flux limits with those obtained by Baksan [15, 16], MACRO [17], Kamiokande [18], and Super-Kamiokande [19] is shown in Fig. 4.

4.3. Search for Relativistic Magnetic Monopoles

Relativistic monopoles with the unit magnetic Dirac charge and velocities greater than the Cherenkov threshold in water ($\beta = v/c > 0.75$) are promising survey objects for underwater neutrino telescopes. For a given velocity β, the monopole Cherenkov radiation exceeds that of a relativistic muon by the factor $(gn/e)^2 = 8.3 \times 10^3$ ($n = 1.33$ is the index of refraction for water). The natural way to search for fast monopoles is based on selection of events with a high multiplicity of hits and high amplitudes. In order to reduce the background from downward atmospheric muons and especially atmospheric muon bundles, we restrict ourselves to monopoles coming from the lower hemisphere.

To select events from monopoles, in the present analysis of the data from the first 234 live days of NT-200, we used cuts on the number of hit channels, on the value of the Z-time correlation, and on the time difference of hit channels and the amplitude in the two channels with the maximum amplitudes [20]. There are no events that survive all cuts. Using the MC calculated acceptance of the NT-200, a 90% C.L. upper limit on the monopole flux has been obtained.

The combined upper limit for an isotropic flux of bare fast magnetic monopoles obtained with the NT-36, NT-96, and NT-200 and the limits from the underground experiments MACRO [21], Soudan2 [22], KGF (Kolar Gold Field) [23], Ohya [24], and AMANDA [25] are shown in Fig. 5.

4.4. Search for High-Energy Neutrinos

The search strategy for high-energy neutrinos relies on the detection of the Cherenkov light emitted by the electromagnetic and (or) hadronic particle cascades and high-energy muons produced at the neutrino telescope. Neutrinos produce showers via CC(NC) interactions with nucleons as well as via resonance production with the resonant energy $E_0 = M_w^2/2m_e = 6.3 \times 10^6$ GeV and cross section of 5.02×10^{-31} cm^2, in the case of electron antineutrino.

We select events with a high multiplicity of hit channels $N_{\rm hit}$ corresponding to bright cascades. The volume considered for generation of cascades is significantly below the geometrical volume of the NT-200. A cut is applied that accepts only time patterns corresponding to the upward-traveling light signal. This cut rejects most events from bremsstrahlung cascades produced by downward-going muons since the majority of muons are close to the vertical; they would cross the detector and generate a downward pattern. Within 234 days of the detector lifetime, 1.67×10^8 events with $N_{\rm hit} \geq 4$ have been selected. For this analysis, we have used events with $N_{\rm hit} \geq 10$. The experimental distribution of the number of hit channels is consistent with what is expected from bremsstrahlung and hadronic showers produced by atmospheric muons for $N_{\rm hit} \geq 18$. Since no events with $N_{\rm hit} \geq 45$ are found in our data, we can derive upper limits on the flux of high-energy neutrinos that produce events with $N_{\rm hit} \geq 50$. The detection volume for neutrino-produced events that fulfill all trigger conditions rises from 2×10^5 m^3 for 10 TeV to 6×10^6 for 10^4 TeV and significantly exceeds the geometrical volume of the NT-200. Given the E^{-2} behavior of the neutrino spectrum and the flavor ratio $(\nu_e + \bar{\nu}_e) : (\nu_\mu + \bar{\nu}_\mu) = 1 : 2$, the combined 90% C.L. upper limit obtained with the NT-200 (234 d) and NT-96 (70 d) is

$$\frac{d\Phi_{(\nu_e+\bar{\nu}_e)}}{dE} E^2 < (1.3\text{–}1.9) \times 10^{-6}\ \text{cm}^{-2}\ \text{s}^{-1}\ \text{sr}^{-1}\ \text{GeV},$$

where the larger value refers to the conservative limit on light scattering in the Baikal water.

Figure 6 shows the upper limits on the isotropic diffuse neutrino flux obtained by BAIKAL, AMANDA [26], and Frejus [27] (triangle), as well as the atmospheric conventional neutrino fluxes from the horizontal and vertical directions [28] (upper and lower curves, respectively) and the atmospheric prompt neutrino flux [29]. Also shown is the model-independent upper limit on the diffuse high-energy neutrino flux obtained in [30] (curve labeled "B") and predictions for diffuse neutrino fluxes from [31] ("SS") and [32] ("P"). Curves labeled "MPR" and "WB" show the upper bound obtained in [33] and [34], respectively. Curves labeled "M(GRB)" and "WB(GRB)" present the upper bounds for the diffuse neutrino flux from GRBs derived in [35] and [36]. The curve labeled "TD" shows the prediction for the neutrino flux from topological defects due to the specific top-down scenario BHS1 [37]. Our combined 90% C.L. limit at the W-resonance energy is

$$\frac{d\Phi_{\bar{\nu}_e}}{dE} < (1.3\text{–}1.9) \times 10^{-19}\ \text{cm}^{-2}\ \text{s}^{-1}\ \text{sr}^{-1}\ \text{GeV}^{-1},$$

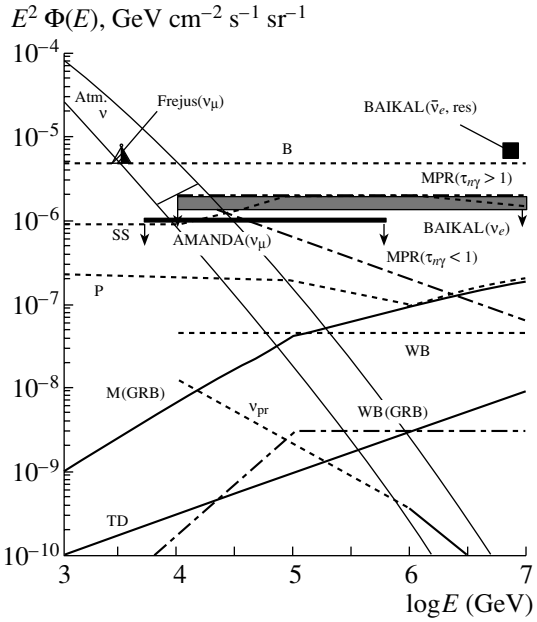

Fig. 6. Experimental upper limits on the neutrino fluxes as well as flux predictions in different of neutrino sources.

shown by the rectangle in Fig. 6.

5. CONCLUSIONS AND OUTLOOK

The deep underwater neutrino telescope NT-200 in Lake Baikal has been taking data since April 1998. It performs studies of atmospheric neutrinos and searches for WIMPs, magnetic monopoles, and extraterrestrial high-energy neutrinos. With an effective area two times larger than Super-Kamiokande, for nearly vertically upward muons ($E_\mu \geq 10$ GeV), the NT-200 will be one of the powerful arrays for indirect search for WIMP annihilation in the center of the Earth during the next few years. Due to high water transparency and low light scattering, the effective volume of the NT-200 for detection of high-energy electron and tau neutrinos considerably exceeds the geometric volume. This will permit a search for diffuse neutrino fluxes from AGN and other extraterrestrial sources at the level of theoretical predictions. In addition to the physical goals, the Baikal neutrino complex can be used as a powerful tool to monitor water parameters. The array constantly records phototube counting rates connected with water luminosity and periodically records water parameters, temperature, pressure, and sound velocity. All these data complement the traditional limnological studies and are of importance to get a comprehensive understanding of the processes occurring in the lake. The Baikal neutrino complex is also a unique environmental laboratory to test deep underwater equipment.

ACKNOWLEDGMENTS

This work was supported by the Russian Ministry of Research (contract no. 102-11(00)-p), the German Ministry of Education and Research, the Russian Foundation for Basic Research (project nos. 9902-18373a, 01-02-31013, 00-15-96794, and 01-02-17227), and the Russian Federal Program "Integration" (project no. 346).

REFERENCES

1. M. A. Markov, in *Proceedings of the 10th International Conference on High Energy Physics, Rochester, 1960,* p. 578.
2. V. S. Berezinsky *et al.*, hep-ph/9603342.
3. I. A. Belolaptikov *et al.*, Astropart. Phys. **7**, 263 (1997).
4. R. I. Bagduev *et al.*, Nucl. Instrum. Methods Phys. Res. A **420**, 138 (1999).
5. R. I. Bagduev *et al.*, in *Proceedings of the International Conference on Trends in Astroparticle Physics, Aachen, 1994,* p. 132.
6. L. B. Bezrukov *et al.*, in *Proceedings of the 2nd NESTOR Workshop, Greece, 1993,* p. 645.
7. V. A. Balkanov *et al.*, Preprint No. 1061/2001, INR (Institute for Nuclear Research, Moscow, 2001).
8. L. A. Kuzmichev, Izv. Akad. Nauk, Ser. Fiz. **65**, 1664 (2001).
9. B. K. Lubsandorjiev *et al.*, in *Proceedings of the 27th ICRC, Hamburg, 2001,* Vol. 3, p. 1294.
10. R. V. Il'yasov, B. K. Lubsandorjiev, *et al.*, in *Proceedings of the 27th ICRC, Hamburg, 2001,* Vol. 3, p. 1291.
11. V. A. Balkanov *et al.*, Yad. Fiz. **62**, 1015 (1999) [Phys. At. Nucl. **62**, 949 (1999)].
12. G. A. Askarijan *et al.*, Nucl. Instrum. Methods Phys. Res. **164**, 267 (1979).
13. V. A. Balkanov *et al.*, Nucl. Phys. B (Proc. Suppl.) **75A**, 409 (2001).
14. I. A. Belolaptikov *et al.*, Astropart. Phys. **12**, 75 (1999).
15. M. M. Boliev *et al.*, Nucl. Phys. B (Proc. Suppl.) **48**, 83 (1996).
16. O. V. Suvorova, hep-ph/9911415.
17. T. Montaruli *et al.*, in *Proceedings of the 25th ICRC, Durban, 1997,* Vol. 7, p. 185.
18. M. Mori *et al.*, Phys. Rev. D **48**, 5505 (1993).
19. A. Okada, astro-ph/0007003.
20. V. A. Balkanov *et al.*, in *Proceedings of the 26th ICRC, Salt Lake City, 1999,* Vol. 2, p. 240.
21. M. Ambrosio *et al.*, Preprint INFN/AE-99/08.
22. J. L. Thorn *et al.*, Phys. Rev. D **46**, 4846 (1992).
23. H. Adarkar *et al.*, in *Proceedings of the 21st ICRC, Adelaide, 1990,* p. 95.
24. S. Orito *et al.*, Phys. Rev. Lett. **66**, 1951 (1991).
25. E. Andres, in *Proceedings of the 8th International Workshop on Neutrino Telescopes, Venice, 1999,* p. 63; astro-ph/9906203.
26. E. Andres *et al.*, Nucl. Phys. B (Proc. Suppl.) **91**, 423 (2001).
27. W. Rhode *et al.*, Astropart. Phys. **4**, 119 (1995).
28. L. V. Volkova, Yad. Fiz. **31**, 1510 (1980) [Sov. J. Nucl. Phys. **31**, 784 (1980)].
29. M. Thunman *et al.*, Astropart. Phys. **5**, 309 (1996).
30. V. S. Berezinsky *et al.*, *Astrophysics of Cosmic Rays* (North-Holland, Amsterdam, 1990).
31. F. Stecker and M. Salamon, astro-ph/9501064.
32. R. J. Protheroe, Astron. Soc. Pac. **163**, 585 (1997); astro-ph/9809144.
33. K. Mannheim *et al.*, astro-ph/9812398.
34. E. Waxman and J. Bahcall, Phys. Rev. D **59**, 023002 (1999).
35. K. Mannheim, astro-ph/0010353.
36. E. Waxman and J. Bahcall, Phys. Rev. Lett. **78**, 2292 (1997).
37. P. Bhattacharjee *et al.*, Phys. Rev. Lett. **69**, 567 (1992).

Physics of Atomic Nuclei, Vol. 66, No. 3, 2003, pp. 509–513. From Yadernaya Fizika, Vol. 66, No. 3, 2003, pp. 536–540.

ANTARES—Deep Undersea Neutrino Observatory: Status Report*

V. I. Lyashuk**
for the ANTARES Collaboration

Institute of Theoretical and Experimental Physics,
Bol'shaya Cheremushkinskaya ul. 25, Moscow, 117259 Russia

Received April 17, 2002

Abstract—The ANTARES project aims at the construction of an array of 900 optical modules to form a high-energy neutrino detector with an effective area of about 0.1 km^2 (ANTARES Collab., astro-ph/9907432; http:/antares.in2p3.fr/). The detector will be built in the Mediterranean Sea, 40 km off the coast near Toulon (France) at a depth of 2400 m. The detector has the following main physics goals: measuring the high-energy neutrino flux in the TeV–PeV range with a good pointing resolution, studying atmospheric neutrino oscillations in the region of the parameter space favored by Super-Kamiokande, and searching for supersymmetric dark matter in a region of model parameters of interest in cosmology and particle physics. © *2003 MAIK "Nauka/Interperiodica".*

1. INTRODUCTION

The study of central engines in high-luminosity distant cosmic sources by direct observation of photons or charged particles is impeded by absorption, energy degradation, or magnetic deflection along the path [1]. Only weakly interacting electrically neutral high-energy particles can escape from the depths of such objects and reach us while still pointing back to their source. The only known probe of this type is the neutrino. High-energy interactions of protons or photons can lead to pions, producing neutrinos in their decay. For example, in a supernova explosion, there can be mechanisms of proton acceleration in the magnetosphere or at the front of the shock wave. The turbulent shells of supernova remnants can be a major galactic source of high-energy cosmic-ray protons through shock front acceleration and—indirectly through interactions near the source—of neutrinos. Only high-energy neutrinos can identify proton acceleration sources and test the corresponding hypotheses. On the other hand, cosmic rays generated in our Galaxy when interacting with the Earth's atmosphere can produce locally "atmospheric" neutrinos up to high energies. Similarly, the solar chromosphere is a source of high-energy neutrinos [2]. The only astrophysical neutrino source outside the Solar System known by observations (from the Kamiokande and IMB detector at MeV energies) is supernova SN 1987A.

Generally, various types of cosmic objects as discussed below are expected to emit high-energy neutrinos. The most luminous objects in the Universe are active galactic nuclei (AGN). The luminosity is evaluated as 10^{35}–10^{41} W [3] with a black hole of 10^4–10^{10} solar masses at the center. Protons accelerated in the black hole accretion region could produce high-energy neutrinos. Additionally, the interaction of protons with radiation in the jet of AGN can contribute importantly to the neutrino flux [4]. X-ray binary systems—containing a neutron star or a black hole—are also very bright point sources. Production of hard γ rays ($E_\gamma > 10^{14}$ eV) [5] through inelastic hadronic interactions can be accompanied by high-energy neutrinos.

The most violent sources known today are gamma-ray bursts (GRB). Many attempts have been made to model the phenomenon; they often assume massive black hole creation, for example, through coalescence of a neutron double-star.

Detection of ultrahigh-energy (UHE) cosmic rays with energies exceeding the Greisen–Zatsepin–Kuz'min (GZK) cutoff at about 5×10^{19} eV has led to top-down models based on annihilation or collapse of topological defects, remnants of the early Universe. In their disappearance, gauge and Higgs bosons can be produced, with subsequent decay cascades. Along with UHE nucleons and γ rays, UHE neutrinos would also emerge. In such models, the defects have a mass larger than 10^{21} eV and cluster in the galactic halo within the GZK range (<100 kpc) [6].

The existence of dark matter—essentially manifested through gravitation only—is inferred from the

*This article was submitted by the author in English.

**e-mail: lyashuk@iris1.itep.ru

1063-7788/03/6603-0509$24.00

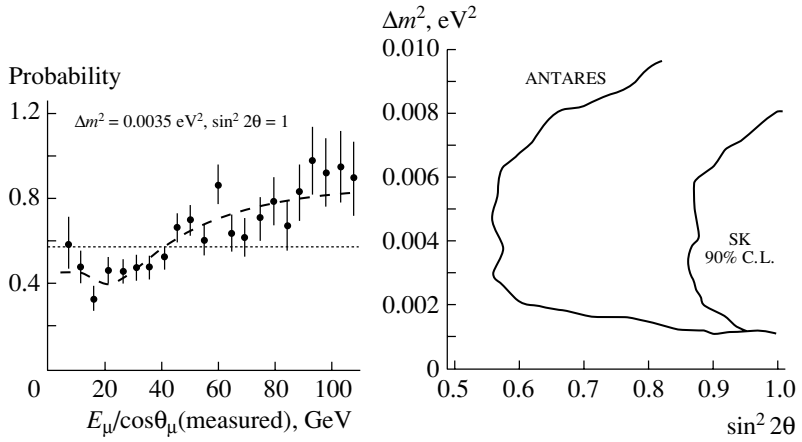

Fig. 1. Left: Expected muon-neutrino survival probability for three years of data taking as a function of the ratio of the reconstructed muon energy and the cosine of the muon zenith angle for $\Delta m^2 = 3.5 \times 10^{-3}$ eV^2 and maximal mixing (statistical errors only). Right: Parameter region, where ANTARES could measure Δm^2 and $\sin^2 2\theta$ with a statistical error less than 33% compared to the 90% C.L. accepted region for Super-Kamiokande.

analysis of galactic rotation and motion in galactic clusters. Dark matter cannot consist primarily of baryons because that would be inconsistent with the abundance of deuterium, whose synthesis is extremely sensitive to baryon density (currently estimated as $\Omega_{\rm bar} \simeq 0.03$). Along with nonzero mass neutrinos, a hypothetical candidate for nonbaryonic dark matter is the neutralino, the lightest supersymmetric particle. Neutralinos would tend to accumulate inside the Earth and Sun and in the centers of galaxies. Upon annihilation, they would produce neutrinos with energy probably below a few hundred GeV (the current mass window).

The ANTARES 0.1-km^2 deep-sea neutrino telescope, at present under construction, aims primarily at studies in the above field by the detection of high-energy neutrinos with a good pointing resolution. This can provide information on the mechanisms of high-energy neutrino sources even at cosmological distances. The telescope will also allow investigations of neutrino oscillations (disappearance) for atmospheric muon neutrinos with a baseline up to the diameter of Earth. For three years of data taking—in terms of statistical errors—the first dip in the survival probability will be observable (see Fig. 1); this can yield significant constraints on the neutrino mass and mixing models. In addition, neutralino dark matter searches will be part of the ANTARES program.

2. THE SITE

A site about 40 km from the coast near Toulon (France) at a depth of 2400 m has been selected for the ANTARES telescope. In an extensive exploration program involving almost 30 successful deployments of autonomous mooring lines, environmental parameters have been measured.

2.1. Light Transmission Properties

Detector efficiency strongly depends on water transparency. Light scattering in the seawater influences the track angular resolution through time delays. Light pulses from a light-emitting diode (LED) were measured at distances of 44 and 24 m by a 1″ fast photomultiplier tube (PMT). The LED luminosity was adjusted so as to give a constant PMT anode current. The distribution of photon arrival times (Fig. 2) shows a peak from direct photons with a tail due to light-scattering effects. It was found that, for blue light ($\lambda \sim 470$ nm), the absorption length is around 55 m, the scattering length is 250 m, and the mean value of $\langle \cos\theta \rangle \approx 0.05$ (where θ is the photon-scattering angle), while the absorption length for UV light ($\lambda \sim 370$ nm) is around 25 m.

2.2. Optical Background Properties

In order to measure background light, two PMTs were installed at fixed distances (0.5 to 1.5 m) from each other with a third PMT successively 10 and 40 m away. The optical background rates and their correlations were monitored. Figure 3 illustrates a typical result: a background, tens of kilohertz, arising from radioactive ^{40}K, varies slowly over a time scale of hours, while bioluminescence bursts of a few seconds appear with rates up to several megahertz.

2.3. Sedimentation and Fouling

Sediment, as well as a layer of (micro)organisms (biofouling), can settle on optically active surfaces. Both processes can decrease the light collection efficiency of PMTs placed inside optical modules

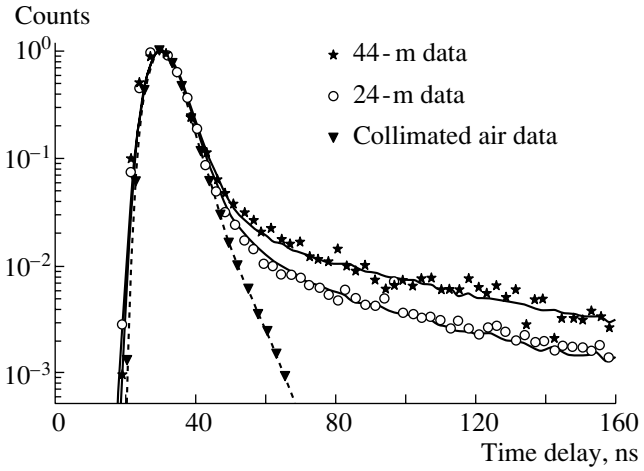

Fig. 2. Distribution of photon arrival times for distances of 24 and 44 m between the photomultiplier and the source. The data for 44 m are normalized to the results for 24 m. Arrival time distributions for two distances and calibration in air are superimposed.

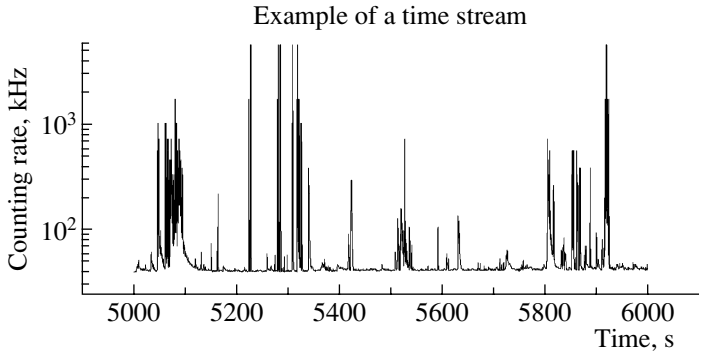

Fig. 3. Variations of the optical background counting rate (kHz) with time.

(OMs). In order to investigate this phenomenon at the ANTARES site, five PIN diodes illuminated by a blue LED were fixed at angles from 50° to 90° from the vertical axis. Results over 240 monitoring days are shown in Fig. 4. For the horizontally positioned diode—viewed through a vertical surface—the loss of light intensity due to fouling ($\sim 2\%$ per year) is small compared to upward viewing parts of the OM surface.

In summary, the site measurements reveal good optical properties of the seawater, the temperature is stable (13°C at the depth of 2400 m), and the currents are slow (~ 5 cm/s).

3. THE TELESCOPE

The ANTARES 0.1-km^2 telescope will consist of an array of ten vertical strings (Fig. 5). Each string consists of an electro-optical-mechanical cable about 460 m in length, anchored on the seabed by means of a ballasted bottom string socket (BSS) and kept vertical by means of a buoy at the upper end. The cable supports 90 OMs, arranged in 30 triplets or stories spaced 12 m apart, with the lowest 100 m of the cable left uninstrumented. Each story has an electronic local control module (LCM). The separation between adjacent strings is approximately 60 m.

An OM consists of a 17″ watertight glass sphere containing a 10″ Hamamatsu PMT and associated electronics. The PMT is housed in a mu-metal wire cage to shield it from the Earth's magnetic field. The three OMs have their PMT face outward from the cable and oriented downwards at 45° to the horizontal. The 30 stories on each string are divided into six sectors of five stories each. The detector is connected to shore by an electro-optical (E/O) cable. It ends at an interface, the junction box (JB), which distributes the power and control signals to and collects data from the individual strings. Each string has its own short E/O cable to the JB, which is connected to the JB after deployment by means of a remotely operated submarine. The read-out system takes care of the digitization of the analog PMT signals. The

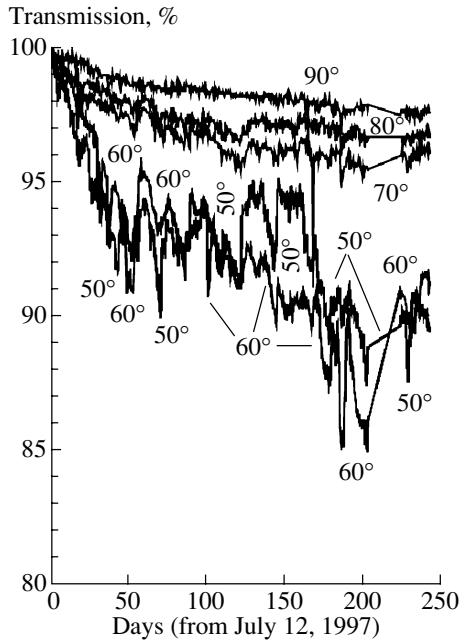

Fig. 4. Variations of the light transmission with time (relative to the first day) for PIN diodes positioned at various angles.

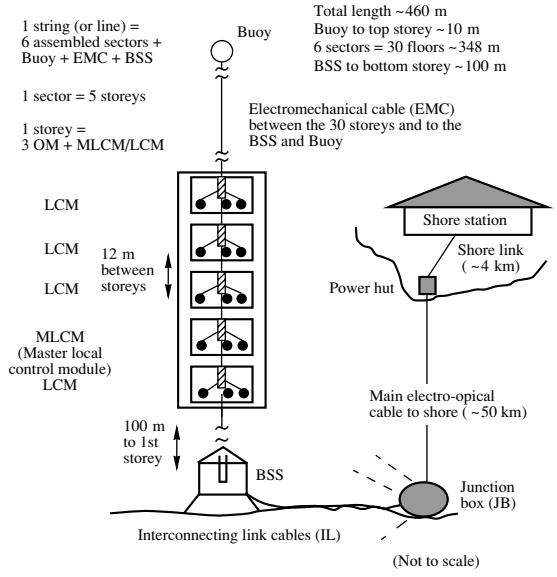

Fig. 5. Schematic view of the string and main subsystems.

data-acquisition system controls the transfer of the data through a high-bandwidth network to an on-shore PC farm for on-line filtering before off-line track reconstruction and analysis. Extensive Monte Carlo simulations have been used to estimate the expected performance of the detector telescope.

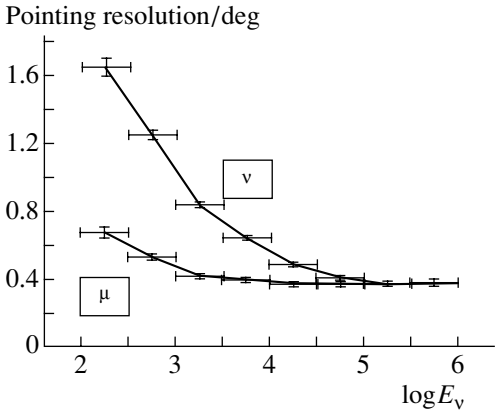

Fig. 6. Angular resolution of the reconstructed muon and its parent neutrino as a function of the neutrino energy.

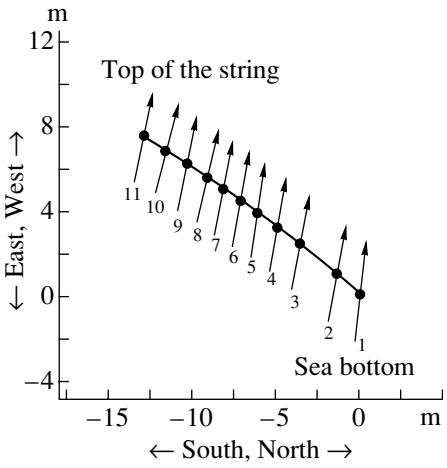

Fig. 7. Reconstructed shape and orientation of the demonstrator string in terms of deviations from the vertical through the bottom of the string.

3.1. Accessible Sky and Pointing Resolution

The main principle of the detector is to observe Cherenkov light from muons produced by up-going muon neutrinos in interactions with surrounding matter. The idea to use a large deep-sea volume as a detector medium [7] was adopted by the DUMAND [8] and the BAIKAL [9] projects. Similarly, Antarctic ice is used as a medium in AMANDA [10].

The PMTs face downward to avoid sedimentation. This also reduces background from the direct flux of muons produced by cosmic rays in the atmosphere above the detector. A significant advantage of the ANTARES telescope—located at a latitude of 42°—is the large solid angle covered: 3.5π, taking the rotation of the Earth into account. The galactic center will be visible most of the time. The overlap in solid angle with AMANDA is 0.5π. The muon energy can

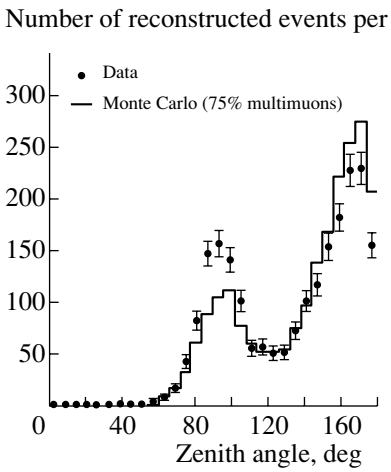

Fig. 8. Angular distribution of muons reconstructed with the demonstrator string. The peak near 90° shows a reconstruction ambiguity reflecting a lack of redundancy in the measurement.

be deduced (with a precision better than a factor of 3) from the number of photons seen by the PMTs. For contained events below 100 GeV, the muon energy can be evaluated more accurately from the deduced muon range.

The pointing resolution for muon tracks is determined by the timing resolution in the detector (<1 ns). At energies above 10 TeV, the muon direction is close to the parent neutrino direction, and the accuracy of the neutrino direction is expected to be better than 0.4°, including light-scattering effects. At muon energies below 10 TeV, the angular error is dominated by the spread in the neutrino–muon relative angle (Fig. 6).

4. THE DEMONSTRATOR

A special string was built to test much of the developed equipment, in particular, the procedure of string deployment including positioning, calibration, and bringing data to shore through an E/O cable. This demonstrator string 340 m in height had 16 stories, where pairs of glass spheres could be mounted. Of these, eight stories were equipped with a single OM an one story with 2 OMs, each containing a horizontally facing PMT. Six stories each had one sphere with various instruments. It was deployed at a site with a depth of 1200 m over a period of several months. The line was connected to the shore by a 37-km E/O cable. The string was equipped with an acoustic positioning system.

4.1. Positioning

The demonstrator string shape and OM positions were determined by means of three range-meters, four transponders on the seabed around the string anchor, hydrophones at every story, and tilt-meters and compasses for measuring the string orientation angles. The positioning is based on the acoustic triangulation method. The position measurement accuracy was shown to be better than 5 cm.

The tilt with respect to the vertical direction was stable within 0.2° around 2.3° over a week. The twist of the string was negligible. Horizontal stability was about 2° over a week. Figure 7 shows the shape of the string and deviations with respect to the vertical line.

4.2. Atmospheric Muons

A large data sample of atmospheric muons was obtained. The data are compared with a Monte Carlo simulation that includes single muons as well as multimuons (Fig. 8). Due to low redundancy in the detector, the reconstruction of muon tracks is not always unique; a ghost peak appears under about 90° both in real data and in Monte Carlo data [11]. Nevertheless, reasonable agreement is obtained.

5. CONCLUSION

The aim of the ANTARES collaboration is to construct a 0.1-km^2 water Cherenkov detector deep in the Mediterranean Sea, optimized for the detection of muons resulting from interactions of high-energy neutrinos of astrophysical origin. The detector will also allow us to study neutrino oscillations and to search for neutralino dark matter. The selected site satisfies the requirements concerning water quality and background properties.

REFERENCES

1. V. S. Berezinsky *et al.*, Astropart. Phys. **1**, 281 (1993).
2. D. Seckel, T. Stanev, and T. K. Gaisser, Astrophys. J. **382**, 652 (1991).
3. T. K. Gaisser, F. Halzen, and T. Stanev, Phys. Rep. **258**, 173 (1995).
4. K. Mannheim and P. L. Biermann, Astron. Astrophys. **253**, L21 (1992).
5. M. Samorski and W. Stamm, Astrophys. J. Lett. **268**, L17 (1983).
6. M. Birkel and S. Sarkar, Astropart. Phys. **9**, 297 (1998).
7. M. A. Markov, in *Proceedings of the 10th International Conference on High Energy Physics, Rochester, 1960,* p. 578.
8. H. Blood, J. Learned, F. Reines, and A. Roberts, in *Proceedings of the International Neutrino Conference, Aachen, 1976,* Ed. by H. Faissner (1977), p. 688.
9. http://www.ifh.de/baikal/
10. http://amanda.berkeley.edu/
11. N. Palanque-Delabrouille, Status Report on the ANTARES Project, Neutrino Telescopes (Venice, Italy, Mar. 6–9, 2001).

Physics of Atomic Nuclei, Vol. 66, No. 3, 2003, pp. 514–516. From Yadernaya Fizika, Vol. 66, No. 3, 2003, pp. 541–543.

TESTS OF NEW PHYSICS IN RARE PROCESSES AND COSMIC RAYS

New Limit on the Proton Lifetime from Neutrino Experiments with Heavy Water*

V. I. Tretyak** **and Yu. G. Zdesenko**

Institute for Nuclear Research, National Academy of Sciences of Ukraine, Kiev, Ukraine

Received April 17, 2002

Abstract—Experimental data on the number of neutrons born in the heavy water targets of large neutrino detectors are used to set the limit on the proton lifetime independently of the decay mode through the reaction $d \to n + ?$ The best up-to-date limit $\tau_p > 4 \times 10^{23}$ yr with 95% C.L. is derived from measurements with the D_2O target (mass of 267 kg) installed near the Bugey reactor. This value can be improved by six orders of magnitude with future data accumulated with the SNO detector containing 1000 t of D_2O.

1. INTRODUCTION

While the baryon (B) and lepton (L) numbers are absolutely conserved in the Standard Model (SM), many extensions of the SM consider conservation of B and L as an approximate law due to absence of any underlying symmetry principle. Incorporation of B- and L-violating interactions in modern gauge theories leads to decay of protons and neutrons bound in nuclei. The processes with $\Delta B = 1$ or 2, $\Delta(B - L) = 0$ or 2 have been discussed [1], while the disappearance of nucleons (or decay into "nothing") has been addressed in connection with the possible existence of extra dimensions [2].

The nucleon instability has been searched for in many underground experiments [3]. About 90 decay modes were investigated, and no evidence for the N (N is p or n) decay was found. For the modes in which N decays to particles strongly or electromagnetically interacting with the detector, the lifetime limits obtained are in the range of 10^{30}–10^{33} yr [4], while, for decays to only weakly interacting products (neutrinos), the bounds are up to ten orders of magnitude lower [4, 5]. However, because it is not known a priori which mode of proton decay is preferable, the limits on the p decay independent of the channel are important. The following approaches were used to establish such limits:

(i) Supposing that the parent nucleus will be destroyed in p decay, the bound $\tau(p \to ?) > 1.2 \times 10^{23}$ yr was determined on the basis of the limit for the branching ratio of ^{232}Th spontaneous fission [6].[1)]

(ii) The limit $\tau(p \to ?) > 3 \times 10^{23}$ yr was obtained by searching for neutrons born in liquid scintillator, enriched in deuterium, as a result of p decay in the d nucleus ($d \to n + ?$) [7].[2)]

(iii) The limit $\tau(p \to 3\nu) > 7.4 \times 10^{24}$ yr was set on the basis of geochemical measurements with Te ore by looking for a possible daughter nuclide ($^{130}\text{Te} \to \cdots \to {}^{129}\text{Xe}$) [8],[3)] while the bound $\tau(p \to 3\nu) > 1.1 \times 10^{26}$ yr was achieved in radiochemical measurements with 1710 kg of potassium acetate $KC_2H_3O_2$ placed deep underground ($^{39}\text{K} \to \cdots \to {}^{37}\text{Ar}$) [9]. These limits are usually quoted as "independent of the channel"; however, it is evident that they are valid only for p decay into invisible channels or disappearance, in which the parent nucleus is not fully destroyed (like ^{232}Th in [6]). At the same time, the bound on p decay from deuterium disintegration requires a less stringent hypothesis on the stability of the daughter nuclear system and, hence, it is less model dependent.

The value based on d disintegration [7] can be improved by using data from modern neutrino experiments with heavy water, well shielded against

*This article was submitted by the authors in English.

**e-mail: vit@tretyak.kiev.ua

[1)]We recalculated the value quoted in [6] $\tau(N \to ?) > 3 \times 10^{23}$ yr (given for 232 particles: 142 neutrons and 90 protons) for 90 protons that should be taken into consideration here.

[2)]Because [7] is not a source easily accessible and because in [4], where this limit is quoted, there is no indication of confidence level, we assume that it corresponds to 68% C.L.

[3)]The value $\tau(N \to 3\nu) > 1.6 \times 10^{25}$ yr quoted in [8] as given for 52 particles (28 neutrons and 24 protons) was recalculated for 24 protons.

1063-7788/03/6603-0514$24.00

cosmic rays and natural radioactivity [10]. With this aim, we analyze the measurements of [11] with the 267-kg D_2O target and show that the limit $\tau(p \to ?)$ can be highly improved with the SNO large-volume detector [12] containing 1000 t of D_2O.

2. REACTOR EXPERIMENTS WITH HEAVY WATER

The experiment [11] aimed to measure the cross sections for d disintegration by reactor $\overline{\nu}_e$ through reactions $\overline{\nu}_e + d \to \overline{\nu}_e + n + p$ and $\overline{\nu}_e + d \to e^+ + n + n$. The detector was located at a depth of 25 m w.e., 18.5 m away from the center of the Reactor 5 core at the Bugey site. The cylindrical tank with 267 kg of 99.85% pure D_2O was surrounded by layers of Pb (10 cm) and Cd (1 mm) to absorb thermal n from external surroundings. The tank and the Pb–Cd shield were inserted in a large liquid-scintillator detector that served as an inner cosmic-ray veto. The subsequent layer of Pb (10 cm) aimed to reduce the flux of external γ quanta with energies $E_\gamma > 2.23$ MeV, which can photodisintegrate deuterons and create background events. However, this shielding itself was a significant source of neutrons in the target detector created due to interaction of cosmic rays with Pb. To suppress this background, an additional layer of cosmic-ray veto detectors was installed outside the Pb shielding; this reduced the n background in the target by a factor of nearly 6. Neutrons were detected by ^{3}He proportional counters installed in the tank with D_2O.

The decay or disappearance of p bound in a d nucleus, which consists only of p and n, will result in appearance of a free neutron: $d \to n + ?$. Thus, the p-lifetime limit can be estimated on the basis of the neutron rate detected in the D_2O volume when the reactor is switched off. To calculate $\lim \tau(p \to ?)$, we use the formula $\lim \tau(p \to ?) = \varepsilon N_d t / \lim S$, where ε is the efficiency for the neutron detection, N_d is the number of deuterons ($N_d = 1.605 \times 10^{28}$), t is the time of measurement, and $\lim S$ is the number of p decays that can be excluded with a given confidence level on the basis of the neutron background measured in the experiment. The mean efficiency for a single n born isotropically throughout the D_2O volume was determined as $\varepsilon = 0.29 \pm 0.01$ [11]. The one-neutron rate with the reactor off, corrected for the software efficiency, is 57.00 ± 1.53 counts/d. For very rough estimation of the p lifetime, we can attribute all neutron events to proton decays and obtain the $\lim S/t$ value of 59.5 counts/d at 95% C.L. Substituting this value into the formula, we get the limit $\tau(p \to ?) > 2.1 \times 10^{23}$ yr with 95% C.L.[4] The τ limit derived in this way is very conservative because the dominant part of the observed n rate has origins other than p decay [15]. The main sources of neutrons are (i) interaction of cosmic μ with the detector, shield, and surrounding materials; (ii) photodisintegration of d by γ quanta with $E_\gamma > 2.23$ MeV originating from the radioactive contamination of the detector materials and shield and from the environment; and (iii) residual n background at the reactor site. The Bugey setups [11, 16] were located at only 25–40 m w.e. overburden and at distance of 15–18 m from the reactor core. Thus, the dominant part of the n background in [11, 16] is associated with the reactor site and μ flux. As was proved by a detailed simulation and careful analysis of the n background in the reactor-off periods of the experiment [16], (67 ± 3)% of the n rate is attributed to the known origin. Thus, we can make a conservative estimate that at least 50% of one-neutron events measured in [11] are caused by sources (i)–(iii). Taking the remaining part of the one-neutron rate as the excluded number of p decays ($\lim S/t = 30$ counts/d), we obtain $\tau(p \to ?) > 4 \times 10^{23}$ yr with 95% C.L., which is higher than the previous limit [7].

3. EXPECTED IMPROVEMENTS WITH THE SNO DETECTOR

The Sudbury Neutrino Observatory (SNO) is a large Cherenkov detector constructed with an emphasis on the study of Solar neutrinos [12]. The detector, containing 1000 t of 99.917% pure heavy water, is located in a nickel mine at the depth of 2039 m (about 6000 m w.e.); this reduces the μ flux to 70 muons per day in the detector area. About 7000 t of ultrapure light water shield the central D_2O detector from natural radioactivity from the surroundings. All components of the detector are made of selected materials with low radioactive contamination.

Solar neutrinos will be detected through the following reactions with electrons and deuterons: $\nu_i + e^- \to \nu_i + e^-$ ($i = e, \mu, \tau$), $\nu_e + d \to e^- + p + p$, and $\nu_i + d \to \nu_i + n + p$. About 9600 PMTs are used to observe the Cherenkov light produced in the D_2O volume by high-energy products. Neutrons released in d disintegration will be detected by n capture on deuterons in pure D_2O, or by capture on ^{35}Cl by dissolving MgCl salt in heavy water, or by capture

[4] The similar limit $\tau(p \to ?) > 1.9 \times 10^{23}$ yr with 95% C.L. can be derived from another neutrino deuteron experiment at the Krasnoyarsk (Russia) nuclear reactor [13]. A more modest result can be obtained from the data of the Rovno experiment [14]: $\tau(p \to ?) > 2.3 \times 10^{22}$ yr with 95% C.L.

on ^{3}He using proportional counters. The expected number of neutrons from all sources in the D_2O volume is calculated as $\approx 5 \times 10^3$ during a 1-yr period of exposition, with the main contribution from the Solar neutrinos. The efficiency for n detection is 83% for n capture on ^{35}Cl [12].

With these unique features of the SNO detector (superlow background, large amount of D_2O, and high sensitivity to neutrons), the limit on the p decay independent of the channel can be highly improved. Again, for rough estimation of the p lifetime, we can conservatively attribute all neutrons in the D_2O volume to p decays and take it as the excluded value of $\lim S$. Substituting $\varepsilon = 0.83$, measuring time $t = 1$ yr, number of deuterons $N_d = 6 \times 10^{31}$, and $\lim S = 5 \times 10^3$ counts into the formula for τ, we obtain $\tau(p \to ?) > 1 \times 10^{28}$ yr, which is about five orders of magnitude higher than the present-day limit.

However, this value can be improved further by considering the n events originating from Solar neutrinos and high-energy γ quanta. The number of n born in the D_2O volume due to disintegration $\nu_i + d \to \nu_i + n + p$ can be estimated independently by using information on the number of Solar ν interactions with the detector volume through the reaction $\nu_i + e^- \to \nu_i + e^-$. Neutrons created by γ quanta can also be calculated if the levels of pollution of the detector components and external γ flux are measured. In this case, the excluded number of n due to possible p decay will be restricted only by statistical uncertainties of the measured n background, which gives $\lim S = 2\sqrt{5000}$ with 95% C.L. The corresponding bound on the p lifetime is $\tau(p \to ?) > 4 \times 10^{29}$ yr with 95% C.L. This value is close to the limits established for the particular modes of nucleon decays to charged or strongly interacting particles and would be of great importance for many extensions of modern gauge theories.

REFERENCES

1. P. Langacker, Phys. Rep. **71**, 185 (1981); M. Goldhaber *et al.*, Science **210**, 851 (1980); H. V. Klapdor-Kleingrothaus and A. Staudt, *Non-Accelerator Particle Physics* (IOP, Bristol, 1995).
2. F. J. Ynduráin, Phys. Lett. B **256**, 15 (1991); G. Dvali *et al.*, hep-ph/9910207; S. L. Dubovsky *et al.*, Phys. Rev. D **62**, 105011 (2000); J. High Energy Phys. **8**, 041 (2000).
3. D. H. Perkins, Annu. Rev. Nucl. Part. Sci. **34**, 1 (1984); R. Barloutaud, Nucl. Phys. B (Proc. Suppl.) **28A**, 437 (1992).
4. Review of Particle Physics, Eur. Phys. J. C **15**, 1 (2000).
5. R. Bernabei *et al.*, Phys. Lett. B **493**, 12 (2000).
6. G. N. Flerov *et al.*, Sov. Phys. Dokl. **3**, 79 (1958).
7. F. E. Dix, PhD Dissertation (Case Western Reserve Univ., Cleveland, Ohio, 1970).
8. J. C. Evans, Jr., and R. I. Steinberg, Science **197**, 989 (1977).
9. E. L. Fireman, in *Proceedings of the International Conference on Neutrino Physics and Neutrino Astrophysics "Neutrino-77"* (Nauka, Moscow, 1978), Vol. 1, p. 53; R. I. Steinberg, J. C. Evans, in *Proceedings of the International Conference on Neutrino Physics and Neutrino Astrophysics "Neutrino-77,"* Vol. 2, p. 321.
10. V. I. Tretyak and Yu. G. Zdesenko, Phys. Lett. B **505**, 59 (2001).
11. S. P. Riley *et al.*, Phys. Rev. C **59**, 1780 (1999).
12. H. H. Chen, Phys. Rev. Lett. **55**, 1534 (1985); R. G. H. Robertson (SNO Collab.), Prog. Part. Nucl. Phys. **40**, 113 (1998); J. Boger *et al.* (SNO Collab.), Nucl. Instrum. Methods. Phys. Res. A **449**, 172 (2000).
13. Yu. V. Kozlov *et al.*, Yad. Fiz. **61**, 1370 (1998) [Phys. At. Nucl. **61**, 1268 (1998)]; **63**, 1091 (2002) [**63**, 1016 (2000)].
14. A. G. Vershinsky *et al.*, JETP Lett. **53**, 513 (1991).
15. J. Busenitz, Yad. Fiz. **63**, 1068 (2000) [Phys. At. Nucl. **63**, 993 (2000)]; L. A. Mikaélyan and V. V. Sinev, Yad. Fiz. **63**, 1077 (2000) [Phys. At. Nucl. **63**, 1002 (2000)]; G. Gratta, Nucl. Phys. B (Proc. Suppl.) **85**, 72 (2000); Y. Declais, Nucl. Phys. B (Proc. Suppl.) **70**, 148 (1999); A. Piepke *et al.*, Nucl. Instrum. Methods. Phys. Res. A **432**, 392 (1999); M. Appolonio *et al.*, Phys. Lett. B **420**, 397 (1998).
16. B. Achkar *et al.*, Nucl. Phys. B **434**, 503 (1995).

Physics of Atomic Nuclei, Vol. 66, No. 3, 2003, pp. 517–522. From Yadernaya Fizika, Vol. 66, No. 3, 2003, pp. 544–549.

TESTS OF NEW PHYSICS IN RARE PROCESSES AND COSMIC RAYS

The Possibility of Searching for New Physics in Cosmic Rays*

A. A. Petrukhin**

Moscow Engineering Physics Institute, Kashirskoe sh. 31, Moscow, 125080 Russia

Received April 17, 2002

Abstract—One possible explanation of cosmic-ray energy spectrum behavior around the knee (3–5 PeV) by means of production of new heavy particles or a new state of matter is considered. It is shown that, in this case, a large excess of muons and neutrinos with energies of >100 TeV must be generated. The existing VHE muon experimental data are analyzed. Possible experiments on VHE muon investigations are discussed. © *2003 MAIK "Nauka/Interperiodica".*

1. INTRODUCTION

In high energy physics, the words "new physics" are usually associated with the discovery of new particles, new states of matter, or new laws of their production or interaction. In the last decades, these discoveries were connected with investigations at accelerators. Practically every step in the increase in accelerator energy was followed by impressive achievements in the search for new physics.

However, it is interesting to remark that the first new particles (positron, muon, pion) were discovered in cosmic rays. Now, a pause in construction of accelerators has come, since the next accelerator—the Large Hadron Collider (LHC) with a total energy of interacting particles up to 14 TeV—will start to operate in no less than five years. Therefore, interest in cosmic-ray investigations has been renewed. The reason is very simple. The most intriguing energy domain is the multi-TeV region, where the next level of new physics is expected. But this energy interval in the c.m. system corresponds to the PeV-energy range in the laboratory frame, in which one particle is moving and another is at rest. And it is at these energies that the famous knee—the change in the slope of the cosmic-ray energy spectrum in the atmosphere—is observed.

In principle, the appearance of the knee can be explained both by a change in the primary cosmic-ray energy spectrum and/or composition and by a change in the character of particle interaction at these energies due to the inclusion of new physical processes (new particle, new state of matter, etc.). It is important to emphasize that experimental evidence for the knee existence was obtained in extensive air shower (EAS) investigations. Therefore, these experimental data are directly related to cosmic-ray propagation through the atmosphere, and various further interpretations of these data are possible.

However, numerous experimental investigations of different components of EAS did not give undeniable evidence for serious changes in the EAS characteristics that could confirm the appearance of new physics at the knee energy. Therefore, at present, most scientists studying cosmic rays adhere to the cosmophysical model of the knee appearance, which is rather verisimilar and relates the knee to an origin, acceleration, and propagation of cosmic rays in the Galaxy. Nevertheless, papers with alternative points of view appear regularly [1].

In the present paper, a new approach to the knee problem is considered that is connected with VHE muons, which can be responsible for the knee appearance.

2. COSMIC-RAY ENERGY SPECTRUM WITHOUT THE KNEE

Results of cosmic-ray energy spectrum measurements around the knee (based on EAS observations) may be described by two power functions

$$N_1 = N_0 \left(\frac{E_0}{E_1}\right)^{\gamma_1}, \qquad N_2 = N_0 \left(\frac{E_0}{E_2}\right)^{\gamma_2}, \quad (1)$$

where $E_0 = E_{\text{knee}} \sim$ 3–5 PeV; N_0 is the intensity of particles at this energy; and E_1 and E_2 are the energies of particles below and above the knee, respectively (Fig. 1).

Let us suppose that above the knee the primary spectrum is unchanged, but some heavy and short-lived particles are generated. These can be any heavy particles or states of matter which are predicted by various theoretical models, but which cannot be produced at existing accelerators, since the position of

*This article was submitted by the author in English.

**e-mail: petruhin@nevod.mephi.ru

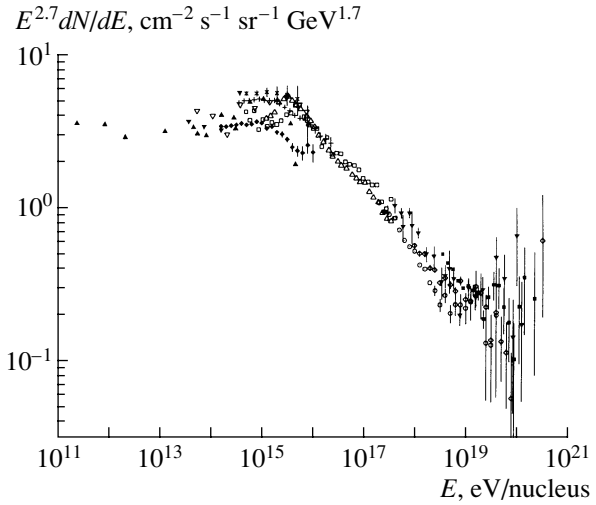

Fig. 1. Cosmic-ray energy spectrum obtained from the results of the EAS investigations [2]. To distinguish the knee more clearly, the spectrum is multiplied by the factor $E^{2.7}$.

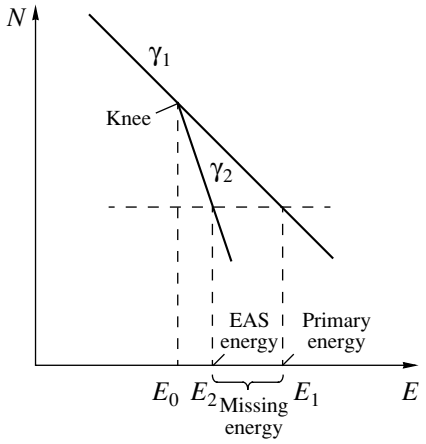

Fig. 2. Missing energy definition.

the knee corresponds to an energy of more than 3 TeV in the c.m. system. If these heavy particles decay (directly or through intermediate particles) into leptons in the final state—e, μ, τ, ν_e, ν_μ, and ν_τ—the energy of e and partially of τ will be included in the usual EAS development, but the energy of ν_e, ν_μ, ν_τ, and μ (!) will be missing energy for EAS arrays (Fig. 2), since muon detectors can measure the number of muons, but not their energy.

From the comparison of two spectra (1) with γ_1 and γ_2 (Fig. 2), the following formula for missing energy $\triangle E$ above the knee may be obtained [3]:

$$\frac{\Delta E}{E_1} = 1 - \left(\frac{E_0}{E_1}\right)^{\Delta\gamma/\gamma_2}, \qquad (2)$$

where $\Delta\gamma = \gamma_2 - \gamma_1$ and E_1 is the energy of the primary particle. Calculations of missing energy give the results presented in the table. The values were obtained for $\gamma_1 = 1.7$, $\gamma_2 = 2.1$ ($\Delta\gamma = 0.4$), and $E_0 = 5$ PeV, although it should be mentioned that the results of the lastest experiments give $\Delta\gamma$ values closer to 0.3 and $E_0 \sim 3$ PeV. As one can see from the table, the missing energy is considerable.

Missing energy ΔE (in PeV)

E_1	E_1/E_0	ΔE
5	1	0
50	10	18
500	100	280

3. ENERGY SPECTRUM OF "NEW" MUONS

Among four leptons (ν_e, ν_μ, ν_τ, μ), only muon energy can be measured. For accurate calculations of the muon energy spectrum, some additional suppositions about the new particle production mechanism, energy dependence of the cross section, etc., are required. Considering that muons can be generated only in weak (decays) and electromagnetic ($\mu^+\mu^-$ pairs) processes, at least two suppositions are necessary.

The first is the large cross section of the production of new particles or a new state of matter in primary cosmic-ray particle interaction (tens of millibarns), which is necessary to change the slope of the cosmic-ray energy spectrum in the atmosphere. Since in a general case the cross section is determined by the formula

$$\sigma = \alpha_x^2(\lambda + R)^2 l(l+1), \qquad (3)$$

there are three possibilities of increasing the value of the cross section: (i) to introduce a new interaction at distances of $\sim 10^{-17}$ cm and correspondingly a new coupling constant α_x; (ii) to postulate interaction of an object with a large size R (fireball, quark–gluon plasma, etc.); (iii) to assume interaction with very large orbital momenta l.

The second supposition is that new particles or a new state of matter must be short-lived and must decay into muons (and neutrinos) directly or through any intermediate particles with large branching. A detailed analysis of possible theoretical models is not a goal of this paper. In any case, what is required is not small corrections to the Standard Model, but introduction of fundamentally new physics.

To evaluate the expected influence of new physical processes on the muon energy spectrum, the simple energy relations for two limiting cases can be used. The maximum flux will correspond to the minimum

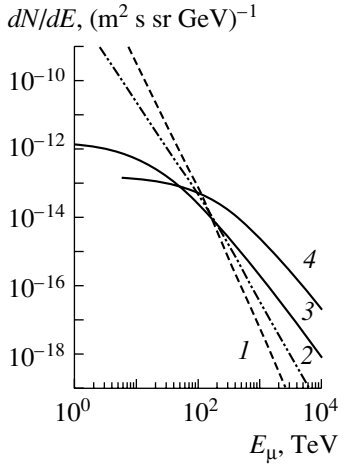

Fig. 3. Differential muon energy spectrum. Curves describe (*1*) the spectrum of muons from π and K decays, (*2*) upper limit of prompt muons from charm production, and (*3*) minimum and (*4*) maximum contribution of new processes.

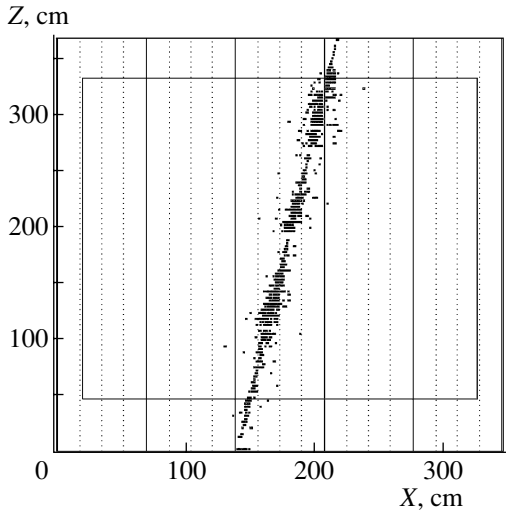

Fig. 4. VHE muon in the NUSEX detector (*ZX* view).

number of produced particles, when each of four particles (three neutrinos and one muon) takes away the energy $\sim\Delta E/4$ (Fig. 3). The minimum flux will correspond to multiple production of muons, when the missing energy ΔE is shared among many particles. The total number of muons in the latter case will be limited by the mass of the new particle (or new state of matter) and the process of their production. For example, if muons are produced through decays of $W(Z)$ bosons, their number cannot exceed ~ 10 particles at $m_x \sim 1$ TeV. In this case, the average muon energy is $\sim\Delta E/40$, but multiple muons will be produced. It is necessary to emphasize that $W(Z)$-boson decay modes with the production of hadrons and electrons contribute to the usual EAS development. One can see from Fig. 3 that the new source of cosmic-ray muons begins to prevail over the known processes of their generation at energies of >100 TeV, i.e., in the region of very high energies.

Of course, some changes in the two-dimensional spatial-energy distribution also have to be observed at lower energies if multiple muons are produced in new processes. But, as one can see from Fig. 3, higher energies give more distinct evidence for new physics.

4. SOME INDICATIONS OF EXISTENCE OF VHE MUON EXCESS

Apparently, the first observation of VHE muons was made by Japanese physicists [4], who found an air shower with energy about 300 TeV at the zenith angle of 86°. This shower could have been generated by muons only, but the probability of the production of such muons in π and K decays is very small. However, if one takes into account new processes of muon generation, the probability of detecting a similar event will become quite reasonable.

The marked excess of muon-induced cascade showers with energies of >10 TeV was observed by the MSU group in x-ray emulsion chambers [5]. The authors interpreted their results as evidence for prompt muons (due to charmed particle decays), but with a large value of the ratio of the fluxes of the so-called prompt muons to charged pions in the upper atmosphere, $R_{\mu\pi} \sim 3 \times 10^{-3}$. This parameter was introduced to describe the contribution of any fast processes of muon generation compared to π and K decays. For example, curve *2* in Fig. 3 corresponds to $R_{\mu\pi} = 10^{-3}$. Modern theoretical calculations give the value of $R_{\mu\pi}$ about 10^{-4} [6]. At the same time, taking into account "new" muons in calculations of the electromagnetic cascade shower spectrum due to muon bremsstrahlung, it is possible to easily explain the result of the MSU group experiment. Some excess of muons with energies >10 TeV was also apparently observed in the underground experiment LVD in Gran Sasso [7].

A very interesting event was found in the NUSEX detector. Multiple interactions of high-energy muons in the detector consisting of 130 iron absorber planes 1 cm thick were analyzed to evaluate the average muon energy at a depth about 5000 m w.e. [8]. In one of the events (Fig. 4), the muon permanently interacts in the target. As calculations show, the probability of the production of secondary cascade showers by the muon increases with energy, reaching a value of ~ 0.9 at an energy about 100 TeV, and the muon begins to look like a practically continuous luminous lace. Considering the relatively small area of the detector

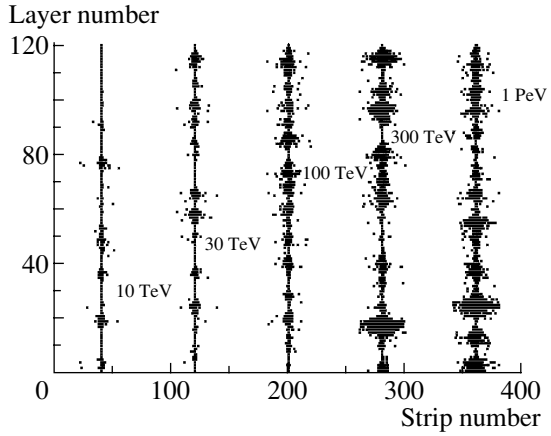

Fig. 5. Results of simulation of muon interactions in MONOLITH.

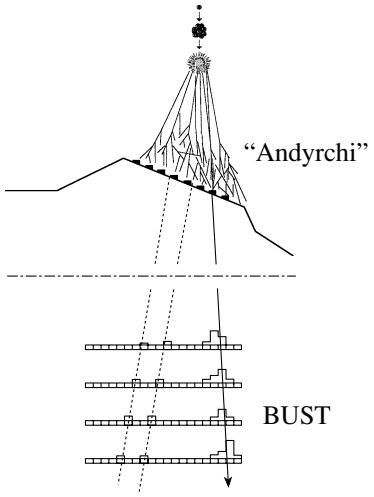

Fig. 6. Schematic view of the Baksan array: Andyrchi and BUST (only horizontal planes of scintillation counters are shown). Dotted lines are usual muons, and the solid line is the VHE muon.

(about 12 m^2) and the large depth of its location, observation of such a muon from conventional sources is improbable.

Thus, this analysis shows that cosmic-ray physics has come very close to a promising region of VHE muons. It is possible that VHE muons from new physical processes are detected in various experiments, but the available data are insufficient to prove that.

5. POSSIBLE FUTURE EXPERIMENTS

Since the number of VHE muons is small, it is impossible to observe them by measuring the total number of muons in EAS on the Earth's surface or in underground laboratories, and direct measurements of their energies are required. At present, no detector exists for measuring muon energies in the 100-TeV region. Therefore, let us consider the possibilities of some proposed experiments and detectors being constructed. The only known method of muon energy measurements in this interval is the pair meter technique [9]. This method allows one to evaluate muon energy from multiple production of electron–positron pairs in a thick layer of matter. The method has no limitation on measurable energy and will work very well at energies about 100 TeV. In order to reach a 50% accuracy of individual muon energy measurements, a thickness about 500 radiation lengths is needed (8 m of Fe or 200 m of water). To detect the expected flux of VHE muons, a sensitive area of more than 500 m^2 is required. The large-scale neutrino detectors of the new generation Baikal and AMANDA and the proposed projects ANTARES, NESTOR, and MONOLITH will have suitable parameters. Unfortunately, in the Baikal and AMANDA setups, most of the photomultipliers are directed downward; therefore, modifications of these detectors are required. A much better situation will be in ANTARES, where PMs are directed near the horizon. In this case, equal conditions for up-going and down-going muons exist. Good conditions for investigating VHE muons from the atmosphere will be achieved at Nestor, where the numbers of PMs directed up- and downward will be equal.

Very good possibilities for muon energy measurements in the interval around 10^2 TeV can be provided by the MONOLITH detector [10], which is a proposed massive (34 kt) magnetized tracking calorimeter at the Gran Sasso Laboratory in Italy, optimized for the detection of atmospheric muon neutrinos. It will consist of 120 plates of iron (8 cm) interleaved with RPC and will have an area about 450 m^2. The main goal of this detector is to prove (or to reject) the neutrino oscillation hypothesis through explicit observation of the first full oscillation swing. But at the same time, MONOLITH will be a very good pair meter for muon energy measurements. In three years, the MONOLITH detector will register about 100 events with surface muon energies exceeding 100 TeV. Figure 5 illustrates the possibilities of this detector in investigation of VHE muons. As one can see from the figure, it is very easy to separate muons with energies greater than 100 TeV. It is interesting to note that the experimental event in Fig. 4 is similar to the simulated one with an energy of 100 TeV in Fig. 5.

From the point of view of the search for new physical processes in cosmic rays, the most direct experiment must include the simultaneous detection of EAS with energies around the knee and VHE muons correlated with them. The absence of these muons at EAS energies below the knee and their appearance

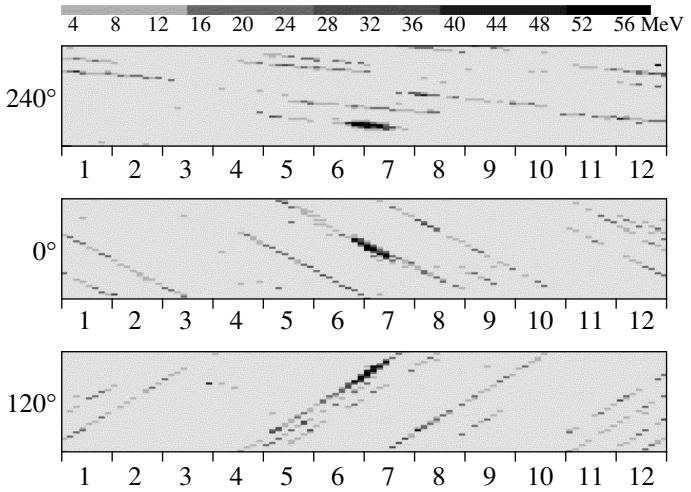

Fig. 7. Inclined muon group in BARS (three views); 0° projection corresponds to top view.

above the knee will be irrefutable proof of the inclusion of new physical processes.

Unfortunately, an appropriate experimental facility for the solution of this problem (an EAS array and a full-scale pair meter) does not exist. After EAS-TOP in Gran Sasso was dismantled (only reanalysis of old data can be performed), there remained one facility in Baksan (Andyrchi with BUST) that had a good EAS array, but not so thick a muon detector. In this situation, to find evidence for influence of a new process, a detailed analysis of spatial and energy distributions of muons is needed.

The schematic view of the Baksan array is shown in Fig. 6. The Baksan underground scintillation telescope (BUST) is a well-known detector with which many investigations of neutrinos, muons, monopoles, etc., in cosmic rays were performed. It consists of 3200 scintillator counters $70 \times 70 \times 30$ cm in size placed in eight planes, four horizontal and four vertical. The size of the detector is $17 \times 17 \times 11$ m. BUST has two separate systems for amplitude data analysis: one for the total signal of each of eight planes, and the other for measurements of signal amplitudes from each scintillation counter. Both systems can be used for evaluation of the muon energy deposit in the detector.

The Andyrchi EAS array is located on the surface of the mountain directly above the scintillation telescope. The array consists of 37 standard scintillation counters separated by distances of about 40 m. The total area of the array is 4.5×10^4 m^2. Andyrchi allows detection of EAS with energies of 0.2–20 PeV, i.e., just in the knee interval [11].

There are two other detectors: BARS (Big liquid-ARgon Spectrometer) in Protvino [12] and NEVOD-DECOR (Cherenkov water calorimeter with coordinate detector) in MEPhI [13], which provide very good conditions for investigations of spatial and energy distributions of muons. But they need to be supplemented with EAS arrays.

BARS was constructed by the Russian–Italian collaboration for experiments in the tagged neutrino beam at the IHEP accelerator in Protvino. It is 3.5 m in diameter and 18 m long and consists of 24 sections of liquid-argon ionization chambers; every section includes 12 planes of 6-cm-wide signal strips. Strip orientation in successive planes is rotated by 120°, thus forming a system of three coordinates in the transverse cross section of the setup.

The BARS spectrometer was constructed for horizontal neutrino beam event observation. Therefore, the best conditions for EAS muon component detection will be provided for inclined showers. For this reason, the shower array will be deployed on one side of BARS along its axis. From this point of view, BARS and BUST complement each other in zenith angle intervals. An example of the inclined EAS muon component detected in BARS is shown in Fig. 7. One

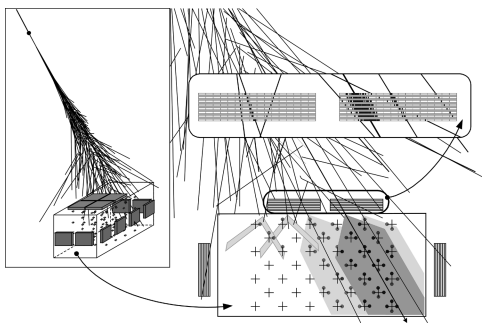

Fig. 8. Scheme of EAS detection in the experimental complex NEVOD-DECOR.

can see that the interacting muon stands out against the background of other muons.

NEVOD-DECOR is a multipurpose experimental facility for investigating various cosmic-ray components on the Earth's surface. The coordinate detector with an area about 100 m^2 and a spatial resolution of 1 cm^2 allows detection of EAS particles in the whole zenith-angle interval (0°–90°). The Cherenkov water calorimeter allows one to determine the direction of motion of the charged particle and to evaluate its energy deposit in water. The first results of muon and shower detection showed [14] that muons and showers could be separated by using the water detector alone. The combined NEVOD-DECOR array has much wider possibilities for various EAS component investigations (Fig. 8).

6. CONCLUSION

The searches for new particles and states of matter are usually related to the construction of new accelerators. In particular, further advancement in the multi-TeV energy region, where the appearance of various kinds of new physics is expected, is associated with the construction of the LHC in CERN. But investigations of VHE muons may give a key to the search for new physical processes in cosmic rays. At present, there are experimental indications that some excess of VHE muons exists. Considering that the multi-TeV region will be investigated at the LHC no earlier than in 2007, cosmic rays provide a real and maybe the last chance to make a serious contribution to the study of matter at distances about 10^{-17} cm. Even a negative result of the search for VHE muons will be very important, since the last possibility of the knee explanation due to new processes of interactions will be closed. Forty years of knee investigations have not given the final solution to the problem of the cosmic-ray energy spectrum slope change. The proposed approach allows one to close this problem. But for this purpose, intensive and very accurate investigations are required.

ACKNOWLEDGMENTS

I am grateful to N. Barbashina and R. Kokoulin for help in the preparation of the paper.

REFERENCES

1. S. I. Nikolsky, Nucl. Phys. B (Proc. Suppl.) **39A**, 228 (1995); **75A**, 217 (1999).
2. Particle Data Group, Eur. Phys. J. C **15**, 155 (2000).
3. A. A. Petrukhin, in *Proceedings of the XI Rencontres de Blois "Frontiers of Matter," Blois, France, 1999* (Gioi Publ., Vietnam, 2001), p. 401.
4. T. Matano *et al.*, in *Proceedings of the International Conference on Cosmic Rays, London, 1965,* Vol. 2, p. 1045.
5. N. P. Il'ina *et al.*, in *Proceedings of the 24th International Cosmic Ray Conference, Rome, Italy,* 1995, Vol. 1, p. 524.
6. G. Gelmini, P. Gondolo, and G. Varieschi, Phys. Rev. D **61**, 036005 (2000).
7. LVD Collab., in *Proceedings of the 25th International Cosmic Ray Conference, Durban, 1997,* Vol. 6, p.341.
8. C. Castagnoli *et al.*, Astropart. Phys. **6**, 187 (1997).
9. R. P. Kokoulin and A. A. Petrukhin, Sov. J. Part. Nucl. **21**, 332 (1990).
10. MONOLITH Collab., Experiment Proposal, LNGS P26/2000, CERN/SPSC 2000-031, SPSC/M657 (2000).
11. A. E. Chudakov *et al.*, in *Proceedings of the 25th International Cosmic Ray Conference, Durban, 1997*, Vol. 6, p. 177; in *Proceedings of the XI International School "Particles and Cosmology," Baksan Valley, 2000,* p. 303.
12. R. P. Kokoulin *et al.*, in *Proceedings of the 26th International Cosmic Ray Conference, Salt Lake City, 1999,* Vol. 2, p. 24.
13. A. A. Petrukhin *et al.*, in *Proceedings of the 26th International Cosmic Ray Conference, Salt Lake City, 1999,* Vol. 2, p. 460.
14. A. A. Petrukhin, in *Proceedings of the 32nd Rencontres de Moriond "Very High Energy Phenomena in the Universe," Les Arcs, 1997,* p. 411.

Physics of Atomic Nuclei, Vol. 66, No. 3, 2003, pp. 523–525. From Yadernaya Fizika, Vol. 66, No. 3, 2003, pp. 550–552.

TESTS OF NEW PHYSICS IN RARE PROCESSES AND COSMIC RAYS

Cosmic Ray "Knee" in the Spectrum and Proton–Proton Cross Section from the Point of View of New Quarks*

V. B. Petkov[1)], O. D. Lalakulich[1)], and G. M. Vereshkov[1)]**

Baksan Neutrino Observatory, Institute for Nuclear Research, Russian Academy of Sciences, Kabardino-Balkaria, Russia

Received April 17, 2002

Abstract—A possible explanation of the "knee" in the cosmic ray spectrum by the change in hadron–hadron interactions at the corresponding energy is discussed. It is shown that, at c.m. energies above 5 TeV, the total proton–proton cross sections obtained from cosmic ray experiments exceed the asymptotic fit made over the collider data. Such a rise of the cross sections favors the hypothesis about new chromodynamically charged degrees of freedom, the threshold of their creation being about $\sqrt{s_{\text{knee}}} \approx 2.3$ TeV. The properties of these new particles which are needed are discussed. © *2003 MAIK "Nauka/Interperiodica".*

1. INTRODUCTION

Recent experimental data on the cosmic-ray spectrum clearly indicate a sharp "knee" at the energy $E_{\text{knee}} \approx 2.8 \times 10^{15}$ eV. Two approaches to explain this phenomenon are currently under discussion. The astrophysical approach [1] presupposes that the knee is a feature of the primary spectrum. The other approach [2, 3] implies that the primary spectrum stays untouched and we observe the knee in the EAS spectrum because of the sudden change in strong (chromodynamical) interactions at the c.m. energy $\sqrt{s_{\text{knee}}} \approx \sqrt{2m_p E_{\text{knee}}} \approx 2.3$ TeV.

One of the latter scenarios has recently been discussed by Petrukhin [3]. The knee energy $\sqrt{s_{\text{knee}}}$ in this scenario is considered as a threshold of new metastable chromodynamically charged particle (new quark) creation, these new quarks being constituents of new metastable mesons. A key element of this hypothesis is that new mesons, which are born above $\sqrt{s_{\text{knee}}}$ in strong interactions of primary particles with the atmosphere, decay only owing to the weak interactions. The currently undetectable products of their decays carry some fraction of the primary energy away, which is the origin of the knee in the EAS spectrum. Any hypothesis about new physics related to the knee presupposes the total *pp* cross-section rise above the threshold of new particle creation.

2. ANOMALOUS GROWTH OF THE PROTON–PROTON CROSS SECTION AS A POSSIBLE SIGNATURE OF NEW QUARKS

Let us suppose that only five metastable quarks and eight gluon degrees of freedom can be hadronized (the t quark cannot be hadronized because $\Gamma_t \gg 100$ MeV). In this case, the high-energy hadronic interactions are described by the Reggeon–Pomeron theory [4], complemented by the AGK rules [5]. In this theory, total cross sections for hadronic interactions asymptotically have Froissart-type behavior, $\sigma_{\text{tot}} \sim C \ln^2(s/s_0)$ [6, 7].

Hadron cross sections are measured in accelerator experiments up to $\sqrt{s} \sim 1800$ GeV for $p\bar{p}$ collisions, $\sqrt{s} \sim 62$ GeV for *pp* collisions, and even lower energies for others, the results being regularly selected and published in [8]. Another source of information is cosmic-ray experiments [9–11]. However, the restoration of the total *pp* cross sections from the nucleon attenuation length measured in such type of experiments is an ambiguous procedure, so the original results of the above-cited authors were reanalyzed [12, 13] and resulted in higher values of the cross sections.

We fit the existing collider data and extend the fit to the high-energy region. So we use a fit that respects unitarity,

$$\sigma = C \ln^2 \frac{s}{s_0} + D \ln \frac{s}{s_0} + A\left(1 + \frac{B}{s + \Lambda^2}\right), \quad (1)$$

which guarantees the correct asymptotic behavior of the cross sections. Since the threshold energy of b-quark creation in soft processes is about $\Lambda_b \sim 4m_b$,

*This article was submitted by the authors in English.

[1)]Also from Research Institute of Physics, Rostov State University, Russia.

** e-mail: petkov@neutr.novoch.ru

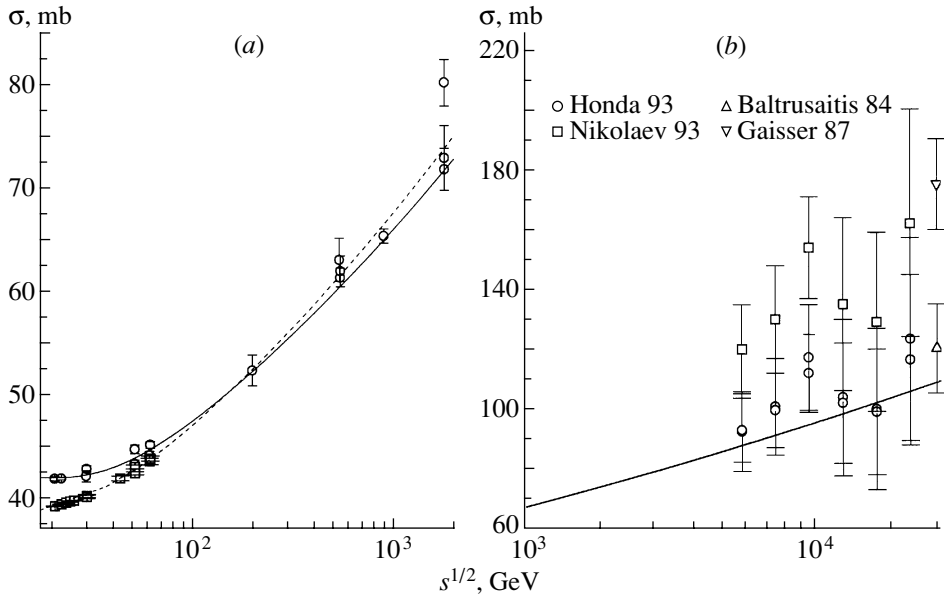

Fig. 1. Fits of pp and $p\bar{p}$ cross sections and cosmic ray data: (*a*) pp (square, solid curve) and $p\bar{p}$ (circles, dashed curve) cross sections at collider energies [fit according to Eq. (1)]. (*b*) Extrapolation of pp fit [according to Eq. (1)] to cosmic-ray data.

we are safe to suppose the asymptotic behavior above $\sqrt{s} \sim 200$ GeV. Unfortunately, only three points (with not small errors) are known in this region [8]. However, we can take advantage of the fact that the asymptotic regime of the cross-section behavior begins to form in the preasymptotic region $\sqrt{s} > \Lambda_b \approx 20$ GeV. Thus, the only dimensional parameter Λ in (1) must be about Λ_b.[2)]

According to the Pomeranchuk theorem [6, 7], at asymptotic energy, the region $[\sigma_{\rm tot}(pp) - \sigma_{\rm tot}(p\bar{p})]/[\sigma_{\rm tot}(pp) + \sigma_{\rm tot}(p\bar{p})] \to 0$; thus, $C_{pp} = C_{p\bar{p}} = C$. One more theorem claims that the difference of total cross sections tends to zero if and only if both elastic cross sections tend to zero [6]. In the energy region under investigation, it is known from the Tevatron data that the elastic cross section rises as fast as the total cross section. Therefore, the pp and $p\bar{p}$ cross sections are really different. It is known that, in this case, parameter s_0 (common for pp and $p\bar{p}$ cross sections) can be chosen such that $D_{pp} = -D_{p\bar{p}}$; the only restriction is $|D| \le C\pi/2$ [7]. We also assume that Λ^2 is common, but A and B are different for pp and $p\bar{p}$ cross sections.

However, as a result of the fit, it appears that $B_{pp} \simeq B_{p\bar{p}}$ and $C\pi/2 - |D| \simeq 0$ with an accuracy of about $\sim 1\%$. Thus, these equalities must be postulated as exact; i.e., the preasymptotic function is universal and the difference in pp and $p\bar{p}$ cross-section rise is critical. The final result of the fitting is as follows:

$$C = 0.1343 \text{ mb}, \quad s_0 = 0.0107 \text{ GeV}^2,$$
$$D_{pp} = -D_{p\bar{p}} = 0.2110 \text{ mb}, \quad A_{pp} = 18.38 \text{ mb},$$
$$A_{p\bar{p}} = 24.52 \text{ mb}, \quad B_{pp} = B_{p\bar{p}} = (11.828 \text{ GeV})^2,$$
$$\Lambda^2 = (17.675 \text{ GeV})^2.$$

Now, let us compare the cosmic-ray data on the cross sections with the fit obtained (see figure). All the central values but one [9, 11] lie above the fitted curve, while the lower error bars are below the curve. As to the recalculated values [12, 13], they are well above the fit.

Thus, we conclude that the excess of the cosmic-ray experimental data on the cross sections over the asymptotic fit favors the hypothesis about the appearence of new metastable quarks above $\sqrt{s_{\rm knee}}$.

In the framework of this hypothesis, a sharp enough rise of the cross section is expected at $\sqrt{s} \sim \sqrt{s_{\rm knee}}$, as is shown in the figure. The data expected at the LHC will be of principal value in this situation. These data are able not only to confirm or reject the hypothesis about new quarks, but also to make it possible to calibrate the cosmic-ray data with respect to the collider data, to reduce the errors significantly, and to go to higher energies in cosmic-ray experiments with lower errors.

[2)] It is known that the Regge-predicted behavior is $1/\sqrt{s}$. However, this term must be strongly suppressed above the energy of the last known resonance, which is about 3 GeV. Thus, in the region of energy under discussion $\sqrt{s} > 20$ GeV, we avoid the term.

3. THE NEEDED PROPERTIES OF NEW QUARKS

Thus, the subject of our discussion is new metastable quarks (or, to be more precise, new chromodynamically charged degrees of freedom) that are able to form new mesons. In order to describe the observed knee in the cosmic-ray spectrum, it is necessary to assume some properties of new quarks.

(i) First of all, new metastable quarks D must be born in soft processes at the threshold energy about $\sqrt{s_{\text{knee}}}$, so their mass must be about $m_D \sim 0.5$ TeV. This is the process of their creation that ensures the rise of the total pp cross section above the threshold energy.

(ii) New quarks are able to form new metastable hadrons if their lifetime strongly exceeds the hadronization time $\tau_D \gg 10^{-24}$ s. The possibility of finding such metastable quarks in the existing extensions of the Standard Model is the subject of further investigation.

(iii) The decays of new hadrons must occur via weak interactions, the hadronic and leptonic branching ratios being comparable. The hadronic decays provide the high multiplicity in pp collisions, and the leptonic (in particular, muon-neutrino) channels lead to the energy being carried away from the EAS. How to detect muons produced in such processes is the subject of investigation of the MEPHI team [3].

(iv) The cross section of new-quark creation must be very high—about 10 mb. This is the most disputed question and it seems to be the main problem of the hypothesis.

If strong interactions of new quarks are pure chromodynamical, then the cross section of their creation is no larger than a few nanobarns and hardly contributes to the total proton–proton cross section. Therefore, new quarks under search must participate in a new type of strong interaction, for example, in technicolor interactions. In this case, one can expect that the nonperturbative fluctuations of new quarks are intensive enough, which increase the cross section of their diffractive creation. Surely, other hypotheses of new strongly interacting objects are also possible.

4. CONCLUSION

Thus, it is shown in this paper that, at c.m. energies above 5 TeV, the total pp cross sections exceed the asymptotic fit made over the collider data. Such a rise of the cross sections may be considered as an indication of new chromodynamically charged degrees of freedom, which in turn can clarify the origin of the knee in the cosmic-ray spectrum. New experimental data on the proton–proton cross section from cosmic-ray experiments in the knee energy region are of principal value to favor or disfavor the hypothesis about the new chromodynamically interacting degrees of freedom.

ACKNOWLEDGMENTS

This work was supported by a grant from the Federal Program "Integration" (project no. E0157).

REFERENCES

1. A. D. Erlykin, S. J. Fatemi, and A. W. Wolfendale, Phys. Lett. B **482**, 337 (2000); Izv. Akad. Nauk, Ser. Fiz. **63**, 473 (1999).
2. S. I. Nikolsky, Nucl. Phys. B (Proc. Suppl.) **75A**, 217 (1999).
3. A. A. Petrukhin, in *XI Rencontres de Blois "Frontiers of Matter", France, June 27–July 3, 1999.*
4. A. B. Kaidalov, Nucl. Phys. B (Proc. Suppl.) **75A**, 81 (1999).
5. V. A. Abramovskiĭ, V. N. Gribov, and O. V. Kancheli, Yad. Fiz. **18**, 595 (1974) [Sov. J. Nucl. Phys. **18**, 308 (1974)].
6. N. N. Bogolyubov, A. A. Logunov, I. T. Todorov, and A. I. Oksak, *General Principles of Quantum Field Theory* (Nauka, Moscow, 1987; Dordrecht, Kluwer, 1990).
7. R. Iden, in *General Principles of Quantum Field Theory and Their Consequencies,* Ed. by V. A. Meshcheryakov (Nauka, Moscow, 1977).
8. Particle Data Group, Eur. Phys. J. C **15**, 1 (2000).
9. R. M. Baltrusaitis *et al.*, Phys. Rev. Lett. **52**, 1380 (1984).
10. T. Hara *et al.*, Phys. Rev. Lett. **50**, 2058 (1983).
11. M. Honda *et al.*, Phys. Rev. Lett. **70**, 525 (1993).
12. T. K. Gaisser, Phys. Rev. D **36**, 1350 (1987).
13. N. N. Nikolaev, Phys. Rev. D **48**, 1904 (1993).

Physics of Atomic Nuclei, Vol. 66, No. 3, 2003, pp. 526–546. Translated from Yadernaya Fizika, Vol. 66, No. 3, 2003, pp. 553–573.

REVIEWS

Physics of Charmed Hadrons

S. V. Semenov*

Institute of Theoretical and Experimental Physics, Bolshaya Cheremushkinskaya ul. 25, Moscow, 117259 Russia

Received February 26, 2002

Abstract—Basic experimental results on charmed-particle physics that have been obtained over the past few years are surveyed. Prospects for studying the properties of charmed particles in the near future are discussed. © *2003 MAIK "Nauka/Interperiodica".*

1. INTRODUCTION

The physics of charmed hadrons has been successfully developed over a period spanning more than 25 years. A few tens of charmed mesons and baryons have been discovered throughout these years, their features have been determined, and their lifetimes have been measured to a high precision; also, a few hundred channels of charmed-particle decays have been explored. In recent years, the attention of researchers switched, to a considerable extent, from the physics of charmed mesons to B-meson physics. A great amount of effort has gone into searches for CP violation in the decays of neutral B mesons. However, impressive advances made in developing detectors for studying B mesons, along with the successful commissioning of B factories (such as BABAR at the SLAC accelerator in the United States and BELLE at the KEK accelerator in Japan), opened new horizons for charmed-particle physics as well. Since B factories produce B mesons and charmed particles at approximately the same rate and since primary selection criteria (trigger conditions) are similar for the two classes of events in question, events featuring charmed particles are selected at B factories, together with B-meson events. Therefore, experiments designed for studying, first of all, B-meson physics furnish a significant fraction of results concerning charmed-particle physics.

The present survey gives information only about the properties of particles involving open charm. Attention here is focused primarily on results that have been obtained over the past three to four years. Information about earlier results can be found in the review article of the present author in [1].

The ensuing exposition is organized as follows. Basic experimental facilities used to study the properties of charmed particles are briefly described in Section 2. Section 3 is devoted to the spectroscopy of charmed mesons and baryons. The results obtained by measuring the lifetimes of charmed hadrons are given in Section 4. New investigations into the leptonic and semileptonic decays of charmed particles are surveyed in Sections 5 and 6. The results obtained in recent years by studying the three-body nonleptonic decays of D mesons are described in Section 7. Experimental results on searches for $D^0\bar{D}^0$ mixing in hadronic and semileptonic decays are compiled in Section 8; also given there are the results of investigations into doubly Cabibbo-suppressed decays of D mesons. Section 9 summarizes the results of searches for rare decays and CP violation in the decays of D mesons. Finally, prospects for charmed-particle physics are briefly discussed in Section 10.

This review article does not include information about investigations of charmed-particle fragmentation. A comprehensive description of such fragmentation processes can be found in [2]. Investigations into the properties of mesons featuring hidden charm are not covered here either. For information about such investigations, the interested reader is referred to the articles quoted in [3].

2. MAIN DETECTORS USED IN STUDYING CHARMED-PARTICLE PHYSICS

Let us briefly describe the detectors that were specially developed for studying charmed particles. The E791 [4], E831(FOCUS) [5], and E781(SELEX) [6] detectors were arranged in secondary beams extracted from the TEVATRON collider at FERMILAB in the United States and were used to accumulate statistics in experiments with fixed targets. In hadron interactions with target nuclei, charmed particles are produced only in one out of a thousand interactions, but, in photon–nucleus interactions, the ratio of useful and background events is not more than several-fold greater (about 1/200). In order to investigate the required number of charmed-particle decays, it was necessary to record on tapes information about a few

*e-mail: ssemenov@iris1.itep.ru

hundred million interactions. In such experiments, data processing takes long periods of time.

With the E791 experimental facility [4], which was placed in a beam of 500-GeV pions, data had been accumulated over a period spanning the years 1991 and 1992. For targets, use was made of a platinum foil 0.5 mm thick and a series of four emerald foils 1.6 mm thick spaced by 15 mm. With the aid of a spatially separated target, it was possible to reduce the background of secondary interactions considerably—that is, to exclude (from the analysis) events in which charmed-particle-decay products underwent interaction in the substance of that part of the target where the decay occurred. On both sides of the beam axis, the target was surrounded by silicon microstrip vertex detectors and proportional wire chambers in order to reconstruct, to a high precision, the decay vertex and the trajectories of charged particles from charmed-particle decay. The momenta of charmed-particle-decay products were determined with the aid of a magnetic spectrometer including two magnets and 35 planes of drift chambers positioned downstream and upstream of the magnets. Two threshold Cherenkov counters made it possible to distinguish between kaons and pions in the momentum range from 6 to 60 GeV/c. The particles involved were identified with the aid of an electron and a hadron calorimeter, a muon system also being used for this.

In experiments with the FOCUS detector [5], data were taken in a photon beam of mean energy 190 GeV. The target consisted of four BeO segments. A few layers of a silicon microstrip vertex detector made it possible to determine the interaction vertex to a precision of 300 μm along the beam axis and to a precision of 6 μm in the plane orthogonal to the beam axis. The momenta of charmed-particle-decay products were determined with the aid of a magnetic spectrometer. Threshold Cherenkov counters identified kaons and pions, while an electromagnetic calorimeter and muon chambers identified electrons and muons, respectively. Data taken over the period spanning the years 1996 and 1997 are still being processed. More than a million charmed mesons and a few tens of thousands of charmed baryons have been reconstructed.

In the SELEX experiment [6], either a 600-GeV beam of negatively charged hyperons and pions (50% Σ^-, 50% π^-) or a 540-GeV beam of protons and positively charged pions (92% p, 8% π^+) was used in accumulating statistics. The interaction of baryons with a target leads to a more frequent production of baryons than in the cases where different particle species interact with the target; therefore, it was possible, in that experiment, to focus on studying the properties of baryons. A segmented target of total thickness equal to 5% of the nuclear-interaction range was used to reduce the background of secondary interactions. Vertex detectors of spatial resolution 270 μm along the beam axis and 4 μm in the plane orthogonal to the beam axis made it possible to determine, to a fairly high precision, the vertices of charmed-particle interaction and decay. The momenta of charmed-particle-decay products were determined with the aid of a magnetic spectrometer. A ring-image Cherenkov counter ensured the separation of kaons and pions up to momenta of 165 GeV/c. In order to select charmed particles during the accumulation of statistics, a special trigger was applied that made it possible to achieve a threefold improvement in the ratio of useful and background events recorded in the experiment. Presently, the processing of data taken in 1996 and 1997 is being continued.

Table 1. Potential of currently performed experiments for studying charmed-particle physics

Experiment	Number of reconstructed particles	
	mesons	baryons
E791 [4]	$\sim 2 \times 10^5$	$\sim 10^4$
FOCUS [5]	$\sim 10^6$	$\sim 10^5$
SELEX [6]	$(2-3) \times 10^5$	$\sim 10^5$
CLEO [7, 8]	$\sim 2 \times 10^6$	$\sim 5 \times 10^4$
BELLE [9]	$\sim 5 \times 10^6$	$\sim 1.5 \times 10^5$
BABAR [10]	$\sim 6 \times 10^6$	$\sim 2 \times 10^5$

Experiments deployed at electron–positron colliders are aimed at studying B-meson physics. Nevertheless, this does not reduce their potential for studying the properties of charmed particles. The accumulation of data at the CLEO II detector [7] was completed in 1999, but the data are still being processed, new results appearing regularly. Over a period spanning the years 2000 and 2001, data taking was performed at the CLEO III facility [8], a modification of the CLEO experiment with an upgraded vertex detector and a new drift chamber. The particle-identification system there was substantially improved in relation to CLEO II. The application of a new ring-image Cherenkov counter makes it possible to distinguish kaons and pions over the entire range of measured particle momenta, thereby remedying one of the weakest points in the CLEO II detector.

The BELLE [9] and BABAR [10] experiments were designed to study B-meson physics—first of all, to measure CP violation in the decays of B mesons. Owing to the universality of the detectors used, both

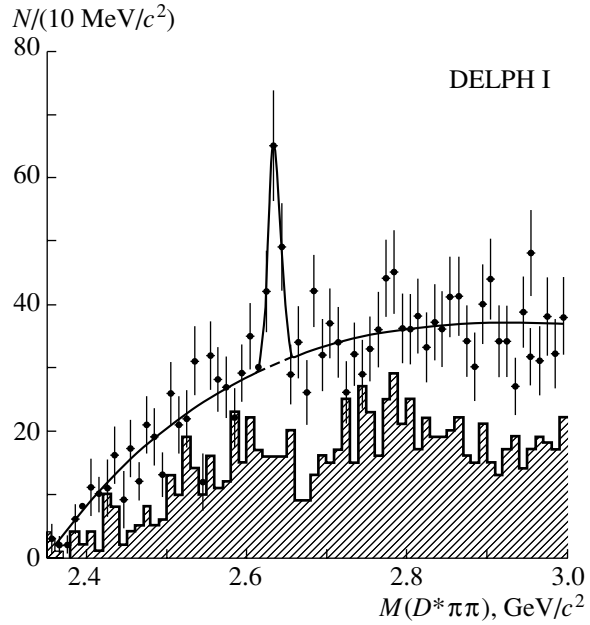

Fig. 1. Invariant-mass distribution of the $D^{*+}\pi^+\pi^-$ system. The solid curve represents a fit to data, while the shaded histogram shows the distribution in question for wrong-sign combinations ($D^{*+}\pi^-\pi^-$).

experiments have good prospects in systematic investigations of charmed particles. High-precision vertex detectors make it possible to determine the interaction vertex to a precision of a few micrometers and to measure the lifetimes of mesons involving a heavy quark. Excellent electromagnetic calorimeters ensure a high efficiency in reconstructing neutral pions and, hence, the possibility of reconstructing D mesons in decay channels involving neutral particles. The separation of charged kaons and pions over the entire momentum range under study with the aid of threshold Cherenkov counters ensures excellent conditions for reconstructing charmed particles in hadronic decay channels. Finally, the trigger conditions developed for isolating B mesons are basically acceptable in selecting charmed particles as well; therefore, there is even no need for evolving a special trigger for isolating charmed particles. The estimated potential of each of the aforementioned experiments for studying the properties of charmed particles is quoted in Table 1. The total number of events recorded by all modifications of the detector is indicated there for CLEO. For the BELLE and BABAR experiments, which are still being continued, data are given that had been obtained by the end of 2001.

3. SPECTROSCOPY OF CHARMED HADRONS

Ground-state charmed mesons have received quite an adequate study. The CLEO Collaboration was able to measure the decay width of the D^{*+} meson [11], thereby providing unique information about the coupling constant for the strong interaction of a system consisting of a heavy and a light quark. The total decay width of the D^{*+} meson can be represented as the sum of three partial widths corresponding to the strong decays $D^{*+} \to D^0\pi^+$ and $D^{*+} \to D^+\pi^0$ and the radiative decay $D^{*+} \to D^+\gamma$;[1)] that is, we have

$$\Gamma(D^{*+}) = \frac{g^2_{D^{*+}\to D^0\pi^+}}{24\pi m^2_{D^{*+}}} p^3_{\pi^+} + \frac{g^2_{D^{*+}\to D^+\pi^0}}{24\pi m^2_{D^{*+}}} p^3_{\pi^0} + \frac{\alpha g^2_{D^{*+}\to D^+\gamma}}{3} p^3_\gamma,$$

where p_{π^+}, p_{π^0}, and p_γ are the momenta of the corresponding particles in the D^{*+}-meson rest frame.

By using the isospin relations $g_{D^*\to D\pi} = -\sqrt{2} g_{D^{*+}\to D^+\pi^0} = g_{D^{*+}\to D^0\pi^+}$ and considering that, in the limit of an infinitely heavy quark, $g_{D^*\to D\pi}$ and the universal constant g for the strong decay of a heavy vector (or pseudoscalar) meson into a pion are related by the equation $g_{D^*\to D\pi} = (2m_{D^*}/f_\pi)g$ [12], we obtain

$$\Gamma(D^{*+}) = \frac{2g^2}{12\pi f^2_\pi} p^3_{\pi^+} + \frac{g^2}{12\pi f^2_\pi} p^3_{\pi^0} + \frac{\alpha g^2_{D^{*+}\to D^+\gamma}}{3} p^3_\gamma.$$

If the contribution of the electromagnetic decay [$\mathrm{Br}(D^{*+} \to D^+\gamma) = (1.68 \pm 0.45)\%$] is disregarded, measurement of the total decay width of the D^{*+} meson makes it possible to extract information about the universal constant g for the strong decay of a heavy meson into a pion. Previously, the ACCMOR Collaboration [13] obtained an upper limit on the decay width of the D^{*+} meson: 131 keV/c^2 (at a 90% C.L.). This was done by using 110 decays of D^{*+} mesons. The CLEO Collaboration employed more than 11 000 D^{*+} mesons reconstructed on the basis of the decay chain $D^{*+} \to D^0\pi^+$, $D^0 \to K^-\pi^+$, which had been studied in minute detail. Since the measured decay width of the D^{*+} meson is much less than the resolution of the facility used (about 150 keV/c^2), it was necessary to study in detail the possible sources of systematic errors. This is not the whole story, however. For want of a physical process that could be used to test results, one had to rely on a thorough comparison of experimental

[1)] Unless otherwise stated, a reference to a specific charged state also implies the inclusion of the charge-conjugate state.

data with the output of a Monte Carlo simulation. In order to study in detail possible systematic effects, the set of signal events was broken down into three groups characterized by different sensitivities to the measured mass difference $Q = M(K^-\pi^+\pi^+) - M(K^-\pi^+) - M(\pi^+)$, to decay properties, and to the quality of reconstruction. This yielded consistent results for the three groups, the averaged width being $\Gamma(D^{*+}) = 96 \pm 4 \pm 22$ keV/c^2. The amplitude extracted for slow-pion emission in charmed-particle decays proved to be $g_{D^*\to D\pi} = 17.9 \pm 1.9$. As a result, a value of $g = 0.59 \pm 0.01 \pm 0.07$ was obtained for the universal constant characterizing strong heavy-meson decay into a pion. Needless to say, it is necessary that this result be verified at B factories that have been brought into operation.

According to heavy-quark effective theory [14], the properties of P-wave mesons ($L = 1$) are determined primarily by the total angular momentum of the light quark, $j_q = L + s_q$, where s_q is the light-quark spin. In the limit of an infinitely heavy charmed quark, there must exist two meson doublets characterized by $j_q = 1/2$ and $j_q = 3/2$. Such mesons undergo predominantly two-body decays into $D^{(*)}\pi$ and $D^{(*)}K$ for $D_J^{(*)}$ and $D_{sJ}^{(*)}$, respectively. In this case, the law of spin–parity conservation determines, for each state, allowed decay channels and allowed wave states [15, 16]. The members of the $j_q = 1/2$ doublet decay in the S wave; therefore, it is expected that the width of these states is about 100 to 200 MeV/c^2. The members of the $j_q = 3/2$ doublet may decay only into a D-wave state, so that they are expected to be narrow (of width 10 to 20 MeV/c^2). All narrow states were discovered and studied in detail in many experiments, their masses and decay channels being reliably established [17].

In studying the decay process $B^- \to D^{*+}\pi^-\pi^-$, the CLEO Collaboration reported in 1999 [18] on the discovery of a broad $D_1^0(j = 1/2)$ state decaying into $D^{*+}\pi^-$. The decay chain $B^- \to D_j^{*0}\pi_1^-$, $D_j^{*0} \to D^{*+}\pi_2^-$, $D^{*+} \to D^0\pi_3^+$ was studied there. In order to reconstruct B mesons, this collaboration measured the momenta of three pions $(\pi_1^-, \pi_2^-, \pi_3^+)$ and imposed constraints dictated by the laws of energy–momentum conservation. The application of this procedure made it possible to improve the efficiency of B-meson reconstruction significantly, albeit at the expense of sizably spoiling background conditions. As many as three D_J^*-meson species may decay into $D^*\pi$—this proceeds through a D wave for D_2^* and D_1 and through an S wave for D_1^*. Since B and π are pseudoscalar particles, D_J^* is produced in a fully polarized state; therefore, the relative probability of its production can be determined from an analysis of the angular distributions of its decay products. A fit to data was constructed in terms of four parameters—these are the angle between the momenta of the pions π_1 and π_2 in the D_J^* rest frame; the angle between the momenta of the pions π_2 and π_3 in the D^* rest frame; the angle between the planes spanned by the momentum vectors of the corresponding pairs of pions; and, finally, the $D^{*+}\pi_2^-$ invariant mass, which must be equal to the mass of the D_J^* state. The fitting procedure has revealed that, along with two well-established narrow resonances [$D_1^0(2420)$, $D_2^{*0}(2460)$], there must exist yet another, broad, state [$D_1^0(j = 1/2)$]. The mass and the width of the broad resonance proved to be $M = 2461^{+41}_{-34} \pm 10 \pm 32$ MeV/c^2 and $\Gamma = 290^{+101}_{-79} \pm 26 \pm 36$ MeV/c^2, respectively.

In [19], the DELPHI collaboration reported on the discovery of a peak at $2637 \pm 2 \pm 6$ MeV/c^2 (66 ± 14 events) in the invariant-mass distribution of the $D^{*+}\pi^+\pi^-$ system, the width of the peak being less than 15 MeV/c^2 (Fig. 1). The invariant-mass distribution for the wrong-sign combinations $D^{*+}\pi^-\pi^-$ (dashed histogram in Fig. 1) has a smooth shape. The authors interpreted this state as a $J^P = 1^-$ radial excitation of the D^{*0} meson. The ratio of the probability of the production of this state to the total probability of the production of the orbitally excited states D_1^0 and D_2^{*0} was

$$R = \frac{N(D^{*+\prime})\mathrm{Br}(D^{*+\prime} \to D^{*+}\pi^+\pi^-)}{N(D_1^0)\mathrm{Br}(D_1^0 \to D^{*+}\pi^-) + N(D_2^{*0})\mathrm{Br}(D_2^{*0} \to D^{*+}\pi^-)} = 0.49 \pm 0.21.$$

In turn, the OPAL and CLEO Collaborations ([20] and [21], respectively) did not reveal an orbitally excited state and set upper limits on the ratio R ($R < 0.21$ at a 95% C.L. and $R < 0.16$ at a 90% C.L., respectively) that contradict the DELPHI results.

The ground states of charmed baryons belong to two $SU(4)$ multiplets, $20'$ and 20, where each of the baryons contains three quarks of one of the four flavors. The first and the second multiplet involve, respectively, (Fig. 2*a*) $J^P = 1/2^+$ and (Fig. 2*b*) $J^P = 3/2^+$ baryons. The $J^P = 1/2^+$ multiplet, whose middle level includes states featuring one c quark, con-

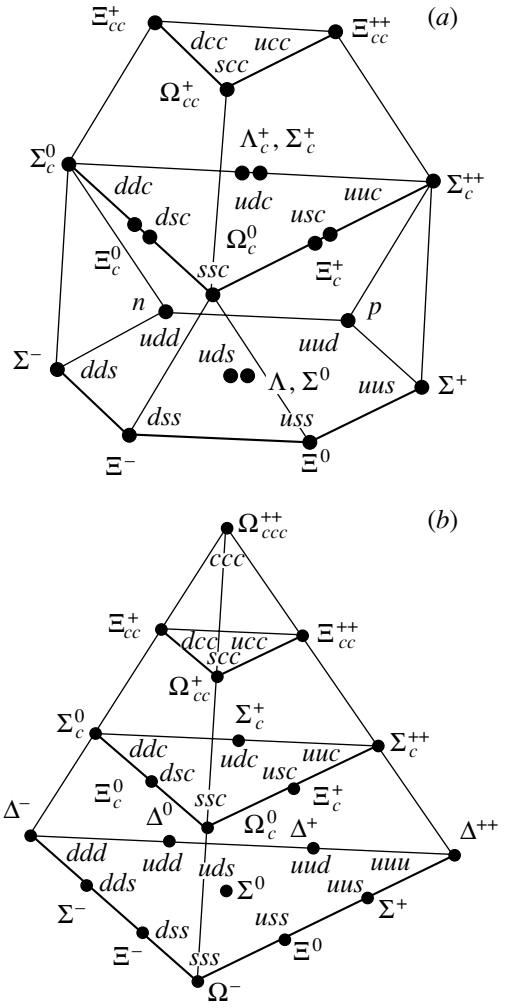

Fig. 2. (*a*) $J^P = 1/2^+$ and (*b*) $J^P = 3/2^+$ baryon multiplets.

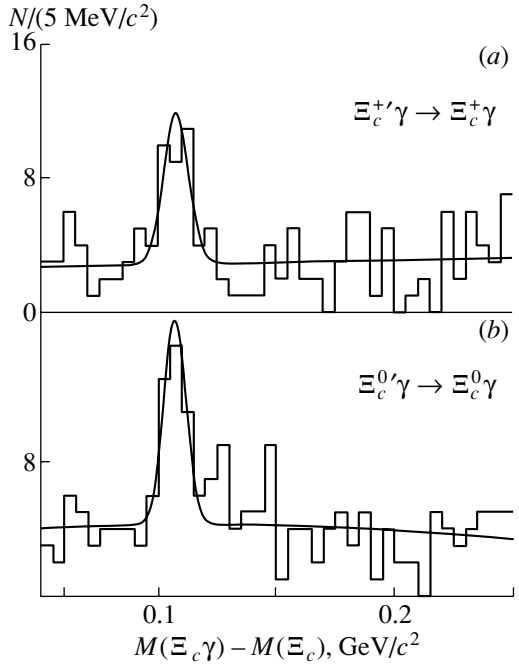

Fig. 3. Distributions with respect to the mass differences (*a*) $M(\Xi_c^+\gamma) - M(\Xi_c^+)$ and (*b*) $M(\Xi_c^0\gamma) - M(\Xi_c^0)$. The solid curve represents a fit to the data.

tains the Λ_c^+ singlet of (cud) quark composition; the triplet formed by the Σ_c^0, Σ_c^+, and Σ_c^{++} states, their quark compositions being (cdd), (cud), and (cuu), respectively; two isotopic doublets, Ξ_c^0, Ξ_c^+ and $\Xi_c^{0\prime}, \Xi_c^{+\prime}$, their quark compositions being (cds) and (cus); and the Ω_c isosinglet of (css) quark composition. The Ξ' and Ξ states differ by the spin state of the wave function for the charmed-quark pair. Since Ξ_c' involves a symmetric diquark wave function, it is expected that these states are heavier than Ξ_c. The decay of Ξ_c' may be accompanied only by photon emission because the mass difference $M(\Xi_c') - M(\Xi_c)$ is less than the pion mass. In 1999, the CLEO Collaboration [22] discovered $\Xi_c^{+\prime}$ and $\Xi_c^{0\prime}$ in the distributions with respect to the mass differences (Fig. 3*a*) $M(\Xi_c^+\gamma) - M(\Xi_c^+)$ and (Fig. 3*b*) $M(\Xi_c^0\gamma) - M(\Xi_c^0)$, correspondingly. A fit to the distributions yielded 25.5 ± 6.5 candidates for $\Xi_c^{+\prime}$ and 28.0 ± 7.1 candidates for $\Xi_c^{0\prime}$, with the resulting mass differences being $M(\Xi_c^{+\prime}) - M(\Xi_c^+) = 107.8 \pm 1.7$ MeV/c^2 and $M(\Xi_c^{0\prime}) - M(\Xi_c^0) = 107.0 \pm 1.4$ MeV/c^2.

The Ω_c^0 baryon still attracts close attention of researchers. A few experiments claimed to discover it in recent years [23–25], but the results of different experiments matched poorly with one another. Moreover, there was no confirmation of the existence of Ω_c from the CLEO Collaboration until recently. In 2001, the CLEO and BELLE Collaborations (see [26] and [27], respectively) published their results obtained by studying the decay process $\Omega_c^0 \to \Omega^-\pi^+$. The two experiments yielded consistent values for the Ω_c^0 mass, $2694.6 \pm 2.6 \pm 1.9$ MeV/c^2 and 2693.7 ± 1.2 MeV/c^2, respectively. Figure 4 displays the invariant-mass distribution for Ω_c^0 candidates that was reconstructed by the CLEO Collaboration on the basis of data on the decay channels $\Omega_c^0 \to \Omega^-\pi^+$, $\Omega_c^0 \to \Omega^-\pi^+\pi^0$, $\Omega_c^0 \to \Omega^-\pi^+\pi^+\pi^-$, $\Omega_c^0 \to \Xi^0 K^-\pi^+$, and $\Omega_c^0 \to \Xi^- K^-\pi^+\pi^+$. After the appearance of the studies reported in [26, 27], one can state that all nine baryon states of spin–parity $J^P = 1/2^+$ that involve one c quark have been reliably recorded in experiments.

In the investigations of $J^P = 3/2^+$ charmed baryons, the priority of course belongs to the CLEO Collaboration, which, in addition to the states discovered previously [28], claimed the discovery of the Σ_c^{*+}

baryon [29] (see Table 2). At the present time, only the existence of Ξ_c^0 has been confirmed by a different experiment (E687) [30]. For the sixplet of $J^P = 3/2^+$ states to become complete, it only remains now to record experimentally the Ω_c^{*0} baryon, whose main decay channel is expected to be $\Omega_c^{*0} \to \Omega_c^0\gamma$.

An excited state of a charmed baryon was first discovered in the ARGUS experiment [31]. The Λ_c^{*+} baryon was reconstructed in the $\Lambda_c^+\pi^+\pi^-$ decay channel. This baryon contains two light quarks (diquark) that have an orbital angular momentum of unity with respect to the heavy (charmed) quark. Therefore, there must exist a doublet of excited charmed baryons having the quantum numbers $J^P = 1/2^-$ and $3/2^-$, and the observed charmed baryon is the $J^P = 3/2^-$ baryon. Presently, it is common practice to denote this state as Λ_{c1}^+ [17], where 1 in the subscript stands for the orbital angular momentum of the light quarks.

In recent years, the CLEO Collaboration discovered four other excited states of charmed baryons. Two of these decay into $\Xi_c^{0\prime}\pi^+$ and $\Xi_c^{+\prime}\pi^-$. The following results were obtained for the mass differences and widths [32]: $M(\Xi_c^{0\prime}\pi^+) - M(\Xi_c^0) = 318.2 \pm 1.3 \pm 2.9$ MeV/c^2 and $\Gamma < 15$ MeV/c^2 for the former and $M(\Xi_c^{+\prime}\pi^-) - M(\Xi_c^+) = 324.0 \pm 1.3 \pm 3.0$ MeV/c^2 and $\Gamma < 15$ MeV/c^2 for the latter case. Two other states decay into $\Xi_c^{*0}\pi^+$ and $\Xi_c^{*+}\pi^-$. Here, the results reported in [33] are $M(\Xi_c^+\pi^+\pi^-) - M(\Xi_c^+) = 348.6 \pm 0.6 \pm 1.0$ MeV/c^2 and $M(\Xi_c^0\pi^+\pi^-) - M(\Xi_c^0) = 347.2 \pm 0.7 \pm 2.0$ MeV/c^2 for the mass differences and $\Gamma < 3.5$ MeV/c^2 and $\Gamma < 6.5$ MeV/c^2 for the widths. The spins and parities of these states were not measured in [32, 33], but the decay channels, masses, and widths are compatible with the assumption that the first two states are the $J^P = 1/2^-$ $\Xi_{c1}(1/2)^+$ and $\Xi_{c1}(1/2)^0$ states analogous to $\Lambda_{c1}(1/2)^+(2593)$, while the other two states are the $J^P = 3/2^-$ $\Xi_{c1}(3/2)^+$ and $\Xi_{c1}(3/2)^0$ states analogous to $\Lambda_{c1}(3/2)^+(2625)$. The main features of excited baryon states are compiled in Table 3. The CLEO Collaboration [34] discovered two other charmed baryons in the distribution with respect to the mass difference $M(\Lambda_c^+\pi^+\pi^-) - M(\Lambda_c^+)$ (Fig. 5). One of these, that of mass 2765.0 ± 2.5 MeV/c^2 and width $\Gamma \approx 50$ MeV/c^2, decays into a final state featuring $\Sigma_c\pi^+$ (possibly, the formation of Σ_c^* also occurs in its decay). The second, which is much narrower, $\Gamma < 8$ MeV/c^2, and which has a mass of 2880.9 ± 2.4 MeV/c^2, undergoes either a decay resulting in the formation of $\Sigma_c\pi$ or a nonresonance decay. Also shown in Fig. 5 to test these statements is the $M(\Lambda_c^+\pi^+\pi^-) - M(\Lambda_c^+)$ distribution for which Λ_c candidates were selected in mass intervals occurring to the left and to the right of actual Λ_c. Experiments that would confirm the discovered states and make it possible to classify them are expected in the future.

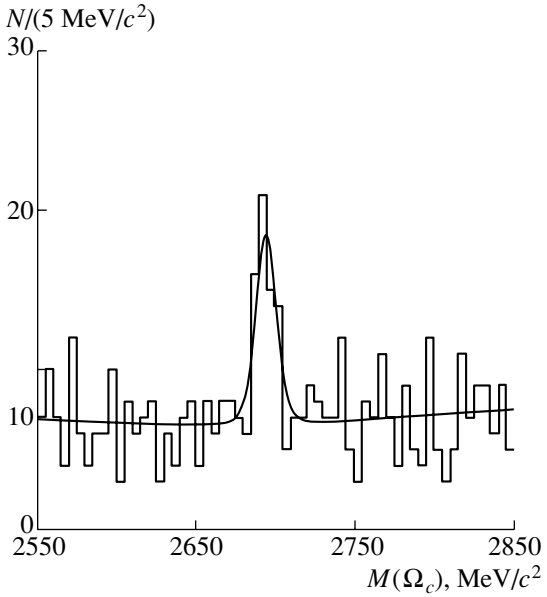

Fig. 4. Invariant-mass distribution for Ω_c^0 candidates reconstructed on the basis of data on the decay channels $\Omega_c^0 \to \Omega^-\pi^+$, $\Omega_c^0 \to \Omega^-\pi^+\pi^0$, $\Omega_c^0 \to \Omega^-\pi^+\pi^+\pi^-$, $\Omega_c^0 \to \Xi^0K^-\pi^+$, and $\Omega_c^0 \to \Xi^-K^-\pi^+\pi^+$. The solid curve represents a fit to the data.

The possibility of recording, at B factories, baryons featuring two c quarks has been vigorously discussed in recent years. In [35], it is stated that the $\Sigma_{cc}^{(*)}$-production cross section $\sigma(\Sigma_{cc}^{(*)})$ with respect to the charm-production cross section $\sigma(c\bar{c})$ is estimated as $\sigma(\Sigma_{cc}^{(*)})/\sigma(c\bar{c}) \sim 7 \times 10^{-5}$; that is, it is commensurate with the cross section for Ω_c-baryon production. In view of the planned severalfold increase in statistics at B factories within the near future, the hopes for discovering there charmed baryons involving two c quarks do not seem unrealistic.

Table 2. $J^P = 3/2^+$ baryons recorded experimentally

Baryon	Mass, MeV/c^2	Main decay channel
Σ_c^{*++}	2519.4 ± 1.5	$\Lambda_c^+\pi^+$
Σ_c^{*+}	2515.9 ± 2.4	$\Lambda_c^+\pi^0$
Σ_c^{*0}	2522.0 ± 1.4	$\Lambda_c^+\pi^-$
Ξ_c^{*+}	2644.6 ± 2.3	$\Xi_c^0\pi^+$
Ξ_c^{*0}	2643.8 ± 1.8	$\Xi_c^+\pi^-$

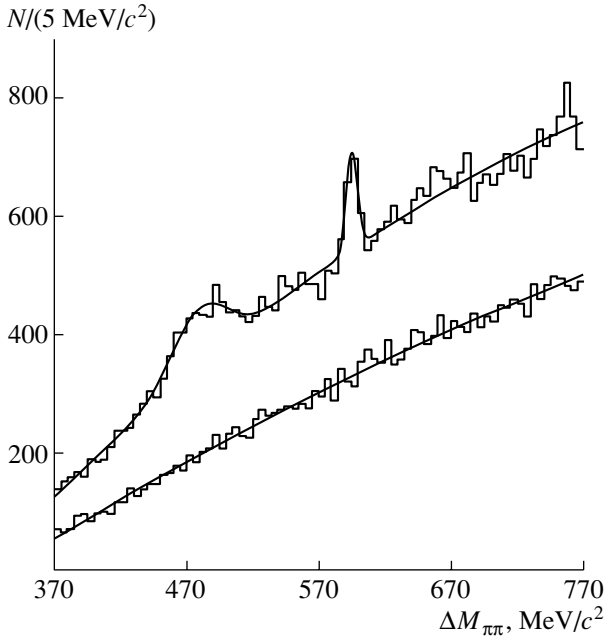

Fig. 5. Distribution with respect to the mass difference $M(\Lambda_c^+\pi^+\pi^-) - M(\Lambda_c^+)$. The lower distribution was obtained for Λ_c candidates selected in mass intervals situated to the left and to the right of actual Λ_c. The solid curves represent fits to the data.

4. LIFETIMES OF CHARMED PARTICLES

Over the past years, a few experiments (E791, SELEX, FOCUS, CLEO, BELLE) have been simultaneously measuring the lifetimes of charmed mesons, the accuracy of the measurements in each experiment being commensurate with the accuracy of world-average values. The results obtained over the last two to three years are quoted in Table 4, along with the values that are averaged over the results of measurements performed to 1998 and to date.

At present, the lifetimes of mesons are known to a percent precision. For many years, the accuracy in measuring the lifetimes of charmed particles in fixed-target experiments was considerably higher than the accuracy of measurements in experiments at electron–positron colliders. But new-generation experiments at electron–positron colliders proved to be quite competitive in measuring the lifetimes of charmed particles, owing primarily to the use of precise vertex detectors. The results listed in Table 4 were obtained by different experimental methods; therefore, the excellent agreement between the results of the different experiments is yet another argument in favor of their reliability.

Table 3. Excited charmed-baryon states detected experimentally

Baryon	Mass, MeV/c^2	Main decay channel
$\Lambda_{c1}(1/2)^+$	2593.6 ± 1.0	$\Sigma_c^0\pi^+$
$\Lambda_{c1}(3/2)^+$	2626.4 ± 0.9	$\Lambda_c^+\pi^+\pi^-$
$\Xi_{c1}(1/2)^+$	2789.4 ± 3.7	$\Xi_c^{0\prime}\pi^+$
$\Xi_{c1}(1/2)^0$	2788.2 ± 3.8	$\Xi_c^{+\prime}\pi^-$
$\Xi_{c1}(3/2)^+$	2814.0 ± 2.0	$\Xi_c^{0*}\pi^+$
$\Xi_{c1}(3/2)^0$	2817.6 ± 3.0	$\Xi_c^{+*}\pi^-$

The high experimental accuracy in measuring the lifetimes of charmed particles provides excellent opportunities for testing nonperturbative QCD. This is of importance because theoretical approaches applied here are analogous to those that are used to solve other problems in heavy-quark physics.

The ratio of the charged-to-neutral D-meson lifetimes, $\tau(D^+)/\tau(D^0)$, is equal to 2.54 ± 0.05. The distinction between the lifetimes of the charged and neutral D mesons is explained by the following main reasons [44].

(i) In contrast to D^0 decays, the decays of D^+ mesons lead to final states involving two antiquarks of the same flavor ($\bar{d}$). Because of the destructive interference between quark diagrams, the probability for the nonleptonic decays of D^+ mesons decreases, with the result that the D^+-meson lifetime increases in relation to the D^0 lifetime.

(ii) Diagrams involving W-boson exchange contribute only to D^0-meson decays; therefore, the D^0 lifetime decreases, causing an increase in the difference of the D^+- and D^0-meson lifetimes. Although the contribution of the diagram involving W-boson exchange must be suppressed because of the violation of the helicity-conservation law, this suppression disappears upon the emission of a bremsstrahlung photon by a light antiquark, so that the contribution of the diagram may increase.

Upon taking into account the aforementioned factors, one obtains, for the above lifetime ratio, a qualitative estimate that agrees with experimental data to within 10–20%. In order to reach better agreement between theoretical and experimental results, one has to include higher order corrections [44].

The contribution of the aforementioned processes to the meson-lifetime difference can be estimated on the basis of experimental data. Denoting by Γ_{SP} and Γ_{SL} the partial widths with respect to decays caused by the spectator and the semileptonic mechanism, correspondingly, and by Γ_{PI} and Γ_{WX} the contributions to the decay width from the processes described in items (i) and (ii), correspondingly, we can represent

Table 4. Lifetimes of charmed mesons (in femtoseconds)

Experiment	D^0	D^+	D_s^+
BELLE [36]	$414.6 \pm 1.7^{+1.9}_{-1.8}$	$1037 \pm 12^{+5}_{-6}$	$485.4^{+7.9+2.9}_{-7.7-4.2}$
CLEO [37]	$408.5 \pm 4.1^{+3.5}_{-3.4}$	$1033.6 \pm 22.1^{+9.9}_{-12.7}$	$486.3 \pm 15.0^{+4.9}_{-5.1}$
E791 [38]	$413 \pm 3 \pm 4$		$518 \pm 14 \pm 7$
FOCUS [39, 40]	409.2 ± 1.3		506 ± 8
SELEX [41, 42]	$407.9 \pm 6.0 \pm 4.3$	1070 ± 36	$472.5 \pm 17.5 \pm 6.6$
PDG98 [43]	415 ± 4	1057 ± 15	467 ± 17
New average value	413.3 ± 1.7	1044.1 ± 9.1	492.0 ± 5.3

Table 5. Lifetimes of charmed baryons (in femtoseconds)

Experiment	Λ_c	Ξ_c^+	Ξ_c^0
CLEO [45]	$179.6 \pm 6.9 \pm 4.4$	$503.6 \pm 47 \pm 18$	
FOCUS [46]	$204.6 \pm 3.4 \pm 2.0$	$439 \pm 22 \pm 9$	109^{+10}_{-9}
SELEX [41]	$198.1 \pm 7.0 \pm 5.6$		
PDG98 [43]	200^{+11}_{-10}	340^{+60}_{-40}	98^{+23}_{-15}
New average value	191 ± 5	433 ± 19	106^{+9}_{-8}

the charged-to-neutral D-meson-lifetime ratio in the form

$$\frac{\tau(D^+)}{\tau(D^0)} = \frac{\Gamma_{\rm SP} + \Gamma_{\rm WX} + \Gamma_{\rm SL}}{\Gamma_{\rm PI} + \Gamma_{\rm SL}}.$$

The ratio $\Gamma_{\rm SP}/\Gamma_{\rm PI}$ can be determined from a comparison of the probabilities of the Cabibbo-allowed decay $D^+ \to K^-\pi^+\pi^+$ and the doubly Cabibbo-suppressed decay $D^+ \to K^+\pi^-\pi^+$,

$$\frac{{\rm Br}(D^+ \to K^+\pi^+\pi^-)}{{\rm Br}(D^+ \to K^-\pi^+\pi^-)} = \frac{\Gamma_{\rm SP}}{\Gamma_{\rm PI}} \tan^4\theta_{\rm C},$$

where $\theta_{\rm C}$ is the Cabibbo angle. By using, for the probability ratio, the world-average value [17]

$$\frac{{\rm Br}(D^+ \to K^+\pi^+\pi^-)}{{\rm Br}(D^+ \to K^-\pi^+\pi^-)} = (0.75 \pm 0.16)\%,$$

we find for the width ratio that $\Gamma_{\rm PI}/\Gamma_{\rm SP} \sim 0.4$.

Substituting the value obtained for $\Gamma_{\rm PI}/\Gamma_{\rm SP}$ into the lifetime ratio and employing the fact that the widths with respect to semileptonic decays are well known, we obtain the estimate $\Gamma_{\rm WX}/\Gamma_{\rm SP} \sim 0.3$.

Owing to measurements performed in recent years, the accuracy in determining the lifetime ratio for D_s^+ and D^0 mesons has been considerably improved: $\tau(D_s^+)/\tau(D^0) = 1.17 \pm 0.02$. There are a few factors (the contribution of each of them is 3–5%) that affect the ratio $\tau(D_s^+)/\tau(D^0)$. These include the violation of $SU(3)$ symmetry; the destructive interference of the Cabibbo-suppressed decays of D_s^+ mesons; and the additional decay channel $D_s^+ \to \tau^+\nu_\tau$, which is absent for the neutral D^0 meson. The total effect from taking these contributions into account leads to the ratio $\tau(D_s^+)/\tau(D^0) \approx 1.03$–$1.07$. The remaining 10% distinction is probably due to the distinction between the contributions of the annihilation diagram (contributing only to D_s^+-meson decays) and the diagram involving W-boson exchange and contributing only to D^0-meson decays. Taking into account the relation

$$\frac{\tau(D_s^+)}{\tau(D^0)} = \frac{\Gamma_{\rm SP} + \Gamma_{\rm WX} + \Gamma_{\rm SL}}{\Gamma_{\rm SP} + \Gamma_{\rm WA} + \Gamma_{\rm SL}},$$

one can quantitatively estimate the possible contribution of the annihilation diagram ($\Gamma_{\rm WA}$) to the lifetime ratio as $\Gamma_{\rm WA}/\Gamma_{\rm SP} \sim 0.1$.

The accuracy in determining baryon lifetimes has also been improved considerably in recent years—its current values are 2% for Λ_c^+ and about 10% for Ξ_c^0 (see Table 5). There are no new results for the Ω_c baryon, and an additional measurement of the Ω_c lifetime is of course necessary.

The following effects make the main contribution to the distinctions between charmed-baryon lifetimes: (i) the destructive interference between quark diagrams, which arises if a u quark enters into the

composition of a baryon (this is so for the Λ_c^+ and Ξ_c^+ baryons); (ii) the constructive interference between quark diagrams in the case of a spectator s quark (Ξ_c^+, Ξ_c^0); and (iii) the exchange-diagram contribution, which is not suppressed for baryons by the requirement of helicity conservation and which is of importance in the case where a d quark enters into the composition of a baryon (Λ_c^+, Ξ_c^0).

Considering that these factors affect the lifetimes of charmed baryons differently, one can obtain the following predictions for the hierarchy of the lifetimes in question [47–49]:

$$\tau(\Omega_c^0) \approx \tau(\Xi_c^0) < \tau(\Lambda_c^+) < \tau(\Xi_c^+),$$

$$\tau(\Omega_c^0) < \tau(\Xi_c^0) < \tau(\Lambda_c^+) \approx \tau(\Xi_c^+),$$

$$\tau(\Omega_c^0) < \tau(\Xi_c^0) < \tau(\Lambda_c^+) < \tau(\Xi_c^+).$$

All of them describe qualitatively the relationships between the lifetimes, but it is of course necessary to improve the accuracy of the predictions substantially.

5. LEPTONIC DECAYS OF D MESONS

The leptonic decay of charmed mesons is the simplest to describe. In this case, the effect of strong interaction can be parametrized by using one parameter referred to as the decay constant. The matrix element describing the decay of the charged pseudoscalar meson $M_{Q\bar{q}}$ into a lepton (l) and a neutrino (ν) can be expressed as [50]

$$\Gamma(M_{Q\bar{q}} \to l\nu) = \frac{G_F^2}{8\pi}|V_{qQ}|^2 f_M^2 M m_l^2 \left(1 - \frac{m_l^2}{M^2}\right)^2,$$

where f_M is the decay constant; V_{qQ} is an element of the Kobayashi–Maskawa matrix [51]; and m_l and M are the masses of the lepton and the charged meson $M_{Q\bar{q}}$, respectively. The decay constant f_M describes the probability of quark annihilation. In the limit of an infinitely heavy quark, the decay constant f_M is given by the nonrelativistic formula $f_M^2 = 12|\psi(0)|^2/M$, where $\psi(0)$ is the wave function for a light antiquark $\bar{q}$ and a heavy quark Q at zero distance between them. The factor m_l^2 appeared in this formula because of suppression induced by the violation of the helicity-conservation law. For the charmed meson $M_{Q\bar{q}}$ of zero spin, the configuration that is favorable in helicity for the decay $M_{Q\bar{q}} \to l\nu$ violates the law of angular-momentum conservation. This leads to the suppression of decays into lighter leptons in relation to decay into a heavier lepton.

Measurement of the constants f_D and f_{D_s} is of paramount importance because this makes it possible to obtain reliable estimates for the B-meson decay constant f_B. At present, it is next to impossible in practice to extract the value of the constant f_B from the results obtained by measuring the probabilities of leptonic B-meson decays. Even for $B^+ \to \tau^+\nu_\tau$, the expected decay probability is about a few units of 10^{-5} [at the same time, the existing experimental limit is an order of magnitude worse: $\mathrm{Br}(B^+ \to \tau^+\nu_\tau) < 5.6 \times 10^{-4}$].

The decay processes $D_s^+ \to \mu^+\nu_\mu$ and $D_s^+ \to \tau^+\nu_\tau$ were explored in the experiments reported in [52–55]. All four experiments, which were performed at LEP, also measured $\mathrm{Br}(D_s^+ \to \tau^+\nu_\tau)$ by reconstructing the decay chain [56]

$$e^+e^- \to Z \to c\bar{c} \to D_s^{*+}X,$$
$$D_s^{*+} \to D_s^+\gamma, \quad D_s^+ \to \tau^+\nu_\tau, \quad \tau^+ \to l^+\nu\bar{\nu}$$
$$(l = e, \mu).$$

Only the reaction $D_s^+ \to \tau^+\nu_\tau$ from the decay process $Z \to c\bar{c}$ was included in the analysis, since the use of $D_s^+ \to \tau^+\nu_\tau$ from the decay process $Z \to b\bar{b}$ leads to a large systematic error stemming from a poor knowledge of the cross section for D_s-meson production in the decay process $Z \to b\bar{b}$. The result averaged over all measurements at LEP [56] is $\mathrm{Br}(D_s^+ \to \tau^+\nu_\tau) = (6.05 \pm 1.04 \pm 1.51)\%$, the main contribution to the systematic uncertainty here coming from the error in measuring the probability of the decay process $D_s^+ \to \phi\pi^+$.

In the BEATRICE experiment, the authors of [57] measured the branching ratio for the decay process $D_s^+ \to \mu^+\nu_\mu$ by studying the distribution with respect to the muon-momentum component orthogonal to the D_s-meson momentum. For the branching fraction extracted in this way, the resulting value is $\mathrm{Br}(D_s^+ \to \mu^+\nu_\mu) = (0.83 \pm 0.23 \pm 0.19)\%$. The experimental results obtained by measuring the decay constant f_{D_s} are quoted in Table 6. Along with the values of f_{D_s} that were taken directly from original studies, also given there are the values of f_{D_s} that were rescaled on the basis of present-day data on the quantities used to calculate f_{D_s} [56] (the distinctions are due to refining the D_s-meson lifetime).

The accuracy in measuring f_{D_s} is constrained predominantly by the accuracy in measuring the branching ratio for the decay $D_s^+ \to \phi\pi^+$. In this connection, the result obtained by the BES Collaboration [55] without recourse to information about the branching ratio for the decay process $D_s^+ \to \phi\pi^+$ is worthy of special mention. The BES Collaboration completely reconstructed three events in which one of the mesons in question (D_s^+ or D_s^-) decayed into a lepton and a neutrino. Upon performing normalization to the

Table 6. Experimental data on the decay constant f_{D_s}

Experiment	Value of f_{D_s}, MeV	
	(published)	(refined)
WA75 [52]	$232 \pm 45 \pm 20 \pm 41$	$239 \pm 47 \pm 52$
CLEO II [54]	$280 \pm 19 \pm 28 \pm 34$	267 ± 187
E653 [53]	$194 \pm 35 \pm 20 \pm 14$	$192 \pm 34 \pm 31$
BES [55]	$430^{+150}_{-130} \pm 40$	$418^{+180+41}_{-83-28}$
BEATRICE [57]	$323 \pm 44 \pm 12 \pm 34$	$309 \pm 43 \pm 35$
L3 [58]	$309 \pm 58 \pm 33 \pm 38$	$273 \pm 52 \pm 43$
OPAL [59]	$286 \pm 44 \pm 41$	$271 \pm 41 \pm 39$
ALEPH [56]	$285 \pm 20 \pm 40$	$273 \pm 52 \pm 43$
DELPHI [56]	$330 \pm 82 \pm 58$	$285 \pm 71 \pm 61$
Averaged [56]		$264 \pm 15 \pm 33$

number of events in which the members of this collaboration were able to reconstruct at least one D_s meson, they determined the branching ratio for the decay process $D_s^+ \to \mu^+\nu_\mu$ and the decay constant f_{D_s}. Unfortunately, the accuracy of this method is not high because of low statistics, but its prospects seem quite good in view of the planned increase in the luminosity of the BEPC accelerator and in view of the intention of the CLEO Collaboration to study charm physics (see Section 10).

Data on the decay process $D^+ \to \mu^+\nu_\mu$ are much scarcer. The MARK III Collaboration [60] was able to set an upper limit on the branching ratio for the decay process $D^+ \to \mu^+\nu_\mu$ and to determine the corresponding constraint on the decay constant f_D, $f_D < 290$ MeV. In the BES experiment [61] at a c.m. energy of 4.03 GeV, the reaction $e^+e^- \to D^{*+}D^-$ was used in searches for a purely leptonic decay of a charged D meson. Only one event was recorded where D^{*+} decayed according to the scheme $D^{*+} \to \pi^+D^0$, $D^0 \to K^-\pi^+$, while D^- decayed through the channel $D^- \to \mu^-\bar{\nu}_\mu$. The resulting estimates for the branching fraction and the decay constant are $\mathrm{Br}(D^- \to \mu^-\bar{\nu}_\mu) = (0.08^{+0.16+0.05}_{-0.05-0.02})\%$ and $f_D = 300^{+180+80}_{-150-40}$ MeV.

6. SEMILEPTONIC DECAYS OF CHARMED HADRONS

The q^2 dependence of the derivative of the $D \to Kl\nu$ decay width with respect to this variable has the form

$$\frac{d\Gamma}{dq^2} = \frac{G_F^2}{24\pi^3}|V_{cs}|^2 P_K^3 f_+(q^2).$$

In this formula, weak interaction is represented by the product $G_F V_{cs}$, where G_F is the coupling constant for weak interaction and V_{cs} is the matrix element for the transition of a c quark into an s quark. The effect of strong interaction is completely absorbed in relevant form factors. One form factor describes the degree to which the D- and K-meson wave functions overlap. For the $D \to K$ transition (in the limit of zero lepton mass), everything is determined by the form factor $f_+(q^2)$, which specifies the amplitude of K-meson formation from the $(s\bar{q})$ pair, $q^2 = M^2(l\nu)$ being the square of the momentum transfer from the c quark involved. The q^2 dependence of the form factor is traditionally parametrized in the form

(i) $f(q^2) = f(q^2_{\max})\exp(-\alpha(q^2_{\max} - q^2)) = f(0)\exp(\alpha q^2)$

or in the form

(ii) $f(q^2) = f(0)/(1 - q^2/M^2_{\mathrm{pole}})$, where the nearest exchange pole with appropriate quantum numbers is that at $M_{\mathrm{pole}} \approx 2.1$ GeV/c^2.

So far, the q^2 dependence of the form factor over the entire range of this variable has been measured only for the Cabibbo-allowed decay process $D^0 \to K^-l^+\nu$. The most precise measurements of the form factor were performed by the E687 Collaboration [62], $f_+(0) = 0.71 \pm 0.03 \pm 0.03$ and $M_{\mathrm{pole}} = 1.87^{+0.11+0.07}_{-0.08-0.08}$ GeV/c^2, and by the CLEO Collaboration [63], $f_+(0) = 0.77 \pm 0.01 \pm 0.04$ and $M_{\mathrm{pole}} = 2.00 \pm 0.12 \pm 0.18$ GeV/c^2. These two results determine almost completely the world-average value of $f_+(0) = 0.76 \pm 0.03$. Figure 6 displays the form factor as a function of q^2 according to the measurements of the CLEO Collaboration for the decay

Table 7. Theoretical predictions for form-factor values at $q^2 = 0$ for $D \to Kl^+\nu(f_+)$ and for $D \to \bar{K}^*l^+\nu(A_1, A_2, V)$ along with experimental data

	$f_+(0)$	$A_2(0)/A_1(0)$	$V(0)/A_1(0)$
ISGW2 [64]		1.3	2.1
BKS [65]		$0.78 \pm 0.08^{+0.17}_{-0.13}$	$2.00 \pm 0.19^{+0.20}_{-0.25}$
LMMS [66]	0.63 ± 0.08	0.38 ± 0.38	1.70 ± 0.21
Wuppertal [67]	0.84 ± 0.16	0.96 ± 0.66	1.83 ± 0.64
APE [68]	0.78 ± 0.08	0.73 ± 0.54	1.61 ± 0.42
BBD [69]	0.6	1.2	2.2
$D \to Kl\nu$	0.76 ± 0.03		
$D \to \bar{K}^*l\nu$		0.78 ± 0.07	1.82 ± 0.09
$D_s \to \phi l\nu$		1.60 ± 0.24	1.92 ± 0.32

process $D^0 \to K^-l^+\nu$. In this figure, the dashed and the dash-dotted curve represent, respectively, the combinatorial-background level and the contribution from $D \to \bar{K}^*l\nu$ decays. Of particular interest is measurement of the q^2 dependence of the form factor f_+ for the Cabibbo-suppressed decay $D^0 \to \pi^-l^+\nu$. In this case, the accessible range of q^2 is much wider ($q^2_{\max} = M_D^2 - M_K^2 = 1.88$ GeV$^2/c^2$ for the Cabibbo-allowed decay $D \to Kl\nu$ and $q^2_{\max} = M_D^2 - M_\pi^2 = 2.98$ GeV$^2/c^2$ for the Cabibbo-suppressed decay $D \to \pi l\nu$), and one can hope to determine the functional dependence of the form factor on q^2 more precisely.

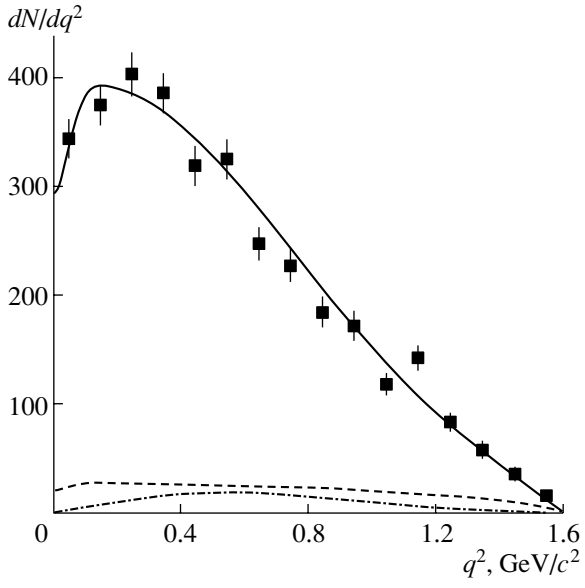

Fig. 6. Form factor for the decay process $D^0 \to K^-l^+\nu$ as a function of q^2. The dashed and the dash-dotted curve represent, respectively, the combinatorial-background level and the contribution from $D \to \bar{K}^*l\nu$ decays. The solid curve corresponds to a fit to experimental data.

Three form factors—the axial-vector form factors $A_1(q^2)$ and $A_2(q^2)$ and the vector form factor $V(q^2)$—are of importance for the decay process $D \to \bar{K}^*l\nu$. In this case, the amplitude for the semileptonic decay has a much more complicated form: $A = G_F/\sqrt{2}V_{cs}L^\mu H_\mu$, where the strong-interaction contribution H_μ is given by [50]

$$H_\mu = A_1(q^2)\epsilon_\mu(M_{DK^*}) - V(q^2) \cdot 2i\epsilon_{\mu\nu\rho\sigma}\epsilon^\nu P^\rho K^\sigma/(M_{DK^*}) - A_2(q^2)(\epsilon_\nu P^\nu)(P+K)_\mu/(M_{DK^*}).$$

Here, M_{DK^*} is the sum of the D and K^* masses, P^μ is the momentum of the D meson, and ϵ^μ (K^μ) is the polarization (momentum) of the K^* meson. The ratio of the form factors is determined by fitting the corresponding distributions in the angle between the momenta of secondary particles. The experimental results are represented as the form-factor ratio at $q^2 = 0$, $r_2 = A_2(0)/A_1(0)$ and $r_V = V(0)/A_1(0)$, while the q^2 dependence of the form factors involved is parametrized as $A, V(q^2) = f(0)/(1 - q^2/M^2_{A,V})$, where $M_V \approx 2.1$ GeV$/c^2$ and $M_A \approx 2.5$ GeV$/c^2$. The averaged experimental values of the form factors and theoretical predictions for them are quoted in Table 7. The BEATRICE Collaboration [70] investigated 763 events of the semileptonic decay $D^+ \to \bar{K}^{*0}l^+\nu$ and measured the form-factor ratios: $r_2 = 1.00 \pm 0.15 \pm 0.03$ and $r_V = 1.45 \pm 0.23 \pm 0.07$. For $D^+ \to \bar{K}^{*0}l^+\nu$ decays, the E791 collaboration [71] investigated 3000 events involving an electron and 3000 events involving a muon in the final state. The accuracy of this measurement determines almost

Table 8. Values of $\sigma\mathrm{Br}$ (in picobarns) for semileptonic decays of baryons

	ARGUS [75]	CLEO II [76]
$\sigma(e^+e^- \to \Lambda_c X)\mathrm{Br}(\Lambda_c \to \Lambda e^+ X)$	$4.20 \pm 1.28 \pm 0.71$	$4.87 \pm 0.28 \pm 0.69$
$\sigma(e^+e^- \to \Lambda_c X)\mathrm{Br}(\Lambda_c \to \Lambda \mu^+ X)$	$3.91 \pm 2.02 \pm 0.90$	$4.43 \pm 0.51 \pm 0.64$
Averaged value	$4.15 \pm 1.03 \pm 1.18$	$4.77 \pm 0.25 \pm 0.66$
$\sigma(e^+e^- \to \Xi_c^0 X)\mathrm{Br}(\Xi_c^0 \to \Xi^- e^+ X)$		$0.63 \pm 0.12 \pm 0.10$
$\sigma(e^+e^- \to \Xi_c^0 X)\mathrm{Br}(\Xi_c^0 \to \Xi^- l^+ X)$	$0.74 \pm 0.24 \pm 0.09$	
$\sigma(e^+e^- \to \Xi_c^+ X)\mathrm{Br}(\Xi_c^+ \to \Xi^0 e^+ X)$		$1.55 \pm 0.33 \pm 0.25$
$\sigma(e^+e^- \to \Omega_c^0 X)\mathrm{Br}(\Omega_c^0 \to \Omega^- e^+ \nu_e X)$	$0.52 \pm 0.23 \pm 0.13$	

completely the accuracy in measuring the ratio of the form factors r_2 and r_V. The E791 Collaboration [72] improved the accuracy in measuring r_2 and r_V for the semileptonic decay $D_s^+ \to \phi l^+ \nu$ as well. If we assume, for a first approximation, that $SU(3)$ symmetry holds, then the replacement of the spectator $\bar{d}$ quark by the spectator $\bar{s}$ quark (in going over from the D^+ to the D_s^+ meson) must not have a sizable effect on form-factor ratios. All of the models quoted in the literature predict the equality of r_2 and r_V for the decays $D^+ \to \bar{K}^* l^+ \nu$ and $D_s^+ \to \phi l^+ \nu$. While the value of r_V complies with the expectations within $SU(3)$ symmetry in the quark flavor, the values of r_2 for the semileptonic decays $D^+ \to \bar{K}^* l^+ \nu$ and $D_s^+ \to \phi l^+ \nu$ exhibit distinctions by nearly three standard deviations.

In order to investigate in detail the q^2 dependence of the form factors for a semileptonic decay involving the production of a vector meson and to study the q^2 dependence of form factors for semileptonic Cabibbo-suppressed decays, it is necessary to enlarge the statistics considerably. Upon processing the entire body of accumulated data, the FOCUS Collaboration hopes to reconstruct 50 000 $D \to \bar{K}^* l\nu$ decays, 30 000 $D \to Kl\nu$ decays, 10 000 $D_s \to \phi l\nu$ decays, and about 5000 Cabibbo-suppressed $D \to \pi l\nu$ and $D \to \rho l\nu$ [73] decays. With such vast statistics, one can perform a detailed investigation of the q^2 dependence of the form factors in question and to compare experimental data with theoretical results.

Experimental data on semileptonic decays of baryons ensure additional information in choosing the best theoretical model. The branching ratios for semileptonic decays of baryons depend significantly on the choice of model for the heavy-baryon wave function and on the nature of the q^2 dependence of the hadronic form factor. According to estimates presented in [74], the semileptonic widths may differ considerably, $\Gamma(\Xi_c \to e^+ \nu X) > 2\Gamma(\Lambda_c \to e^+ \nu X)$, while the branching fraction of the semileptonic decay of Ω_c^0 may amount to 10–15%. Measurement of the branching ratios for the semileptonic decays of charmed baryons will make it possible to estimate the contribution of the constructive interference of s quarks in the final state.

Unfortunately, no advances toward solving this problem have been made in recent years. As before, the main contribution to measurements of semileptonic decays of charmed baryons comes from ARGUS and CLEO experiments (see [75] and [76], respectively). The results of these experiments devoted to determining the branching fractions for all known semileptonic decays are given in Table 8. It goes without saying that, in order to perform a detailed comparison of the branching fractions for semileptonic decays of charmed baryons with the predictions of theoretical models, it is necessary to

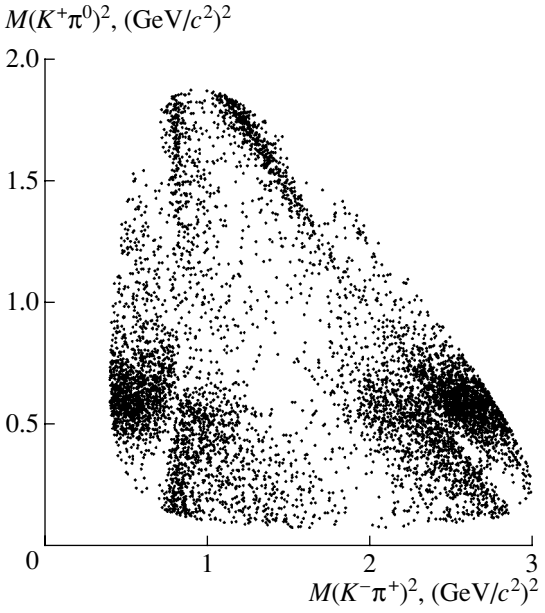

Fig. 7. Dalitz distribution for 7070 $D^0 \to K^-\pi^+\pi^0$ candidates according to data of the CLEO Collaboration.

Table 9. Resonance structure of the decay $D_s^+ \to \pi^+\pi^+\pi^-$

Decay channel	E791 [79]		FOCUS [80]	
	branching fraction, %	phase shift, deg	branching fraction, %	phase shift, deg
$f_0(980)\pi^+$	$56.5 \pm 4.3 \pm 4.7$	0 (fix.)	94.4 ± 2.5	0 (fix.)
$\rho(770)\pi^+$	$5.8 \pm 2.3 \pm 3.7$	$109 \pm 24 \pm 5$		
$\rho(1450)\pi^+$	$4.4 \pm 2.1 \pm 0.2$	$162 \pm 26 \pm 17$	4.1 ± 0.7	188 ± 14
$f_2(1270)\pi^+$	$19.7 \pm 3.3 \pm 0.6$	$133 \pm 13 \pm 28$	9.8 ± 1.2	140 ± 6
$S_0(1475)\pi^+$			17.4 ± 2.2	250 ± 4
$f_0(1370)\pi^+$	$32.4 \pm 7.7 \pm 1.9$	$198 \pm 19 \pm 27$		
Nonresonance production	$0.5 \pm 1.4 \pm 1.7$	$181 \pm 94 \pm 51$	25.5 ± 4.4	246 ± 4

Table 10. Resonance structure of the decay $D^+ \to \pi^+\pi^+\pi^-$

Decay channel	Confidence level 0.001%		Confidence level 75%	
	branching fraction, %	phase shift, deg	branching fraction, %	phase shift, deg
$\rho(770)\pi^+$	20.8 ± 2.4	0 (fix.)	$33.6 \pm 3.2 \pm 2.2$	0 (fix.)
Nonresonance production	38.6 ± 9.7	150 ± 12	$7.8 \pm 6.0 \pm 2.7$	$57 \pm 20 \pm 6$
$f^0(980)\pi^+$	7.4 ± 1.4	152 ± 16	$6.2 \pm 1.3 \pm 0.4$	$165 \pm 11 \pm 3$
$f_2(1270)\pi^+$	6.3 ± 1.9	103 ± 16	$19.4 \pm 2.5 \pm 0.4$	$57 \pm 8 \pm 3$
$f_0(1370)\pi^+$	10.7 ± 3.1	143 ± 10	$2.3 \pm 1.5 \pm 0.8$	$105 \pm 18 \pm 1$
$\rho(1450)\pi^+$	22.6 ± 3.7	46 ± 15	$0.7 \pm 0.7 \pm 0.3$	$319 \pm 39 \pm 11$
$\sigma\pi^+$			$46.3 \pm 9.0 \pm 2.1$	$206 \pm 8 \pm 5$

improve the accuracy of experimental results significantly. There is every reason to believe that this will be done in the near future.

7. NONLEPTONIC DECAYS OF D MESONS

Three-particle final states provide rich possibilities for studying the interference between intermediate resonance states and for exploring the effect of final-state interactions on decay probabilities. Three-particle final states arise predominantly upon charmed-particle decays through intermediate resonances. These intermediate resonances manifest themselves as nonuniform distributions of events over phase space in two-dimensional distributions with respect to the squares of the invariant masses of final-state-particle pairs. Such distributions are referred to as Dalitz distributions [77]. Figure 7 displays a characteristic Dalitz distribution that was obtained by the CLEO Collaboration [78] for the decay process $D^0 \to K^-\pi^+\pi^0$. Since all events of this three-body decay have the same final state, resonances occurring in the same phase-space region will interfere with one another. Owing to this, it is possible to measure the amplitudes and relative phases of intermediate resonances. One can even deduce information about very broad intermediate resonances by investigating their interference with comprehensively studied resonances.

The E791 and FOCUS Collaborations performed (in [79] and [80], respectively) an analysis of the Dalitz distributions for the decay process $D_s^+ \to \pi^+\pi^+\pi^-$. This decay is of interest because it receives contributions both from the spectator diagram involving the production of an intermediate $s\bar{s}$ resonance, which decays into a $\pi^+\pi^-$ pair either directly or owing to final-state interaction, and from the annihilation diagram involving the production of a rho meson decaying into a $\pi^+\pi^-$ pair. A high probability of rho-meson production would be indicative of the annihilation-diagram contribution or of the final-state-interaction effect. The results of the analysis in question are given in Table 9. The branching fraction obtained for the decay process $D_s \to \rho\pi^+$ from a fit to data is quite modest. A large contribution of the $f_0(980)$ meson,

Table 11. Resonance structure of the decay $D^+ \to K^-\pi^+\pi^+$

Decay channel	Confidence level 10^{-11}%		Confidence level 95%	
	branching fraction, %	phase shift, deg	branching fraction, %	phase shift, deg
Nonresonance production	90.9 ± 2.6	0 (fix.)	$13.0 \pm 5.8 \pm 2.6$	$349 \pm 14 \pm 8$
$\bar{K}^*(892)\pi^+$	13.8 ± 0.5	54 ± 2	$12.3 \pm 1.0 \pm 0.9$	0 (fix.)
$\bar{K}_0^*(1430)\pi^+$	30.6 ± 1.6	54 ± 2	$12.5 \pm 1.4 \pm 0.4$	$48 \pm 7 \pm 10$
$\bar{K}_2^*(1430)\pi^+$	30.4 ± 0.1	33 ± 8	$0.5 \pm 0.1 \pm 0.2$	$306 \pm 8 \pm 6$
$\bar{K}^*(1680)\pi^+$	3.2 ± 0.3	66 ± 3	$2.5 \pm 0.7 \pm 0.2$	$28 \pm 13 \pm 15$
$\kappa\pi^+$			$47.8 \pm 12.1 \pm 3.7$	$187 \pm 8 \pm 17$

which has a mass below the threshold for $K\bar{K}$ production, but which is produced quite frequently owing to a large width (about 300 MeV/c^2), is worthy of special note.

The results of the E791 Collaboration that were obtained by analyzing the Dalitz distributions for the decay process $D^+ \to \pi^+\pi^+\pi^-$ [81] are given in Table 10. An unsatisfactory description at a confidence level of 10^{-5} is obtained if all known resonances are included in a fit to the relevant Dalitz distribution. At the same time, the description appears to be excellent as soon as a broad scalar sigma meson that is thus far unknown is included in a fit, the sigma-meson parameters as determined from this fit being $M_\sigma = 478^{+24}_{-23} \pm 17$ MeV/c^2 and $\Gamma_\sigma = 324^{+42}_{-40} \pm 21$ MeV/c^2. Numerous tests were conducted (additional vector and tensor states were included in the fit), but the analysis revealed that the best description is obtained upon the inclusion of a scalar meson.

Analysis of the decay process $D^+ \to K^-\pi^+\pi^+$ runs into two problems: First, the contribution of nonresonance production is very large (more than 2/3). Second, a satisfactory description cannot be achieved even under the assumption of a large nonresonance contribution (the confidence level is 10^{-11}). The E791 Collaboration [82] performed an analysis of the Dalitz distribution for the decay process $D^+ \to K^-\pi^+\pi^+$ using vast statistics that include more than 15 000 reconstructed events. The results of this analysis are given in Table 11. By analogy with what was done for the decay process $D^0 \to \pi^-\pi^+\pi^+$, a previously unknown scalar resonance κ was included in the analysis. This resulted in a sevenfold reduction of the nonresonance contribution, with the confidence level reaching 95%. The κ-meson parameters as determined from the fit are $M_\kappa = 797 \pm 19 \pm 42$ MeV/c^2 and $\Gamma_\kappa = 410 \pm 43 \pm 85$ MeV/c^2.

The CLEO Collaboration [78] performed an analysis of the Dalitz distribution for the decay process $D^0 \to K^-\pi^+\pi^0$ using vast statistics of more than 7000 reconstructed events. (The statistics of previous investigations reported in [83–85] did not exceed 1000 events). Only D^0 mesons from the de-

Table 12. Resonance structure of the decay $D^0 \to K^-\pi^+\pi^0$

Decay channel	Branching fraction, %	Phase shift, deg
$K^-\rho^+$	78.7 ± 2.0	0 (fix.)
$K^{*-}\pi^+$	16.1 ± 0.7	163 ± 2.3
$\bar{K}^{*0}\pi^0$	12.7 ± 0.9	-0.2 ± 3.3
$K^-\rho(1700)^+$	5.7 ± 0.8	171 ± 6
$K_0(1430)^+\pi^-$	3.3 ± 0.6	55.5 ± 5.8
$\bar{K}_0(1430)^0\pi^0$	4.1 ± 0.6	166 ± 5
$K^*(1680)^-\pi^+$	1.3 ± 0.3	103 ± 8
Nonresonance production	7.5 ± 0.9	31 ± 4

Table 13. Experimental results for the ratio $R^{K\pi}_{\mathrm{DCSD}}$ of the probabilities of Cabibbo-allowed and doubly Cabibbo-suppressed decays

Experiment	$R^{K\pi}_{\mathrm{DCSD}}$, %	Number of events
CLEO [88]	$0.77 \pm 0.25 \pm 0.25$	22.3 ± 7.1
E791 [89]	$0.68^{+0.34}_{-0.33} \pm 0.07$	34
ALEPH [90]	$1.77^{+0.60}_{-0.56} \pm 0.31$	21.3 ± 7.0
CLEO [86]	$0.332^{+0.063}_{-0.065} \pm 0.040$	$44.8^{+9.7}_{-8.7}$
FOCUS [87]	$0.404 \pm 0.085 \pm 0.025$	149 ± 31
Average value [87]	0.376 ± 0.035	

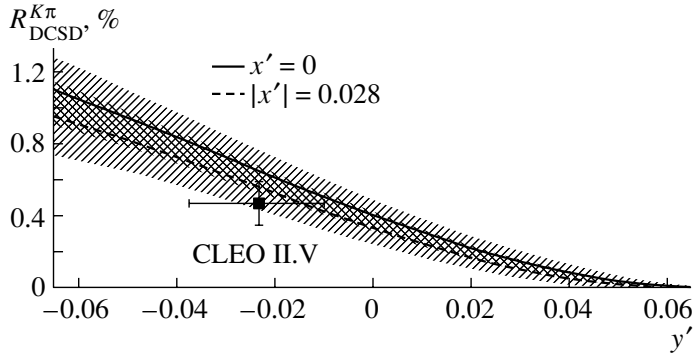

Fig. 8. Dependence of $R^{K\pi}_{\mathrm{DCSD}}$ on y' for various values of x' (the $R^{K\pi}_{\mathrm{DCSD}}$ value obtained by the CLEO Collaboration takes into account the possible contribution from D^0–$\bar{D}^0$ mixing).

cay process $D^{*+} \to D^0\pi^+$ were used in order to obtain a nearly background-free set of reconstructed events. In the case of CLEO, an attempt at describing this decay process in terms of only three resonances ($K^-\rho^+$, $K^{*-}\pi^+$, $\bar{K}^{*0}\pi^0$) and a nonresonance contribution (by analogy with what was done in [83–85]) led to a very low confidence level. For this reason, the procedure of fitting was extended by including all known intermediate resonances that are allowed by conservation laws. The resulting parameters of the resonances whose contributions are significant are quoted in Table 12. The CLEO Collaboration also performed an analysis, including, in the consideration, the scalar resonance κ whose existence was claimed by the E791 Collaboration [82]. In the decay channel $D^0 \to \kappa\pi^0$, the contribution of the κ meson having the width and mass identical to those determined in [82] proved to be $(0.4 \pm 0.3)\%$, which is obviously at odds with the results of the E791 experiment [82].

8. D^0–$\bar{D}^0$ MIXING

In the Standard Model, the probability of the $D^0 \to \bar{D}^0$ transition is suppressed to a considerable extent in relation to the probabilities of the analogous $K^0 \to \bar{K}^0$ and $B^0 \to \bar{B}^0$ transitions. Nonetheless, not only does investigation of D^0–$\bar{D}^0$ mixing make it possible to obtain additional information about D^0 transitions of this type, but it is also of great interest from the point of view of searches for new physics beyond the Standard Model. It is the smallness of the mixing effects expected within the Standard Model that would enable one to isolate the possible signal from new physics.

In general, the magnitude of D^0–$\bar{D}^0$ mixing is specified in terms of two dimensionless parameters, $x_D = \Delta m/\Gamma_+$ and $y_D = \Gamma_-/\Gamma_+$. The quantities $\Gamma_\pm$ and Δm are defined as $\Gamma_\pm = (\Gamma_1 + \Gamma_2)/2$ and $\Delta m = m_2 - m_1$, where m_i and Γ_i ($i = 1.2$) are, respectively, the masses and the decay widths of two CP eigenstates corresponding to the eigenvalues of -1 and $+1$. Assuming that the magnitude of mixing is small (as is indeed the case for D mesons)—that is, Δm, $\Delta\Gamma \ll \Gamma$ (and, hence, $x_D, y_D \ll 1$)—we obtain $R_D = (x_D^2 + y_D^2)/2$. Mixing may be due either to a nonzero value of x_D (in which case, it is associated with the $D^0 \to \bar{D}^0$ transition) or to a nonzero value of y_D (in which case it is associated with the fact that the two components decay at different rates). Theoretical estimates reveal that, within the Standard Model, the magnitude of D^0–$\bar{D}^0$ mixing does not exceed 10^{-4}–10^{-3}.

Experiments devoted to searches for D^0–$\bar{D}^0$ mixing can be partitioned into two classes. The first class includes experiments studying $D^0 \to \bar{D}^0 \to \bar{f}$ decay processes, where $\bar{f}$ is a Cabibbo-allowed final state, such as $K^+\pi^-$ or $K^+\mu^-\bar{\nu}$. The second class comprises experiments measuring the difference of the lifetimes (and, hence, of the widths) between the two CP eigenstates; that is,

$$y_{CP} = \frac{\tau_- - \tau_+}{\tau_- + \tau_+} = \frac{\Delta\Gamma}{2\Gamma} = y.$$

Search for D^0–$\bar{D}^0$ mixing by studying final states involving wrong-sign combinations. Such investigations were performed both in purely hadronic and in semileptonic final states. The decay process $D^0 \to K^+\pi^-(X)$ proceeds either owing to D^0–$\bar{D}^0$ mixing followed by the Cabibbo-allowed decay $\bar{D}^0 \to K^+\pi^-(X)$ or owing to the doubly Cabibbo-suppressed decay $D^0 \to K^+\pi^-(X)$. In order to ensure a reliable separation of precisely this decay, use was made of D^0 mesons from the decay process $D^{*+} \to D^0\pi^+$. The method used involved selecting events where there is a slow pion of the same charge as the kaon from the decay of the D^0 meson and studying the distribution with respect to the mass

Table 14. Experimental data on y_{CP}

Experiment	y_{CP}^{KK}, %	$y_{CP}^{\pi\pi}$, %	y_{CP}, %
FOCUS [39]	$3.42 \pm 1.39 \pm 0.79$		$3.42 \pm 1.39 \pm 0.79$
CLEO [94]	$-1.9 \pm 3.0 \pm 1.0$	$0.5 \pm 4.6 \pm 1.4$	$-1.2 \pm 2.5 \pm 0.9$
E791 [38a]	$0.8 \pm 2.9 \pm 1.0$		$0.8 \pm 2.9 \pm 1.0$
BELLE [95]	$-0.5 \pm 1.0^{+0.7}_{-0.8}$		$-0.5 \pm 1.0^{+0.7}_{-0.8}$
BABAR [96]	$-1.0 \pm 2.2 \pm 1.7$		$-1.0 \pm 2.2 \pm 1.7$

Table 15. CP asymmetry in the decays of D^0 and D^+ mesons

Decay channel	E791 [102]	FOCUS [103]	Averaged value
$D^0 \to K^-K^+$	$-0.010 \pm 0.049 \pm 0.012$	$-0.001 \pm 0.022 \pm 0.015$	0.009 ± 0.021
$D^0 \to \pi^-\pi^+$	$-0.049 \pm 0.078 \pm 0.030$	$0.048 \pm 0.039 \pm 0.025$	0.03 ± 0.04
$D^+ \to K^+K^-\pi^+$	-0.014 ± 0.029	$0.006 \pm 0.011 \pm 0.005$	0.002 ± 0.011
$D^+ \to \bar{K}^{*0}K^+$	-0.010 ± 0.050		-0.02 ± 0.052
$D^+ \to \pi^+\pi^+\pi^-$	-0.017 ± 0.042		-0.017 ± 0.042

difference $\Delta M = M(D^{*+}) - M(D^0) - M(\pi^+)$ for such events. In this method, the main difficulty consists in isolating a small contribution from D^0–$\bar{D}^0$ mixing against the background of doubly Cabibbo-suppressed decays, which is at least two orders of magnitude greater. The ratio of the $D^0 \to K^+\pi^-$ and $D^0 \to K^-\pi^+$ decay widths changes according to the law

$$r_D^{K\pi}(t) = \frac{\Gamma(D^0(t) \to K^+\pi^-)}{\Gamma(D^0 \to K^-\pi^+)} \sim R_{\text{mix}}^{K\pi}(t) + R_{\text{DCSD}}^{K\pi} + R_{\text{int}}^{K\pi}(t),$$

where $R_{\text{DCSD}}^{K\pi}$ is the time-independent contribution of doubly Cabibbo-suppressed decays; $R_{\text{mix}}^{K\pi}(t) \sim (x'^2 + y'2)t^2$ is the contribution that comes from D^0–$\bar{D}^0$ mixing and which is proportional to t^2 (here, $y' = y\cos\delta - x\sin\delta$ and $x' = x\cos\delta + y\sin\delta$, with δ being the strong-interaction-induced phase shift between the amplitudes for doubly Cabibbo-suppressed and Cabibbo-allowed decays); and, finally, $R_{\text{int}}^{K\pi}(t) = \sqrt{R_{\text{DCSD}}^{K\pi}(t)}y't$ is the interference term, which depends linearly on time. It follows that, by studying the time dependence of $r_D^{K\pi}(t)$ for D^0 mesons, one can separate the contribution of doubly Cabibbo-suppressed decays from the contribution of D^0–$\bar{D}^0$ mixing. Moreover, it is also possible to separate the contributions of y' and x'. Such an analysis was performed by the CLEO Collaboration [86]. More specifically, this analysis involved studying the fraction of the wrong-sign decays $D^0 \to K^+\pi^-$ as a function of $R_{\text{DCSD}}^{K\pi}$, y', and x'. This yielded the following constraints on y' and x': $(1/2)x'^2 < 0.041\%$ and $-5.8\% < y' < 1\%$. On the basis of $44.8^{+9.7}_{-8.7}$ events of the decay $D^0 \to K^+\pi^-$, the value of $R_{\text{DCSD}}^{K\pi} = (0.332^{+0.063}_{-0.065} \pm 0.040)\%$ was obtained under the assumption that the contribution from D^0–$\bar{D}^0$ mixing is negligible. The FOCUS Collaboration [87] performed similar investigations and measured $R_{\text{DCSD}}^{K\pi}$ as a function of y' and x'. Figure 8 displays $R_{\text{DCSD}}^{K\pi}$ as a function of y' at $|x'| = 0$ and 0.028. The same figure shows the $R_{\text{DCSD}}^{K\pi}$ value obtained by the CLEO Collaboration with allowance for the possible contribution from D^0–$\bar{D}^0$ mixing. Table 13 presents the values of $R_{\text{DCSD}}^{K\pi}$ that were obtained without taking into account the possible contributions from mixing and CP violation. Owing to new results, the value of $R_{\text{DCSD}}^{K\pi}$ was determined to a precision of 10%. For the doubly Cabibbo-suppressed decays $D^0 \to K^+\pi^-\pi^0$ and $D^0 \to K^+\pi^-\pi^-\pi^+$, the CLEO Collaboration [91] reported experimental results on the quantity R_{DCSD}. These are $(0.43^{+0.11}_{-0.10} \pm 0.07)\%$ [91] and $(0.41^{+0.12}_{-0.11} \pm 0.04)\%$ [92] for, respectively, the former and the latter decay process.

The E791 Collaboration [89] studied D^0–$\bar{D}^0$ mixing using both hadronic final states and semileptonic decays. The investigation of hadronic final

Table 16. Upper limits (UL) on the branching ratios of rare decays (in 10^{-5} units)

Decay type	Decay channel	Best UL	Experiment
FCNC	$D^0 \to e^+e^-(\mu^+\mu^-)$	0.62(0.41)	CLEO [105], BEATRICE [106]
	$D^0 \to \rho^0 e^+e^-(\mu^+\mu^-)$	10 (23)	CLEO [105], E653 [107]
	$D^0 \to \pi^0 e^+e^-(\mu^+\mu^-)$	4.5 (18)	CLEO [105], E653 [107]
	$D^0 \to \eta e^+e^-(\mu^+\mu^-)$	11 (53)	CLEO [105]
	$D^0 \to \omega e^+e^-(\mu^+\mu^-)$	18 (83)	CLEO [105]
	$D^0 \to \phi e^+e^-(\mu^+\mu^-)$	5.2 (41)	CLEO [105]
	$D^0 \to \bar{K}^0 e^+e^-(\mu^+\mu^-)$	11 (26)	CLEO [105], E653 [107]
	$D^+ \to \pi^+ e^+e^-(\mu^+\mu^-)$	5.2 (1.5)	E791 [108]
	$D^+ \to K^+ e^+e^-(\mu^+\mu^-)$	20 (4.4)	E687 [109], E791 [108]
	$D_s^+ \to \pi^+ e^+e^-(\mu^+\mu^-)$	27(14)	E791 [108]
	$D_s^+ \to K^+ e^+e^-(\mu^+\mu^-)$	160(14)	E791 [108]
LNVF	$D^0 \to \mu^\pm e^\mp$	0.81	E791 [108]
	$D^0 \to \pi^0 \mu^\pm e^\mp$	8.6	CLEO [105]
	$D^0 \to \rho^0 \mu^\pm e^\mp$	4.9	CLEO [105]
	$D^0 \to \eta \mu^\pm e^\mp$	10	CLEO [105]
	$D^0 \to \omega \mu^\pm e^\mp$	12	CLEO [105]
	$D^0 \to \bar{K}^0 \mu^\mp e^\pm$	10	CLEO [105]
	$D^+ \to \pi^+ \mu^\pm e^\mp$	3.4	E791 [108]
	$D^+ \to K^+ \mu^\pm e^\mp$	6.8	E791 [108]
LNV	$D^+ \to \pi^- e^+e^+(\mu^+\mu^+)$	9.6 (1.7)	E791 [108]
	$D^+ \to \pi^- \mu^+e^+$	5.0	E791 [108]
	$D^+ \to K^- e^+e^+(\mu^+\mu^+)$	12(12)	E687 [109]
	$D^+ \to K^- \mu^+e^+$	13	E687 [109]
	$D^+ \to \rho^- \mu^+\mu^+$	56	E653 [107]
	$D_s^+ \to \pi^- e^+e^+(\mu^+\mu^+)$	63(8.2)	E791 [108]
	$D_s^+ \to K^- e^+e^+(\mu^+\mu^+)$	63(18)	E791 [108]

states yielded the following constraint on this mixing: $R_{\text{mix}} < 0.85\%$. The doubly Cabibbo-suppressed decay does not contribute to the semileptonic-decay process $D^0 \to \bar{D}^0 \to Kl^-\bar{\nu}$. Only the semileptonic decays of D^0 mesons from the decay $D^{*+} \to D^0\pi^+$ were explored in this analysis. By the sign of the slow pion from the decay of a D^* meson, one can unambiguously find out in such decays whether it was a D^0 or a $\bar{D}^0$ meson that decayed. Despite the presence of an antineutrino in the final state of the decay process $D^0 \to \bar{D}^0 \to K^+l^-\bar{\nu}$, it is possible to reconstruct the D^0 meson by using information about the lepton and the kaon involved, information about the direction of the D^0 momentum, and the requirement that the invariant mass of three particles be equal to the D^0-meson mass. In investigating semileptonic decays, the E791 Collaboration [89] obtained a more stringent constraint on the mixing in question, $R_{\text{mix}} < 0.5\%$. Previously, the D^0–$\bar{D}^0$ mixing in semileptonic decays was also studied by the E615 Collaboration [93]. In the E615 experiment, charmed particles were produced in the interaction of 225-GeV pions with a tungsten target. By studying the number of muon pairs of the same sign, the constraint $R_{\text{mix}} < 0.56\%$ on the magnitude of mixing was obtained there at a confidence level of 90%.

Investigation of D^0–$\bar{D}^0$ mixing by the lifetime difference. In view of rapid advances in measuring the lifetimes of charmed mesons, the method for studying D^0–$\bar{D}^0$ mixing on the basis of measurements of the difference of D^0-meson lifetimes with respect to decays into a CP-even and a CP-odd state has recently become widespread. The time dependence of the fraction of D^0 mesons decaying into a specific CP eigenstate f can be represented as $R(t) \sim \exp[-t\Gamma(1 - y_{CP}\eta_{CP})]$, where $\eta_{CP} = \pm 1$. If it is assumed that CP violation in the decay process $D^0 \to K^-\pi^+$ can be disregarded and that, in the final state of the decay $D^0 \to K^-\pi^+$, the fraction of CP-even events is equal to the fraction of CP-odd events, the width with respect to decay through this channel can be written as $\Gamma(K\pi) \approx (\Gamma_+ + \Gamma_-)/2$. At the same time, we know that the decays $D^0 \to K^-K^+$ and $D^0 \to \pi^-\pi^+$ generate CP-even final states. Therefore, the quantity $y = y_{CP}$ can be determined from the relation

$$y_{CP} = \frac{\tau(D \to K\pi)}{\tau(D \to KK)} - 1 = \frac{\tau(D \to K\pi)}{\tau(D \to \pi\pi)} - 1.$$

By measuring the D^0-meson lifetimes in the decay channels $D^0 \to K^-\pi^+$ and $D^0 \to K^-K^+$ ($D^0 \to \pi^-\pi^+$), one can determine the value of y_{CP}. Such measurements were performed in several experiments, and the results are compiled in Table 14. Only the FOCUS Collaboration [39] obtained a y_{CP} value that differs from zero by two standard deviations. The results of other experiments are compatible with zero, and the value averaged over all experiments, $y_{CP} = (1.3 \pm 0.9) \times 10^{-2}$, is also compatible with zero.

9. SEARCHES FOR RARE AND FORBIDDEN DECAYS OF D MESONS

Violation of CP symmetry in D mesons decays. In the Standard Model, CP asymmetry is specified by a complex-valued phase in the Kobayashi–Maskawa matrix [51], which describes transitions between quarks. Until recently, CP asymmetry was recorded only in studying the decays of neutral kaons. In 2001, some pieces of evidence for a large value of CP asymmetry in the decays of neutral B mesons were obtained in experiments at the BABAR and BELLE B-meson factories [97]. Within the Standard Model [98], a much smaller effect of CP violation is expected in the decays of charmed particles. Therefore, it is appropriate to use the decays of charmed particles in testing the Standard Model [99] and in seeking phenomena beyond it. The presence of CP asymmetry is suggested by the distinction between the branching ratios for D-meson decays into the final state f and the complex-conjugate state $\bar{f}$. For such an asymmetry to exist, the interference of at least two independent processes having a nonzero relative phase is necessary.

In D^0–$\bar{D}^0$ mixing, CP asymmetry arises because of the interference between the direct decay of the D^0 meson into a final state f and the process in which the transformation of D^0 into $\bar{D}^0$ owing to mixing is followed by the decay $\bar{D}^0 \to f$. Within the Standard Model, the asymmetry is expected here at a level of 10^{-3}. However, it is difficult to estimate it reliably because of uncertainties associated with the calculation of long-range effects.

In direct decays, CP asymmetry may arise in decays of both neutral and charged mesons. For this, final-state interactions must generate a shift of the strong-interaction phase, with the result that the strong- and weak-interaction phases become different. Within the Standard Model, CP asymmetry in direct decays is predicted to be maximal in the Cabibbo-suppressed decays of D mesons (at a level of 10^{-3}) owing to the interference between the tree and the penguin diagram. No sizable asymmetry is expected in Cabibbo-allowed and doubly Cabibbo-suppressed decays [98]. However, the asymmetry can arise owing to the interference of Cabibbo-allowed and doubly Cabibbo-suppressed decays.

Finally, CP asymmetry can manifest itself as the result of the interplay of direct decays and D^0–$\bar{D}^0$ mixing.

Searches for CP asymmetry were performed in the experiments of the E691, E687, CLEO, E791, and FOCUS collaborations (see [100], [101], [94], [102], and [103], respectively). The experimental accuracy in the measurements of CP asymmetry is at a level of one percent, and no CP violation has been discovered in the decays of D mesons at this level. The data from two experiments, E791 [102] and FOCUS [103], that achieved the best results are quoted in Table 15, along with the averaged value for each decay channel.

Rare decays. Processes generated by flavor-changing neutral currents (FCNC) include $D^0 \to l^+l^-$, $\gamma\gamma$ and $D \to X\gamma$, $X\nu\bar{\nu}$, Xl^+l^-, where l is an electron or a muon. Such processes may proceed through mechanisms associated with electromagnetic or weak penguin diagrams and, in some cases, through mechanisms associated with the contribution of box diagrams. Estimates of decay probabilities involve large uncertainties, and one can assess their upper limits rather than specific values. The calculation of the branching ratio for decay $D^0 \to \mu^+\mu^-$ in [104] leads to an upper limit of 3×10^{-15}; for $D^+ \to \pi^+e^+e^-(\mu^+\mu^-)$, the branching ratio does not exceed 10^{-8}. The discovery of FCNC-generated

processes with a probability exceeding the predictions of the Standard Model would be indicative of the existence of new physics beyond the Standard Model. The most stringent experimental constraints on the branching ratios for such decays are given in Table 16. Also given there are upper limits for processes that are accompanied by lepton-number violation (LNV) and lepton-number violation in a given family of leptons (LNVF) and which are strictly forbidden within the Standard Model. Such processes can be easily identified, and their occurrence would also be a signal from new physics beyond the Standard Model. All of the results obtained so far comply well with the predictions of the Standard Model.

10. FURTHER PLANS FOR STUDYING CHARMED-PARTICLE PHYSICS

The future of charmed-particle physics looks quite promising. The fixed-target experiments E791 [4] and SELEX [6] are continuing to furnish new results. An ever greater amount of interesting results have been coming from the FOCUS Collaboration [5]. At present, the majority of the results are preliminary and are based on a treatment of half the existing information. However, the processing will soon be completed, and a great many new results of interest will become available.

Experiments at electron–positron colliders are also in great form. The CLEO Collaboration [7, 8], which has completed this year data accumulation in the $\Upsilon(4S)$-resonance region, will have continued data processing for years. The BELLE and BABAR B-meson factories (see [9] and [10], respectively) have gained momentum; even at present, the number of charmed particles reconstructed there is severalfold greater than the corresponding numbers in other experiments, and it is planned to double statistics at these factories within the next year. At the moment, the attention of large international collaborations is concentrated on B-meson physics, but it is highly probable that investigations into charmed-hadron physics will be extended in the future.

The COMPASS Collaboration [110] began accumulating data only in 2001. Investigation of charmed-hadron spectroscopy is one of the main objectives of this experiment, which is deployed in a 300-GeV pion beam extracted from the SPS accelerator at CERN. In that experiment, it is planned to reconstruct a few million charmed hadrons. In addition, a broad program of searches for baryons featuring two c quarks is proposed.

The project of a collider that is intended for studying the physics of charmed hadrons and tau leptons and which is referred to as a tau–charm factory [111] has been intensively discussed over the last decade. At present, there appears the possibility of implementing an experimental facility that will become a real factory of results on charmed-particle physics, although it is less ambitious than that of the tau–charm factory. The point is that the CLEO Collaboration, which operated in the Υ-resonance region, could not stand up to the competition of successfully developing B-meson factories and decided to concentrate on studying charmed particles. All the necessary work on the upgrade of the detector and accelerator will have been completed by the end of 2003, and the collaboration is going to begin accumulating data at a luminosity of $L = (1–5) \times 10^{32}$ cm^{-2} s^{-1} [112]. This luminosity value is severalfold lower than that which was planned for tau–charm factories, but it is an order of magnitude higher than that of the BEPC accelerator (China) currently operating in this energy region.

Investigation of charmed particles at the production threshold has a number of serious advantages. First, we have here the largest production cross section for specific particles, since the production cross section decreases in inverse proportion to the square of the c.m. energy. (Frequently, the cross section for charmed-particle production proves to be still larger owing to the presence of charmed resonances—for example $\psi''(3.77)$, which decays almost always into $D^0\bar{D}^0$ and D^+D^-.) Second, the background conditions for such investigations are very favorable: near the threshold, charmed particles appear in extremely simple final states involving only a charmed particle and an antiparticle, since the available energy is insufficient for producing extra hadrons; therefore, each charmed particle can be identified by reconstructing the decay of its charmed partner. A high selection efficiency, a nearly vanishing background, and a simple normalization method that makes it possible to determine the absolute values of decay widths are the main advantages of this approach. Finally, charmed particles are produced virtually at rest at the threshold; therefore, their decay products have low momenta, and this simplifies particle identification considerably.

In charmed-particle physics, the majority of the problems have received an explanation at the qualitative level, but there remain many issues that have yet to be described quantitatively and many rare processes that are to be recorded and studied. Presently, the efforts of experimental charmed-particle physics must be aimed at measuring the fundamental parameters of the Standard Model, making advances in theoretically describing nonperturbative strong interactions involved in weak quark decays, and testing the existing theories and approaches. Particular attention must be given to searches for and investigation of rare processes and anomalous effects that could be indicative of the existence of new physics

beyond the Standard Model. The presence of new physics could be suggested by an anomalously large magnitude of $D^0-\bar{D}^0$ mixing or CP asymmetry and by the discovery of processes violating conservation laws (for example, flavor-changing neutral currents).

A one to two orders of magnitude increase in the statistics of charmed hadrons would of course lead to new interesting results and would make it possible to solve the aforementioned problems. The beginning of the new century proved to be seminal for charmed-particle physics. There is every reason to believe that we are on the eve of many interesting results and discoveries.

REFERENCES

1. S. V. Semenov, Usp. Fiz. Nauk **169**, 937 (1999) [Phys. Usp. **42**, 847 (1999)].
2. S. Frixione, M. L. Mangano, P. Nason, and G. Ridolfi, Adv. Ser. Direct. High Energy Phys. **15**, 609 (1998).
3. W. Toki, *Invited Talk at the Workshop on Charm Physics, Beijing, China, 1987*, p. 89; D. Cords, *Lecture Presented at the International School of Elementary Particle Physics, Kupari-Dubrovnik, Yugoslavia, 1977*; Preprint DESY-78/32.
4. J. A. Appel, Annu. Rev. Nucl. Part. Sci. **42**, 367 (1992); D. Summers *et al.*, hep-ex/0009015; S. Amato *et al.*, Nucl. Instrum. Methods Phys. Res. A **324**, 535 (1993); E. M. Aitala *et al.*, Eur. Phys. J. C **4**, 1 (1999).
5. D. Pedrini, in *Proceedings of the 3rd International Conference on Hyperons, Charm and Beauty Hadrons, Genoa, Italy, 1998,* Nucl. Phys. B (Proc. Suppl.) **75B**, 105 (1999).
6. V. Smith, in *Proceedings of the 7th International Conference on Hadron Spectroscopy (HADRON-97), 1997,* Ed. by S.-U. Chung and H. Willutski, p. 627.
7. Y. Kubota *et al.*, Nucl. Instrum. Methods Phys. Res. A **320**, 66 (1992).
8. S. E. Kopp *et al.*, Nucl. Instrum. Methods Phys. Res. A **384**, 61 (1996).
9. A. Abashian *et al.*, Nucl. Instrum. Methods Phys. Res. A **479**, 117 (2002).
10. B. Aubert *et al.*, Nucl. Instrum. Methods Phys. Res. A **479**, 1 (2002).
11. A. Anastassov *et al.*, Phys. Rev. D **65**, 032003 (2002).
12. V. M. Belyaev *et al.*, Phys. Rev. D **51**, 6177 (1995); P. Singer, Acta Phys. Pol. B **30**, 3849 (1999); K. O. E. Henriksson *et al.*, Nucl. Phys. A **686**, 355 (2001).
13. S. Barlag *et al.*, Phys. Lett. B **278**, 480 (1992).
14. N. Isgur and M. B. Wise, Phys. Rev. D **42**, 2388 (1990).
15. N. Isgur and M. B. Wise, Phys. Rev. Lett. **66**, 1130 (1991).
16. J. L. Rosner, Comments Nucl. Part. Phys. **16**, 109 (1986).
17. Particle Data Group (D. E. Groom *et al.*), Eur. Phys. J. C **15**, 1 (2000).
18. S. Anderson *et al.*, Nucl. Phys. A **663**, 647 (2000).
19. P. Abreu *et al.*, Phys. Lett. B **426**, 231 (1998).
20. G. Abbiendi *et al.*, Eur. Phys. J. C **20**, 445 (2001).
21. J. L. Rodríguez, in *Proceedings of the 4th Workshop on Heavy Quarks at Fixed Target "Batavia 1998,"* p. 280.
22. C. P. Jessop *et al.*, Phys. Rev. Lett. **82**, 492 (1999).
23. H. Albrecht *et al.*, Phys. Lett. B **288**, 367 (1992); J. Stiewe, in *Proceedings of the 26th International Conference on HEP, New York, 1993,* p. 1076.
24. P. L. Frabetti *et al.*, Phys. Lett. B **300**, 190 (1993); **338**, 106 (1994).
25. H. W. Siebert, *Invited Talk at Production and Decay of Hyperons, Charm and Beauty Hadrons, Strasbourg, France, 1995;* Nucl. Phys. B (Proc. Suppl.) **50**, 162 (1996).
26. D. Cronin-Hennessy *et al.*, Phys. Rev. Lett. **86**, 3730 (2001).
27. S. Semenov, in *Proceedings of the Europhysics International Conference on High Energy Physics, Budapest, 2001,* Ed. by D. Horvath, P. Levai, and A. Patkos, JHEP (http://jhep.sissa.it/), PrHEP-hep2001/107.
28. P. Avery *et al.*, Phys. Rev. Lett. **75**, 4364 (1995); L. Gibbons *et al.*, Phys. Rev. Lett. **77**, 810 (1996); G. Brandenburg *et al.*, Phys. Rev. Lett. **78**, 2304 (1997).
29. R. Ammar *et al.*, Phys. Rev. Lett. **86**, 1167 (2001).
30. P. L. Frabetti *et al.*, Phys. Lett. B **426**, 403 (1998).
31. H. Albrecht *et al.*, Phys. Lett. B **317**, 227 (1993).
32. S. E. Csorna *et al.*, Phys. Rev. Lett. **86**, 4243 (2001).
33. J. P. Alexander *et al.*, Phys. Rev. Lett. **83**, 3390 (1999).
34. M. Artuso *et al.*, Phys. Rev. Lett. **86**, 4479 (2001).
35. V. V. Kiselev, A. K. Likhoded, and M. V. Shevlyagin, Phys. Lett. B **332**, 411 (1994).
36. B. Yabsley, in *Proceedings of the Europhysics International Conference on High Energy Physics, Budapest, 2001,* Ed. by D. Horvath, P. Levai, and A. Patkos, JHEP (http://jhep.sissa.it/), PrHEP-hep2001/059.
37. G. Bonvicini *et al.*, Phys. Rev. Lett. **82**, 4586 (1999).
38. E. M. Aitala *et al.*, Phys. Rev. Lett. **83**, 32 (1999); Phys. Lett. B **445**, 449 (1999).
39. J. M. Link *et al.*, Phys. Lett. B **485**, 62 (2000).
40. H. W. K. Cheung, hep-ex/9912021; in *Proceedings of the 8th International Symposium on Heavy Flavour Physics, Southampton, 1999,* PRHEP-hf8/022.
41. A. Kushnirenko *et al.*, Phys. Rev. Lett. **86**, 5243 (2001).
42. M. Iori *et al.*, Phys. Lett. B **523**, 22 (2001).
43. Particle Data Group (C. Caso *et al.*), Eur. Phys. J. C **3**, 1 (1998).
44. G. Bellini, I. I. Bigi, and P. J. Dornan, Phys. Rep. **289**, 1 (1998).

45. A. H. Mahmood *et al.*, Phys. Rev. Lett. **86**, 2232 (2001); Phys. Rev. D **65**, 031102 (2002).
46. J. M. Link *et al.*, Phys. Lett. B **523**, 53 (2001); E. Vaandering, in *Proceedings of the IX International Conference on Hadron Spectroscopy (HADRON 2001), Protvino, Russia, 2001.*
47. B. Guberina, R. Ruckl, and J. Trampetic, Z. Phys. C **33**, 297 (1986).
48. M. B. Voloshin and M. A. Shifman, Zh. Éksp. Teor. Fiz. **91**, 1180 (1986) [Sov. Phys. JETP **64**, 698 (1986)].
49. B. Blok and M. Shifman, in *Proceedings of the Third Workshop on the Physics at a Tau-Charm Factory, Marbella, Spain, 1993,* Ed. by J. Kirkby and R. Kirkby (Editions Frontières, Gif-sur-Yvette, 1994).
50. J. D. Richman and P. R. Burchat, Rev. Mod. Phys. **67**, 893 (1995).
51. M. Kobayashi and T. Maskawa, Prog. Theor. Phys. **49**, 652 (1973).
52. S. Aoki *et al.*, Prog. Theor. Phys. **89**, 131 (1993).
53. K. Kodama *et al.*, Phys. Lett. B **382**, 299 (1996).
54. M. Chadha *et al.*, Phys. Rev. D **58**, 3202 (1998).
55. J. Z. Bai *et al.*, Phys. Rev. Lett. **74**, 4599 (1995).
56. S. Sõldner-Rembold, in *Proceedings of the Europhysics International Conference on High Energy Physics, Budapest, 2001,* Ed. by D. Horvath, P. Levai, and A. Patkos, JHEP (http://jhep.sissa.it/), PrHEP-hep2001/093.
57. Yu. Alexandrov *et al.*, Phys. Lett. B **478**, 31 (2000).
58. M. Acciarri *et al.*, Phys. Lett. B **396**, 327 (1997).
59. G. Abbiendi *et al.*, Phys. Lett. B **516**, 236 (2001).
60. J. Adler *et al.*, Phys. Rev. Lett. **60**, 1375 (1988).
61. J. Z. Bai *et al.*, Preprint SLAC-PUB-7147 (1996).
62. P. L. Frabetti *et al.*, Phys. Lett. B **364**, 127 (1995).
63. A. Bean *et al.*, Phys. Lett. B **317**, 647 (1993).
64. D. Scora and N. Isgur, Phys. Rev. D **52**, 2783 (1995).
65. C. W. Bernard, Z. X. El-Khadra, and A. Soni, Phys. Rev. D **45**, 869 (1992).
66. V. Lubicz, G. Martinelli, M. S. McCarthy, and C. T. Sachrajda, Phys. Rev. B **274**, 415 (1992).
67. S. Gusken, K. Schilling, and G. Siegert, Prog. Theor. Phys. Suppl. **122**, 129 (1996).
68. C. R. Allton *et al.*, Phys. Lett. B **345**, 513 (1995).
69. P. Ball, Y. M. Braun, and H. G. Dosch, Phys. Rev. D **44**, 3567 (1991).
70. M. Adamovich *et al.*, Eur. Phys. J. C **6**, 35 (1999).
71. E. M. Aitala *et al.*, Phys. Rev. Lett. **80**, 1393 (1998).
72. E. M. Aitala *et al.*, Phys. Lett. B **440**, 435 (1999).
73. B. O'Reilly, in *Proceedings of the 3rd International Conference on Hyperons, Charm and Beauty Hadrons, Genoa, Italy, 1998;* Nucl. Phys. B (Proc. Suppl.) **75B**, 20 (1999).
74. M. B. Voloshin, Phys. Lett. B **385**, 369 (1996).
75. H. Albrecht *et al.*, Phys. Lett. B **269**, 234 (1991); **303**, 368 (1993).
76. T. Bergfeld *et al.*, Phys. Lett. B **323**, 219 (1994); J. P. Alexander *et al.*, Phys. Rev. Lett. **74**, 3113 (1995).
77. R. H. Dalitz, Philos. Mag. **44**, 1068 (1953).
78. S. Kopp *et al.*, Phys. Rev. D **63**, 092001 (2001).
79. E. M. Aitala *et al.*, Phys. Rev. Lett. **86**, 765 (2001).
80. K. Stenson, hep-ex/0111083.
81. E. M. Aitala *et al.*, Phys. Rev. Lett. **86**, 770 (2001).
82. C. Gõbel, hep-ex/0110052.
83. J. Adler *et al.*, Phys. Lett. B **196**, 107 (1987).
84. J. C. Anjos *et al.*, Phys. Rev. D **48**, 56 (1993).
85. P. L. Frabetti *et al.*, Phys. Lett. B **331**, 217 (1994).
86. R. Godang *et al.*, Phys. Rev. Lett. **84**, 5038 (2000).
87. J. M. Link *et al.*, Phys. Rev. Lett. **86**, 2955 (2001).
88. D. Cinabro *et al.*, Phys. Rev. Lett. **72**, 1406 (1994).
89. E. M. Aitala *et al.*, Phys. Rev. D **57**, 13 (1998).
90. R. Barate *et al.*, Phys. Lett. B **436**, 211 (1998).
91. G. Brandenburg *et al.*, Phys. Rev. Lett. **87**, 071802 (2001).
92. S. A. Dytman *et al.*, Phys. Rev. D **64**, 111101(R) (2001).
93. W. C. Louis *et al.*, Phys. Rev. Lett. **56**, 1027 (1986).
94. S. E. Csorna *et al.*, hep-ex/0111024 (submitted to Phys. Rev. D).
95. K. Abe *et al.*, Phys. Rev. Lett. **88**, 162001 (2002).
96. B. Aubert *et al.*, hep-ex/0109008.
97. K. Abe *et al.*, Phys. Rev. Lett. **87**, 091802 (2001); B. Aubert *et al.*, Phys. Rev. Lett. **87**, 091801 (2001).
98. M. Golden and B. Grinstein, Phys. Lett. B **222**, 501 (1989); F. E. Close and N. J. Lipkin, Phys. Lett. B **372**, 306 (1996).
99. A. Le Yaouanc, L. Oliver, and J.-C. Raynal, Phys. Lett. B **292**, 353 (1992).
100. J. C. Anjos *et al.*, Phys. Rev. D **44**, R3371 (1991).
101. P. L. Frabetti *et al.*, Phys. Rev. D **50**, R2953 (1994).
102. E. M. Aitala *et al.*, Phys. Lett. B **421**, 405 (1998); **403**, 377 (1997).
103. J. M. Link *et al.*, Phys. Lett. B **491**, 232 (2000).
104. J. L. Hewett, hep-ph/9505246.
105. A. Freyberger *et al.*, Phys. Rev. Lett. **76**, 3065 (1996).
106. M. Adamovich *et al.*, Phys. Lett. B **408**, 469 (1997).
107. K. Kodama *et al.*, Phys. Lett. B **345**, 85 (1995).
108. E. M. Aitala *et al.*, Phys. Lett. B **462**, 401 (1999).
109. P. L. Frabetti *et al.*, Phys. Lett. B **398**, 239 (1997).
110. G. Baum *et al.*, Preprint CERN-SPSLC-96-14 (1996).
111. J. Kirkby, Preprint CERN-PPE-96-112 (1996).
112. T. Pedlar, in *Proceedings of the Europhysics International Conference on High Energy Physics, Budapest, 2001,* Ed. by D. Horvath, P. Levai, and A. Patkos, JHEP (http://jhep.sissa.it/), PrHEP-hep2001/180.

Translated by A. Isaakyan

Physics of Atomic Nuclei, Vol. 66, No. 3, 2003, pp. 547–557. Translated from Yadernaya Fizika, Vol. 66, No. 3, 2003, pp. 574–583.

NUCLEI
Experiment

Cross Sections for the Photofission of ^{243}Cm, ^{245}Cm, ^{249}Bk, and ^{249}Cf Isotopes in the Energy Range from the Threshold to 10–12 MeV

A. S. Soldatov

Institute of Physics and Power Engineering, pl. Bondarenko 1, Obninsk, Kaluga oblast, 249020 Russia

Received December 10, 2001; in final form, April 15, 2002

Abstract—The relative method was used to measure the photofission cross sections for ^{243}Cm and ^{249}Cf isotopes in the energy range from 6 to 12 MeV, for ^{245}Cm in the energy range from 5 to 10 MeV, and for ^{249}Bk in the energy range from 5.5 to 10 MeV. The measurements were performed with an energy step of 50 to 200 keV by using the microtron installed at the Institute of Physics and Power Engineering (Obninsk). The cross section for ^{238}U photofission was used as a reference in these measurements. Data on the cross sections for ^{243}Cm, ^{245}Cm, and ^{249}Bk photofission were obtained for the first time, while data on the cross section for ^{249}Cf photofission were obtained for the first time only in the energy region $E < 10$ MeV. The data on the ^{245}Cm nucleus suggest that, in the energy region around 6 MeV, the cross section for its photofission has a maximum, which is likely to be due to the low-energy resonance structure of the dipole-photoabsorption cross section. For ^{249}Cf, an anomalously large value of the photofission cross section is observed in the region of the first maximum of the giant dipole resonance ($E \approx 11$ MeV). By comparing the energy dependences obtained for the fissilities of the ^{243}Cm and ^{249}Bk isotopes from photofission data with the fissilities from direct-reaction data, it is found that the observed fission thresholds agree and that there is a plateau-like dependence at energies above 7.5 MeV. For the ^{245}Cm and ^{249}Cf nuclei, there are no similar data for performing such a comparison. Data on the fissilities as obtained from the present series of relative measurements that employ the microtron bremsstrahlung spectrum are analyzed.

INTRODUCTION

The photofission reaction is appealing as a means for studying the fission process, since it possesses some unique properties, such as the simplicity of the spectrum of angular-momentum transfers to the nucleus undergoing fission and the absence of constraints at low energies. To the greatest extent, the advantages of photofission manifest themselves in studying the process in the vicinity of the threshold, but the results of photofission-cross-section measurements in the region of the so-called first fissility plateau ($E < 12$ MeV) and at higher energies, where data were obtained for a rather limited range of nuclei, are of interest for some problems—in particular, for the transmutions of first actinide elements.

Despite difficulties involved in reconstructing cross sections from integrated data on the yields from photofission reactions, the application of the bremsstrahlung spectrum as a source of gamma radiation makes it possible to extend considerably possibilities for performing systematic experimental investigations—for example, in studying the dependences of the photofission cross sections on the excitation energy and on the nucleonic composition of nuclei undergoing fission. One of the methodological solutions that enabled one to make advances in applying the bremsstrahlung spectrum consists in the use of the relative method of measurements, which is extensively employed in neutron measurements. One can make sure that this is so by comparing the energy dependences obtained for the photofission cross sections by using the relative method in experiments employing the bremsstrahlung spectrum with the corresponding dependences obtained with monochromatic photons—for example, in [1] for ^{232}Th. Attempts at using this approach in measuring yields and cross sections were previously made in [2–6].

The present study completes the series of photofission-cross-section measurements performed by the relative method with bremsstrahlung photons from a microtron. The results reported here are those for the ^{243}Cm, ^{245}Cm, ^{249}Bk, and ^{249}Cf isotopes. In just the same way as in the overwhelming majority of preceding measurements, the cross section for ^{238}U photofission was used as a reference.

1063-7788/03/6603-0547$24.00

Table 1. Thicknesses of fissile targets (t) and distances from them to the tungsten part of a braking target (L)

Assembly of fissile targets	$t_{\text{test. is.}}$, μg/cm^2	$t_{\text{ref.}}$, μg/cm^2	L, mm
^{243}Cm–^{238}U	1.2	2.5	28
^{245}Cm–^{238}U	100	500	28
^{249}Bk–^{238}U	75	520	21
^{249}Cf–^{238}U	75	520	35

DESCRIPTION OF THE EXPERIMENT

By using the microtron installed at the Institute of Physics and Power Engineering (Obninsk), the measurements were performed in the region of the endpoint energy of the bremsstrahlung spectrum: $E_{\max} = 6.05$–12.45 MeV for ^{243}Cm, $E_{\max} = 5.05$–10.1 MeV for ^{245}Cm, $E_{\max} = 5.55$–10.1 MeV for ^{249}Bk, and $E_{\max} = 5.95$–12.45 MeV for ^{249}Cf. In these measurements, the energy step was 0.05 MeV in the threshold energy region, 0.1 MeV in the energy region $E_{\max} < 6.5$–8.5 MeV, and 0.2 MeV at still higher energies. The procedure used in relative measurements of photofission cross sections with bremsstrahlung photons was described in detail elsewhere [7, 8]. As was mentioned above, the cross section for ^{238}U photofission was used as a reference [7].

A water-cooled device consisting of a 1-mm-thick tungsten disk and a 12-mm-thick aluminum absorber of electrons served as a braking target. Fissile layers of the oxides of isotopes being studied and of ^{238}U on aluminum or platinum substrates of thickness 0.1 to 0.2 mm were arranged adjacent to each other in back-to-back geometry. The relative positions of individual holders with fissile targets in the experimental facility and their thicknesses are indicated in Table 1.

For each isotope being investigated, use was made of one holder enclosing two layers, one containing the isotope in question and the other containing reference nuclei. The fissile layers were covered with a diaphragm whose aperture diameter was 10 mm. Fission fragments were detected by solid-state tracking detectors made from TV mica and positioned downstream of diaphragms that were rigidly fixed to the fissile layers, their aperture diameter being 12 mm. The distance from a fissile layer to the diaphragm was 1.5 mm.

The quantity measured experimentally was the ratio of the yield from the photofission of each isotope under study, $Y(E_{\max})$, to the yield from the analogous reaction with the reference nucleus, $Y_0(E_{\max})$,

$$R(E_{\max}) = Y(E_{\max})/Y_0(E_{\max}). \qquad (1)$$

The yield from the photofission reaction induced by bremsstrahlung photons as a function of the endpoint energy $E_{\max}$ and the photofission cross section $\sigma_f(E)$ as a function of the nuclear excitation energy E are related by the equation

$$Y(E_{\max}) = C(E_{\max}) \int_0^{E_{\max}} \sigma_f(E) N(E, E_{\max}) dE, \quad (2)$$

where $N(E, E_{\max})$ is the spectrum of bremsstrahlung photons and $C(E_{\max})$ is a factor whose value depends on the normalization of the spectrum $N(E, E_{\max})$, on the number of nuclei in the target undergoing fission, and on the efficiency of fission-fragment detection in the detector used. The yield from the photofission of the reference nucleus, $Y_0(E_{\max})$, is related to the cross section for the photofission of the reference nucleus, $\sigma_f^0(E)$, by the analogous equation.

EXPERIMENTAL RESULTS

Curium-243

Figure 1*a* displays the energy dependence of the ratio $R(E_{\max})$ of the yield from the photofission of the ^{243}Cm isotope to the corresponding yield for the ^{238}U nucleus. The measurements of $R(E_{\max})$ for ^{243}Cm were performed simultaneously with the analogous measurements for the americium isotopes, but the results for americium were reported previously (see [9]). A substance that was almost isotopically pure in ^{243}Cm (the admixture of other curium isotopes was less than 0.01%) was deposited on a platinum foil of thickness 0.2 mm.

The ratios of the numbers of nuclei in fissile targets of the isotope being studied to that of ^{238}U nuclei were determined in a dedicated experiment by irradiating, with a flux of 5-MeV monochromatic photons, the same assemblies of layers as those that were used in measuring the photofission-yield ratios. The statistical accuracy of those measurements was about 3%. In calculating the ratios in question, the neutron-induced-fission cross sections σ_{nf} were set to 2.06 b for ^{243}Cm [10] and to 0.541 b for ^{238}U [11].

The statistical accuracy in the measurements of $R(E_{\max})$ in the energy region $E < 7.2$ MeV (about 10%) is more than two times lower than the accuracy of the measurements in the high-energy region. The exposure times were deliberately increased in the high-energy measurements, and this made it possible to obtain results with errors of about 3%. The background of spontaneous-fission events was nearly equal to zero.

By multiplying the experimental dependences $R(E_{\max})$ obtained in back-to-back geometry by the integral where the estimate obtained in [7] for the reference photofission cross section $\sigma_f^0(E)$ (that for ^{238}U) is integrated over the bremsstrahlung spectrum [12], these dependences were transformed into the integrated energy dependences of the photofission-reaction yields, $Y(E_{\max})$. With the aid of an iterative procedure for minimizing directional discrepancies [13], the photofission cross sections $\sigma_f(E)$ were then calculated for the curium isotope being studied. In doing this, the integral of the cross section for reference-nucleus photofission was considered as a smooth dependence that is universal for our relative measurements of photofission cross sections and which is free from errors, whence it is clear that the errors in the estimated reference photofission cross sections $\sigma_f^0(E)$ were disregarded in our calculations.

The errors in $\sigma_f(E)$ were determined from the scatter of results that were obtained by repeatedly solving the integral Eq. (2) with the left-hand side, $Y(E_{\max})$, distributed according to the Poisson law for the case of the error $\Delta Y(E_{\max})$ calculated from $\Delta R(E_{\max})$ in just the same way as $Y(E_{\max})$ was determined from $R(E_{\max})$.

The photofission cross sections obtained for ^{243}Cm upon a mathematical data treatment according to the procedure outlined above are displayed in Fig. 1*b*. The input experimental data on $R(E_{\max})$ for this nuclear species have large statistical errors in the low-energy region, where the structure of photofission cross sections predominantly manifests itself. Although the measurements of the energy dependence $\sigma_f(E)$ were quite comprehensive, it would hardly be justifiable to present the results of the mathematical treatment of such data and to discuss the resulting resonances in the photofission cross section. In view of this, the dependences $Y(E_{\max})$ were subjected to smoothing prior to processing them according to the method of minimizing directional divergences. In the region $E_{\max} < 7.2$ MeV, where the statistical errors are large, the smoothing was performed on the basis of five experimental points, while, in the region $E_{\max} > 7.2$ MeV, use was made of three points. The results obtained in the present study furnish information only about the behavior of the dependence $\sigma_f(E)$ on average. The data displayed in Fig. 1*b* make it possible to estimate the observed threshold for the ^{243}Cm nucleus at about 6.5 MeV.

The present results on the fission of the ^{243}Cm isotope can be contrasted against experimental data on the fission probability from the relevant direct (^{3}He, tf) reaction [14]. With this aim in view, the photofission cross sections were represented in the form of

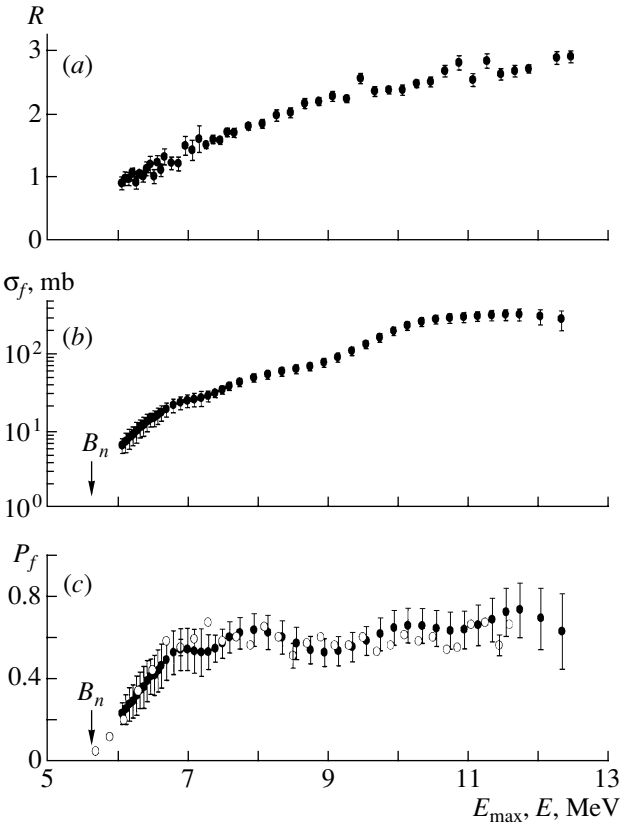

Fig. 1. (*a*) Ratio $R(E_{\max})$ of the yields from ^{243}Cm and ^{238}U photofission as a function of the endpoint bremsstrahlung-spectrum energy $E_{\max}$. (*b*) Cross section $\sigma_f(E)$ for ^{243}Cm photofission as a function of energy. (*c*) Fissility $P_f(E)$ of ^{243}Cm as a function of energy. In all of the panels, closed circles represent the photofission data of the present study. The open circles in Fig. 3*c* correspond to data from [14] that were obtained by studying the relevant direct (^{3}He, tf) reaction. In this figure and in the next three ones (Figs. 2–4), B_n is the neutron binding energy.

fissilities—that is, their ratios to the photoabsorption cross section. Since the dipole-photoabsorption process is dominant in the energy region being studied, the fissilities were defined as

$$P_f(E) \approx \sigma_f(E)/\sigma_{c1}(E), \qquad (3)$$

where $\sigma_{c1}(E)$ is the cross section for dipole photoabsorption. For the ^{243}Cm isotope, there are no direct experimental data on the cross section for dipole photoabsorption. For this reason, the fissility $P_f(E)$ was calculated, in this case, by using, for the energy dependence $\sigma_{c1}(E)$, the two-Lorentzian approximation

$$\sigma_{c1}(E) = \sum_{i=1}^{2} \sigma_i \frac{E^2\Gamma_i^2}{(E^2 - E_i^2)^2 + E^2\Gamma_i^2}, \qquad (4)$$

with the parameter values being $\sigma_1 = 311$ mb, $\Gamma_1 = 2.37$ MeV, $E_1 = 10.77$ MeV, $\sigma_2 = 459$ mb, $\Gamma_2 =$

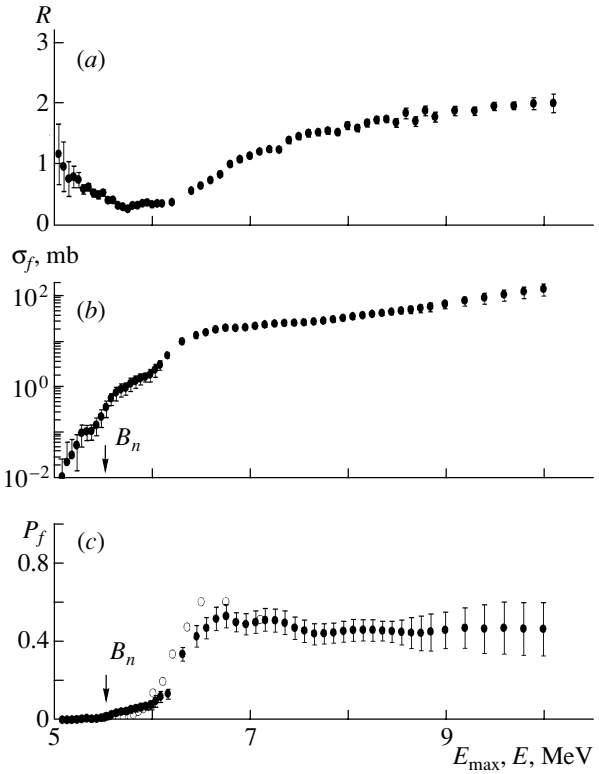

Fig. 2. (*a*) Ratio $R(E_{\max})$ of the yields from the photofission of ^{245}Cm and ^{238}U as a function of the endpoint bremsstrahlung-spectrum energy $E_{\max}$. (*b*) Cross section $\sigma_f(E)$ for ^{245}Cm photofission as a function of energy. (*c*) Fissility $P_f(E)$ of ^{245}Cm as a function of energy. In all of the panels, closed circles represent the photofission data of the present study. The open circles in Fig. 3*c* correspond to data on the relevant (n, f) reaction from [19].

5.13 MeV, and $E_2 = 13.8$ MeV, which was obtained in [15] for ^{238}U. In the present relative measurements of photofission cross sections, the reference cross section from [7] was estimated at energies above 7 MeV by using the same experimental data from [15] on the cross section for ^{238}U photofission as those that were employed in deriving the Lorentzian parameters in (4). Since the same information on the cross section for ^{238}U photofission is used in multiplying $R(E_{\max})$ by the integral of $\sigma_f^0(E)$ over the bremsstrahlung spectrum to calculate $Y(E_{\max})$ and in dividing the cross section to evaluate the fissilities $P_f(E)$, there are grounds to hope that the uncertainties in $P_f(E)$ that are associated with the choice of $\sigma_f^0(E)$ and $\sigma_{c1}(E)$ are suppressed to some extent.

The fissilities $P_f(E)$ obtained in the present study for ^{243}Cm as a function of energy are shown in Fig. 1*c*; also given in this figure are $P_f(E)$ values measured in the relevant direct (^{3}He, tf) reaction [14]. The general character of the dependences $P_f(E)$ in the present study is close to that in [14]: the subbarrier decrease in the fissility with decreasing energy begins nearly at the same point, and the so-called fissility plateau is observed in the energy range between 7 and 11 MeV in either case. The fissility values given by the two methods in question agree within the errors over the major part of the energy range being considered, and only for $E < 7$ MeV does the fissility $P_f(E)$ determined in the present study fall short of that from the direct-reaction data, as was previously observed in [9] for americium. This distinction can be attributed to an overestimation of the dipole-photoabsorption cross section $\sigma_{c1}(E)$ obtained from the low-energy approximation used in [15]. In the review article of Ostapenko *et al.* [16], it is shown that, for the photofission of a number of isotopes (thorium, uranium, neptunium, plutonium), a good description of the dependence $\sigma_{c1}(E)$ by the two-Lorentzian form (4) in the energy region corresponding to the giant dipole resonance leads to an overestimation of $\sigma_{c1}(E)$ at low energies.

Curium-245

Measurements of the yield ratios $R(E_{\max})$ for ^{245}Cm and ^{238}U were performed simultaneously with measurements for plutonium isotopes, the results of the latter being previously reported in [17]. Fissile material that was almost isotopically pure (the admixture of other Cm isotopes was less than 0.008%) was deposited on a platinum foil 0.2 mm thick.

The ratio of the number of nuclei of the isotope being studied in a fissile target to that of ^{238}U nuclei was measured by the method that is traditional for this series of experiments and which involves irradiating, with monochromatic neutrons of energy 5 MeV, the same assemblies of targets as those that were used in the measurements of the photofission-yield ratios. The statistical accuracy of those measurements was about 3%. In calculating the above ratios, the neutron-induced-fission cross section σ_{nf} was set to 1.675 b for ^{245}Cm [18] and to 0.541 b for ^{238}U [11].

In the energy region $E_{\max} < 5.05$ MeV, the background of spontaneous-fission events prevented measurement of $R(E_{\max})$. With increasing energy, the background decreased, from 80% of the number of fission fragments recorded by the detector at $E_{\max} = 5.05$ MeV to about 5% at $E_{\max} = 6$ MeV and further to a negligible value.

Figure 2*a* shows the dependence $R(E_{\max})$ for ^{245}Cm. In the energy region around $E_{\max} < 6.5$ MeV, the measurement errors in $R(E_{\max})$ are about 10% everywhere, with the exception of a few points where

the spontaneous-fission background is significant. At energies above 6.5 MeV, the errors vary around 3.5%.

As was described above for ^{243}Cm, the experimental dependences $R(E_{max})$ obtained in back-to-back geometry were transformed into the integrated dependences of the photofission-reaction yields $Y(E_{max})$ and, upon smoothing, were processed by the method of minimizing directional discrepancies [13] in order to derive the photofission cross section as a function of energy, σ_f(E). The results of the calculations are displayed in Fig. 2*b*. The errors in the cross sections were determined in just the same way as for ^{243}Cm. Despite the smoothing of $Y(E_{max})$, a resonance-type irregularity in the energy region around 5.7 MeV is observed quite clearly, albeit within the errors. The emergence of the irregularity in this energy region may be attributed either to the competition with the neutron channel (the neutron binding energy for ^{245}Cm is $B_n = 5.52$ MeV) or to the resonance behavior of the photofission cross section as a function of energy, as was assumed in the case of ^{237}Np and ^{241}Am [8, 9]. According to the results of our measurements, the observed threshold for the cross section for ^{245}Cm photofission occurs at 6.3 MeV. At higher energies, the cross section for ^{245}Cm photofission does not show any irregularities.

Experimental data on ^{245}Cm photofission were obtained for the first time, and they can be compared with the results of other experiments only upon representing these data in the form of fissilities. While, for other nuclei studied in the experiments being described, the fissilities from the data of these experiments were compared with fissilities from direct-reaction data, for ^{245}Cm, only the data on the fissility from the neutron-induced fission reaction ^{244}Cm$(n, f)^{245}$Cm [19] are available for a comparison. Figure 2*c* displays the energy dependence of the fissility of ^{245}Cm according to the present data, from which this dependence was obtained in just the same way as above for ^{243}Cm. Also given in this figure are the data on the fissility of ^{245}Cm from the reaction of neutron-induced fission [19]. In the energy dependence of the fissility from the relevant (n, f) reaction, there is no irregularity in the energy region $E = 5.7$ MeV. This circumstance can be used as an argument in favor of the statement that the irregularity in question is a manifestation of the resonance structure in the photoabsorption cross section. As the energy increases up to about $E = 6.5$ MeV, the fissility in photofission, in just the same way as its counterpart in the neutron-induced fission reaction, increases; at higher energies, it remains virtually constant, as for other nuclei, exhibiting a fission plateau. Taking into account the above comment that the photoabsorption cross section used in the present calculations is overestimated for $E < 7$ MeV, one can state that the energy dependences $P_f(E)$ in the two reactions under comparison are very close in Fig. 2*c*.

Berkelium-249

The measurements of the photofission cross section for ^{249}Bk, which, through beta decay, transforms into ^{249}Cf, the corresponding half-life being $T_{1/2} =$ 320 d, were performed by using a fissile substance from the mixture of the ^{249}Bk and ^{249}Cf isotopes. In addition to the mixture of the ^{249}Bk and ^{249}Cf isotopes, the fissile substance contained less than 0.1% of admixtures of other isotopes.

The first series of measurements aimed at determining the energy dependences of the ratios of the yields from the photofission of the fissile substance under study to the corresponding yields from ^{238}U photofission was performed for the case where the ratio of the numbers of nuclei of the ^{249}Bk and ^{249}Cf isotopes was close to unity. The measurements were performed for 20 days, within which the number of ^{249}Bk nuclei decreased by about 4%. The second series of measurements was performed after a lapse of four years, when there remained not more than 3% of ^{249}Bk nuclei in the fissile substance. Throughout this time, the rate of spontaneous fission of the fissile substances was measured at regular intervals, while, before each series of the measurements of the ratios $R(E_{max})$, the ratios of the numbers of nuclei in the fissile targets from the mixture of the ^{249}Bk and ^{249}Cf isotopes to the number of reference nuclei were determined in dedicated experiments employing irradiation with monochromatic neutrons of energy 5 MeV. Because of a heavy spontaneous-fission background, the statistical accuracy of these measurements in the first series was 5%; in the second series, the accuracy was 3%. In calculating the ratios in question, the neutron-induced-fission cross section σ_{nf} was set to 1.47 b for ^{249}Bk, 2.067 b for ^{249}Cf, and 0.541 b for ^{238}U [11].

At the beginning of the first series of measurements, the spontaneous-fission background was slightly below one fission event per second, and this prevented the use of the experimental results obtained in the energy range 5–5.5 MeV. At an energy of 5.5 MeV, the background exceeded the number of photofission events by a factor of 6, but, by 5.7 MeV, it became commensurate with the photofission rate; in the energy region around $E_{max} \simeq 7$ MeV and above, the spontaneous-fission background was at a level of 10%. The background itself and its time dependence, which is predominantly caused by ^{249}Bk

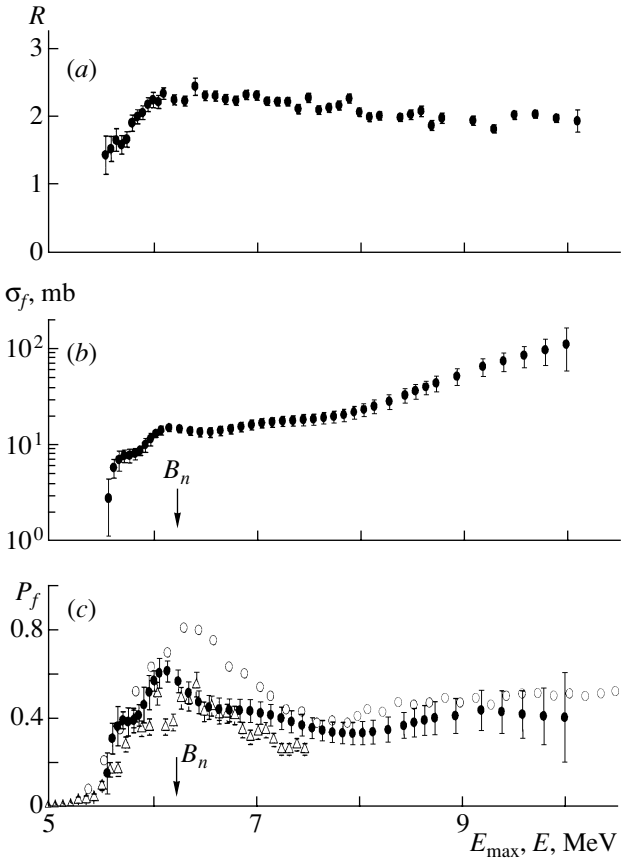

Fig. 3. (*a*) Ratio $R(E_{max})$ of the yields from the photofission of ^{249}Bk and ^{238}U as a function of the endpoint bremsstrahlung-spectrum energy E_{max}. (*b*) Cross section $\sigma_f(E)$ for ^{249}Bk photofission as a function of energy. (*c*) Fissility $P_f(E)$ of ^{249}Bk as a function of energy. In all of the panels, closed circles represent photofission data of the present study. The open circles and triangles in Fig. 3*c* correspond to data obtained by studying the relevant direct (^{3}He, *df*) reaction in [19] and [20], respectively.

nuclei undergoing beta decay, were measured to a precision of about 1%. During the second series of measurements, the spontaneous-fission background was 80% only at the first points around 6 MeV; it decreased to 10% at 6.5 MeV and was 1–3% at higher energies.

Given the data on the time dependence of the spontaneous-fission rate and the results of two experiments devoted to determining the ratio of the number of nuclei in fissile targets from the mixture of ^{249}Bk and ^{249}Cf to the corresponding number of ^{238}U reference nuclei, one could find, upon a few iterations, the ratio of the numbers of ^{249}Bk and ^{249}Cf nuclei during the first and the second series of measurements of the energy dependences $R(E_{max})$ and obtain data on these dependences for ^{249}Bk and ^{249}Cf individually. In experiments with monochromatic neutrons, an assembly containing ^{238}U and having a fissile-layer depth measured independently was used to perform an absolute normalization in the quantities of fissile substances. This made it possible to establish that, at the beginning of the first series of measurements, the fissile target from the mixture of ^{249}Bk and ^{249}Cf contained 32 μg of ^{249}Bk and 25 μg of ^{249}Cf. During the second series of measurements, there remained less than 2 μg of the ^{249}Bk isotope in the fissile layer.

Upon taking into account the spontaneous-fission background, the statistical accuracy in the first series of measurements of $R(E_{max})$ for a mixture of the ^{249}Bk and ^{249}Cf isotopes was at the level of the majority of the present relative measurements and improved with the reduction of the exposure time from 16% at an energy of 5.5 MeV to 3% at 6 MeV and higher. In the second series of measurements, when the fissile substance contained predominantly the ^{249}Cf isotope, the statistical accuracy improved from 10% at an energy of 6 MeV to 3% at $E \geq 7$ MeV. The introduction of corrections for the admixture of the ^{249}Cf isotope in the results of the first series of measurements led to an increase in their statistical error by a value of up to 2%.

Figure 3*a* shows the dependence $R(E_{max})$ for ^{249}Bk. The errors in the experimental data are quite large; for this reason, the energy dependences of the photofission yields, $Y(E_{max})$, were first subjected to smoothing (prior to processing), as in the case of ^{243}Cm, in order to obtain the energy dependence of the photofission cross section. The corresponding curve for σ_f(E) is depicted in Fig. 3*b*. In the subthreshold region, the dependence σ_f(E) exhibits an irregularity at $E = 5.7$ MeV, despite smoothing—the photofission cross section begins to grow much more slowly, and this can be interpreted as a manifestation of an unresolved resonance. As will be shown below, there is an indication of a similar effect at approximately the same energy in the investigation performed in [19] for ^{249}Bk fission via a direct reaction. In all probability, we are dealing here with an irregularity in the fission channel. After the plateau of $\sigma_f(E)$ above the neutron binding energy of $B_n = 6.22$ MeV, the photofission cross section shows a slight decrease, which is likely to be due to the competition between the fission and neutron channels of compound-nucleus decay. According to the results of our measurements, the observed threshold for the cross section for ^{249}Bk photofission lies at an energy of 5.8 MeV. At higher energies, the cross section for ^{249}Bk photofission does not exhibit any irregularities.

In order to compare the data on ^{249}Bk fission that were obtained in the present study with data from direct reactions, the photofission cross sections $\sigma_f(E)$

were rescaled (by the same method as in the case of ^{243}Cm) into the energy dependences of the fissilities. These dependences are displayed in Fig. 3*c*, along with the results reported in [19, 20] and obtained by studying the reaction ^{248}Cm(^{3}He, *df*)^{249}Bk. The general character of the dependence $P_f(E)$ in our measurements is rather close to that in direct reactions, and there is even some proximity of the details in the threshold energy region between the present data and those in [19], as was indicated above. It is hardly advisable to compare absolute fissility values because, as can be seen from Fig. 3*c*, they differ strongly even in studying the same direct reaction.

Californium-249

Data characterizing the fissile substance used in the measurements with ^{249}Cf and the corresponding background conditions are presented in the first paragraphs of the subsection devoted to berkelium-249.

Figure 4*a* displays the dependence $R(E_{\max})$ for ^{249}Cf. Prior to processing this experimental information with the aim of obtaining the energy dependence of the photofission cross section, the dependences of the photofission yields, $Y(E_{\max})$, were also subjected to smoothing. The corresponding curve for $\sigma_f(E)$ is shown in Fig. 4*b*. The errors in the cross sections were determined by the method that is traditional for the present series of experiments. According to the results of these measurements, the observed threshold for ^{249}Cf photofission occurs at an energy of 6.5 MeV. All of the small irregularities of the subthreshold increase in the photofission cross section in the energy region below $E = 7$ MeV are within the errors. An unusually high maximum in the energy region around 11 MeV is a special feature of the above-threshold behavior of the cross section $\sigma_f(E)$.

This feature of ^{249}Cf fission is more clearly seen in the fissility $P_f(E)$ calculated as a function of energy by formula (3) with the photofission cross section for ^{238}U and presented in Fig. 4*c*. In the energy region around 11 MeV, the fissility increases by a factor greater than 1.5. In addition, Fig. 4*c* shows the fissility $P_f(E)$ calculated as a function of energy on the basis of the cross sections for ^{249}Cf photofission (Fig. 4*b*), which were obtained in an experiment also performed with bremsstrahlung photons from a microtron [in this case, the one installed at the Joint Institute for Nuclear Research (JINR, Dubna)], the energies in that experiment being in excess of 10 MeV [21]. The latter dependence also shows an approximately 1.5-fold increase, but this occurs at an energy higher by 1 MeV. Nevertheless, this change in the fissility occurs below the threshold for the reaction ^{249}Cf(γ, nf)

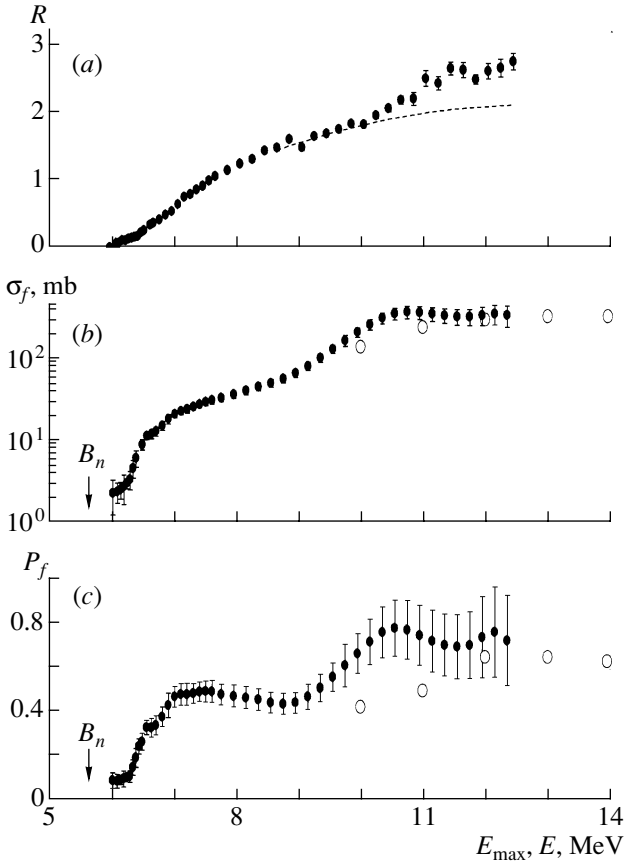

Fig. 4. (*a*) Ratio $R(E_{\max})$ of the yields from the photofission of ^{249}Cf and ^{238}U nuclei as a function of the endpoint bremsstrahlung-spectrum energy $E_{\max}$. The meaning of the dashed curve is explained in the main body of the text (see subsection devoted to californium-249). (*b*) Cross section $\sigma_f(E)$ for ^{249}Cf photofission as a function of energy. (*c*) Fissility $P_f(E)$ of ^{249}Cf as a function of energy. Points represent photofission data from (closed circles) the present study (in all of the panels) and (open circles) [21] (*b*, *c*).

(12.62 MeV) both in [21] and in the present study, whence we conclude that it can hardly be due to the opening of a yet another fission channel. There are no data on the fissility of ^{249}Cf in some other reactions.

It is difficult to explain the emergence of a maximum by some experimental error. None of the nuclei studied simultaneously with ^{249}Cf in the same assembly (three Am isotopes and ^{243}Cm) has such an anomaly in $P_f(E)$. At the same time, the dependence $R(E_{\max})$ calculated under the assumption that $P_f(E)$ is constant over the entire energy range 7–12 MeV lies far beyond the experimental errors (dashed curve in Fig. 4*a*).

The observed increase in the cross section is of a resonance character and occurs at an energy of 11 MeV, which corresponds to the left maximum

Table 2. Averaged values of $\bar{P}_f$ within the fissility plateau, energy intervals ΔE over which averaging was performed, and observed fission thresholds E_{obs} for the nuclei under investigation

Fissile nucleus	$\bar{P}_f$	ΔE, MeV	E_{obs}, MeV	Nuclear Reaction	References
^{243}Cm	0.61 ± 0.02	7–12.3	6.3	(γ, f)	Present study
	0.59 ± 0.01	7–11.6	6.25	$(^3\text{He}, tf)$	[14]
^{245}Cm	0.46 ± 0.02	7–10	6.2	(γ, f)	Present study
	0.50	6.5–7.1	6.2	(n, f)	[19]
^{249}Bk	0.38 ± 0.02	7–10	5.6	(γ, f)	Present study
	0.30 ± 0.01	6.9–7.5	5.6	$(^3\text{He}, df)$	[19]
	0.47 ± 0.03	8.0–10.5	5.6	$(^3\text{He}, df)$	[20]
^{249}Cf	0.45 ± 0.02	7–9	6.4	(γ, f)	Present study
	0.45	10–11	–	(γ, f)	[21]

of the giant dipole resonance. The fissility obtained from the dependence $\sigma_f(E)$ [21] does not confirm the existence of a cross-section maximum in this energy range, but the integrated data also presented here for the photofission yields $Y(E_{\max})$ are compatible with the existence of this maximum, albeit within the experimental errors. A fairly sharp distinction between the photofission cross sections for ^{249}Cf and ^{238}U in the region of the left giant-dipole-resonance maximum—such distinctions were experimentally observed, for example, in [22] for ^{237}Np and ^{238}U and in [15, 23] for ^{233}U and ^{238}U—may be one of the reasons behind this behavior of $P_f(E)$ for ^{249}Cf. Among 19 nuclear species investigated in the present series of measurements of photofission cross sections by the relative method, deviations of about 10 to 15% from the plateau-like behavior of the fissility in the energy region being considered were observed for five more nuclei, but all of these deviations are within the experimental errors of these measurements.

The data on the fissilities and the observed fission thresholds from the present experiment are compiled in Table 2, along with relevant data from the literature.

DISCUSSION

The present study completes the series of experiments aimed at measuring the photofission cross sections for a wide range of nuclei by the universal relative method with the cross section for ^{238}U fission as a reference. Here and in [9], a unified approach that employs, for the nuclear species being studied, the dipole-photoabsorption cross section $\sigma_{c1}(E)$ for ^{238}U was used to calculate, from the energy dependences of $P_f(E)$ for the Am, Cm, Bk, and Cf isotopes in the energy region corresponding to the first fissility plateau, the fissilities $\bar{P}_f$ averaged over the energy range $E = 10 \pm 1$ MeV (see Table 2). In order to represent the entire body of fission data from this series of measurements in a form that is convenient for a comparative analysis of these data and for a comparison with data from other investigations of the fission process, the averaged fissilities $\bar{P}_f$ were obtained from the photofission-cross-section values found previously [1, 7, 8, 17, 24]. This was done by a method similar to that used in [9]. With the aid of the relation

$$\Gamma_n/\Gamma_f = 1/\bar{P}_f - 1, \qquad (5)$$

the averaged fissilities were rescaled into the ratios of the mean neutron and fission widths, Γ_n/Γ_f. These ratios are displayed in Fig. 5 versus the mass number A of the compound nucleus, along with the data on Γ_n/Γ_f that were computed by using the systematics compiled in [25] for the parameters of the neutron-induced-fission reaction for $Z \geq 92$ nuclei. For the $Z = 91$ nucleus (Pa), the earlier systematics from [26] had to be invoked, the calculated values of Γ_n/Γ_f from it for the neighboring uranium nucleus being virtually coincident with the Γ_n/Γ_f values from the systematics in [25]. In comparing experimental data with the calculated values of Γ_n/Γ_f, neither of these systematics is applicable in the case of thorium isotopes ($Z = 90$), since the complicated structure of the external barrier B, which determines the fission parameters of these nuclei, is disregarded in both of them.

For some isotopes studied in the present series of relative measurements of photofission cross sections, the solid lines in Fig. 5 connect the calculated values

of Γ_n/Γ_f that were obtained on the basis of neutron-data systematics from [25, 26]. The open circles in the same figure represent Γ_n/Γ_f values determined by applying the method described above to data on the photofission cross sections. The displayed experimental errors are purely statistical. From Fig. 5, it can be seen that all open circles lie systematically higher than the curves representing the neutron data. Let us try to analyze this circumstance. It can be assumed that a systematic error in going over from integrated data on photofission yields to photofission cross sections is the reason behind this discrepancy. In order to verify this assumption, the parameter Γ_n/Γ_f was calculated, for all nuclei studied here, in terms of the fissilities $\bar{P}_f(X)$ obtained directly from the integrated data on the photofission yields $Y(X)$. This was done with the aid of the relation

$$\bar{P}_f(X) = \bar{P}_f(^{238}\mathrm{U})\frac{Y(X)}{Y(^{238}\mathrm{U})}\frac{(NZ/A)_{^{238}\mathrm{U}}}{(NZ/A)_X}, \quad (6)$$

which was used in [5, 6]. In accordance with the sum rule, the last factor in this relation reflects the distinction between the total photoabsorption cross section for a specific nucleus and that for ^{238}U. This distinction slightly exceeds 5% in the most unfavorable case, and it was disregarded in calculating $\bar{P}_f$ on the basis of data on the photofission cross sections. The authors of [5, 6] relied on the assumption that the energy dependences of the total dipole-photoabsorption cross sections are similar for all nuclei. The factor NZ/A apart, this is equivalent to the assumption adopted here that, in calculating the fissility P_f, the photoabsorption cross section for all nuclei studied here is equal to the cross section $\sigma_{c1}(E)$ for ^{238}U. This is precisely what makes it possible to compare the parameters Γ_n/Γ_f obtained from photofission cross sections with those obtained from integrated data. In Fig. 5, the Γ_n/Γ_f values deduced from the integrated data are shown by inclined crosses. From Fig. 5, it can be seen that, for the overwhelming majority of the nuclei studied here, the photofission parameters Γ_n/Γ_f obtained by the different methods are in reasonably good agreement. The agreement between the parameters extracted from integrated data on photofission yields and those extracted from the energy dependences of the photofission cross sections can be taken as one more piece of evidence that there are no significant systematic errors in calculating the latter.

For the ^{249}Cf nuclei, the values of Γ_n/Γ_f are given for two energy ranges: $E = 7$–9 and 10–12 MeV. For the latter, the value of Γ_n/Γ_f (closed circle in Fig. 5) lies below the curve of the systematics, and this casts some doubt on its reliability. Although the integrated value was calculated on the basis of data for the energy $E_{\max}$ between 11 and 12 MeV, it carries information about the fission process at lower energies inclusive. Accordingly, it occupies an intermediate position.

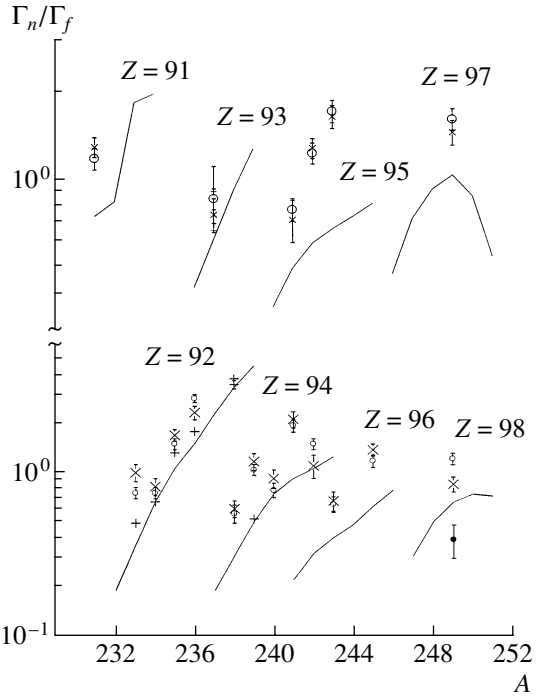

Fig. 5. Ratio Γ_n/Γ_f of the mean neutron and fission widths according to calculations on the basis of photofission data versus the nucleonic composition of nuclei. The dashed lines connect the estimates of Γ_n/Γ_f that were obtained on the basis of the neutron-data systematics from [25, 26]. The points represent Γ_n/Γ_f values obtained (open circles) by averaging fissilities calculated on the basis of the photofission cross sections from the present series of relative measurements, (crosses) from the integrated data of the present series of measurements, (vertical crosses) from measurements employing quasi-monochromatic photons in [15, 22, 23], and (closed circle) for ^{249}Cf in the region of the anomalous photofission-cross-section resonance (10–12 MeV).

The direct crosses in Fig. 5 represent the parameters Γ_n/Γ_f obtained in experiments with monochromatic photons, where the photofission and photoabsorption cross sections were measured in the same experiment [15, 22, 23]. For seven nuclei studied here, the parameters Γ_n/Γ_f agree fairly well with the estimates based on the neutron-data systematics from [25]. For the eighth nucleus of ^{232}Th, it is impossible to perform the corresponding comparison. Considering that, in the energy range 8–11 MeV, the photofission cross sections obtained in our relative measurements agree well with the cross sections from [15, 23], one can conclude that the choice of the cross section $\sigma_{c1}(E)$ for ^{238}U photofission in calculating the fissilities P_f as a universal reference for all

nuclei studied here leads to a rather large systematic error.

In all probability, the assumption put forth in [6] that the photoabsorption cross sections for different heavy nuclei differ in magnitude only by the factor NZ/A is quite rough. In view of the results of the present experiment for ^{249}Cf and data of the measurements of $\sigma_{c1}(E)$ in experiments with monochromatic photons [15, 22, 23], there is also some doubt about the assumption that the energy dependences $\sigma_{c1}(E)$ are similar in form for different nuclei.

CONCLUSION

The energy dependences of the cross sections for the photofission of ^{243}Cm, ^{245}Cm, ^{249}Bk, and ^{249}Cf isotopes have been obtained in the energy range from 5 or 6 to 10 or 12 MeV by using the microtron installed at the Institute of Physics and Power Engineering (Obninsk). The photofission cross sections in question have been measured by the relative method with bremsstrahlung photons, the cross section for ^{238}U photofission being used as a reference. Data on the cross sections for the photofission of ^{243}Cm, ^{245}Cm, and ^{249}Bk have been obtained for the first time. For the ^{249}Cf nuclei, experimental results were available for $E > 10$ MeV [21], but the data in the energy region $E < 10$ MeV have been obtained for the first time. As in [8, 9], evidence has been found here for the existence of an irregularity in the energy region around 6 MeV. In all probability, it originates from the low-energy resonance structure of the dipole-photoabsorption cross section [27]. For ^{249}Cf, an anomalously large photofission cross section has been observed in the region of the lower (in energy) maximum of the giant dipole resonance ($E \approx 11$ MeV). The results deduced for the ^{243}Cm and ^{249}Bk isotopes by calculating their fissilities versus energy from photofission data have been compared with the corresponding fissilities from data on the relevant direct (^{3}He, *df*) reactions. This comparison has revealed the agreement of the observed fission thresholds and the presence of a plateau-like dependence at energies above 7.5 MeV.

The present study completes the series of relative measurements of photofission cross sections with bremsstrahlung photons. This series resulted in obtaining, by means of a universal procedure, photofission data for 19 fissile nuclei from the fission threshold to $E = 10$–12 MeV (this study and [1, 7–9, 17, 24]). In going over from the energy dependences of the photofission cross sections to fissilities, the relevant cross section for the ^{238}U nucleus was taken for the photoabsorption cross section as a universal quantity for all nuclei. An analysis of the entire body of data on fissilities revealed that they are exaggerated in relation to fissilities obtained by simultaneously measuring photofission and photoabsorption cross sections [15, 22, 23]. In all probability, the reason for this lies in employing the rough approximation of Aleksandrov *et al.* [6], who assumed that the photoabsorption cross sections for heavy nuclei differ in magnitude only by the factor NZ/A. In view of the results of the present experiment for ^{249}Cf and data obtained in [15, 22, 23] by measuring $\sigma_{c1}(E)$ in experiments with monochromatic photons, the assumption that the energy dependences $\sigma_{c1}(E)$ for different nuclei are similar is also questionable.

ACKNOWLEDGMENTS

I am grateful to Yu. B. Ostapenko for stimulating discussions on the results of this study and to V. E. Rudnikov for participation in the measurements.

REFERENCES

1. G. N. Smirenkin and A. S. Soldatov, Yad. Fiz. **59**, 203 (1996) [Phys. At. Nucl. **59**, 185 (1996)].
2. V. E. Zhuchko *et al.*, Yad. Fiz. **28**, 1170 (1978) [Sov. J. Nucl. Phys. **28**, 602 (1978)].
3. A. S. Soldatov *et al.*, At. Énerg. **69**, 267 (1990).
4. K. N. Ivanov and K. A. Petrzhak, At. Énerg. **36**, 404 (1974).
5. I. S. Koretskaya *et al.*, Yad. Fiz. **30**, 910 (1979) [Sov. J. Nucl. Phys. **30**, 472 (1979)].
6. B. M. Aleksandrov *et al.*, Yad. Fiz. **43**, 290 (1986) [Sov. J. Nucl. Phys. **43**, 185 (1986)].
7. A. S. Soldatov and G. N. Smirenkin, Yad. Fiz. **55**, 3153 (1992) [Sov. J. Nucl. Phys. **55**, 1757 (1992)].
8. A. S. Soldatov *et al.*, Yad. Fiz. **56** (10), 16 (1993) [Phys. At. Nucl. **56**, 1307 (1993)].
9. A. S. Soldatov, Yad. Fiz. **64**, 211 (2001) [Phys. At. Nucl. **64**, 169 (2001)]
10. B. I. Fursov *et al.*, in *Proceedings of the International Conference on Nuclear Data for Science and Technology, Trieste, 1997,* Ed. by G. Reffo, A. Ventura, and C. Grandi (Trieste, 1997), Part I, p. 488.
11. The ENDF/B-6, Neutron Cross Section Measurement Standards.
12. M. Z. Tarasko *et al.*, At . Énerg. **65**, 290 (1988).
13. M. Z. Tarasko, Preprint No. 1446, FÉI (Institute of Physics and Power Engineering, Obninsk, 1983).
14. A. Gavron *et al.*, Phys. Rev. C **13**, 2374 (1976).
15. J. T. Caldwell *et al.*, Phys. Rev. C **21**, 1215 (1980).
16. Yu. B. Ostapenko *et al.*, Fiz. Élem. Chastits At. Yadra **12**, 1364 (1981) [Sov. J. Part. Nucl. **12**, 545 (1981)].
17. A. S. Soldatov, A. I. Blokhin, A. V. Ignatyuk, and A. N. Storozhenko, Yad. Fiz. **63**, 34 (2000) [Phys. At. Nucl. **63**, 31 (2000)].
18. É. F. Fomushkin *et al.*, At . Énerg. **63**, 242 (1987).

19. B. B. Back *et al.*, in *Proceedings of the International Symposium on Physics and Chemistry of Fission, Rochester, 1973* (IAEA, Vienna,1974), Vol. I, p. 3.
20. A. Gavron *et al.*, Phys. Rev. C **15**, 2238 (1977).
21. N. I. Tarantin and Kim Su Men, in *Proceedings of the XIV Meeting on Physics of Nuclear Fission, Obninsk, 2000* (SSC RF IPPE, 2000), p. 211.
22. A. Veyssière *et al.*, Nucl. Phys. A **199**, 45 (1973).
23. B. L. Berman *et al.*, Phys. Rev. C **34**, 2201 (1986).
24. A. S. Soldatov and G. N. Smirenkin, Yad. Fiz. **58**, 224 (1995) [Phys. At. Nucl. **58**, 182 (1995)]; A. S. Soldatov *et al.*, At . Énerg. **78**, 400 (1995); A. S. Soldatov, A. I. Blokhin, A. V. Ignatyuk, and A. N. Storozhenko, Yad. Fiz. **61**, 1427 (1998) [Phys. At. Nucl. **61**, 1325 (1998)].
25. V. M. Kupriyanov, G. N. Smirenkin, and B. I. Fursov, Yad. Fiz. **39**, 281 (1984) [Sov. J. Nucl. Phys. **39**, 176 (1984)].
26. V. M. Kupriyanov *et al.*, Yad. Fiz. **32**, 355 (1980) [Sov. J. Nucl. Phys. **32**, 184 (1980)].
27. G. A. Bartholomew *et al.*, Adv. Nucl. Phys. **7**, 229 (1973).

Translated by A. Isaakyan

Physics of Atomic Nuclei, Vol. 66, No. 3, 2003, pp. 558–564. Translated from Yadernaya Fizika, Vol. 66, No. 3, 2003, pp. 584–590.

NUCLEI
Theory

Temperature Generalization of the Quasiparticle Random-Phase Approximation with Allowance for a Continuum

E. V. Litvinova, S. P. Kamerdzhiev, and V. I. Tselyaev[1)]

Institute of Physics and Power Engineering, pl. Bondarenko 1, Obninsk, Kaluga oblast, 249020 Russia

Received March 11, 2002; in final form, July 8, 2002

Abstract—The method developed previously by the present authors on the basis of the quasiparticle random-phase approximation with allowance for a single-particle continuum is generalized to the case of finite temperatures and is implemented numerically for the isovector $E1$ resonance in the nuclei of even tin isotopes—specifically, in the stable nucleus ^{120}Sn and in the unstable nucleus ^{104}Sn. The temperature dependence of the integrated features of the resonance and the temperature dependence of its envelope are discussed. © *2003 MAIK "Nauka/Interperiodica".*

INTRODUCTION

At present, a theoretical description of nuclear systems at finite temperatures is of particular importance in the physics of giant resonances. Despite a great number of studies in these realms (see [1–4] and references therein), the role of a continuous single-particle spectrum or the width $\Gamma\uparrow$ received virtually no adequate study at nonzero temperatures. For magic nuclei, this was done in [2] for ^{40}Ca. For nonmagic nuclei, a procedure for taking into account a continuum at nonzero temperatures was developed within the self-consistent theory of finite Fermi systems [5], but this procedure is applicable only to a static case.

The role of the continuous spectrum at nonzero temperatures in nonmagic nuclei is worth studying in the dynamical case as well. For nonmagic nuclei, it is necessary to take into account, in contrast to what was done for magic nuclei, the temperature dependence of the pairing gap for $T < T_c = 0.57\Delta(0)$, where T_c is the critical temperature at which pairing disappears and $\Delta(0)$ is the pairing gap at $T = 0$. In general, it is natural to expect a singular behavior of various dynamical quantities (including an integrated strength and mean energies) in the vicinity of the point $T = T_c$. Within the conventional quasiparticle random-phase approximation (QRPA) taking no account of the continuous spectrum, this issue was discussed previously (see, for example, [3] and references therein). For giant multipole resonances in the neutral channel, the QRPA method allowing for a single-particle continuum (QRPA-plus-continuum method, also referred to as the CQRPA method) was proposed and implemented numerically in [6, 7] at zero temperature.

In this article, we present the first results obtained by calculating giant resonances within the temperature generalization of the CQRPA method [6, 7] (TCQRPA method). In the physics of giant resonances, this means that two competing effects—the temperature smearing of the Fermi surface and the decrease in this smearing because of the reduction of the pairing gap with increasing temperature—affect the formation of that part of the resonance width which is determined by the escape of particles from a nucleus ($\Gamma\uparrow$ is the relevant width) and by the Landau damping (these phenomena are well known in cold nuclei).

In our approach, the single-particle continuum is taken completely into account at the level of the random-phase approximation (RPA). For charge-exchange excitations at zero temperature, a similar method for the inclusion of a continuum was developed in [8]. It is based on the technique of the mixed (r, λ) representation that was applied in [9] to describe the first 2^+ levels in a neutral channel and which was also employed in [6, 7]. In contrast to the method used in [8], our approach is not self-consistent; that is, our calculations rely on the mean-field potential of the Woods–Saxon form and the effective particle–hole interaction whose parameters are known. The calculations were performed for the isovector $E1$ resonance in the stable isotope ^{120}Sn and in the unstable isotope ^{104}Sn.

[1)]Institute of Physics, St. Petersburg State University, Universitetskaya nab. 7/9, St. Petersburg, 199164 Russia.

1063-7788/03/6603-0558$24.00

BASIC RELATIONS AND DETAILS OF THE CALCULATIONS

In this study, we consider EL resonances for which the corresponding matrix elements in the QRPA or in the theory of finite Fermi systems are off-diagonal. For such resonances, the contribution from the variation of the gap in an external field can be disregarded [10] (in terms of the theory of the finite Fermi systems, this means that the following equalities hold for the effective fields: $d^{(1)} = d^{(2)} = 0$). In this section, all formulas are obtained in this approximation; basic expressions are given in a form that arises upon separating angular variables (for details, the interested reader is referred to [7]).

Heating induces changes in all of the quantities that are of importance for a microscopic description of a nucleus, including the mean field (of course, a change in the mean field entails a change in single-particle energies and wave functions), effective interaction, local charges, occupation numbers of quasiparticles, and the gap. These changes can be taken into account by the method of Green's functions, and the majority of these were analyzed in [11]. It was shown that, for $T \leq 2$–3 MeV, the main effect reduces to changes in occupation numbers and in the Cooper gap. In order to avoid strong complications, we restrict ourselves to the case of such temperatures. This means that only the particle–hole (ph) propagator is subjected to a temperature generalization.

We calculate the cross section for the electric L-pole photoabsorption of a photon of energy E by a nucleus at a nonzero temperature T. We have

$$\sigma_L(E,T) = \frac{8\pi^3(L+1)e^2}{L[(2L+1)!!]^2}\left(\frac{E}{\hbar c}\right)^{2L-1} S_L(E,T),$$

where the strength function

$$S_L(E,T) = -\frac{1}{\pi}\mathrm{Im}\Pi_L(\omega,T), \tag{1}$$
$$\Pi_L(\omega,T) = (2L+1)$$
$$\times \sum_{S,\tau}\delta_{S0}e_\tau \int_0^\infty dr\, r^{J+2}\delta\rho_{S,\tau}(r;\omega;T),$$
$$\omega = E + i\eta, \quad \eta \to +0,$$

is expressed in terms of a change in the density-matrix of a nuclear system in an external field, $\delta\rho$; L is the orbital angular momentum of the electric excitation involved; S is the spin index ($S = 0, 1$); τ is the isotopic index ($\tau = n, p$); $J = L$ at $L \geq 1$; and e_τ is the local nucleon charge.

For the quantity $\delta\rho$, we will solve the set of equations of the theory of finite Fermi systems in the coordinate representation. After the separation of angular variables, this set of equations takes the form

$$\delta\rho_{S,\tau}(r_1;\omega;T) = \delta\rho^{(0)}_{S,\tau}(r_1;\omega;T) \tag{2}$$
$$-\sum_{S',\tau'}\int_0^\infty dr_2 r_2^2 \mathcal{A}^{(\tau)L}_{LS,LS'}(r_1,r_2;\omega;T)$$
$$\times \mathcal{F}^{\tau\tau'}_{S'}(r_2)\delta\rho_{S',\tau'}(r_2;\omega;T),$$

$$\delta\rho^{(0)}_{S,\tau}(r_1;\omega;T) \tag{3}$$
$$= -e_\tau \int_0^\infty dr_2 r_2^{J+2}\mathcal{A}^{(\tau)L}_{LS,L0}(r_1,r_2;\omega;T),$$

where $\mathcal{F}$ is the amplitude of the effective ph interaction.

For nuclei involving a fully developed pairing, the particle–hole propagator at a nonzero temperature is calculated by the technique of temperature Green's functions (see, for example, [12]).

For the problem at hand, the radial part of the ph propagator, $\mathcal{A}^{(\tau)L}_{LS,LS'}(r_1,r_2;\omega;T)$, can be represented as

$$\mathcal{A}^{(\tau)L}_{LS,LS'}(r_1,r_2;\omega;T) = \mathcal{A}^{\mathrm{cont}(\tau)L}_{LS,LS'}(r_1,r_2;\omega;T) \tag{4}$$
$$+ \mathcal{A}^{\mathrm{disc}(\tau)L}_{LS,LS'}(r_1,r_2;\omega;T),$$

where $\mathcal{A}^{\mathrm{cont}}$ is that part of the propagator which describes transitions from paired levels of the discrete spectrum to a continuum, the pairing being disregarded in the continuum. Specifically, we have

$$\mathcal{A}^{\mathrm{cont}L}_{LS,LS'}(r,r';\omega;T) \tag{5}$$
$$= -\sum_1 v_1^2(T)(1-n_1(T))R_1(r)R_1(r')\sum_{l_2j_2}T^{LSS'}_{12}$$
$$\times\Big[\mathcal{G}_{l_2j_2}(r,r';\mu(T)-E_1(T)+\omega)$$
$$+(-1)^{S+S'}\mathcal{G}_{l_2j_2}(r,r';\mu(T)-E_1(T)-\omega)\Big]$$
$$-\sum_1 u_1^2(T)n_1(T)R_1(r)R_1(r')\sum_{l_2j_2}T^{LSS'}_{12}$$
$$\times\Big[\mathcal{G}_{l_2j_2}(r,r';\mu(T)+E_1(T)+\omega)$$
$$+(-1)^{S+S'}\mathcal{G}_{l_2j_2}(r,r';\mu(T)+E_1(T)-\omega)\Big],$$

where

$$n_1(T) = \frac{1}{1+\exp(E_1(T)/T)},$$
$$v_1(T) = \frac{1}{2}\left(1-\frac{\epsilon_1-\mu(T)}{E_1(T)}\right),$$
$$E_1(T) = \sqrt{(\epsilon_1-\mu(T))^2+\Delta_1^2(T)};$$

$R_1(r)$ is the radial single-particle wave function; and $1 \equiv (n_1, l_1, j_1)$ is the set of single-particle quantum numbers in a spherical nucleus. Hereafter, we omit isotopic indices in order to avoid encumbering relevant formulas. The partial-wave components $\mathcal{G}_{lj}$ of the radial Green's function without pairing can be calculated exactly [13], which makes it possible to take completely into account the single-particle continuum at the RPA level. The quantity $\mathcal{A}^{\rm disc}$ stands for that part of the propagator which involves pairing corrections to the spectrum section where the Cooper gap is nonzero; that is,

$$\mathcal{A}^{{\rm disc}L}_{LS,LS'}(r,r';\omega;T) \tag{6}$$
$$= \sum_{12}^{\rm disc} R_1(r)R_2(r')R_1(r')R_2(r)T_{21}^{LSS'}$$
$$\times \Bigg[\mathcal{L}_{12}(\omega,T) + \frac{v_2^2(T)(1-n_2(T))}{\omega+\mu(T)-\epsilon_1-E_2(T)} - \frac{v_1^2(T)(1-n_1(T))}{\omega-\mu(T)+\epsilon_2+E_1(T)} + \frac{u_2^2(T)n_2(T)}{\omega+\mu(T)-\epsilon_1+E_2(T)} - \frac{u_1^2(T)n_1(T)}{\omega-\mu(T)+\epsilon_2-E_1(T)} + (-1)^S\mathcal{M}_{12}(\omega,T)\Bigg],$$

where

$$\mathcal{L}_{12}(\omega,T) = -A_{ph}(\omega,T) \tag{7}$$
$$\times \Big[(u_1^2u_2^2+v_1^2v_2^2)(E_1-E_2) - (u_1^2u_2^2-v_1^2v_2^2)\omega\Big] - A_{pp}(\omega,T)\Big[-(u_1^2v_2^2+v_1^2u_2^2)(E_1+E_2) + (u_1^2v_2^2-v_1^2u_2^2)\omega\Big],$$
$$\mathcal{M}_{12}(\omega,T) = \frac{\Delta_1\Delta_2}{2E_1E_2}\Big[A_{ph}(\omega,T)(E_1-E_2) + A_{pp}(\omega,T)(E_1+E_2)\Big],$$
$$A_{ph}(\omega,T) = \frac{n_1(T)-n_2(T)}{(E_1-E_2)^2-\omega^2},$$
$$A_{pp}(\omega,T) = \frac{1-n_1(T)-n_2(T)}{(E_1+E_2)^2-\omega^2};$$

$\sum_{12}^{\rm disc}$ denotes summation over the discrete part of the single-particle basis, which, in our calculations, involves the levels from the bottom of the well to 5 MeV; u_1 and v_1 are the occupation numbers for Bogolyubov quasiparticles; Δ_1 is the relevant matrix element of the Cooper gap; and $T_{12}^{LSS'}$ is the product of the reduced matrix elements of spherical tensor operators:

$$T_{12}^{LSS'} = \frac{1}{2L+1}\langle j_1 l_1 \parallel T_{LLS} \parallel j_2 l_2\rangle \times \langle j_1 l_1 \parallel T_{LLS'} \parallel j_2 l_2\rangle. \tag{8}$$

The single-particle wave functions and levels for ^{104}Sn were calculated by using the standard Woods–Saxon potential. For ^{120}Sn, the potential parameters were fitted to the known experimental quasi-single-particle levels that were borrowed from [14]. In the calculations, we used the particle–hole interaction from the theory of finite Fermi systems [10]; that is,

$$F(\mathbf{r},\mathbf{r}') = C_0\Big[f(r) + f'(r)\boldsymbol{\tau}_1\cdot\boldsymbol{\tau}_2 + (g+g'\boldsymbol{\tau}_1\cdot\boldsymbol{\tau}_2)\boldsymbol{\sigma}_1\cdot\boldsymbol{\sigma}_2\Big]\delta(\mathbf{r}-\mathbf{r}'), \tag{9}$$
$$f(r) = f_{\rm ex} + (f_{\rm in}-f_{\rm ex})\frac{\rho_0(r)}{\rho_0(0)},$$

where the parameters were set to the values identical to those in [6, 7] and $\rho_0(r)$ is the ground-state nuclear density. The forced-consistency procedure developed in [7] for the zero-temperature case is included in our temperature generalization. The matrix elements of the Cooper gap $\Delta_1(T)$ were calculated (with allowance for the law of particle-number conservation) in the diagonal-pairing approximation according to the equation

$$\hat{j}_\nu\Delta_\nu(T) = -\sum_{\nu'}\Gamma^{\xi}_{\nu\nu'}\frac{\hat{j}_{\nu'}\Delta_{\nu'}(T)}{2E_{\nu'}(T)}(1-2n_{\nu'}(T)), \tag{10}$$

where $\hat{j}_\nu = \sqrt{2j_\nu+1}$ and ν is the set of single-particle quantum numbers where the projection of the total angular momentum is excluded. The matrix elements of the local amplitude that is associated with the interaction in the two-particle channel and which is renormalized according to the theory of finite Fermi systems are given by

$$\Gamma^{\xi}_{\nu\nu'} = \gamma_0^{\xi}(-1)^{l_\nu+l_{\nu'}}\frac{\sqrt{(2j_\nu+1)(2j_{\nu'}+1)}}{4\pi} \times \int_0^\infty drr^2R_\nu^2(r)R_{\nu'}^2(r), \tag{11}$$
$$\gamma_0^{\xi} = \frac{C_0}{\ln(c_p/\xi)}, \qquad \xi = \sqrt{\xi_1\xi_2},$$

where $C_0 = 300$ MeV fm^3 and c_p is a phenomenological parameter that was set to 1 MeV in our calculations. The quantities ξ_1 and ξ_2 determine the boundaries of the basis in which the gap equation is solved and which, as in (6), includes states from the bottom of the well to 5 MeV.

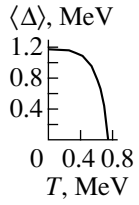

Fig. 1. Temperature dependence of the gap averaged over states in the vicinity of the Fermi surface for the ^{120}Sn nucleus.

The temperature dependence of the gap averaged over states in the vicinity of the Fermi surface for the ^{120}Sn nucleus is shown in Fig. 1. The critical temperature for this nucleus proved to be $T_c = 0.75$ MeV. In calculating the strength function by formula (1), we used the finite value of $\eta = 200$ keV for the imaginary part of the energy variable. We chose it in such a way that it was on the same order of magnitude with the experimental resolution, on one hand, and that the effect of the single-particle continuum was quite pronounced, on the other hand. The energy-weighted sum rule (EWSR) is defined as follows (in %):

$$\mathrm{EWSR} = \sigma_{\mathrm{int}}/\sigma_{\mathrm{int}}^{\mathrm{TRK}}, \qquad (12)$$

$$\sigma_{\mathrm{int}} = \int dE\sigma(E),$$

$$\sigma_{\mathrm{int}}^{\mathrm{TRK}} = 60\frac{NZ}{A}\,(\mathrm{mb\ MeV}),$$

where $\sigma_{\mathrm{int}}^{\mathrm{TRK}}$ is the integrated Thomas–Reiche–Kuhn photoabsorption cross section. The averaged energy of the resonance is given by [7]

$$\bar{E} = \left(\frac{m_1}{m_{-1}}\right)^{1/2}, \quad m_k = \int dES(E)E^k. \qquad (13)$$

The resonance width is defined as the width of the Lorentz distribution approximating the model strength function. According to [15], the expression for the resonance width has the form

$$\Gamma = -\sqrt{2}\left(\frac{m_1}{\bar{E}^2 P_L^R(\bar{E})} + 1\right)\bar{E}, \qquad (14)$$

$$P_L^R(E) = Re\Pi_L(Ee^{i\pi/4}).$$

In expressions (12)–(14), the quantities involved are assumed to be temperature-dependent.

DISCUSSION OF THE RESULTS

The results of the calculations are presented in Figs. 1–8.

As was already indicated, Fig. 1 shows the temperature dependence of the gap averaged over states in the vicinity of the Fermi surface for the ^{120}Sn nucleus. The dependence $\langle\Delta\rangle(T)$ is close to a root-square form, and this is in accord with the Bardeen–Cooper–Schrieffer (BCS) theory. For this nucleus, the ratio $\gamma = T_c/\langle\Delta\rangle(0) = 0.62$ is also in reasonably good agreement with the results of BCS theory ($\gamma_{\mathrm{BCS}} = 0.57$).

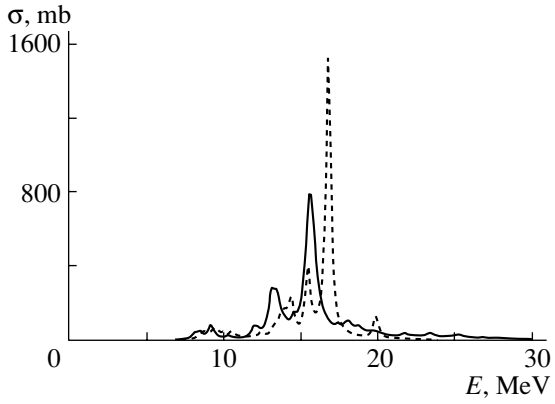

Fig. 2. Dipole-photoabsorption cross section for the ^{120}Sn nucleus at $T = 0$: (solid curve) results of the CQRPA calculation and (dashed curve) results of the calculations taking no account of the single-particle continuum.

In Figs. 2 and 3, the dipole-photoabsorption cross sections for the ^{120}Sn nucleus are given at temperatures of 0 and 2 MeV, respectively. The dashed curves represent the cross sections calculated without taking into account the single-particle continuum. In this way, we clearly illustrate the continuum contribution, which is significant both in a cold and in a hot nucleus—we see that the resonance strength is noticeably redistributed upon the inclusion of the continuum. By and large, the behavior of the cross

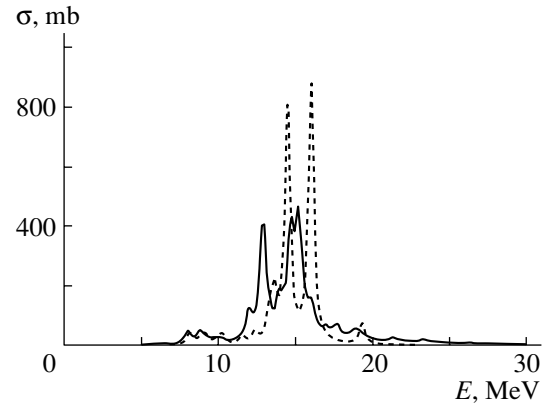

Fig. 3. Dipole-photoabsorption cross section for the ^{120}Sn nucleus at $T = 2$ MeV: (solid curve) results of the TCQRPA calculation and (dashed curve) results of the calculation taking no account of the single-particle continuum.

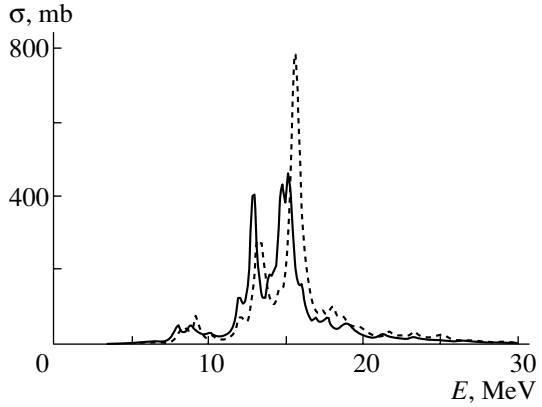

Fig. 4. Dipole-photoabsorption cross sections for the ^{120}Sn nucleus according to the calculations within (dashed curve) the CQRPA at $T = 0$ and (solid curve) the TCQRPA at $T = 2$ MeV .

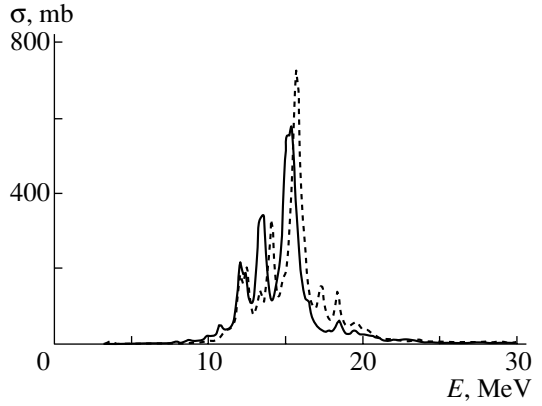

Fig. 5. $E1$ resonance in ^{104}Sn at (solid curve) $T = 2$ MeV and (dashed curve) at $T = 0$.

section at $T = 0$ reproduces the results obtained in [6, 7], some deviations being due to the fact that, in this study, we have calculated the matrix elements of the gap operator on the basis of the BCS model, taking into account the dependence of the gap on the single-particle quantum numbers, whereby we obtained a result that is more correct than the empirical value used in [7]. At $T = 0$, we obtained a 101% contribution to the EWSR value. As to the position of the resonance centroid or the averaged energy $\bar{E}$, whose experimental value is 15.4 MeV [16], its theoretical value depends noticeably on the definition of this quantity (see below) since, upon the inclusion of the continuum, the resonance develops a high-energy tail that makes different contributions for different definitions of $\bar{E}$. The calculation of the centroid position according to (13) yields a value of 14.4 MeV. We have also calculated $\bar{E}$ by the formula $\bar{E} = \sqrt{m_2/m_0}$ and obtained a value of 15.7 MeV, which is in fairly good agreement with experimental data.

For the sake of comparison, the dipole-photoabsorption cross section for ^{120}Sn is displayed in Fig. 4 (dashed curve) at zero temperature and (solid curve) at 2 MeV. As the nucleus is heated, the resonance sinks somewhat as a whole: the main peak is significantly suppressed, while additional peaks are enhanced.

Figure 5 demonstrates the behavior of the same cross sections as in Fig. 4, but for ^{104}Sn. It should be noted that our calculations for ^{104}Sn are rather of a methodological value since the single-particle levels of this nucleus were not fitted to their experimental counterparts in this study.

The temperature dependences of the EWSR and of the mean energy of the $E1$ resonance for the ^{120}Sn nucleus are shown in Figs. 6 and 7, respectively. Since the Cooper gap vanishes abruptly at $\mathrm{T} = T_c$, these quantities have a characteristic cusp. It was shown in [3], however, that, in calculations for deformed nuclei without allowing for the continuous spectrum, a somewhat overestimated value of the EWSR for $\mathrm{T} < T_c$ is explained by the elimination of the particle–particle channel from our considerations—upon the inclusion of this channel, the EWSR appears to be virtually independent of temperature over the entire range from 0 to 2 MeV. A similar temperature dependence of the quadrupole sum rule was observed in the calculations performed in [17] for ^{114}Sn without taking into account the continuous spectrum and in the approximation of separable forces. Thus, it is necessary to take into account the particle–particle channel prior to drawing physical conclusions on the temperature dependence.

According to our calculations, the averaged energy decreases with temperature (see Fig. 7), and this result complies with that of the self-consistent RPA calculations for ^{208}Pb in [18], but this effect proved to be stronger in our case.

It should be noted here that the value calculated by formula (13) (as in [7]) for the position of the $E1$-resonance centroid differs from its counterpart in [6], where $\bar{E} \equiv \bar{E}_{3;1} = (m_3/m_1)^{1/2}$. As can easily be seen, the definition of the centroid as $\bar{E}_{3;1}$ highlights the role of the single-particle continuum and of the high-energy tail, whereas $\bar{E}_{1;-1}$, on the contrary, underestimates somewhat the role of the continuum and exaggerates the contribution of the low-lying part of the resonance to the averaged energy. Moreover, the inclusion of the continuum in the consideration affects the quantities $\bar{E}_{3;1}$ and $\bar{E}_{1;-1}$ differently: $\bar{E}_{3;1}$ is enhanced by 2 MeV, while $\bar{E}_{1;-1}$ is slightly reduced (by 0.3 MeV), the latter being in better agreement with the shift of the resonance as a discrete unit

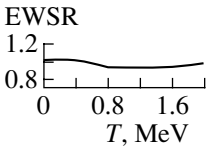

Fig. 6. Temperature dependence of the EWSR for the ^{120}Sn nucleus.

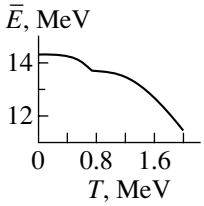

Fig. 7. Temperature dependence of the averaged energy of the $E1$ resonance for the ^{120}Sn nucleus.

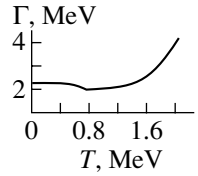

Fig. 8. Temperature dependence of the $E1$-resonance width for the ^{120}Sn nucleus.

toward lower energies, as is seen in the graphs of $\sigma(E)$.

It was previously mentioned in [7] that a significant distinction between the averaged energies $\bar{E}_{3;1}$ and $\bar{E}_{1;-1}$ (on average, around 3 MeV for the ^{104}Sn and ^{120}Sn nuclei) confirms that it is of paramount importance to take into account the single-particle continuous spectrum. Additionally, our calculations have shown that the effect of the continuum on the centroid position becomes noticeably greater with increasing temperature of a nucleus.

In Fig. 8, the temperature dependence of the $E1$-resonance width Γ is shown according to the calculations by formula (14) for the ^{120}Sn nucleus. As was discussed above, the particle–particle channel must be taken into account first of all at $T < T_c$. For $T > T_c$, the shape of the curve is in fairly good agreement with experimental data (see, for example, [19]). However, the width value calculated here proved to be approximately one-half as large as its experimental counterpart, since we have taken no account of either complex configurations or thermal fluctuations.

CONCLUSION

By considering the example of a non-charge-exchange $E1$ resonance, the method constructed as a temperature generalization of the CQRPA for the case where there is no dynamical correlation with particle–particle interaction has been implemented numerically for the first time. The results obtained by calculating the dipole-photoabsorption cross sections at finite temperatures for the nonmagic tin isotopes of ^{120}Sn and ^{104}Sn (a stable and an unstable one, respectively) have been presented. Variations in the giant dipole resonance and its integrated features in response to the heating of a nucleus have been demonstrated. The effect of taking into account the single-particle continuous spectrum on the integrated features of the resonance at finite temperatures has been studied. The results obtained here have also revealed that, upon simultaneously taking into account the continuum and temperature, particle–particle interaction and a correct choice of method for calculating mean energies appear to be factors that are more significant within this method for spherical nuclei than within earlier versions of calculations; hence, these factors require a more detailed consideration.

The fact that effects associated with the excitation of configurations that are more complicated than those included in the QRPA have been disregarded here prevents us from taking our results for the resonance width too seriously. At the same time, the numerical realization of the method solves a number of rather important problems even at the present stage: our calculations have clearly demonstrated the importance of taking into account the single-particle continuum, which is significant for describing the envelope of the resonance, and have also made it possible to establish the behavior of the $E1$ resonance and its integrated features versus the temperature of a nonmagic nucleus. The approach developed here is appropriate for calculating giant resonances of arbitrary multipole order in any medium-mass and heavy nuclei. The universality of the interaction parameters and the inclusion of the single-particle continuous spectrum make it possible to perform calculations for nuclei whose binding energy is relatively close to zero, which is of great topical interest now. The method presented here is open to refinements and generalizations—in particular, it admits the inclusion of complex configurations in the consideration. An attempt at this type of refinement will be the next step of our investigations.

ACKNOWLEDGMENTS

We are grateful to I.N. Borzov for stimulating discussions.

REFERENCES

1. P. E. Bortignon, R. A. Broglia, *et al.*, Nucl. Phys. A **460**, 149 (1986).
2. J. Bar-Touv, Phys. Rev. C **32**, 1369 (1985).
3. S. Kamerdzhiev and D. Zawischa, Phys. Lett. B **275**, 1 (1992); in *Proceedings of the 4th International Seminar on Nuclear Structure "The Building Blocks of Nuclear Structure," Amalfi, Italy, 18–22 May 1992,* Ed. by A. Covello (World Sci., Singapore, 1992), p. 499.
4. K. A. Snover, Nucl. Phys. A **687**, 337c (2001); P. Heckman, D. Bazin, J. R. Beene, *et al.*, Nucl. Phys. A **687**, 225c (2001).
5. M. V. Zverev and E. E. Saperstein, Yad. Fiz. **57**, 2196 (1994) [Phys. At. Nucl. **57**, 2113 (1994)].
6. V. I. Tselyaev, S. P. Kamerdzhiev, R. Liotta, and E. V. Litvinova, Izv. Akad. Nauk, Ser. Fiz. **62**, 1081 (1998).
7. S. Kamerdzhiev, R. Liotta, E. Litvinova, and V. Tselyaev, Phys. Rev. C **58**, 172 (1998).
8. I. N. Borzov, E. L. Trykov, and S. A. Fayans, Yad. Fiz. **52**, 985 (1990) [Sov. J. Nucl. Phys. **52**, 627 (1990)]; I. N. Borzov and E. L. Trykov, Yad. Fiz. **52**, 52 (1990) [Sov. J. Nucl. Phys. **52**, 33 (1990)].
9. A. P. Platonov and É. E. Sapershteĭn, Yad. Fiz. **46**, 437 (1987) [Sov. J. Nucl. Phys. **46**, 437 (1987)]; A. P. Platonov and E. E. Saperstein, Nucl. Phys. A **486**, 118 (1988).
10. A. B. Migdal, *Theory of Finite Fermi Systems and Applications to Atomic Nuclei* (Nauka, Moscow, 1983).
11. G. G. Bunatyan, Yad. Fiz. **26**, 979 (1977) [Sov. J. Nucl. Phys. **26**, 518 (1977)]; **29**, 10 (1979) [**29**, 4 (1979)].
12. A. A. Abrikosov, A. P. Gor'kov, and I. E. Dzyaloshinskiĭ, *Methods of Quantum Field Theory in Statistical Physics* (Fizmatgiz, Moscow, 1962; Prentice-Hall, Englewood Cliffs, 1963).
13. S. Shlomo and G. Bertsch, Nucl. Phys. A **243**, 507 (1975); E. E. Saperstein, S. A. Fayans, and V. A. Khodel, Preprint No. 2580 IAE (Institute of Atomic Energy, Moscow 1976).
14. A. H. Wapstra and K. Bos, At. Data Nucl. Data Tables **19**, 177 (1977); Nucl. Data Sheets **67**, 2 (1992); **64**, 2 (1991).
15. V. I. Tselyaev, Izv. Akad. Nauk, Ser. Fiz. **64**, 541 (2000).
16. S. S. Dietrich and B. L. Berman, At. Data Nucl. Data Tables **38**, 199 (1988).
17. G. G. Dussel, H. Fortunato, and H. M. Sofia, Phys. Rev. C **42**, 2093 (1990).
18. J. Meyer, P. Quentin, and M. Brack, Phys. Lett. B **133B**, 279 (1983).
19. Y. Alhassid, Nucl. Phys. A **649**, 107c (1999).

Translated by A. Isaakyan

Physics of Atomic Nuclei, Vol. 66, No. 3, 2003, pp. 565–574. Translated from Yadernaya Fizika, Vol. 66, No. 3, 2003, pp. 591–600.

ELEMENTARY PARTICLES AND FIELDS
Experiment

Total Cross Section for Photon–Nucleon Interaction in the Energy Range $\sqrt{s} = 40$–250 GeV

G. M. Vereshkov[1),2)], O. D. Lalakulich[3),2)], Yu. F. Novoseltsev[3)*], and R. V. Novoseltseva[3)]

Received November 28, 2001; in final form, April 1, 2002

Abstract—Results obtained by directly measuring the total cross section for photon–nucleon interaction through recording photoproduction processes at the Baksan underground scintillation telescope of the Institute for Nuclear Research (Russian Academy of Sciences, Moscow) are presented. The effect of a faster growth of photon–hadron cross sections in relation to hadron–hadron cross sections is confirmed in the energy range $\sqrt{s} = 40$–130 GeV. It is shown that an increase in the number of additive quarks in photon-hadronization products may be one of the reasons behind this effect. Experimental data on the cross sections for photon–nucleon and photon–photon interactions are subjected to a comparative analysis, and the status of the results obtained from direct and indirect cross-section measurements in the high-energy region is discussed. © *2003 MAIK "Nauka/Interperiodica".*

1. INTRODUCTION: CALIBRATION CURVE AND STATUS OF EXPERIMENTAL DATA

In the energy region $\sqrt{s} < 18.6$ GeV, the total cross sections for photon–proton interactions, $\sigma_{\gamma p}(s)$, were measured more than 20 years ago in accelerator experiments. Results obtained in the range $\sqrt{s} = 100$–250 GeV have been widely discussed in recent years. Over the entire energy region indicated above, $\sigma_{\gamma p}(s)$ values were determined indirectly—on the basis of DESY data on proton structure functions in deep-inelastic electron–proton scattering [1] via an extrapolation of those data to the mass shell of a real photon [2]. At some points of the energy scale around $\sqrt{s} = 200$ GeV, the cross sections in question were measured directly—by recording photoproduction processes [3, 4]. By and large, the experimental situation is not free from uncertainties, but the results suggest a faster growth of $\sigma_{\gamma p}(s)$ with increasing $\sqrt{s}$ in relation to the cross sections for hadron–hadron interactions. Missing data needed to clarify the experimental situation include those on $\sigma_{\gamma p}(s)$ in the energy range $\sqrt{s} = 30$–100 GeV not covered by currently operating accelerators.

In this article, we present results that were obtained by directly measuring $\sigma_{\gamma p}(s)$ in the range $\sqrt{s} = 40$–130 GeV at the Baksan underground scintillation telescope installed at the Baksan neutrino observatory of the Institute for Nuclear Research (Russian Academy of Sciences, Moscow). A preliminary treatment of data from this telescope was reported in [5]. Our data are also indicative of the effect of a faster growth of photon–hadron cross sections.

Information contained in $\sigma_{\gamma p}(s)$ about the hadronic structure of the photon is discussed on the basis of various models (see, for example, [6–8]). The vector-meson-dominance model (VMDM) is invoked first of all. According to this model, we have

$$\sigma_{\gamma p}(s) = \sum_V P_{\gamma\to V}(s)\sigma_{Vp}(s), \qquad (1)$$

where $P_{\gamma\to V}(s)$ is the probability of photon transition into a vector meson V and $\sigma_{Vp}(s)$ is the total cross section for V-meson interaction with a proton. In [9], it is shown that, within this model, one can take into account highly excited vector resonances lying on the ρ, ω, and ϕ trajectories; the charmonium and bottomonium families; and additional two-pion contributions that are generated by the instability of vector mesons. The use of the additive quark model [10] and of the $U(3)$ symmetry of baryon–meson interactions yields

$$\sigma_{Vp}(s) = \frac{2}{3}\bar{\sigma}_{Np}(3s/2), \quad V = \rho, \omega, \phi, \qquad (2)$$

which makes it possible to isolate in (1) the contributions of ρ, ω, and ϕ mesons; that is,

$$\sigma^{(0)}_{\gamma p}(s) = P_{\gamma\to\rho\omega\phi}(s)\frac{2}{3}\bar{\sigma}_{Np}(3s/2), \qquad (3)$$

[1)]Institute for Nuclear Research, Russian Academy of Sciences, pr. Shestidesyatiletiya Oktyabrya 7a, Moscow, 117312 Russia.
[2)]Institute of Physics, Rostov State University, pr. Stachki 194, Rostov-on-Don, 344090 Russia.
[3)]Institute for Nuclear Research, Russian Academy of Sciences, pr. Shestidesyaletiya Oktyabrya 7a, Moscow, 117312 Russia.
[*]e-mail: YuNovoselt@yandex.ru

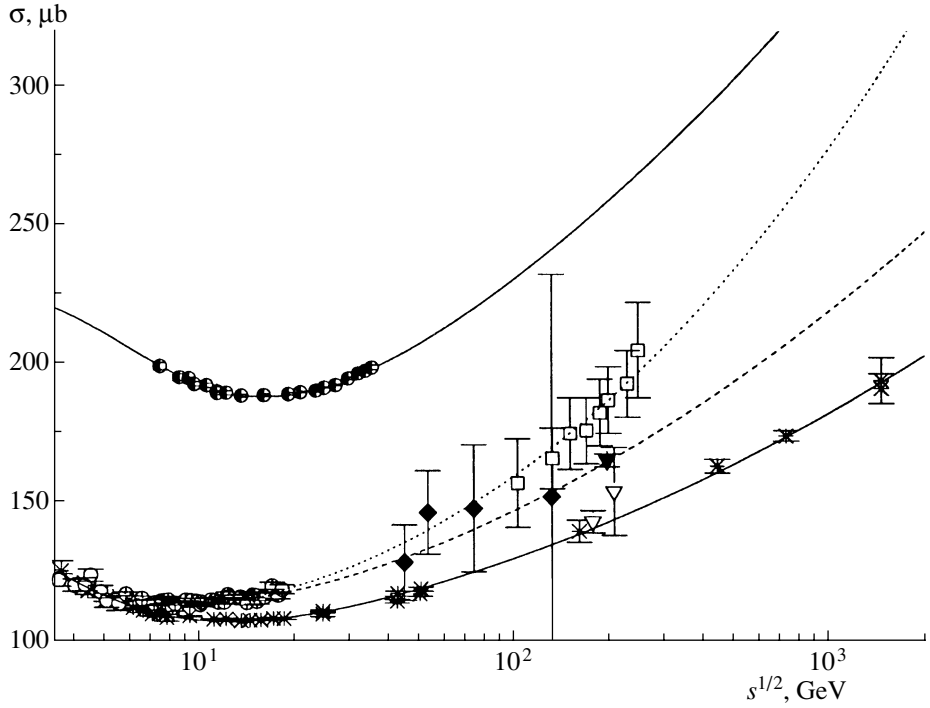

Fig. 1. Calibration curves (solid curves) and cross section for photon–proton interaction. The lower calibration curve (5) was plotted according to data of the experiments reported in [11–18] and devoted to nucleon–proton interactions (asterisks), while the upper calibration curve (13) is based on the data from [11, 12] on pion–proton interaction (half-closed circles). The displayed experimental data are represented by points: (open boxes) extrapolation [2] of the ZEUS BPC data [1], (open circles) low-energy photoproduction data from [19], (closed diamonds) photoproduction data from the Baksan underground scintillation telescope (our study), (open inverted triangles) ZEUS photoproduction data of 1992 and 1994 [3], and (closed inverted triangle) H1 photoproduction data of 1995 [4]. The dotted curve is a fit on the basis of Eqs. (14), (16), and (18) that employs indirect ZEUS data from [1], while the dashed curve is a fit on the basis of Eqs. (14), (16), and (17) to H1 data of 1995.

where

$$P_{\gamma\to\rho\omega\phi}(s) = \sum_{V=\rho,\omega,\phi} P_{\gamma\to V}(s), \qquad (4)$$

$$\bar{\sigma}_{Np} = \frac{1}{4}(\sigma_{pp} + \sigma_{\bar{p}p} + \sigma_{np} + \sigma_{\bar{n}p}).$$

The dominant (from the point of view of the additive quark model) quark content of the photon is approximately taken into account in the averaged nucleon–proton cross section $\bar{\sigma}_{Np}$. A multiplicative transformation of the argument on the right-hand side of Eq. (2) ($3s/2$ instead of s) is caused by the fact that the energies per pair of interacting quarks are different in the Vp and the Np system, $s/6$ in the first and $s/9$ in the second case. The photon-hadronization probability of $P_{\gamma\to\rho\omega\phi} \approx P^{(0)}_{\gamma\to\rho\omega\phi} = 1/250$ is known from experimental data on $\gamma \to V$ transitions on the mass shells of vector mesons. The use of this value makes it possible to express the ρ, ω, and ϕ contributions—that is, the function $\sigma^{(0)}_{\gamma p}(s)$—in terms of experimental data on the cross sections for nucleon–proton interactions exclusively. Since experimental data specifying the function $\sigma^{(0)}_{\gamma p}(s)$ are independent and since physical ideas associated with this function are absolutely clear, it will be referred to as the calibration curve for the cross sections describing photon–proton interactions. Obviously, a deviation of the measured values of $\sigma_{\gamma p}(s)$ from the calibration curve carries additional information about photon hadronization—that is, information that is disregarded in $\sigma^{(0)}_{\gamma p}(s)$.

In order to plot the calibration curve in the energy range $\sqrt{s} = 5.93$–22.97 GeV, we used the results [11, 12] of measurements of all four nucleon–proton cross sections. In the range $\sqrt{s} = 30.4$–62.7 GeV, we relied on the data from [13, 14] on the cross sections $\sigma_{pp}(s)$ and $\sigma_{\bar{p}p}(s)$ (one can assume that the relations $\sigma_{pp} = \sigma_{np}$ and $\sigma_{\bar{p}p} = \sigma_{\bar{p}n}$ hold to a high precision in this energy range). Finally, we took data on $\sigma_{\bar{p}p}$ from [15–18] at the energies of $\sqrt{s} = 200$, 546, 900, and 1800 GeV, at which the distinctions between the different nucleon–nucleon cross sections can be disregarded. On the basis of these experimental data, subjected to the scale transformation $3s_{Np}/2 = s_{\gamma p} \equiv s$, the calibration curve was fitted in terms of

the expression

$$\sigma_{\gamma p}^{(0)} = C\ln^2\frac{s}{s_0} + A\left(1+\frac{\Lambda_{01}^2}{s+\Lambda_{02}^2}\right), \qquad (5)$$
$$C = 0.5777\ \mu\text{b}, \quad \sqrt{s_0} = 2.198\ \text{GeV},$$
$$A = 95.65\ \mu\text{b}, \quad \Lambda_{01} = 2.774\ \text{GeV},$$
$$\Lambda_{02} = 3.589\ \text{GeV}.$$

Figure 1 displays points used to plot the calibration curve; experimental data on $\sigma_{\gamma p}(s)$, including data from the Baksan underground scintillation telescope; and a fit to experimental results for two versions of the set of high-energy points. The upper solid curve represents the cross section $\sigma_{\gamma p}(s)$ for the case where only a strongly bound $\pi^+\pi^-$ system results from photon hadronization. A physical motivation behind the introduction of this curve is discussed in Section 3. We note that the points according to which the lower (upper) calibration curve (5) [(13)—see below] is plotted were obtained by applying a scale transformation to experimental data on the cross sections for nucleon–nucleon interaction [pion–nucleon interaction for (13)] with allowance for the requirements of the additive quark model and the vector-meson-dominance model.

The experimental nucleon–proton cross sections [11, 12] used to plot the low-energy segment of the calibration curve have a statistical uncertainty not greater than 1 μb. Experimental data from [19] on $\sigma_{\gamma p}(s)$ have a similar uncertainty. Low-energy accelerator data are quite reliable. In view of this, the fact that, at low energies, the cross sections for photon–proton interactions asymptotically approach the calibration curve is noteworthy. In all probability, this means that the argument used to plot the calibration curve reflects adequately the physics of photon–proton interactions in the region of extremely low energies. Significant deviations from the calibration curve are observed for $\sqrt{s} > 8$ GeV; in the region of precisely measured nucleon–proton and photon–proton cross sections, they are as large as 10% at $\sqrt{s} = 18.6$ GeV. From Fig. 1, it can be seen that, at higher energies, there is a trend toward an increase in the deviation of the experimental values of $\sigma_{\gamma p}(s)$ from the calibration curve. At $\sqrt{s} = 200$ GeV, the deviation of the cross section as obtained by recording photoproduction events becomes as great as 25%. The deviations of $\sigma_{\gamma p}(s)$ values derived via an extrapolation [2] of ZEUS data are still greater [1]. It should be noted, however, that the extrapolation method is plagued by systematic errors associated, for example, with the arbitrariness in the approximation of the structure function $F_2(x, Q^2)$ for $Q^2 \to 0$. It is conceivable that, as soon as the accuracy of direct measurements becomes higher, the latter values will acquire the status of a reference in discriminating between different approximations. For this reason, data from the Baksan underground scintillation telescope must be compared, first of all, with data of other direct measurements. A fit to data of direct measurements is shown by the dashed curve in Fig. 1. A fit to an alternative set of data, which contains, for high-energy points, results of an extrapolation of structure functions, is depicted by the dotted curve in Fig. 1 (for details, see Section 3).

The ensuing exposition is organized as follows. The procedure for measuring the cross sections for photon–nucleon interaction with the Baksan underground scintillation telescope is described in Section 2. Physical factors that are responsible for a faster growth of photon–hadron cross sections in relation to hadron–hadron cross sections are discussed in Section 3. A physical motivation for choosing curves used to fit experimental data is also given there. A criterion for discriminating between different versions of the high-energy behavior of $\sigma_{\gamma p}(s)$ is proposed in Section 4 on the basis of a comparison of experimental data on the cross sections for photon–proton and photon–photon interactions.

2. MEASUREMENT OF THE CROSS SECTIONS FOR PHOTON–PROTON INTERACTIONS AT THE BAKSAN UNDERGROUND SCINTILLATION TELESCOPE: PROCEDURE AND RESULTS

2.1. Measured Quantities

At the Baksan underground scintillation telescope, an experiment measuring the cross sections $d\sigma_{\mu A}^{(h)}(E_\mu, E_c, q^2)/dE_c$ for the inelastic scattering of cosmic-ray muons on the nuclei of atoms of a telescope material with a mean number of intranuclear nucleons that is equal to $\bar{A} = 26$ was performed from 1983 to 1989 over the energy region $E_c > 700$ GeV (here, $E_c = E_\mu - E'_\mu$ is defined as the energy transfer from a muon to the nuclear cascade, with E_μ and E'_μ being the muon energies in the laboratory frame prior to and after the interaction event). The description of the Baksan underground scintillation telescope and of its potential as a measuring instrument was given in [20].

In such experiments, the mean square of the 4-momentum transfer, $-\overline{q^2} = \overline{Q^2} < 1\ \text{GeV}^2$, is much less than the characteristic value of the energy squared in the photon–nucleon c.m. frame, $s_{\gamma N} > (40\ \text{GeV})^2$. This makes it possible to address the problem of experimentally determining the cross section for real-photon interaction with a nucleon, $\sigma_{\gamma N}(s)$. In processing experimental data on nuclear

(hadronic) cascades, one can factor out and integrate the Q^2 dependence in the expression for the cross section describing the formation of such cascades and express this cross section directly in terms of $\sigma_{\gamma N}(E_c)$ [21]. As a result, one obtains

$$\frac{d\sigma_{\mu A}^{(h)}(E_\mu, E_c)}{dE_c} = \frac{\alpha}{2\pi}\frac{AE_c}{E_\mu^2}\sigma_{\gamma N}(E_c)F(E_\mu, E_c, A), \tag{6}$$

where $F(E_\mu, E_c, A)$ is a function that takes into account the shadowing of nucleons in a nucleus; the explicit form of this function is presented in [21].

In the experiment described in [5, 22, 23], four horizontal scintillation planes of the Baksan underground scintillation telescope, together with connecting pieces between them, formed a calorimeter used to record electromagnetic and nuclear cascades generated by cosmic-ray muons in rock above the facility ($\bar{A} = 25$) or in the facility itself ($\bar{A} = 27$). The experiment measured the differential spectra of energy depositions in the facility from electromagnetic ($j = e$) and nuclear ($j = h$) cascades; that is,

$$\frac{dN_j(\epsilon)}{d\epsilon} = \int \frac{\partial N_\mu(E_\mu;\theta,\phi)}{\partial E_\mu}\frac{d\sigma_{\mu A}^{(j)}(E_\mu, E_c)}{dE_c}n \tag{7}$$
$$\times\, W(E_c, \epsilon;\theta,\phi)S(\theta,\phi)dE_\mu dE_c \sin\theta d\theta d\phi,$$

where ϵ is the sum of the energy depositions in the four horizontal scintillation layers of the Baksan underground scintillation telescope, $\partial N_\mu(E_\mu;\theta,\phi)/\partial E_\mu$ is the differential spectrum of muons in a given direction at the facility location, $d\sigma_{\mu A}^{(j)}(E_\mu, E_c)/dE_c$ is the differential cross section for the process in which a muon of energy E_μ produces an electromagnetic or a nuclear cascade shower of energy E_c, n is the number of nuclei in a unit volume of the detector (or rock), $W(E_c, \epsilon;\theta,\phi)$ is the probability that a shower of energy E_c deposits an energy ϵ in the facility, and $S(\theta,\phi)$ is the area of the facility in the direction specified by the angles θ and ϕ.

The integrated energy spectrum of muons for the zenith-angle region $\theta < 25^\circ$ was obtained in the same experiment [23]; to within 5%, it can be approximated by the expression

$$N_\mu(>E;\theta,\phi) = k(E + E_H)^{-2.83}, \tag{8}$$

where $E_H = 230$ GeV and $k = \text{const}$. For $\theta > 25^\circ$, use was made of the muon spectrum computed in [24, 25].

In calculating the probability $W(E_c, \epsilon;\theta,\phi)$, we employed the electromagnetic and the nuclear cascade curve obtained by the Monte Carlo method with allowance for the actual structure of the facility. The function $W(E_c, \epsilon;\theta,\phi)$ takes into account the geometry of the experiment and the spatial features of the cascade curves.

Needless to say, the measured and the calculated muon spectrum are determined with nonnegligible uncertainties. As will be shown below, however, the method used to process experimental data is such that the systematic uncertainties in the muon spectrum, the facility area $S(\theta,\phi)$, and the energy-deposition probability $W(E_c, \epsilon;\theta,\phi)$ have virtually no effect on the final result.

In the cross section $d\sigma_{\mu A}^{(e)}(E_\mu, E_c)/dE_c$ in (7) for the production of an electromagnetic cascade, we took into account cascade showers generated in the following processes: (i) photon bremsstrahlung, (ii) the production of electron–positron pairs, and (iii) the formation of energetic delta electrons. For these processes, we used expressions for the cross sections from [26, 27].

It should be noted that, for an individual event, we did not attempt to reconstruct the shower energy on the basis of the energy deposition ϵ. The error in determining E_c by this method is as great as 30–60%. However, the mean energies of electromagnetic and nuclear cascades generating, in the facility, an energy deposition in a given interval $\epsilon_i \le \epsilon < \epsilon_{i+1}$ can be determined to a rather high precision (2 to 3%).

The amplitude channels of the Baksan underground scintillation telescope make it possible to measure the energy deposition in each individual detector (the dimensions of a detector are $70 \times 70 \times 30$ cm^3). In this experiment, one can therefore obtain not only the energy feature of a cascade but also the spatial pattern of an event—that is, the axis direction, the cascade-development length, and the lateral distribution of shower particles with respect to the axis. Such possibilities offered by the Baksan underground scintillation telescope permit distinguishing cascades generated on different muon trajectories (in cases where a cascade is accompanied by a muon group), as well as two successive cascades on the same trajectory, whereby one eliminates errors in determining ϵ that are associated with these factors.

The problem of distortions in the energy spectrum of showers (energy depositions) in the calorimeter because of secondary muon interactions was studied in [28] quite comprehensively for the case of an iron calorimeter. An overestimation of the energy deposition from the main shower can be characterized by the quantity $\overline{\epsilon/\eta}$, where η is the energy deposition from the main shower and ϵ is the total energy deposition in the calorimeter ($\epsilon = \eta +$ secondary showers). At $y = E_c/E_\mu = 0.1$, this overestimation is $\overline{\epsilon/\eta} \simeq 1.02$, but it decreases as y grows above this value. In

cosmic-ray-muon experiments, we have $\bar{y} \sim 0.5$, in which case $\overline{\epsilon/\eta} \simeq 1.01$.

There is also the possibility of studying a soft photon in inelastic interactions. This effect was considered in [28], where it was shown that the correction to the shower energy due to soft-photon emission is about 2 to 3%.

For the material of the Baksan underground scintillation telescope, the mean nuclear charge is $\bar{Z} \simeq 13$; therefore, the effect of the aforementioned processes on the measurement of the energy deposition from the main shower is still weaker.

2.2. Separation of Cascades

In order to separate nuclear and electromagnetic cascades, use was made of the number of decays $\pi \to \mu \to e$ recorded in a given event [5, 22]. The separation procedure relied on the results obtained by simulating electromagnetic cascades and consisted in the following:

(i) The probability $P(m, \epsilon)$ of recording m decays in an electromagnetic cascade that causes an energy deposition ϵ in the facility was calculated [22].

(ii) A separation criterion $m_o(\epsilon)$ was defined in such way that the probability χ of recording the number $m > m_o(\epsilon)$ of decays in an electromagnetic cascade was not greater than 10^{-2}; that is,

$$\sum_{m=0}^{m_o} P(m;\epsilon) = 1 - \chi(m_o, \epsilon) \geq 0.99. \qquad (9)$$

(iii) Cascades where $m \leq m_o(\epsilon)$ were taken to be electromagnetic.

(iv) The calculated number of electromagnetic cascades where $m > m_o(\epsilon)$ was subtracted from the number of cascades where $m > m_o(\epsilon)$ [that is, the occurrence of the tails of the distributions $P(m, \epsilon)$ in the region $m > m_o(\epsilon)$ was taken into account]. On the basis of (9), one can write

$$N(m \leq m_o(\epsilon)) = N_e(\epsilon) - N_e(\epsilon)\chi(m_o, \epsilon),$$

where $N_e(\epsilon)$ is the true number of electromagnetic cascades. Therefore, the total number of electromagnetic cascades in the interval $\Delta\epsilon$ is

$$N_e(\Delta\epsilon) = \frac{N(m \leq m_o(\Delta\epsilon))}{1 - \chi(m_o, \Delta\epsilon)}.$$

The remaining cascades were taken to be nuclear.

(v) We disregarded the occurrence of nuclear cascades in the region of electromagnetic cascades. The calculations revealed that the fraction of nuclear cascades where $m \leq m_o(\epsilon)$ did not exceed 3%, which is much less than the statistical uncertainty in the number of nuclear cascades.

Thus, the efficiency of separating electromagnetic from nuclear cascades is not less than 99%, the efficiency of separating nuclear from electromagnetic cascades being about 97%.

2.3. Results of the Measurements

Experimental data on the numbers of electromagnetic and nuclear cascades [$N_e(\Delta\epsilon)$ and $N_h(\Delta\epsilon)$, respectively] recorded in various intervals $\Delta\epsilon = \epsilon_{\min} - \epsilon_{\max}$ of the energy deposition in the facility are quoted in the table. The last interval $\Delta\epsilon$ is not bounded from above: $\epsilon > 573$ GeV. A nonmonotonic character of the spectra is due to a shorter detection time at small ϵ ($T_{\det} = 31\,650$ h). The quantity $\bar{E}_\gamma \equiv \bar{E}_c^{(h)}$ is the mean energy of nuclear cascades depositing energy in the range $\epsilon_{\min} \leq \epsilon < \epsilon_{\max}$ (the photon energy is identified with the nuclear-cascade energy), while $E_{\gamma(\min)}$ and $E_{\gamma(\max)}$ are, respectively, the left- and the right-hand boundary of the range of cascade energies $E_c^{(h)}$ for given values of $\Delta\epsilon$. In the last two columns of the table, we present relevant energies in the photon–nucleon c.m. frame and the corresponding total cross sections for photon–nucleon interactions.

Information about $\sigma_{\gamma p}(s)$ was extracted from the ratio of the numbers of nuclear and electromagnetic cascades,

$$R(\Delta\epsilon) = \frac{N_h(\Delta\epsilon)}{N_e(\Delta\epsilon)}, \qquad (10)$$

under the assumption that the cross sections for electromagnetic processes are known.

The use of the ratio $R(\Delta\epsilon)$ has an important advantage over the procedure where $\sigma_{\gamma N}$ is determined directly from data on nuclear cascades. The results obtained for $\sigma_{\gamma p}(s)$ from (10) feature virtually no dependence either on the possible uncertainties in determining the acceptance of the facility or on the energy spectrum of muons in (7) (especially on the latter). In order to illustrate this statement, we consider the approximate expression obtained for $R(\Delta\epsilon_i)$ by applying the theorem of mean:

$$R(\Delta\epsilon) = \sigma_{\gamma N}(\bar{E}_\gamma) \qquad (11)$$
$$\times \frac{\dfrac{\alpha}{2\pi} A \bar{E}_\gamma (E_{\gamma(\max)} - E_{\gamma(\min)}) \int \dfrac{\partial N_\mu}{\partial E_\mu} FWS \dfrac{dE_\mu}{E_\mu^2} d\Omega}{\displaystyle\int \frac{\partial N_\mu}{\partial E_\mu} \frac{\partial \sigma_{\mu A}^{(e)}(E_\mu, E_c)}{dE_c} WS dE_\mu dE_c d\Omega}.$$

With the exception of the theoretically known cross sections $\partial\sigma_{\mu A}^{(e)}(E_\mu, E_c)/dE_c$ for electromagnetic processes and the sought cross section $\sigma_{\gamma N}(\bar{E}_\gamma)$, all of the quantities that appear in (11) were either measured experimentally or simulated precisely for our

Data on cascades and on the cross sections for photon–nucleon interactions

$\epsilon_{\min}$	$\epsilon_{\max}$	$N_e(\Delta\epsilon)$	$N_h(\Delta\epsilon)$	$E_{\gamma(\min)}$	$E_{\gamma(\max)}$	$\bar{E}_\gamma$	$\sqrt{s}$	$\sigma_{\gamma N}$
77	133	1050	96	744	1260	1100	45.4	128 ± 14
133	230	1006	102	1260	2100	1550	53.9	146 ± 15
230	573	445	45	2100	4980	3030	75.4	148 ± 23
573		36	4	4980		9500	133.5	152 ± 80

Note: All of the energies are given in GeV, while the cross section is given in microbarns.

experimental facility. It can easily be seen, however, that $\partial N_\mu/\partial E_\mu$, $W(E_c, \epsilon; \theta, \phi)$, and $S(\theta, \phi)$, whose values are known within some errors, appear in the expression for $\sigma_{\gamma N}$ only in the form of the ratio of integrals.

Final results for $\sigma_{\gamma N}(E_\gamma)$ were obtained by integrating the cross section for photon–nucleon interaction over the interval $\Delta E_\gamma = f(\Delta\epsilon)$ with allowance for its dependence on energy within this interval. For this purpose, we employed the dependence $\sigma_{\gamma N}(E_\gamma)$ predicted in [21], which consistently refines a fit to experimental data that was used to find the calculated value $R_{\text{calc}}(\Delta\epsilon_i)$. The deviation of the actually measured cross sections from a fit to them was determined on the basis of the deviation of the experimental value $R_{\text{expt}}(\Delta\epsilon_i)$ from its calculated counterpart.

3. ON THE POSSIBLE PHYSICAL REASONS BEHIND THE GROWTH OF THE CROSS SECTIONS FOR PHOTON–PROTON INTERACTIONS

It is well known that the hadronization of a photon is a dynamical process that involves the nonperturbative QCD vacuum [29]. Since a consistent quantitative theory of this process has yet to be developed, various models, which are phenomenological to some extent varying from one model to another, are used for it. A simplified qualitative pattern is the following. In the region of a photon–proton collision, the participant photon interacts with the quark component of the vacuum quark–gluon condensate, which is slightly deformed in the vicinity of the proton involved. This interaction is basically inelastic—the photon energy is expended in creating a quark bag in the quark–gluon condensate[3)] and a vacuum (Pomeron) channel connecting the bag to the proton. Of course, the analogous process proceeds on the side of the proton. Quark bags are identified with the regions of photon and proton fragmentation (diffractive dissociation), while the Pomeron channel is identified with the central-interaction region.

The above pattern highlights two problems that arise in reducing photon–hadron to hadron–hadron interactions. The first is that of the initial hadron state. In hadron–hadron interactions, the initial hadron state is fixed on the mass shells of hadrons featuring a specific quark content and a gluon core, while, in photon–proton interactions, the initial state is formed by the proton of known quark–gluon structure and the quark bag that was created by the photon, but whose structure is not known and is moreover of a statistical character. A recourse to the vector-meson-dominance model is an attempt at fixing the initial hadron state, whereby the calibration curve $\sigma_{\gamma p}^{(0)}(s)$ is obtained if use is additionally made of the additive quark model. As can be seen from Fig. 1, this idea reflects adequately the actual physical situation only in the region of extremely low energies.

The uncertainty in the initial hadron state brings about the question of whether the ideas of photon–hadron quasiscaling, which make it possible to reduce $\sigma_{\gamma p}(s)$ first to $\sigma_{Vp}(s)$ and then to $\bar{\sigma}_{Np}(s)$, are reasonable. One can attempt to describe the deviations of $\sigma_{\gamma p}(s)$ from the calibration curve by assuming a strong violation of quasiscaling. Processes producing minijets of transverse momenta in the range $p_t = 1.5$–2 GeV owing to a specific gluonic content of photon-hadronization products are considered in [7, 8] as a factor that may be responsible for the violation of quasiscaling. If the gluonic core of the object generated by the photon involved differs from the known gluonic core of the proton, the contributions caused by this distinction do not appear in (1).

One more facet of the first problem is formulated in terms of the additive quark model: What is the number of additive quarks that is needed to parametrize the quark bag generated by the photon? This question naturally arises if one considers that vector resonances are quite broad. By way of example, we indicate that, in the case of photon transition into a rho meson, two alternative situations are possible: either

[3)] A quark bag is a bounded spatial region that arises in the quark–gluon condensate owing to the stabilizing effect of valence quarks and quark–antiquark pairs and which involves a rearranged dion structure.

the rho meson is taken to be the initial hadronic state, interacting, in this status, with the proton involved, or the strongly bound two-pion system originating from rho-meson decay is treated as the initial state. But a bag that is formed by four additive quarks is precisely one of the possible representations of a strongly bound two-pion system. In photon transitions into highly excited vector resonances, whose stability is very low, the number of additive quarks in photon-hadronization products may be still greater. One even cannot rule out the case where, in general, the mean number of additive quark–antiquark pairs has to be treated as a function of the energy of photon–proton interaction.

The second problem is associated with the energy dependence of the photon-hadronization probability $P_{\gamma\to V}(s)$. Even within the simplest version of the vector-meson-dominance model, we have to recognize that the quantity $P_{\gamma\to V}$ is known only on the mass shells of the rho, omega, and phi mesons. The photon-hadronization probability may increase owing, for example, to off-diagonal transitions of the $\gamma\to V^*\to V$ type, where V^* is a highly excited resonance and $V=\rho,\omega,\phi,\ldots$. According to [9], such transitions, predicted by the generalized vector-meson-dominance model, may lead to an increase of 10 to 20% in the hadronization probability for $\sqrt{s}>10$ GeV.

Within the phenomenological model that somewhat generalizes the simplest version of the modified vector-meson-dominance model, one can try to take into account some of the aforementioned effects, invoking specific mathematical structures to describe them and fixing numerical values of the parameters involved by fitting experimental data. In our opinion (see also [9]), the process in which the formation of a two-pion system through the transition $\gamma\to V\to 2\pi$ is followed by the interaction of this system with the proton is one of the most important effects here. In order to estimate this effect, we assume that the strongly bound two-pion system is described by a model of four additive quarks. Within this model, the cross section for $2\pi p$ interaction in the additive-quark model with allowance for a multiplicative transformation of the argument is estimated according to the formula

$$\sigma_{2\pi p}(s)=2\bar\sigma_{\bar\pi p}(s/2),\qquad \bar\sigma_{\bar\pi p}=\frac{1}{2}(\sigma_{\pi^+p}+\sigma_{\pi^-p}).$$

We further introduce the probability $P_{V\to 2\pi}(s)$ that the vector meson V is converted into a 2π system prior to undergoing interaction with the proton. The cross section for photon–proton interaction can then be represented in the form

$$\sigma_{\gamma p}(s)=\sum_V P_{\gamma\to V}(s)\,(1-P_{V\to 2\pi}(s))\,\sigma_{Vp}(s) \quad (12)$$
$$+\sum_V P_{\gamma\to V}(s)P_{V\to 2\pi}(s)\sigma_{2\pi p}(s)$$
$$=\frac{2}{3}\sum_V P_{\gamma\to V}(s)\,(1-P_{V\to 2\pi}(s))\,\bar\sigma_{\bar N p}(3s/2)$$
$$+2\sum_V P_{\gamma\to V}(s)P_{V\to 2\pi}(s)\bar\sigma_{\bar\pi p}(s/2).$$

By formally setting $\sum_V P_{\gamma\to V}=P^{(0)}_{\gamma\to V}=1/250$ and $P_{V\to 2\pi}=1$ in (12), we obtain the so-called conditional calibration curve

$$\sigma^{(1)}_{\gamma p}(s)=2P^{(0)}_{\gamma\to V}\bar\sigma_{\bar\pi p}(s/2).$$

In order to plot it, we have employed the measured data from [11, 12] on both pion–proton cross sections in the energy range $\sqrt{s}=5.38$–25.28 GeV. A fit to these data yielded

$$\sigma^{(1)}_{\gamma p}=C_1\ln^2\frac{s}{s_1}+A_1\left(1+\frac{\Lambda_{11}^2}{s+\Lambda_{12}^2}\right), \quad (13)$$
$$C_1=1.1554\ \mu\text{b},\quad \sqrt{s_1}=1.672\ \text{GeV},$$
$$A_1=152.03\ \mu\text{b},\quad \Lambda_{11}=5.006\ \text{GeV},$$
$$\Lambda_{12}=6.658\ \text{GeV}.$$

We note that, by virtue of the universality of the Froissart asymptotic behavior of hadronic cross sections, the parameter $C_1=2C$ within the additive quark model was fixed on the basis of a combinatorial analysis. In Fig. 1, the fit specified by Eq. (13) is represented by the upper solid curve.

Isolating terms in (12) that correspond to the calibration curves, we obtain

$$\sigma_{\gamma p}(s)=k(s)\big[\big(1-\bar P_{V\to 2\pi}(s)\big)\,\sigma^{(0)}_{\gamma p}(s) \quad (14)$$
$$+\bar P_{V\to 2\pi}(s)\sigma^{(1)}_{\gamma p}(s)\big],$$

where

$$k(s)=1+\frac{1}{P^{(0)}_{\gamma\to V}}\sum_{V,V'}\Delta P_{\gamma\to V^*\to V}(s), \quad (15)$$
$$\Delta P_{\gamma\to V^*\to V}(s)=\sum_{V,V^*}P_{\gamma\to V^*\to V}(s)-P^{(0)}_{\gamma\to V},$$
$$P^{(0)}_{\gamma\to V}\simeq\sum_{V=\rho,\omega,\phi}P_{\gamma\to V}(s)$$

[see Eqs. (3), (4)]; here, $k(s)$ is a function that takes into account the increase in the photon-hadronization probability owing to off-diagonal transitions, while $\bar P_{V\to 2\pi}$ is the pionization probability averaged over all vector mesons.

Let us now proceed to fit experimental data. As can be seen from Fig. 1, all of the measured cross sections for photon–proton interactions fall between the two calibration curves. This gives grounds to believe that

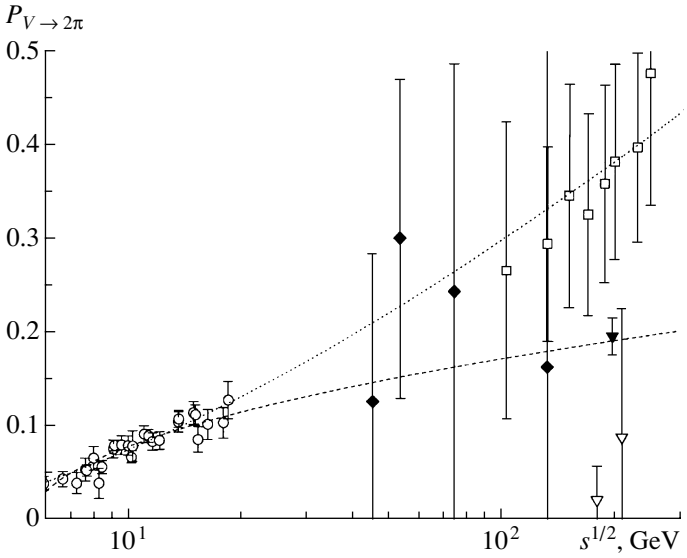

Fig. 2. Probability of the pionization of vector mesons in photon–proton interactions. The displayed experimental data are represented by points: (open boxes) extrapolation [2] of the ZEUS BPC data from [1], (open circles) low-energy photoproduction data from [11, 12], (closed diamonds) photoproduction data from the Baksan underground scintillation telescope, (open inverted triangles) ZEUS photoproduction data of 1992 and 1994 [3], and (closed inverted triangle) H1 photoproduction data of 1995 [4]. The dotted curve is a fit to indirect data on the basis of Eqs. (16) and (18), while the dashed curve is a fit to data of direct measurements on the basis of Eqs. (16) and (17).

the experimental data in question can be interpreted under the assumption that the pionization probability (or, what is the same, the probability of the emergence of a quark bag that consists of four additive quarks) has a special energy dependence. In the following, we assume that the pionization of vector mesons is a dominant effect. Disregarding all other factors, including the increase in the photon-hadronization probability owing to off-diagonal transitions, we can set $k(s) = 1$ in (14) and express the probability of the pionization of vector mesons in terms of experimental data exclusively:

$$\bar{P}_{V\to 2\pi}(s) = \frac{\sigma_{\gamma p} - \sigma_{\gamma p}^{(0)}}{\sigma_{\gamma p}^{(1)} - \sigma_{\gamma p}^{(0)}}.$$

In Fig. 2, the values of the function $\bar{P}_{V\to 2\pi}(s)$ that were calculated on the basis of experimental data are displayed (points) along with the results obtained by fitting this function for two sets of high-energy data (low-energy data are common to the two fits in question).

The first fit, which is represented by the dashed curve, is based exclusively on data from direct measurements at the Baksan underground scintillation telescope and from direct measurements reported in [3, 4]. The second fit (dotted curve) relies on data from the Baksan underground scintillation telescope and on indirect data obtained in [2] via an extrapolation of structure functions. The form of the fitted function was

$$\bar{P}_{V\to 2\pi}(s) = w \ln^n \frac{s}{s_2}, \qquad (16)$$

and the resulting parameter values appeared to be the following:

$$w = 0.0712, \quad \sqrt{s_2} = 5.465 \text{ GeV}, \quad n = 1/2 \quad (17)$$

for direct measurements;

$$w = 0.0140, \quad \sqrt{s_2} = 2.166 \text{ GeV}, \quad n = 3/2 \quad (18)$$

for indirect data.

The substitution of (16) into (14) leads to curves fitting the two data sets given in Fig. 1 for $\sigma_{\gamma p}(s)$, the dashed and the dotted curve corresponding to direct measurements and indirect high-energy data, respectively.

In our opinion, the results suggest that the mean number of additive quarks in photon-hadronization products increases monotonically with energy, following the law

$$\bar{n}_{\gamma\to h}(s) = 2\left(1 + w \ln^n \frac{s}{s_2}\right).$$

At currently achievable accuracy of the measurements in question, those data from the Baksan underground scintillation telescope that were obtained in the region not covered by presently operating accelerators are unfortunately insufficient for choosing between the alternative sets of high-energy experimental data. In searches for additional sources of information, we invoke the results produced by a simulation

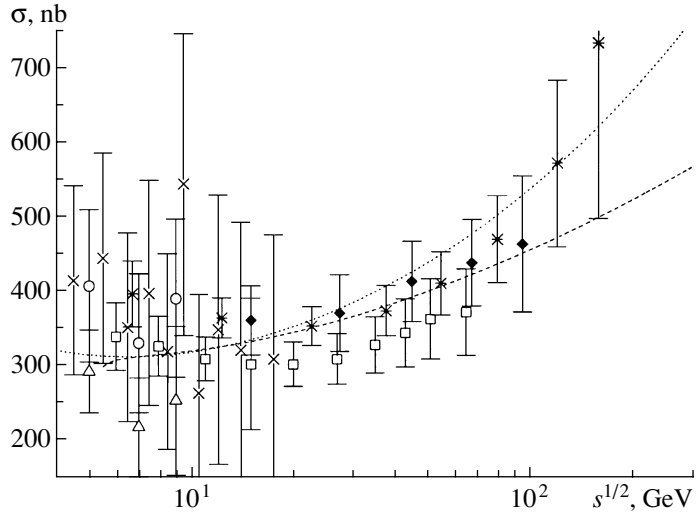

Fig. 3. Cross section for photon–photon interaction and its simulation. The displayed experimental data were borrowed from [30]: (asterisks) Acciarri 01, (open boxes) Acciarri 97, (closed diamonds) Abbiendi 99, (open boxes) Aihara 90, (crosses) Bintinger 85, and (open triangles) Berger 84. The dashed and the dotted curve represent the prediction that is specified by Eq. (21) and which is based on the data of, respectively, direct [the parameter values in (17)] and indirect [the parameter values in (18)] measurements.

of the cross section for photon–photon interaction on the basis of the cross sections for photon–proton interactions.

4. SIMULATION OF THE CROSS SECTION FOR PHOTON–PHOTON INTERACTION AND COMPARISON OF ITS RESULTS WITH EXPERIMENTAL DATA

The cross section for photon–photon interaction is expressed in terms of the same photon-hadronization probability and hadron–hadron cross section as those that appear in the γp-interaction model inspired by the additive-quark model and described in Section 3. The first step does not require explanations:

$$\sigma_{\gamma\gamma}(s) = k^2(s)\left(P^{(0)}_{\gamma\to V}\right)^2 \times \Big[\left(1-\bar{P}_{V\to 2\pi}(s)\right)^2\sigma_{VV}(s) + 2\bar{P}_{V\to 2\pi}(s)\left(1-\bar{P}_{V\to 2\pi}(s)\right)\sigma_{2\pi V}(s) + \bar{P}^2_{V\to 2\pi}(s)\sigma_{2\pi 2\pi}(s)\Big]. \quad (19)$$

Further, we express the cross sections for meson and two-pion interactions in terms of experimentally measured cross sections, simultaneously performing, for the arguments, the scale transformations dictated by the additive-quark model:

$$\sigma_{\gamma\gamma}(s) = k^2(s)\left(P^{(0)}_{\gamma\to V}\right)^2 \times \Big[\left(1-\bar{P}_{V\to 2\pi}(s)\right)^2\frac{4}{9}\sigma_{Np}(9s/4) + 2\bar{P}_{V\to 2\pi}(s)\left(1-\bar{P}_{V\to 2\pi}(s)\right)\frac{4}{3}\sigma_{\pi p}(3s/4) + \bar{P}^2_{V\to 2\pi}(s)\cdot 4\frac{\sigma^2_{\pi p}(3s/8)}{\sigma_{Np}(9s/16)}\Big]. \quad (20)$$

In deriving Eq. (20), we have used yet another relation following from the additive quark model:

$$\sigma_{\pi\pi}(s) = \frac{\sigma^2_{\pi p}(3s/2)}{\sigma_{Np}(9s/4)}.$$

It is convenient to represent the final result in a form where the calibration curves are isolated explicitly:

$$\sigma_{\gamma\gamma}(s) = k^2(s)\frac{1}{250} \times \frac{2}{3}\Big[\left(1-\bar{P}_{V\to 2\pi}(s)\right)^2\sigma^{(0)}_{\gamma p}(3s/2) + 2\bar{P}_{V\to 2\pi}(s)\left(1-\bar{P}_{V\to 2\pi}(s)\right)\sigma^{(1)}_{\gamma p}(3s/2) + \bar{P}^2_{V\to 2\pi}(s)\frac{\left(\sigma^{(1)}_{\gamma p}(3s/4)\right)^2}{\sigma^{(0)}_{\gamma p}(3s/8)}\Big]. \quad (21)$$

Experimental data on the cross section $\sigma_{\gamma\gamma}(s)$ from [30] are presented in Fig. 3, along with the results obtained by simulating this cross section according to (21) at $k(s) = 1$ for two versions of the hadronization of a photon, that which is specified in (17) and that which is specified in (18).

The errors in the measurements give no way to choose a version of the high-energy behavior of the cross sections $\sigma_{\gamma p}(s)$ and $\sigma_{\gamma\gamma}(s)$ unambiguously in

this case as well. If, however, the analysis is restricted to data on $\sigma_{\gamma\gamma}(s)$ for $\sqrt{s} \lesssim 100$ GeV, which have relatively small errors, these data are in better agreement with the prediction based on the results of direct measurements of the cross sections for photon–proton interactions.

5. CONCLUSIONS

(i) The experimental data on the cross sections for photon–nucleon interactions from the Baksan underground scintillation telescope in the energy region not covered by currently operating accelerators confirm the effect of a faster growth of $\sigma_{\gamma p}(s)$ in relation to the cross sections for hadron–hadron interactions.

(ii) An increase in the number of additive quarks in photon-hadronization products with increasing energy of photon–proton interaction may be one of the physical reasons behind this effect.

(iii) The cross section calculated for photon–photon interaction in the energy region $\sqrt{s} \lesssim 100$ GeV on the basis of direct measurements of the cross sections for photon–proton interactions (Baksan underground scintillation telescope, DESY H1 1995) agrees better with experimental data than a similar prediction relying on indirect data.

(iv) The results obtained by simulating the cross sections for photon–proton and photon–photon interactions on the basis of the additive-quark model indicate that the ideas of the hadronization of a photon that have been adopted here are intrinsically consistent. In principle, the specific energy dependences of the parameters of this effect can be established upon refining the relevant experimental data over the entire energy scale.

ACKNOWLEDGMENTS

We are grateful to V.N. Bakatanov, who made a large contribution to the implementation of this experiment, and to L. B. Bezrukov, S. P. Mikheev, and A. V. Butkevich for stimulating discussions.

This work was supported by the Federal Goal-Oriented Program Integration (project no. E0157).

REFERENCES

1. ZEUS Collab. (J. Breitweg *et al.*), Phys. Lett. B **407**, 432 (1997); Preprint DESY-00-071 (Hamburg, 2000).
2. A. Bornheim, in *Proceedings of the LAFEX International School on High Energy Physics (LISHEP 98), Brazil, 1998*; hep-ex/9806021.
3. ZEUS Collab. (M. Derrick *et al.*), Phys. Lett. B **293**, 465 (1992); Z. Phys. C **63**, 391 (1994).
4. H1 Collab. (S. Aid *et al.*), Z. Phys. C **69**, 27 (1995).
5. V. N. Bakatanov, Yu. F. Novosel'tsev, *et al.*, Pis'ma Zh. Éksp. Teor. Fiz. **48**, 129 (1988) [JETP Lett. **48**, 129 (1988)].
6. C. Bourelly, J. Soffer, and T. T. Wu, Mod. Phys. Lett. A **15**, 9 (2000).
7. A. Corsetti, R. M. Godbole, and G. Pancheri, Phys. Lett. B **435**, 441 (1998).
8. M. M. Block, E. M. Gregores, F. Halzen, and G. Pancheri, Phys. Rev. D **60**, 54024 (1999).
9. L. B. Bezrukov and É. V. Bugaev, Yad. Fiz. **32**, 1636 (1980) [Sov. J. Nucl. Phys. **32**, 847 (1980)].
10. V. V. Anisovich, M. N. Kobrinsky, J. Nyiri, and Yu. M. Shabelski, Usp. Fiz. Nauk **144**, 553 (1984) [Sov. Phys. Usp. **27**, 901 (1984)].
11. P. V. Denisov *et al.*, Phys. Lett. B **36B**, 415 (1971); Nucl. Phys. B **65**, 1 (1973).
12. R. Carrol *et al.*, Phys. Lett. B **61B**, 303 (1976); **80B**, 423 (1979).
13. N. Amos *et al.*, Nucl. Phys. B **262**, 689 (1985).
14. G. Carboni *et al.*, Nucl. Phys. B **254**, 697 (1985).
15. G. Arnison *et al.*, Phys. Lett. B **128B**, 336 (1983).
16. F. Abe *et al.*, Phys. Rev. D **50**, 5550 (1994).
17. G. J. Alner *et al.*, Z. Phys. C **32**, 153 (1986).
18. N. Amos *et al.*, Phys. Rev. Lett. **68**, 2433 (1992); C. Avila *et al.*, Phys. Lett. B **445**, 419 (1998).
19. D. O. Caldwell *et al.*, Phys. Rev. D **7**, 1362 (1973); Phys. Rev. Lett. **40**, 1222 (1978).
20. E. N. Alexeyev *et al.*, in *Proceedings of the 16th ICRC, Kyoto, 1979,* Vol. 10, p. 276.
21. L. B. Bezrukov and É. V. Bugaev, Yad. Fiz. **33**, 1195 (1981) [Sov. J. Nucl. Phys. **33**, 635 (1981)].
22. Yu. F. Novosel'tsev, Candidate's Dissertation in Physics and Mathematics (Institute for Nuclear Research AN SSSR, Moscow, 1988).
23. V. N. Bakatanov, Yu. F. Novosel'tsev, R. V. Novosel'tseva, *et al.*, Yad. Fiz. **55**, 2107 (1992) [Sov. J. Nucl. Phys. **55**, 1169 (1992)].
24. V. I. Gurentsov, Preprint No. P-0379, IYaI AN SSSR (Institute for Nuclear Research, Moscow, 1984).
25. V. I. Gurentsov, G. T. Zatsepin, and E. D. Mikhal'chi, Yad. Fiz. **23**, 1001 (1976) [Sov. J. Nucl. Phys. **23**, 527 (1976)] .
26. É. V. Bugaev, Yu. D. Kotov, and I. L. Rozental', *Cosmic Muons and Neutrinos* (Atomizdat, Moscow, 1970).
27. L. B. Bezrukov and E. V. Bugaev, in *Proceedings of the 17th ICRC, Paris, 1981,* Vol. 7, p. 102.
28. A. Okada, K. Mitsui, *et al.*, Fortschr. Phys. **32**, 135 (1984).
29. M. A. Shifman, A. I. Vainstein, and V. I. Zakharov, Nucl. Phys. B **147**, 385 (1979).
30. Particle Data Group (D. E. Groom *et al.*), Eur. Phys. J. C **15**, 1 (2000).

Translated by A. Isaakyan

Physics of Atomic Nuclei, Vol. 66, No. 3, 2003, pp. 575–581. Translated from Yadernaya Fizika, Vol. 66, No. 3, 2003, pp. 601–607.

ELEMENTARY PARTICLES AND FIELDS
Theory

Photoproduction of J/ψ Mesons at High Energies within the Parton Model and in the $k_\top$-Factorization Approach

V. A. Saleev*

Samara State University, ul. Akademika Pavlova 1, Samara, 443011 Russia

Received August 30, 2001; in final form, January 11, 2002

Abstract—The photoproduction of J/ψ mesons is considered on the basis of the parton model and in the $k_\top$-factorization approach in the leading order in α_s. It is shown that, at specific values of the charmed-quark mass and the J/ψ-meson wave function at the origin, the predictions of the two approaches for the total cross section and z spectra of J/ψ mesons nearly coincide and agree with experimental data obtained at the HERA ep collider. At the same time, the parton model and the theory of semihard processes predict significantly different $p_\top$ spectra of J/ψ mesons and significantly different transverse-momentum dependences of the ratio of the cross sections for the production of longitudinally and transversely polarized J/ψ mesons. It is expected that nontrivial effects of low-x physics will clearly manifest themselves in experimentally testing this fact. © *2003 MAIK "Nauka/Interperiodica"*.

1. INTRODUCTION

The photoproduction of J/ψ mesons on protons at high energies is dominated by the parton subprocess of photon–gluon fusion [1]. From the theoretical point of view that is based on nonrelativistic QCD (NRQCD) [2], the cross section for J/ψ photoproduction is determined by the gluon distribution in the proton, the hard parton amplitude for the production of a $c\bar{c}$ quark pair, and the mechanism of formation of a color-singlet bound state of these quarks with the quantum numbers of the J/ψ meson. Thus, this approach assumes the factorization of soft initial-state-interaction processes described by the distribution of gluons in the proton; a hard parton amplitude, which can be calculated within perturbative QCD at a small coupling constant $\alpha_s(\mu)$, where $\mu \sim 2m_c$; and the transformation of a $c\bar{c}$ pair into the final meson through a soft process, which can be described by using another small parameter of the problem, v—the relative velocity of the heavy quarks in the J/ψ meson. In the leading order in the small parameters α_s and v (for the J/ψ meson, $v \sim \alpha_s \sim 0.2$), the octet mechanism producing quarks in the color-octet state contributes to the photoproduction of J/ψ mesons, along with the singlet mechanism producing quarks through a hard subprocess in the color-singlet state. However, a comparison of the calculations performed in [3] with experimental data on J/ψ photoproduction that were obtained at the HERA ep collider [4] shows that the contribution of the octet mechanism to J/ψ photoproduction must be considerably less than what is expected with allowance for the octet-model parameters determined from a fit to data on the hadronic production of J/ψ mesons. It was shown in [3] that, over a wide region of kinematical variables, data on J/ψ photoproduction at the HERA collider can be described within the model of color singlets, so that the contribution of the octet mechanism is not required. Taking the aforesaid into consideration, we will allow here only for the singlet mechanism of J/ψ-meson production. Specifically, we analyze the role of the gluon distribution in the proton for J/ψ-photoproduction processes, considering the relevant distribution function within the standard parton model and within the $k_\top$-factorization approach [5], which is based on the Balitsky–Fadin–Kuraev–Lipatov (BFKL) equation of QCD evolution [6]. In addition to the large logarithms $\log(Q^2/\Lambda^2_{\mathrm{QCD}})$ included in the standard Dokshitzer–Gribov–Lipatov–Altarelli–Parisi (DGLAP) equation of QCD evolution [7], the BFKL equation also takes into account $\log(1/x)$, where $x \sim Q^2/s \ll 1$, $Q^2 \sim m_c^2$, and s is the squared total energy of colliding particles in the c.m. frame.

2. CROSS SECTION FOR THE PROCESS $\gamma p \to J\psi X$ WITHIN THE $k_\top$-FACTORIZATION APPROACH

At the moment, there are two approaches to calculating the cross sections for the high-energy production of J/ψ mesons (quarkonia or merely heavy quarks). In the standard parton model [8], it is assumed that the cross section for the hadronic process, $\sigma(\gamma p \to J/\psi X, s)$, is related to the cross section

*e-mail: saleev@ssu.samara.ru

of the partonic subprocess, $\hat{\sigma}(\gamma g \to J/\psi g, \hat{s})$, by the equation

$$\sigma^{\mathrm{PM}}(\gamma p \to J/\psi X, s) = \int dx \hat{\sigma}(\gamma g \to J/\psi g, \hat{s}) G(x, Q^2), \quad (1)$$

where $\hat{s} = xs$ and $G(x, Q^2)$ is the gluon distribution in the proton; it depends on x, the proton-momentum fraction carried away by the gluon, and Q^2, the characteristic value of the square of the 4-momentum transfer in the parton subprocess. The dependence of $G(x, Q^2)$ on x and Q^2 is described by the DGLAP equation of QCD evolution [7], where it is assumed that the momentum transfer is quite high, $Q^2 \gg \Lambda^2_{\mathrm{QCD}}$. In the region of high energies ($s \gg Q^2$) and high momentum transfers, $x \ll 1$. As a result, the series of perturbative QCD in the constant α_s involves large coefficients of the form $\log(1/x)$ in addition to the large logarithms $\log(Q^2/\Lambda^2_{\mathrm{QCD}})$. Upon taking this circumstance into account, we arrive at the BFKL evolution equation [6] for the noncollinear gluon-distribution function $\Phi(x, q^2, Q^2)$ not integrated with respect to the gluon virtuality q^2. This function is related to the collinear gluon-distribution function by the equation

$$xG(x, Q^2) = \int_0^{Q^2} \Phi(x, \mathbf{q}_\top^2, Q^2) d\mathbf{q}_\top^2. \quad (2)$$

In standard kinematics, the gluon 4-momentum q is expressed in terms of the proton 4-momentum p_N as

$$q = xp_N + q_\top,$$

where the 4-vector $q_\top = (0, \mathbf{q}_\top, 0)$ has only transverse components, $p_N = (E_N, 0, 0, |\mathbf{p}_N|)$, and $q^2 = q_\top^2 = -\mathbf{q}_\top^2$. Therefore, the fact that the initial gluon participating in the parton subprocess is off the mass shell and has a dominant t-channel longitudinal polarization described by the polarization 4-vector $\varepsilon^\mu = q_\top^\mu/|\mathbf{q}_\top|$ is a significant point of the $k_\top$-factorization approach. Within the $k_\top$-factorization approach, the cross sections for the hadronic process and the parton subprocess are related by the equation

$$\sigma(\gamma p \to J/\psi X) = \int \frac{dx}{x} \int d\mathbf{q}_\top^2 \int \frac{d\phi}{2\pi} \Phi(x, \mathbf{q}_\top^2, Q^2) \times \hat{\sigma}(\gamma g^* \to J/\psi g, \hat{s}, \mathbf{q}_\top^2), \quad (3)$$

where $\hat{\sigma}(\gamma g^* \to J/\psi g)$ is the cross section for J/ψ photoproduction on virtual gluons and ϕ is the azimuthal angle in the xy plane orthogonal to the reaction axis (z axis) between the vector $\mathbf{q}_\top$ and the x axis, which is fixed. In the limit $\mathbf{q}_\top^2 \ll \hat{s}$, we can neglect the gluon virtuality in the cross section for the parton subprocess; upon averaging over the angle ϕ, we then obtain the cross section for the partonic photoproduction of J/ψ on real gluons:

$$\lim_{\mathbf{q}_\top^2 \to 0} \int \frac{d\phi}{2\pi} \hat{\sigma}(\gamma g^* \to J/\psi g, \hat{s}, q_\top^2) = \hat{\sigma}(\gamma g \to J/\psi g, \hat{s}). \quad (4)$$

3. GLUON DISTRIBUTION WITHIN THE $k_\top$-FACTORIZATION APPROACH

To calculate the noncollinear distribution of gluons in the proton, $\Phi(x, \mathbf{q}_\top^2, Q^2)$, we will use the results presented by Blumlein [9], who showed that constructing a solution that satisfies the BFKL evolution equation and condition (2) reduces to calculating the convolution of a preset collinear gluon-distribution function $G(x, Q^2)$ with universal weight functions; that is,

$$\Phi(x, \mathbf{q}_\top^2, Q^2) = \int_x^1 \mathcal{G}(\eta, \mathbf{q}_\top^2, Q^2) \frac{x}{\eta} G\left(\frac{x}{\eta}, Q^2\right) d\eta, \quad (5)$$

where

$$\mathcal{G}(\eta, \mathbf{q}_\top^2, Q^2) = \frac{\bar{\alpha}_s}{\eta \mathbf{q}_\top^2} J_0\left[2\sqrt{\bar{\alpha}_s \ln\left(\frac{1}{\eta}\right) \ln\left(\frac{Q^2}{\mathbf{q}_\top^2}\right)}\right] \quad (6)$$

for $\mathbf{q}_\top^2 \le Q^2$,

$$\mathcal{G}(\eta, \mathbf{q}_\top^2, Q^2) = \frac{\bar{\alpha}_s}{\eta \mathbf{q}_\top^2} I_0\left[2\sqrt{\bar{\alpha}_s \ln\left(\frac{1}{\eta}\right) \ln\left(\frac{\mathbf{q}_\top^2}{Q^2}\right)}\right] \quad (7)$$

for $\mathbf{q}_\top^2 > Q^2$.

Here, J_0 and I_0 are Bessel functions of, respectively, a real and an imaginary argument and $\bar{\alpha}_s = \dfrac{\alpha_s}{3\pi}$. We use the GRV(LO) parametrization [10] for the input distribution function $\tilde{G}(x, Q^2)$. In order to test the method used to calculate $\Phi(x, \mathbf{q}_\top^2, Q^2)$, we compare the input collinear distribution function with the distribution function $\tilde{G}(x, Q^2)$ obtained by integrating $\Phi(x, \mathbf{q}_\top^2, Q^2)$ with respect to $\mathbf{q}_\top^2$. Figure 1 displays the calculated ratio $R(x, Q^2) = \tilde{G}(x, Q^2)/G(x, Q^2)$. It is clear that, for $x \le 0.01$, the ratio R differs from unity by not more than 1 to 2%. We note that, in J/ψ photoproduction on protons, $x \sim M/\sqrt{s}$, where M is the J/ψ mass; that is, $x \sim 0.03$ at $\sqrt{s} = 100$ GeV.

4. AMPLITUDE OF J/ψ PHOTOPRODUCTION ON GLUONS

In the color-singlet model [1], the parton subprocess $\gamma g^* \to J/\psi g$ in the lowest order of perturbation theory in the constants of strong and electromagnetic interactions (α_s and α, respectively) is described by six Feynman diagrams in Fig. 2. In the nonrelativistic approximation, the J/ψ meson is considered as a two-particle system in a state where the orbital angular momentum and spin are $L = 0$ and $S = 1$, respectively. We neglect the binding energy and the relative momentum of quarks within the meson; that is, $M = 2m_c$ and $p_c = p_{\bar{c}} = \dfrac{p}{2}$, where p is the J/ψ-meson 4-momentum and p_c and $p_{\bar{c}}$ are, respectively, the quark and the antiquark 4-momentum. Within the projection-operator formalism [11], the amplitude of the process $\gamma g^* \to J/\psi g$ can be obtained from the $\gamma g^* \to \bar{c}cg$ amplitude by means of the substitution

$$V^i(p_{\bar{c}})\bar{U}^j(p_c) \to \frac{\Psi(0)}{2\sqrt{M}}\hat{\varepsilon}(p)(\hat{p}+M)\frac{\delta^{ij}}{\sqrt{3}}, \quad (8)$$

where $\hat{\varepsilon}(p) = \varepsilon_\mu(p)\gamma^\mu$, $\varepsilon_\mu(p)$ being the 4-vector of J/ψ-meson polarization; $\dfrac{\delta^{ij}}{\sqrt{3}}$ is a color factor; $\Psi(0)$ is the nonrelativistic J/ψ wave function at the origin; and $V^i(p_{\bar{c}})$ and $\bar{U}^j(p_c)$ are, respectively, the $\bar{c}$-antiquark and the c-quark spinors. The amplitudes of the process $\gamma g^* \to J/\psi g$ that correspond to the diagrams in Fig. 2 are given by

$$M_i = KC^{ab}\varepsilon_\alpha(k_1)\varepsilon^a_\mu(q)\varepsilon^b_\beta(k_2)\varepsilon_\nu(p)M_i^{\alpha\beta\mu\nu}, \quad (9)$$

where

$$M_1^{\alpha\beta\mu\nu} = \mathrm{tr}\left[\gamma^\nu(\hat{p}+M)\gamma^\alpha\frac{\hat{p}_c-\hat{k}_1+m_c}{(p_c-k_1)^2-m_c^2}\gamma^\mu\frac{-\hat{p}_{\bar{c}}-\hat{k}_2+m_c}{(p_{\bar{c}}+k_2)^2-m_c^2}\gamma^\beta\right], \quad (10)$$

$$M_2^{\alpha\beta\mu\nu} = \mathrm{tr}\left[\gamma^\nu(\hat{p}+M)\gamma^\beta\frac{\hat{p}_c+\hat{k}_2+m_c}{(p_c+k_2)^2-m_c^2}\gamma^\alpha\frac{\hat{q}-\hat{p}_{\bar{c}}+m_c}{(q-p_{\bar{c}})^2-m_c^2}\gamma^\mu\right], \quad (11)$$

$$M_3^{\alpha\beta\mu\nu} = \mathrm{tr}\left[\gamma^\nu(\hat{p}+M)\gamma^\alpha\frac{\hat{p}_c-\hat{k}_1+m_c}{(p_c-k_1)^2-m_c^2}\gamma^\beta\frac{\hat{q}-\hat{p}_{\bar{c}}+m_c}{(q-p_{\bar{c}})^2-m_c^2}\gamma^\mu\right], \quad (12)$$

$$M_4^{\alpha\beta\mu\nu} = \mathrm{tr}\left[\gamma^\nu(\hat{p}+M)\gamma^\mu\frac{\hat{p}_c-\hat{q}+m_c}{(p_c-q)^2-m_c^2}\gamma^\alpha\frac{-\hat{p}_{\bar{c}}-\hat{k}_2+m_c}{(k_2+p_{\bar{c}})^2-m_c^2}\gamma^\beta\right], \quad (13)$$

$$M_5^{\alpha\beta\mu\nu} = \mathrm{tr}\left[\gamma^\nu(\hat{p}+M)\gamma^\beta\frac{\hat{p}_c+\hat{k}_2+m_c}{(p_c+k_2)^2-m_c^2}\gamma^\mu\frac{\hat{k}_1-\hat{p}_{\bar{c}}+m_c}{(k_1-p_{\bar{c}})^2-m_c^2}\gamma^\alpha\right], \quad (14)$$

$$M_6^{\alpha\beta\mu\nu} = \mathrm{tr}\left[\gamma^\nu(\hat{p}+M)\gamma^\mu\frac{\hat{p}_c-\hat{q}+m_c}{(p_c-q)^2-m_c^2}\gamma^\beta\frac{\hat{k}_1-\hat{p}_{\bar{c}}+m_c}{(k_1-p_{\bar{c}})^2-m_c^2}\gamma^\alpha\right]; \quad (15)$$

k_1, q, and k_2 are the 4-momenta of, respectively, the photon, the initial gluon, and the final gluon; and

$$K = e_c e g_s^2\frac{\Psi(0)}{2\sqrt{M}}, \qquad C^{ab} = \frac{1}{\sqrt{3}}\mathrm{tr}[T^aT^b]$$

with

$$e_c = \frac{2}{3}, \quad e = \sqrt{4\pi\alpha}, \quad g_s = \sqrt{4\pi\alpha_s},$$

$T^a = \dfrac{\lambda^a}{2}$, λ^a being the Gell-Mann matrices. Summation over photon, J/ψ-meson, and final-gluon polarizations is performed in the standard covariant way:

$$\sum_{\mathrm{spin}}\varepsilon_\alpha(k_1)\varepsilon_\beta(k_1) = -g_{\alpha\beta}, \quad (16)$$

$$\sum_{\mathrm{spin}}\varepsilon_\alpha(k_2)\varepsilon_\beta(k_2) = -g_{\alpha\beta}, \quad (17)$$

$$\sum_{\mathrm{spin}}\varepsilon_\mu(p)\varepsilon_\nu(p) = -g_{\mu\nu} + \frac{p_\mu p_\nu}{M^2}. \quad (18)$$

Summation over initial-gluon polarizations is performed according to the expression

$$\sum_{\mathrm{spin}}\varepsilon_\mu(q)\varepsilon_\nu(q) = \frac{q_{\top\mu}q_{\top\nu}}{\mathbf{q}_\top^2}. \quad (19)$$

In the case of a longitudinal polarization, the J/ψ-meson polarization vector for $s \gg M^2$ can be represented in the form

$$\varepsilon_L^\mu(p) = \frac{p^\mu}{M} - \frac{Mp_N^\mu}{(pp_N)}, \quad (20)$$

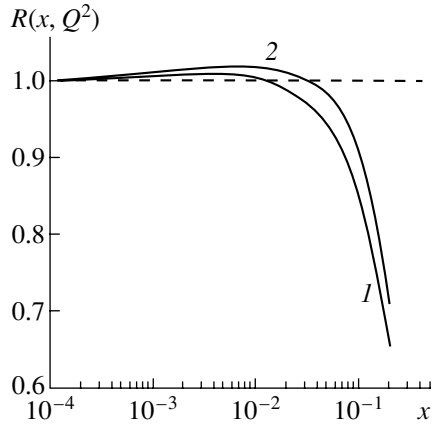

Fig. 1. Ratio $R(x, Q^2)$ at $Q^2 = 10$ and 100 GeV^2 (curves *1* and *2*, respectively).

the relations $(\varepsilon_L \varepsilon_L) = -1$ and $(\varepsilon_L p) = 0$ being satisfied.

In describing the photoproduction of quarkonia, use is traditionally made of the covariant variable $z = (pp_N)/(k_1 p_N)$, which determines the degree of inelasticity of the process being considered. In the proton rest frame, it is equal to the ratio of the J/ψ-meson and photon energies, $z = E_\psi/E_\gamma$. Within the $k_\top$-factorization approach, the double-differential (with respect to $p_\top$ and z) cross section for J/ψ production assumes the form

$$\frac{d\sigma}{dp_\top^2 dz} = \frac{1}{z(1-z)} \times \int \frac{d\phi}{2\pi} \int d\mathbf{q}_\top^2 \Phi(x, \mathbf{q}_\top^2, Q^2) \frac{\overline{|M|^2}}{16\pi(xs)^2}. \quad (21)$$

Numerical calculations are performed in the proton–photon c.m. frame, where

$$p_N = \frac{\sqrt{s}}{2}(1,0,0,1), \quad k_1 = \frac{\sqrt{s}}{2}(1,0,0,-1),$$
$$p = (E, \mathbf{p}_\top, p_\parallel), \quad q = \left(\frac{\sqrt{s}}{2}x, \mathbf{q}_\top, \frac{\sqrt{s}}{2}x\right).$$

Here, we have considered that the J/ψ-meson 3-momentum $\mathbf{p}$ lies in the xz plane and that $(\mathbf{q}_\top \cdot \mathbf{p}_\top) = |\mathbf{p}_\top||\mathbf{q}_\top| \cos\phi$. The expression for the squared modulus of the amplitude, $\overline{|M|^2}$, as a function of the variables $\hat{s} = (k_1 + q)^2$, $\hat{t} = (p - k_1)^2$, $\hat{u} = (p - q)^2$, $\mathbf{p}_\top^2$, $\mathbf{q}_\top^2$, and $\cos\phi$ is calculated with the aid of the REDUCE system for analytic calculations and is represented in the form of a file in the FORTRAN format, and it is the form that is used in the ensuing calculations. Setting $\mathbf{p}_\top^2 = \hat{t}\hat{u}/\hat{s}$ upon the integration of the squared modulus of the amplitude with respect to the angle ϕ, we can show, by means of a direct calculation, that

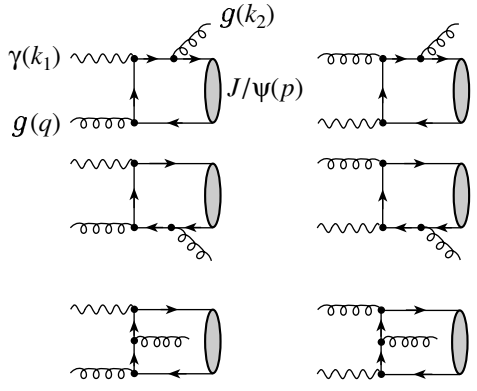

Fig. 2. Diagrams for the subprocess $\gamma + g^* \to J/\psi + g$.

$$\lim_{\mathbf{q}_\top^2 \to 0} \int_0^{2\pi} \frac{d\phi}{2\pi} \overline{|M|^2} = \overline{|M_{\mathrm{PM}}|^2}, \quad (22)$$

where $\overline{|M_{\mathrm{PM}}|^2}$ is the squared modulus of the amplitude for J/ψ photoproduction on a real gluon [3], with its spin density matrix being

$$\sum_{\mathrm{spin}} \varepsilon_\mu(q) \varepsilon_\nu^*(q) = -g_{\mu\nu}. \quad (23)$$

In the limit $\mathbf{q}_\top^2 = 0$, expression (21) yields the differential cross section in the parton model:

$$\frac{d\sigma^{\mathrm{PM}}}{dp_\top^2 dz} = \frac{\overline{|M_{\mathrm{PM}}|^2} x G(x, Q^2)}{16\pi(xs)^2 z(1-z)}. \quad (24)$$

In the calculations within the parton model, we use expression (21) rather than its limit (24), performing integration with respect to $\mathbf{q}_\top^2$ and ϕ numerically. In this way, we can fix a common normalization in the two approaches and explicitly isolate effects associated with the virtuality of the initial gluon in the amplitude of the parton subprocess.

5. RESULTS OF THE CALCULATIONS

Once the collinear gluon-distribution function $G(x, Q^2)$ is fixed, there remain only two parameters that determine the general normalization of the calculated cross sections: $\Psi(0)$ and m_c. We can determine the value of the J/ψ wave function at the origin from the calculations in the potential model for charmonium or extract it from the known value of the width with respect to the leptonic decay $J/\psi \to \mu^+\mu^-$. In our calculations, we used the numerical value of $|\Psi(0)|^2 = 0.0876$ GeV^3 [3]. In the nonrelativistic approximation, it is natural to set the charmed-quark mass to $m_c = M/2 = 1.55$ GeV. If, however,

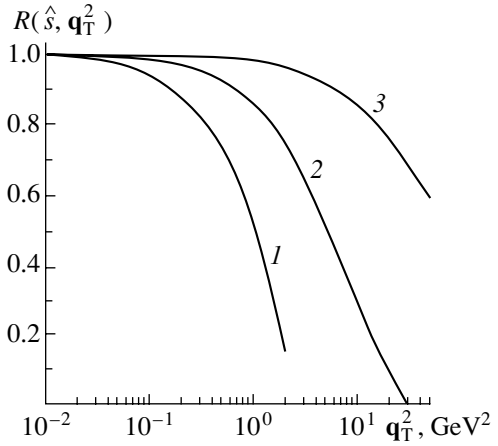

Fig. 3. Ratio $R(\hat{s}, \mathbf{q}_\top^2)$ at $\hat{s} = 15$, 20, and 100 GeV^2 (curves *1*, *2*, and *3*, respectively).

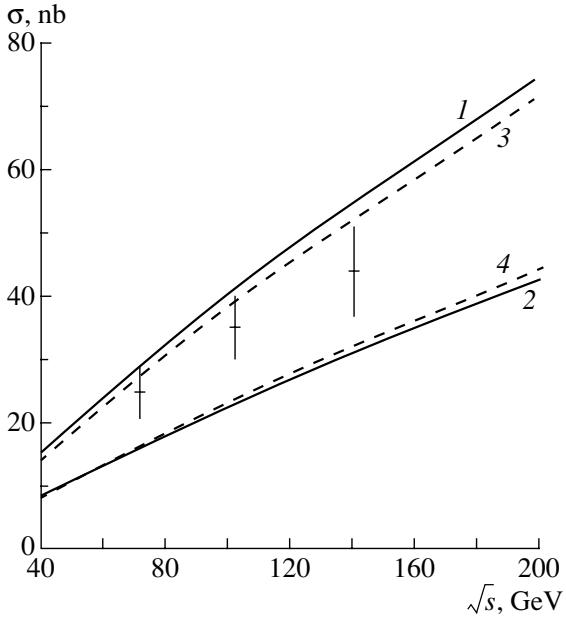

Fig. 4. Cross section for J/ψ photoproduction versus $\sqrt{s}$ for $0.4 < z < 0.9$ and $p_\top^2 > 1$ GeV^2: (points) experimental data from [4]; (curves *1, 2*) theoretical results obtained within the $k_\top$-factorization approach at $m_c = 1.4$ and 1.55 GeV, respectively; and (curves *3, 4*) theoretical results obtained on the basis of the parton model at $m_c = 1.4$ and 1.55 GeV, respectively.

we assume that the hard partonic process produces current quarks, the c-quark mass must be lower—for example, $m_c = 1.4$ GeV. We will perform further calculations with these two values of the c-quark mass, and this will give us a theoretical corridor that is associated with the uncertainty in choosing the charmed-quark mass. We consider the kinematical region specified by the inequalities $0.4 < z < 0.9$ and $p_\top^2 > 1$ GeV^2 in order to eliminate the possible contributions from the octet production mechanism ($z > 0.9$) and from the photon structure function ($z < 0.2$) (recall that we disregard these contributions here). There is yet another reason for doing this: we want to compare the results of our calculations with the experimental data obtained by the H1 and ZEUS collaborations with these constraints on z and $p_\top$ [4].

Figure 3 displays the ratio of the total cross sections for J/ψ production in the partonic subprocesses $\gamma g^* \to J/\psi g$ and $\gamma g \to J/\psi g$ as a function of $\mathbf{q}_\top^2$ at various $\hat{s}$:

$$R(\hat{s}, \mathbf{q}_\top^2) = \frac{\hat{\sigma}(\hat{s}, \mathbf{q}_\top^2)}{\hat{\sigma}_{\mathrm{PM}}(\hat{s})}. \qquad (25)$$

As might have been expected, the ratio in (25) decreases with increasing $\mathbf{q}_\top^2$, the rate of this decrease becoming higher as the invariant quantity $\hat{s}$ decreases.

We have already mentioned that the results of the calculations depend strongly on the numerical value of the c-quark mass. Figures 4–6 show the results of our calculations for two limiting values of the c-quark mass, $m_c = 1.4$ and 1.55 GeV. The dependence of the results on the choice of hard scale is weaker; we set $Q^2 = M^2 + p_\top^2$ in the gluon distribution function and in the running coupling constant $\alpha_s(Q^2)$.

Figure 4 shows the total cross section for J/ψ photoproduction on protons as a function of the invariant quantity $\sqrt{s}$. It is clear that the distinction between the predictions of the parton model and the $k_\top$-factorization approach is much less than the uncertainty associated with the choice of the c-quark mass. At $m_c = 1.55$ GeV, the calculated cross sections are smaller than the experimental values [4] by a factor of 1.5 to 2 [4], but, at $m_c = 1.4$ GeV, the theoretical curves are slightly above the experimental points.

The predictions of the parton model and the $k_\top$-factorization approach for z spectra of J/ψ mesons do not differ very strongly either. It is clear from Fig. 5 that the experimental points lie within the theoretical corridor both in the calculations on the basis of the parton model and within the $k_\top$-factorization approach.

Allowance for the transverse momentum in the $k_\top$-factorization approach results in the smoothing of the $p_\top$ spectra of J/ψ mesons in relation to the predictions of the parton model. This effect was noticed first in [12] and then in [13, 14]. Figure 6 displays the results of our calculations of the $p_\top$ spectra of J/ψ mesons and experimental data from [4]. The spectrum is harder in the $k_\top$-factorization approach than in the parton model. The results of the calculations based on the $k_\top$-factorization approach

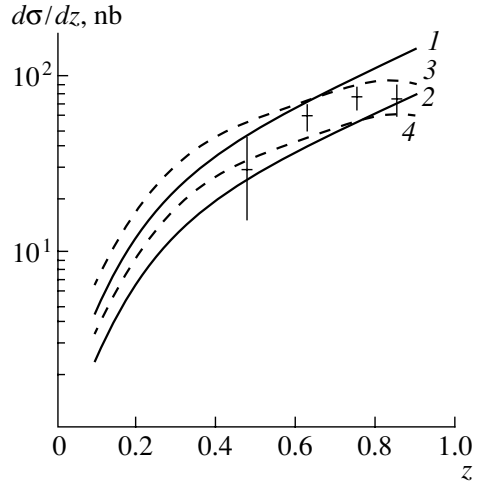

Fig. 5. z spectrum of J/ψ mesons at $\sqrt{s} = 100$ GeV and $p_\top^2 > 1$ GeV^2. The displayed experimental data were borrowed from [4], and the notation for the curves is identical to that in Fig. 4.

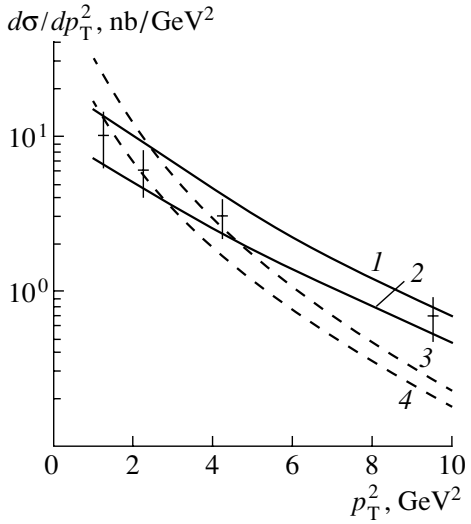

Fig. 6. Spectrum of J/ψ mesons with respect to $p_\top^2$ at $\sqrt{s} = 100$ GeV and $0.4 < z < 0.9$. The displayed experimental data were borrowed from [4], and the notation for the curves is identical to that in Fig. 4.

agree with experimental data from [4] within the theoretical uncertainty associated with the choice of the c-quark mass. However, this effect cannot be considered as a direct manifestation of nontrivial low-x physics. In [3], the $p_\top$ spectra of J/ψ mesons in the parton model were calculated in the next order of perturbation theory in α_s, and it was shown that the inclusion of the α_s correction also leads to the smoothing of the $p_\top$ spectrum of J/ψ mesons, enabling one to describe the experimentally observed behavior.

The choice of the spin density matrix in the form (19) rather than in the form (23), which is typical of the parton model, is yet another significant distinction between the $k_\top$-factorization approach and the standard parton model. It is clear that different spin states of the initial gluons must result in observable spin effects in the production of polarized J/ψ mesons. We have calculated the dependence of the spin parameter

$$\alpha(z) = \left(\frac{d\sigma_{\rm tot}}{dz} - 3\frac{d\sigma_L}{dz}\right) \Big/ \left(\frac{d\sigma_{\rm tot}}{dz} + \frac{d\sigma_L}{dz}\right) \quad (26)$$

or

$$\alpha(p_\top^2) = \left(\frac{d\sigma_{\rm tot}}{dp_\top} - 3\frac{d\sigma_L}{dp_\top}\right) \Big/ \left(\frac{d\sigma_{\rm tot}}{dp_\top} + \frac{d\sigma_L}{dp_\top}\right) \quad (27)$$

on z and $p_\top$ within the parton model and within the $k_\top$-factorization approach. In (26) and (27), $\sigma_{\rm tot} = \sigma_L + \sigma_T$ is the total cross section for the production of J/ψ mesons, σ_L is the cross section for the production of longitudinally polarized J/ψ, and σ_T is that for transversely polarized J/ψ. The parameter α is determined experimentally by measuring the angular distribution of leptons in the decay $J/\psi \to \mu^+\mu^-$. In the J/ψ rest frame, the differential distribution of the $J/\psi \to \mu^+\mu^-$ decay width with respect to the angle θ is

$$\frac{d\Gamma}{d\cos^2\theta} \sim 1 + \alpha\cos\theta. \quad (28)$$

In the region considered here, $p_\top^2 > 1$ GeV^2 and $0.4 < z < 0.9$, the parameter $\alpha(z)$ is close to zero both in the parton model and in the $k_\top$-factorization approach, as is clear from Fig. 7. For $z > 0.9$, J/ψ mesons will be predominantly produced with a transverse polarization in both approaches. In the parton model, $\alpha(z)$ tends to unity much faster for $z \to 1$.

The predictions for the dependence of the spin

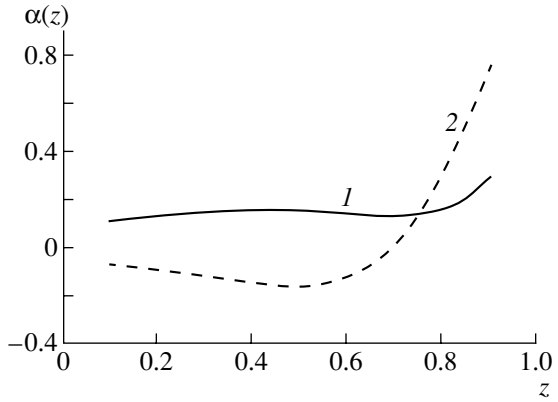

Fig. 7. Parameter α versus z at $\sqrt{s} = 100$ GeV, $p_\top^2 > 1$ GeV^2, and $m_c = 1.55$ GeV: (curve *1*) results based on the $k_\top$-factorization approach and (curve *2*) results based on the parton model.

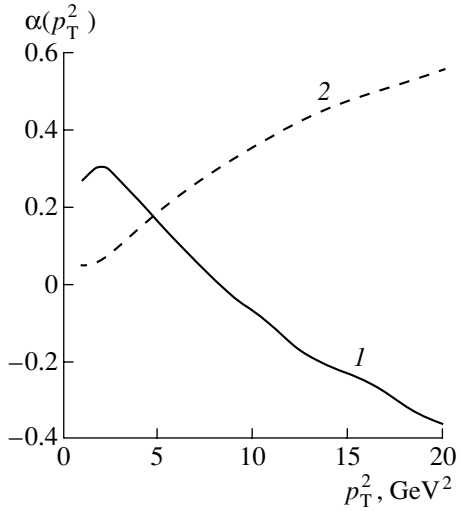

Fig. 8. Parameter α versus $p_\top^2$ at $\sqrt{s} = 100$ GeV, $0.4 < z < 0.9$, and $m_c = 1.55$ GeV: (curve *1*) results in the $k_\top$-factorization approach and (curve *2*) results in the parton model.

parameter $\alpha(p_\top^2)$ on the J/ψ-meson transverse momentum are opposite in the parton model and in the $k_\top$-factorization approach, as is clear from Fig. 8. At high $p_\top$, J/ψ mesons are produced in the parton model with a transverse polarization [$\alpha(p_\top^2) \approx 0.6$ at $p_\top^2 = 20$ GeV^2]; in the $k_\top$-factorization approach, they are produced with a longitudinal polarization [$\alpha(p_\top^2) \approx -0.4$ at $p_\top^2 = 20$ GeV^2]. The exact answer to the question of whether the inclusion of α_s corrections in the parton model would make it possible to reproduce the results obtained on the basis of the $k_\top$-factorization approach, as this occurred in the case of the $p_\top$ spectra of J/ψ mesons, is unknown at the moment. We assume that this is possible. Indeed, the J/ψ transverse momentum in the Born approximation of the color-singlet model is compensated at high $p_\top$ by one hard gluon, whence it follows that the production of transversely polarized J/ψ mesons dominates. In the next order of perturbation theory in α_s at high $p_\top$, the diagram involving two final hard gluons will be dominant. Owing to the momentum-conservation law, this would increase the cross section for the production of longitudinally polarized J/ψ mesons.

ACKNOWLEDGMENTS

I am grateful to S.P. Baranov, V.V. Kiselev, and A.K. Likhoded for interest in this study and stimulating discussions.

This work was supported by the Russian Foundation for Basic Research (project no. 02-02-16253).

REFERENCES

1. E. L. Berger and D. Jones, Phys. Rev. D **23**, 1521 (1981); R. Baier and R. Ruckl, Phys. Lett. B **102B**, 364 (1981); S. S. Gershteĭn, A. K. Likhoded, and S. R. Slabospitskiĭ, Yad. Fiz. **34**, 227 (1981) [Sov. J. Nucl. Phys. **34**, 128 (1981)].
2. G. T. Bodwin, E. Braaten, and G. P. Lepage, Phys. Rev. D **51**, 1125 (1995).
3. M. Kramer, Nucl. Phys. B **459**, 3 (1996).
4. H1 Collab. (S. Aid *et al.*), Nucl. Phys. B **472**, 32 (1996); ZEUS Collab. (J. Breitweg *et al.*), Z. Phys. C **76**, 599 (1997).
5. L. V. Gribov, E. M. Levin, and M. G. Ryskin, Phys. Rep. **100**, 1 (1983); J. C. Collins and R. K. Ellis, Nucl. Phys. B **360**, 3 (1991); S. Catani, M. Ciafoloni, and F. Hautmann, Nucl. Phys. B **366**, 135 (1991).
6. E. A. Kuraev, L. N. Lipatov, and V. S. Fadin, Zh. Éksp. Teor. Fiz. **71**, 840 (1976) [Sov. Phys. JETP **44**, 443 (1976)]; Ya. Ya. Balitskiĭ and L. N. Lipatov, Yad. Fiz. **28**, 1597 (1978) [Sov. J. Nucl. Phys. **28**, 822 (1978)].
7. V. N. Gribov and L. N. Lipatov, Yad. Fiz. **15**, 781 (1972) [Sov. J. Nucl. Phys. **15**, 438 (1972)]; Yu. A. Dokshitser, Zh. Éksp. Teor. Fiz. **73**, 1216 (1977) [Sov. Phys. JETP **46**, 641 (1977)]; G. Altarelli and G. Parisi, Nucl. Phys. B **126**, 298 (1977).
8. G. Sterman *et al.*, Rev. Mod. Phys. **67**, 157 (1995).
9. J. Blumlein, Preprint DESY 95-121 (1995).
10. M. Glück, E. Reya, and A. Vogt, Z. Phys. C **67**, 433 (1995).
11. B. Guberina *et al.*, Nucl. Phys. B **174**, 317 (1980).
12. V. A. Saleev and N. P. Zotov, Mod. Phys. Lett. A **9**, 151 (1994); **11**, 25 (1996).
13. A. V. Lipatov and N. P. Zotov, Mod. Phys. Lett. A **15**, 695 (2000).
14. S. P. Baranov, Phys. Lett. B **428**, 377 (1998).

Translated by M. Kobrinsky

Physics of Atomic Nuclei, Vol. 66, No. 3, 2003, pp. 582–598. Translated from Yadernaya Fizika, Vol. 66, No. 3, 2003, pp. 608–624.

FUTURE PUBLICATIONS

Effect of Nuclear Matter on Hadron Formation in Deep-Inelastic Neutrino Scattering

N. M. Agababyan, V. V. Ammosov, M. R. Atayan, N. G. Grigoryan, G. R. Gulkanyan, A. A. Ivanilov, Zh. K. Karamyan, and V. A. Korotkov

The inclusive spectra of hadrons are measured with the aid of the SKAT propane–freon bubble chamber irradiated with a beam of 3- to 30-GeV neutrinos from the Serpukhov accelerator. The resulting data indicate that the intranuclear absorption of leading quark-fragmentation products is enhanced as the energy transfer to the quark involved decreases or as the quark-energy fraction z acquired by the product hadron increases. An analysis of the data on the basis of the color-string model reveals that the cross section for the intranuclear absorption of positively charged hadrons that are characterized by z values in the range between 0.7 and 0.9 is close to the inelastic cross section for pion–nucleon interaction.

Measurement of the Differential Cross Section and the Tensor and Vector Analyzing Powers for the Fragmentation of 4.5-GeV/c Deuterons on a Beryllium Target in the Process Leading to Proton Emission at an Angle of 80 mrad

L. S. Azhgirey, V. V. Arkhipov, S. V. Afanas'ev, V. K. Bondarev, V. N. Zhmyrov, L. S. Zolin, V. I. Ivanov, A. Yu. Isupov, A. A. Kartamyshev, V. A. Kashirin, V. I. Kolesnikov, V. A. Kuznetsov, V. P. Ladygin, N. B. Ladygina, A. G. Litvinenko, S. G. Reznikov, P. A. Rukoyatkin, A. Yu. Semenov, I. A. Semenova, G. D. Stoletov, G. Filipov, A. N. Khrenov, and N. P. Yudin

The invariant differential cross section, the tensor analyzing power A_{yy}, and the vector analyzing power A_y for the reaction $^9\mathrm{Be}(d,p)X$ are measured at an initial deuteron momentum of 4.5 GeV/c and a proton detection angle of about 80 mrad. The data obtained for the differential cross section are consistent with the results of measurements at 3.5 and 5.78 GeV/c and a proton emission angle of 2.5°. The values found for the tensor analyzing power A_{yy} are compared with similar data obtained previously for the deuteron-fragmentation process occurring on a carbon target at various values of the initial deuteron momentum and leading to proton emission at zero angle. The data on the differential cross section for the reaction $^9\mathrm{Be}(d,p)X$ can be satisfactorily described within the relativistic impulse approximation by using standard deuteron wave functions; however, the approach based on this conceptual framework proves to be inadequate in dealing with data on the tensor analyzing power. These results indicate that it is necessary either to change the method for describing the relativistic deuteron or to take into account additional mechanisms.

Contribution of the $\pi\pi$ Component of the σ and ρ Mesons to πN Scattering

A. N. Almaliev, I. V. Kopytin, and M. A. Shikhalev

For elastic πN scattering at a collision energy below the threshold for the production of two pions, dynamical effects are studied that are induced by the presence of a $\pi\pi$ component in the structure of the $\sigma(400-1200)$ and $\rho(770)$ resonances. These effects manifest themselves both in the Green's functions for the σ and ρ mesons and in the form factors for the interaction of these mesons with nucleons. The scattering amplitude is calculated on the basis of the K-matrix formalism, the mechanism of dressing being taken into account in the πNN and $\pi N\Delta$ form factors and in the nucleon and delta-isobar Green's functions. The method of dispersion relations is used to calculate the real parts of the form factors and functions that parametrize self-energy operators. It is shown that, if strong interaction is taken explicitly into account in the $\pi\pi$ system, elastic πN scattering can be described satisfactorily without introducing the σ meson as an elementary particle.

On the Correlation between the Properties of the Deuteron and the Low-Energy Parameters of np Scattering in the Triplet State

V. A. Babenko and N. M. Petrov

The correlation relationship between the asymptotic normalization constant for the deuteron, A_S, and the np scattering length for the triplet case, a_t, is investigated. It is found that 99.7% of the asymptotic constant

1063-7788/03/6603-0582$24.00

A_S is determined by the scattering length a_t. It is shown that the linear correlation relationship between the quantities A_S^{-2} and $1/a_t$ can be successfully used to test the correctness of various models of nucleon–nucleon interaction. It is revealed that, for the normalization constant A_S and for the root-mean-square deuteron radius r_d, the results obtained with the experimental value recommended at present for the triplet scattering length a_t are exaggerated with respect to their experimental counterparts. By using the latest experimental data obtained for phase shifts by the group headed by Arndt, it proved to be possible to derive, for the low-energy parameters of scattering (a_t, r_t, P_t) and for the properties of the deuteron (A_S, r_d), results that comply well with experimental data.

T-Odd Angular Asymmetry in Nuclear Reactions Involving Sequential Particle Emission

A. L. Barabanov, V. E. Bunakov, I. S. Guseva, and G. A. Petrov

A triple T-odd angular correlation in the kinematically similar reactions $^{10}\mathrm{B}(n,\alpha\gamma)$ and $^{233}\mathrm{U}(n,\alpha f)$ induced by cold polarized neutrons is discussed. It is shown that, in the first of these reactions, the triple T-odd correlation in question is suppressed by the double selection rule in parity because of a two-step character of the process; at the same time, T invariance imposes no specific constraints on the magnitude of this correlation. The mechanism of formation of the T-odd correlation that was discovered in ternary-fission processes is closely related, in all probability, to the fact that the nucleus involved disintegrates into two fragments and an alpha particle almost simultaneously.

Production of Ω_{scb} Baryons in e^-e^+ Collisions

S. P. Baranov and V. L. Slad'

The total and differential cross sections for the production of Ω_{scb} baryons in e^-e^+ collisions at the Z-boson pole are calculated.

Elastic Scattering of Alpha-Cluster Nuclei by ^{12}C Nuclei

Yu. A. Berezhnoy and V. P. Mikhailyuk

The differential cross sections for the elastic scattering of ^{12}C and ^{16}O nuclei by ^{12}C nuclei are calculated on the basis of the theory of multiple diffractive scattering and the alpha-cluster model involving dispersion. The calculations were performed by using either an effective or a free amplitude for $\alpha\alpha$ scattering. It is shown that the results obtained in these two cases are noticeably different.

Charm Contribution to the Proton Structure Function in Deep-Inelastic Scattering at the HERA ep Collider

A. V. Berezhnoy, V. V. Kiselev, and A. K. Likhoded

Predictions are obtained for the structure function F_2^c within a charm-production model motivated by perturbative QCD, and the results derived in this way are compared with data obtained by the H1 and ZEUS Collaborations at the HERA collider. It is shown that, for the production of D^* mesons, the spectator mechanism, which is independent of the flavor of the hadronic residue, comes into play for $p_T > 10$ GeV and that, in calculating the cross section for charm production in the kinematical region studied at the HERA collider, it is not necessary to take into account the evolution of the c quark in the initial hadron.

Parameters of the Proton Shell Structure of the ^{40,42,44,46,48}Ca Nuclei and Their Analysis within the Dispersion Optical Model

O. V. Bespalova, I. N. Boboshin, V. V. Varlamov, B. S. Ishkhanov, E. A. Romanovsky, and T. I. Spasskaya

By matching data on proton-stripping and proton-pickup reactions occurring on the same nuclear species, new experimental results for single-particle energies, occupation probabilities, and fragmentation widths of proton states in the vicinity of the Fermi energy are obtained for the even–even isotopes ^{40,42,44,46,48}Ca. These results, along with the experimental values determined in the relevant $(p,2p)$ reaction for the single-particle

energies of deep hole states in ^{40}Ca, are analyzed on the basis of the dispersion-optical-model version proposed in the present study. The results of this analysis are compared with the predictions of different nuclear models, including the relativistic mean-field model.

Measurement of the Total Cross Sections for pp Interaction at Colliders by New Methods

A. A. Bogdanov, A. N. Vasil'ev, S. B. Nurushev, A. Penzo, M. F. Runzo, O. V. Selyugin, and M. N. Strikhanov

A method is proposed for determining the total cross section for pp interaction, $\sigma_T(pp)$, from a measurement of the analyzing power for elastic pp scattering in the region of Coulomb–nuclear interference. Contributions to the uncertainty in determining $\sigma_T(pp)$ that come from various sources, including single-spin-flip interaction, are estimated. The applicability of the quality factor in extracting $\sigma_T(pp)$ from experimental data is briefly discussed. It is concluded that, under specific conditions, the measured analyzing power $A_N(t)$ may provide a workable approach to determining $\sigma_T(pp)$.

Investigation of Logarithmic Contributions in the Electron-to-Muon Mass Ratio to the Shift of Muonium S Levels

N. A. Boikova, S. V. Kleshchevskaya, Yu. N. Tyukhtyaev, and R. N. Faustov

New logarithmic corrections in the mass ratio to the shift of the $1S$ and $2S$ energy levels in the muonium atom are calculated analytically. Corrections of this type that have been obtained so far are discussed and systematized.

Transverse Lepton Polarization Induced in $B \to Dl\nu_l$ Processes by Electromagnetic Final-State Interaction

V. V. Braguta, A. A. Likhoded, and A. E. Chalov

The emergence of transverse lepton polarization in $B^0 \to D^- l^+ \nu_l$ and $B^+ \to \bar{D}^0 l^+ \nu_l$ processes is considered on the basis of the Standard Model in the approximation of heavy-quark effective theory for $l = \tau, \mu$. It is shown that a nonzero transverse lepton polarization appears owing to one-loop electromagnetic final-state interaction. Diagrams involving intermediate D and D^* mesons and making a nonzero contribution to the transverse polarization of the final lepton are analyzed. If only these diagrams are taken into account in the decay processes $B^0 \to D^- \tau^+ \nu_l$ and $B^+ \to \bar{D}^0 \tau^+ \nu_l$, the mean values of the tau-lepton polarization appear to be 2.60×10^{-3} and -1.59×10^{-3}, respectively. In the case of final-state muons, the transverse-polarization values averaged over the Dalitz region are 2.97×10^{-4} and -6.79×10^{-4}.

New Possibilities for Studying N^* on the Basis of an Analysis of Polarization Observables and Angular Distributions off the Scattering Plane in the Reaction $\gamma_v p \to \pi^+ \pi^- p$

V. Burkert, V. I. Mokeev, M. Ripani, M. Anghinolfi, M. Battaglieri, A. A. Boluchevsky, E. N. Golovach, R. De Vita, L. Elouadrini, B. S. Ishkhanov, M. V. Osipenko, N. S. Markov, G. Ricco, M. Taiuti, and G. V. Fedotov

A model for describing the production of charged-pion pairs by photons in the energy region of N^* excitation is further developed for calculating the angular distributions of reaction products off the scattering plane and the polarization asymmetry of the beam used. It is shown that investigation of these observables has rich potential for extracting pioneering data of the Coulomb excitation of N^* and for separating the contributions of various helicity amplitudes to the excitation of N^* by photons.

Measurement of the Coefficient of Forward–Backward Asymmetry in the Reaction $^{35}\mathrm{Cl}(n,p)^{35}\mathrm{S}$ Induced by Resonance Neutrons

V. A. Vesna, Yu. M. Gledenov, I. S. Okunev, A. Aupris, V. I. Salatzky, P. V. Sedyshev, and P. I. Shalan'ski

A P-odd forward–backward correlation is measured for the reaction $^{35}\mathrm{Cl}(n,p)^{35}\mathrm{S}$ induced by a beam of unpolarized resonance neutrons from the IBR-30 pulsed source. For three neutron-energy ranges centered at 3.1, 195, and 398 eV, the values of the coefficient α_{FB} characterizing the forward–backward asymmetry in

question are found to be $(5.3 \pm 7.6) \times 10^{-3}$, $(1.68 \pm 0.50) \times 10^{-1}$, and $-(7.4 \pm 3.6) \times 10^{-3}$, respectively. An estimation of the weak-interaction matrix element and an analysis of the possible values of the amplitudes of the neutronic and protonic widths with respect to channels that are characterized by the total-angular-momentum values of $j = 1/2$ and $3/2$ are performed with allowance for the results of an experiment that employed polarized thermal neutrons to determine a P-odd correlation and a P-even left–right correlation in the reaction being considered.

Discovery of a New Resonance at 2000 MeV in the $K_S K_S$ System

V. V. Vladimirsky, V. K. Grigoriev, I. A. Erofeev, O. N. Erofeeva, A. F. Karelin, Yu. V. Katinov, V. I. Lisin, V. N. Lusin, V. N. Nozdrachev, V. V. Sokolovsky, E. A. Fadeeva, and Yu. P. Shkurenko

This article continues a series of publications devoted to the observation of previously unknown narrow resonances in the $K_S K_S$ system on the basis of experimental data coming from the 6-m spectrometer installed at the Institute of Theoretical and Experimental Physics (ITEP, Moscow). The statistics of K_S-meson pair production were obtained in $\pi^- p$ interactions at 40 GeV by using a neutral trigger. At a mass of about 2000 MeV, a maximum of width not exceeding 15 MeV is observed in the $K_S K_S$ system, the statistical significance of this maximum being not less than five standard deviations. With a high degree of reliability, the spin–parity of this structure is $J^P = 4^+$. This phenomenon may be interpreted as a resonance whose parameters are equal to the above values.

Searches for Self-Consistent Vacuum States of the Gluon Field

V. V. Vladimirsky

A theory of a non-Abelian gauge field that possesses the property of asymptotic freedom is considered on the basis of an effective Lagrangian. In this theory, the confinement–deconfinement phase transition has a nontrivial scenario according to which the two phases may exist in the same spacetime region. In the low-momentum region $|p^2| < \Lambda^2_{\mathrm{QCD}}$, we have a confining regime in the presence of a gluon condensate, while, in the high-momentum region $|p^2| \gg \Lambda^2_{\mathrm{QCD}}$, perturbative QCD holds. An iterative scheme for refining parameters of the effective Lagrangian is outlined.

Features of pC Interactions at a Momentum of 4.2 GeV/c versus the Degree of Centrality of Proton Interaction with a Carbon Nucleus: Multiplicities of Secondary Particles

A. S. Galoyan, E. N. Kladnitskaya, O. V. Rogachevski, R. Togoo, and V. V. Uzhinskii

New experimental data obtained for the multiplicities of charged pions and protons from the interaction of 4.2-GeV/c protons with a carbon nucleus by using the 2-m propane bubble chamber installed at the Laboratory of High Energies at the Joint Institute for Nuclear Research (JINR, Dubna) are presented versus the degree of collision centrality. The parameter Q defined for each individual event as the difference of the total multiplicities of positively and negatively charged particles without allowing for the multiplicity of evaporation protons whose momentum is less than 0.3 GeV/c is taken for a criterion of the degree of collision centrality. It is shown that, with increasing Q, the multiplicity of positively charged pions and the multiplicity of participant protons from the target nucleus grow considerably; concurrently, the multiplicity of negatively charged pions remains at nearly the same level, while the mean multiplicity of evaporation protons decreases sharply. Our experimental data are compared with the results of calculations based on the cascade–evaporation model and the modified FRITIOF model. Within the FRITIOF model, nonnucleon degrees of freedom in nuclei (Δ^+-, Δ^0 isobars) are taken into account for the first time, and the resulting description of the features of secondary particles appears to be by and large satisfactory.

Independent Yields of Kr and Xe Isotopes in the Photofission of Heavy Nuclei

Yu. P. Gangrsky, V. I. Zhemenik, G. V. Myshinsky, N. Yu. Maslova, Yu. E. Penionzhkevich, and O. Selesh

The results obtained by measuring the yields of primary Kr ($A = 87$–93) and Xe ($A = 138$–143) fragments originating from the photofission of ^{232}Th, ^{238}U, and ^{244}Pu nuclei are presented. The experiments were

performed by using bremsstrahlung photons from a microtron at an accelerated-electron energy of 25 MeV. The procedure used involved the transfer of fragments emitted from the target by a gas flow along a capillary and the condensation of Kr and Xe inert gases in a heat bath at liquid-nitrogen temperature. The fragments of all other elements were stopped by a filter at the inlet of the capillary. The isotopes of Kr and Xe were identified by the γ spectra of their daughter products. The mass-number distributions of the independent yields of the isotopes of Kr and Xe were obtained, and these distributions were compared with similar data for fission induced by thermal and fast neutrons. The shifts of the fragment charges with respect to unbiased charge distributions were determined. Prospects for the use of photofission fragments in studying the structure of nuclei that are characterized by a large neutron excess are discussed.

Production of Neutral and Charged Pions in the Reaction $^{12}C(\gamma, \pi p)$ within the Second Resonance Region

I. V. Glavanakov

The results are presented that were obtained by investigating the formation of pion–proton pairs in the reaction $^{12}C(\gamma, \pi p)$. The experiment in question was performed in the second resonance region of photon energy. The results of this measurement are analyzed on the basis of a model that takes into account the processes of single and pair quasifree pion photoproduction.

Small-Scale Anisotropy and Composition of $E_0 \approx 10^{17}$ eV Cosmic Rays according to Data from the Yakutsk Array for Studying Extensive Air Showers

A. V. Glushkov

The results are presented that are obtained from an analysis of the directions of arrival of $E_0 = 10^{16.9-17.2}$ eV cosmic rays that are characterized by zenith angles in the region $\theta \leq 45^\circ$ and which were recorded by the Yakutsk array for studying extensive air showers over the period between 1974 and 2001. It is shown that a significant part of these enter into clusters that have a small-scale cellular structure and which, in all probability, consist of neutral particles having an extragalactic origin.

Scaling Property of Semi-inclusive Events in Proton–Proton Interactions

A. I. Golokhvastov

A normalized single-particle semi-inclusive double-differential spectrum of negatively charged pions from proton–proton interactions at 6.6–400 GeV/c and a relative concentration of neutral pions and K^0_S mesons in such events involving a fixed number of negatively charged pions can be fully characterized by specifying any feature of this spectrum—for example, $\langle y^2 \rangle_n$ or $\langle E \rangle_n$. Thus, the two-parameter set of semi-inclusive events, which depends on energy and multiplicity, reduces to a one-parameter set whose parameter is now dependent on $\sqrt{s}$ and n.

Inversion of $K^\pi = 1^-$ States in the ^{156}Gd and ^{170}Yb Nuclei

E. P. Grigoriev

For the ^{156}Gd and ^{170}Yb nuclei, where the inversion of levels in the $K^\pi = 1^-$ bands is observed, the energies of rotational levels are calculated on the basis of the Coriolis interaction model for the states of two bands whose quantum numbers are $K^\pi = 1^-$ and 0^-. A new $J^\pi K = 3^-0$ level is introduced in ^{170}Yb, and the structure of ^{170}Er is refined. The interaction parameters calculated for six nuclei are considered within the structure predicted by the quasiparticle–phonon model.

Nucleon Structure Functions, Resonance Form Factors, and Duality

V. V. Davidovsky and B. V. Struminsky

The behavior of nucleon structure functions in the resonance region is explored. For form factors that describe resonance production, expressions are obtained that are dependent on the photon virtuality Q^2, which

has a correct threshold behavior, and which take into account available experimental data on resonance decay. Resonance contributions to nucleon structure functions are calculated. The resulting expressions are used to investigate quark–hadron duality in electron–nucleon scattering by taking the example of the structure function F_2.

Application of the Unitarity Conditions to Calculating Interaction Amplitudes for Ramond States in Superstring Theory

G. S. Danilov

The unitary conditions for superstring amplitudes of boson interaction are used to calculate the interaction amplitudes for Ramond states—that is, for 10-spinor states and Ramond bosons. It is shown that, from the unitarity conditions, it follows, among other things, that local quantities specifying the sought amplitudes satisfy some integral relations. The amplitude for the transition of two massless Neveu–Schwarz bosons into a system of two massless Ramond states is obtained in an arbitrary order in the number of loops. For this amplitude, the aforementioned integral relations are verified in the tree approximation.

Structure of the ^{90,94}Zr Nuclei: Global Analysis of Data on Elastic and Inelastic Scattering Alpha Particles by These Nuclear Species and on the Total Cross Sections for Corresponding Interactions

A. D. Duisebaev, K. A. Kuterbekov, I. N. Kukhtina, B. M. Sadykov, L. I. Slusarenko, V. V. Tokarev, and S. A. Fayans†

A global analysis of experimental data on the elastic and inelastic scattering of alpha particles by ^{90,94}Zr nuclei and on the total cross sections for their interaction with these nuclei is performed. The deformation lengths and the neutron-to-proton multipole-matrix-element ratios for the 2_1^+ and 3_1^- states of the ^{90,92,94,96}Zr nuclei are obtained for various projectile species, and a comparative analysis of these quantities is performed. With the aim of revealing the origin of the phase shifts found in the present study, experimental data on the inelastic scattering of 35.4-, 40.0-, 50.1-, and 65.0-MeV alpha particles on ^{90,94}Zr nuclei are analyzed on the basis of a unified approach.

Instanton Liquid at a Finite Density of Quark Matter

G. M. Zinovjev and S. V. Molodtsov

For the case of finite quark and baryon densities, the interaction of light quarks with an instanton liquid is considered in a phase that involves a nonvanishing chiral condensate. The generating functional is analyzed in the tadpole approximation, and the behavior of the dynamical quark mass and the behavior of the chiral condensate, as well as the behavior of the instanton-liquid (gluon-condensate) density, which grows slightly with the quark chemical potential, are explored. Arguments are presented in favor of the statement that the quark-density threshold for the emergence of a diquark condensate grows sizably owing to interaction with the instanton liquid.

Diquark Condensate and Quark Interaction with an Instanton Liquid

G. M. Zinovjev and S. V. Molodtsov

The interaction of light quarks with an instanton liquid is considered at nonzero quark- and baryon-matter densities in a phase where the chiral condensate is nonzero. It is shown that, the inclusion of the relevant perturbation of the instanton liquid leads to an increase in the quark chemical potential μ_c. This in turn induces a considerable growth of the threshold quark-matter density at which one expects the emergence of color superconductivity.

Processes of Heavy-Quark Production in Proton–Antiproton Interactions and Nonintegrated Gluon Distributions

N. P. Zotov, A. V. Lipatov, and V. A. Saleev

The inclusive production of heavy quarks (c and b) in proton–antiproton interactions at high energies is considered within a semihard approach inspired by QCD. The heavy-quark cross section $\sigma(\mathbf{p}_T > \mathbf{p}_T^{\min})$ is investigated as a function of nonintegrated gluon distributions. Our theoretical results are compared with experimental data obtained by the D0 and CDF collaborations at the TEVATRON collider.

Electroproduction of J/ψ Mesons within the Semihard QCD Approach and within the Color-Singlet Model

N. P. Zotov and A. V. Lipatov

The deep-inelastic production of J/ψ mesons in electron–proton interactions at the HERA collider is considered within the semihard (k_T-factorization) approach inspired by QCD and within the color-singlet model. The dependence of the Q^2, $\mathbf{p}_T^2$, z, y^*, and W distributions of J/ψ mesons on various sets of nonintegrated gluon distributions and the dependence of the spin parameter α on $\mathbf{p}_T^2$ and Q^2 are investigated. The results of the calculations are compared with the latest experimental data obtained by the H1 and ZEUS collaborations at the HERA collider. It is shown that experimental investigations of the polarization properties of J/ψ mesons over the kinematical region $Q^2 < 1$ GeV^2 may provide an additional test of the statement that the dynamics of gluon distributions is governed by the Balitsky–Fadin–Kuraev–Lipatov equations.

Radiative Corrections to Observables in the Production of W Bosons in Polarized-Hadron Collisions

V. A. Zykunov

A scheme is proposed for studying the nucleon spin with the aid of observables in the production of single W bosons in hadron–hadron collisions. Special attention is given to determining the distributions of polarized quarks in the low-x region. Lowest order electroweak radiative corrections to observables are calculated. For the conditions of future experiments at the RHIC collider, the relevant cross sections and single and double asymmetries are estimated numerically with allowance for radiative corrections.

Photofission Accompanied by Pion Emission

A. S. Iljinov and L. N. Latysheva

The main features of the channel in which the nuclear-fission process induced by photons of energy in the range $150 < \mathrm{E}_\gamma < 600$ MeV is accompanied by pion emission are predicted on the basis of the cascade–evaporation–fission model. Specifically, predictions are obtained for the total cross section; the angular and differential distributions of pions; the excitation-energy, mass-number, and charge-number distributions of compound nuclei; and the mass distribution of fission fragments. For primary energies in the above range, these features of the channel in question are compared for the nuclear-fission process induced by photons and by protons.

Coulomb Breakup of Light Nuclei in the Field of a Heavy Ion at Relativistic Collision Energies

B. F. Irgaziev, Sh. Kalandarov, and A. M. Mukhamedzhanov

A simple method for calculating the amplitude and the cross section for the Coulomb breakup of a light nucleus into two fragments in the field of a heavy ion at relativistic collision energies is proposed on the basis of time-dependent perturbation theory. It is shown that the resulting amplitude for the process in question has a correct nonrelativistic limit. The contribution of the longitudinal component of the Coulomb field of a heavy ion tends to zero in the ultrarelativistic limit. A specific implementation of the method is demonstrated by taking the example of the Coulomb breakup reaction $^{208}\mathrm{Pb}(^8\mathrm{B}, ^7\mathrm{Be}p)^{208}\mathrm{Pb}$ at various collision energies. The results are found to be in agreement with experimental data.

(p, n) Charge-Exchange Reaction on ^{48}Ca as a Means for Determining the Isospin Structure of the Mean Spin–Orbit Nuclear Field

V. I. Isakov

The isotopic dependence of spin–orbit splittings, which was discovered previously in the spectra of heavy nuclei that are close to doubly magic ones, is tested in polarization effects that arise in (p, n) charge-exchange reactions between isobaric states of $A = 48$ nuclei.

Semimicroscopic Description of the Gross Structure of the Giant Dipole Resonance in Light Nonmagic Nuclei

B. S. Ishkhanov and V. N. Orlin

A simple model is formulated that makes it possible to describe the configuration and deformation splittings of the giant dipole resonance in light nonmagic nuclei. The gross structure of the cross sections for photoabsorption on ^{12}C, ^{24}Mg, and ^{28}Si nuclei is described on the basis of this model.

Parity Nonconservation in Binary and Ternary Nuclear Fission Induced by Polarized Neutrons

S. G. Kadmensky

Within the quantum-mechanical theory of the nuclear-fission process, the conditions of the emergence of coherent effects in the angular distributions of fragments originating from the binary and ternary fission of polarized nuclei are analyzed with allowance for the properties of transition fission states. The coefficients of P-odd asymmetry in the angular distributions of a light particle and a third particle, which is taken here to be an alpha particle, are calculated under the assumption that the third particle and two fragments are produced through the one step mechanism. In order to confirm the ideas developed here, it is proposed to repeat, at a higher level of statistical accuracy, experiments devoted to seeking P-odd asymmetries for alpha particles in the ternary fission of nuclei.

Unitary Scalar–Vector Mixing in the ξ Gauge

A. E. Kaloshin and A. E. Radzhabov

The effect of the unitary mixing of scalar and vector fields is considered in the ξ gauge. For this effect to emerge, it is necessary that the vector current not be conserved; in the ξ gauge, there arise additional complications because of the presence of an unphysical scalar field. Solutions to the Dyson–Schwinger equations are obtained, and the renormalization of complete propagators is investigated. The use of the Ward identity, which relates a few different Green's functions, is a key point in performing this renormalization. It is shown that the dependence on the gauge parameter ξ disappears in the renormalized matrix element.

Internal Conversion in Hydrogen-like Ions

F. F. Karpeshin, Yu. N. Novikov, and M. B. Trzhaskovskaya

The probability of internal gamma-ray conversion is theoretically investigated for hydrogen-like ions versus the corresponding neutral atoms. The relevant calculations are performed by the relativistic Dirac–Fock method. The results reveal that the effect of multiple ionization on the coefficients of internal conversion in the K shell is maximal near the ionization threshold and for transitions of high multipole order, where the effect can be as great as a few orders of magnitude. The distinction decreases with increasing transition energy, but it remains sizable for transitions of practical importance. It is found that the ionization of an atom to a hydrogen-like ion with allowance for convergence in external atomic shells may change significantly (by up to eight orders of magnitude) the lifetime of the nucleus being considered. The predicted effects can be observed in experiments with beams of relativistic heavy ions.

Inelastic Scattering of Antineutrinos from a Tritium Source on the Atomic Electrons of Germanium

V. I. Kopeikin, L. A. Mikaelyan, and V. V. Sinev

The inelastic magnetic and weak scattering of antineutrinos generated by a tritium beta source on the bound electrons of a germanium atom is considered. The results obtained by calculating the spectra and cross sections are presented for the energy-transfer range between 10 eV and 18 keV.

Thermonuclear Fusion in the Irradiation of Large Clusters of Deuterium Iodide with a Field of a Superatomic Femtosecond Laser Pulse

V. P. Krainov and M. B. Smirnov

A theory of thermonuclear fusion caused by the irradiation of deuterium-iodide clusters with the field of a superatomic femtosecond laser pulse is developed. It is based on considering the process in which the sequential above-barrier multiple internal ionization of atomic ions within a cluster is accompanied by external field ionization. The theory is illustrated by taking the example of a cluster that is formed by 10^6 molecules of deuterium iodide and which is irradiated with a laser pulse of duration 50 fs and intensity 2×10^{18} W/cm^2 at the peak. This case is dominated by I^{26+} atomic ions. The yield of neutrons from thermonuclear fusion in a deuteron–deuteron collision upon the passage of a laser pulse is calculated. The result is 10^5 neutrons per laser pulse. The mean kinetic energy of deuterons is estimated at 50 keV. Owing to induced inverse bremsstrahlung in scattering on multiply charged atomic ions, the electron temperature increases up to 28 keV. The role of the Mie resonance in the heating of the electron component is discussed.

Cancellation of Divergences in Rare Processes

V. I. Kuksa

The structure of divergences in effective vertices that generate flavor-changing neutral currents is considered. For the simplest examples, it is shown that divergences are completely canceled in rare processes governed by such vertices. Methodological facets of the cancellation and renormalization process are discussed.

Angular Correlations in the Decays of Two Unstable Identical Particles Having Close Momenta

P. Lednicki, V. V. Lyuboshitz, and V. L. Lyuboshitz

Angular correlations between the momenta of products originating from the decays of two identical particles that have close momenta are considered on the basis of the model of independent single-particle sources emitting unstable unpolarized particles of nonzero spin. These correlations reflect spin correlations that are caused by quantum-statistics and final-state-interaction effects. A general theory of angular correlations in the decays of two arbitrarily polarized particles (resonances) is constructed.

One-Loop Corrections of Orders $(Z\alpha)^6 m_1/m_2$ and $(Z\alpha)^7$ to the Muonium Fine Structure

A. P. Martynenko and R. N. Faustov

Corrections of orders $(Z\alpha)^6 m_1/m_2$ and $(Z\alpha)^7$ from one-loop two-photon amplitudes to the energy spectra of hydrogen-like atoms are calculated by expanding the relevant integrand in a Taylor series. A method for averaging the resulting quasipotential in the d-dimensional coordinate representation is formulated. Numerical values are obtained for the contributions to the muonium, hydrogen-atom, and positronium fine structure.

Helicity Components of the Cross Section for the Production of Charged-Pion Pairs on a Proton by Real Photons

V. I. Mokeev, M. Ripani, M. Anghinolfi, M. Battaglieri, R. De Vita, E. N. Golovach, B. S. Ishkhanov, N. S. Markov, M. B. Osipenko, G. Ricco, V. V. Sapunenko, M. Taiuti, and G. V. Fedotov

Within the phenomenological approach developed previously to describe pion-pair production on a nucleus by photons, the helicity cross-section components $\sigma_{1/2,3/2}$ are calculated for this exclusive channel. It is shown that the asymmetry $\sigma_{1/2}-\sigma_{3/2}$ is highly sensitive to the contributions of nucleon resonances whose electromagnetic helicity amplitudes $A_{1/2}$ and $A_{3/2}$ are strongly different. This feature is of importance for seeking "missing" baryon states.

Nuclear Composition of 1- to 20-PeV Primary Cosmic Rays according to Lateral Features of the Electron–Photon Component of All Extensive Air Showers and of Extensive Air Showers Accompanying High-Energy Gamma Rays and Hadrons in X-Ray Emulsion Chambers at the Tien Shan Level

N. M. Nesterova, V. P. Pavlyuchenko, A. P. Chubenko, and S. B. Shaulov

Data from the Tien Shan Hadron array on the dependence of the lateral distributions of the electron–photon component (age parameter S) in extensive air showers of cosmic rays on the number of electrons, N_e, which is a quantity that characterizes the primary-nucleus energy E_0, are subjected to a comparative analysis. The distributions in question are given both for all showers and for showers accompanying high-energy gamma rays and hadrons in x-ray emulsion chambers. According to calculations, events associated with the latter are generated predominantly by primary protons, and this makes it possible to assess their role at various values of E_0. The distributions with respect to S suggest a significant fraction of light nuclei, predominantly protons, in the region after the knee in the spectrum for $N_e > 10^6$, at least up to $N_e = 5.6 \times 10^6$ ($E_0 \sim 10$ PeV).

Effects of Four-Fermion Contact Interactions in the Bhabha Process at Linear e^+e^- Colliders

A. A. Pankov

Effects induced by four-fermion contact interactions in the process $e^+e^- \to e^+e^-$ at linear e^+e^- colliders of energy in the range $\sqrt{s} = 0.5$–1 TeV are investigated for the case of longitudinally polarized initial beams. Model-independent constraints on the parameters of four-fermion contact interactions are obtained. It is shown that the sensitivity of the Bhabha process to the parameters of four-fermion contact interactions featuring off-diagonal helicity indices (LR) is significantly higher than the corresponding sensitivity of the leptonic process $e^+e^- \to \mu^+\mu^-$, but that their counterparts for interactions featuring diagonal helicity indices (RR and LL) are close in magnitude.

Contributions of Scalar Leptoquarks to the Cross Sections for the Production of Quark–Antiquark Pairs in e^+e^- Annihilation

A. V. Povarov and A. D. Smirnov

The contributions of scalar-leptoquark doublets to the cross sections $\sigma_{Q\tilde{Q}'}$ for the production of quark–antiquark pairs in e^+e^- annihilation are calculated within the minimal model based on the four-color symmetry of quarks and leptons. These contributions are analyzed versus the scalar-leptoquark masses and the mixing parameters of the model at colliding-particle energies in the range 250–1000 GeV. It is shown that the contributions in question are of greatest importance for processes leading to t-quark production. In particular, it is found that, with allowance for the contribution of the scalar leptoquark of charge 5/3 and mass in the range 250–500 GeV, the cross section $\sigma_{t\tilde{t}}$ calculated at a mixing-parameter value of $k_t \sim 1$ may be severalfold larger than the corresponding cross section $\sigma_{t\tilde{t}}^{(\mathrm{SM})}$ within the Standard Model. The possibility of setting constraints on the scalar-leptoquark masses and on the mixing parameters by measuring such contributions at future e^+e^- colliders is indicated.

Effective Probabilities in a New Approach to Analyzing Angular Distributions in Elastic Heavy-Ion Scattering

Yu. A. Pozdnyakov

A new approach proposed previously to analyze angular distributions in elastic heavy-ion scattering is generalized to cases where total partial probabilities (that is, those that are summed over all channels) of the enhancement of fusion (in general, complete and incomplete fusion, quasifission, and deep-inelastic-scattering reactions) are commensurate with the total partial probabilities of the suppression of fusion. This could be done with the aid of effective total partial probabilities, each of these being defined as a linear combination of actual total partial probabilities. It is shown that the probabilities introduced in this way have a specific physical meaning. Indeed, the effective total partial probabilities make it possible to compute the cross section for fusion through the input channel and some reference total cross sections for peripheral processes, and a conclusion on whether fusion and peripheral reactions are enhanced or suppressed can be drawn from a comparison of the calculated or measured results for, respectively, the fusion cross section and the total cross section for peripheral reactions with the above two cross sections. It is also found that the enhancement of fusion is accompanied by the suppression of peripheral reactions, and vice versa.

Elastic Scattering of a Deuteron on a Deuteron and Reaction Involving the Flip of Their Spins and Isospins into a Singlet versus the Predictions of the Supermultiplet Potential Model for Cluster Interaction

B. G. Struzhko, V. M. Lebedev, and V. G. Neudatchin

A brief survey of experimental results on elastic deuteron–deuteron scattering is given. Data from an experiment performed at the Institute for Nuclear Research (National Academy of Sciences of Ukraine, Kiev) at $E_{\text{c.m.}} = 23.4$ and 25.0 MeV and data from the literature at $E_{\text{c.m.}} = 11.6$ MeV are used to analyze the reaction involving the flip of the spins and isospins of two dinucleons into a singlet, $d + d \to d_s + d_s$ or $(pp)_s + (nn)_s$. Two-dimensional coincidence spectra of protons from the reaction $d + d \to p + p + n + n$ are simulated with allowance for dominant quasibinary processes, including quasifree proton scattering and final-state nucleon–nucleon interaction. It is concluded that this reaction is dominated by the mechanism involving the double flip of the spin and isospin. The differential cross sections $d\sigma/d\Omega$ for the reaction $^2H(d, d_s)d_s$ at $E_{\text{c.m.}} = 23.4$ MeV and the reaction $^2\text{H}(d, (pp)_s)(nn)_s$ at $E_{\text{c.m.}} = 11.6$ MeV are determined. The elastic-scattering cross sections and the cross sections for spin-flip reactions leading to the formation of a singlet ground state are compared with the results of the supermultiplet potential model where the interaction between clusters A and B is described by a potential $V^{[f]}(R)$ ($[f]$ is an orbital Young diagram). The theory faithfully reproduces experimental results, but data on the flip of the spins and isospins of two deuterons are scanty (it is desirable to supplement them).

Resonances in the $K_SK_SK_L$ System Formed in Collisions of Negatively Charged Pions with a Carbon Target at a Momentum of 40 GeV

G. D. Tikhomirov, I. A. Erofeev, O. N. Erofeeva, and V. N. Lusin

The experimental spectrum of the $K_SK_SK_L$ system from the reaction $\pi^-\text{C} \to K_SK_SK_L + Y$ at a momentum of 40 GeV was obtained experimentally with the aim of studying resonance states featuring open strangeness and occurring in the high-mass region. The experiment was performed at the 6-m spectrometer installed at the Institute of Experimental and Theoretical Physics (ITEP, Moscow). The spectrum displays, along with well-known resonances [$K_1(1640)$, $K_2(1770)$, $K_2(1820)$, $K_2(1980)$], which fit in the quark–antiquark classification, the exotic resonances $K_2(2280)$ and $K_4(2500)$. The $K_2(2280)$ resonance shows the properties of a hybrid and has an exotic decay mode producing a triplet of known resonance states related to each other by quark–gluon mixing. The mechanism of the formation of the observed hybrid $K_2(2280)$ is dominated by the exchange of a natural spin–parity in the t channel of the reaction. The mode of decay into $f_0(980)K_L$ and the mode of decay into $f_2(1270)K_L$ are observed for the $K_2(1770)$ and the $K_2(1980)$ resonance, respectively.

Spectrum of ^{10}Be in the Approximation of the Leading Irreducible Representation of the $SU(3)$ Group

G. F. Filippov, K. Kato, S. V. Korennov, and Yu. A. Lashko

The algorithm realizing the approximation that employs the leading irreducible representation of the $SU(3)$ group is expounded for a microscopic Hamiltonian involving the potential energy of nucleon–nucleon interaction. An effective Hamiltonian is constructed that reproduces the results of the calculations with nucleon–nucleon potentials used in the theory of light nuclei. It is shown that, in many respects, the structure of the effective Hamiltonian is similar to the structure of the Hamiltonian of a triaxial rotor and that the wave functions in the Elliott scheme can be transformed to a space where linear combinations of Wigner D functions appear to be their images, but where their normalization requires dedicated calculations.

Investigation of the Yields of Fragments of ^{239}U Fission at Anomalously High Values of the Total Kinetic Energy

V. A. Khryachkov, M. V. Dunaev, I. V. Dunaeva, N. N. Semenova, and A. I. Sergachev

The yields of fragments originating from ^{238}U fission induced by 5-MeV neutrons are investigated. The accumulated statistics of 2.5×10^6 binary-fission events make it possible to study the yields of fragments at anomalously high values of the total kinetic energy. The spectra of the cold fragmentation of ^{239}U are obtained. Events characterized by a total kinetic energy equal to the total reaction energy are observed for some fragment masses. Computer-treatment methods make it possible to identify these rare events with a high reliability. It is proposed to interpret the observed phenomenon on the basis of the liquid-drop model of the fission process.

Fermion Production and Correlations Due to a Time Variation of the Effective Mass

I. V. Andreev

Fermion production due to a time variation of the effective mass is considered. Diagonal polarization states are found to be definite helicity states. The strength of the production process, as well as specific fermion–antifermion correlations, is calculated. The production of fermion–antifermion pairs and the relative two-particle correlations appear to be large for a sharp and significant change in the mass depending also on fermion occupancy in the initial state.

Two-Photon Partial Widths of Tensor Mesons

A. V. Anisovich, V. V. Anisovich, M. A. Matveev, and V. A. Nikonov

We calculate partial widths of the $\gamma\gamma$ decay of the tensor $q\bar{q}$ states $a_2(1320)$, $f_2(1270)$, and $f_2(1525)$; their radial excitations $a_2(1660)$, $f_2(1640)$, and $f_2(1800)$; and $^3F_2 q\bar{q}$ states. Calculations are performed in the framework of the same approach as that used before to study the radiative decays $f_0(980) \to \gamma\gamma$, $a_0(980) \to \gamma\gamma$, and $\phi(1020) \to \gamma f_0(980)$: the assumption made is that of the $q\bar{q}$ structure of $f_0(980)$ and $a_0(980)$. The description of the decay partial widths for $a_2(1320)$, $f_2(1270)$, $f_2(1525)$ $f_0(980)$, and $a_0(980)$ is reached with the approximately equal radial wave functions, thus giving a strong argument in favor of the fact that these scalar and tensor mesons are to be classified as members of the same P-wave $q\bar{q}$ multiplet.

Quark–Gluonium Content of the Scalar–Isoscalar States $f_0(980)$, $f_0(1300)$, $f_0(1500)$, $f_0(1750)$, and $f_0(1420^{+150}_{-70})$ from Hadronic Decays

V. V. Anisovich, V. A. Nikonov, and A. V. Sarantsev

On the basis of the decay couplings $f_0 \to \pi\pi, K\bar{K}, \eta\eta, \eta\eta'$, which were found before, in the study of analytic ($IJ^{PC} = 00^{++}$) amplitude in the mass range 450–1900 MeV, we analyze the quark–gluonium content of the resonances $f_0(980)$, $f_0(1300)$, $f_0(1500)$, and $f_0(1750)$ and the broad state $f_0(1420^{+150}_{-70})$. The K-matrix technique used in the analysis makes it possible to evaluate the quark–gluonium content both for the states with switched-off decay channels (bare states, f_0^{bare}) and the real resonances. We observe a significant change in the quark–gluonium composition in the evolution from bare states to real resonances, which is due to the

mixing of states in the transitions $f_0(m_1) \to$ real mesons $\to f_0(m_2)$ responsible for the decay processes as well. For $f_0(980)$, the analysis confirmed the dominance of $q\bar{q}$ component, thus proving the $n\bar{n}/s\bar{s}$ composition found in the study of the radiative decays. For the mesons $f_0(1300)$, $f_0(1500)$, and $f_0(1750)$, the hadronic decays do not allow one to determine uniquely the $n\bar{n}$, $s\bar{s}$, and gluonium components, providing relative percentage only. The analysis shows that the broad state $f_0(1420^{+150}_{-70})$ can mix with the flavor singlet $q\bar{q}$ component only, which is consistent with gluonium origin of the broad resonance.

Process $\pi p \to \pi\pi N$ at High Energies and Moderate Momenta Transfers to the Nucleon and Determination of Parameters of $f_0(980)$ and $f_0(1300)$

V. V. Anisovich and A. V. Sarantsev

We present the results of a simultaneous analysis of the S-wave $\pi\pi$ spectra in the reactions $\pi^- p \to (\pi\pi)_S n$ at $p_{\rm lab} = 38$ GeV/c (GAMS) and $\pi^- p \to (\pi\pi)_S n$ at $p_{\rm lab} = 18$ GeV/c (E852 collaboration) at moderate momenta transfers to the nucleon, $|t| \lesssim 1.5$ (GeV/c)^2. The t distributions are described by the Reggeized π and a_1 exchanges provided by the leading and daughter trajectories, while the $M_{\pi\pi}$ spectra are determined by a set of scalar–isoscalar resonances. With $M_{\pi\pi}$ distributions averaged over different t intervals, we found several solutions given by different t-channel-exchange mechanisms at $|t| \sim 0.5$–1.5 (GeV/c)^2, with resonance parameters close to each other. We conclude that despite poor knowledge of the structure of the t exchange, the characteristics of resonances, such as masses and widths, can be reliably determined by using the processes under discussion. As to pole positions, we found $(1031 \pm 10) - i(35 \pm 6)$ MeV for $f_0(980)$ and $(1315 \pm 20) - i(150 \pm 30)$ MeV for $f_0(1300)$.

Wavelet Analysis of Data in Particle Physics: Vector Mesons in e^+e^- Annihilation

T. S. Belozerova, V. K. Henner, and P. G. Frick

We demonstrate the advantages provided by the wavelet analysis (WA) for resolving the structures in experimental data. Due to good scaling properties of the wavelets, one can consider the data with various resolution which allows one to separate the resonances from noise and from each other. The WA is much less sensitive to the noise than any other analysis and allows a substantial reduction of the role of statistical errors. We apply the WA to the e^+e^- annihilation into hadron states with quantum numbers of ρ and ω mesons and to p wave $\pi\pi$ scattering. Distinguishing the resonance structures from experimental noise and the background allows us to draw a more reliable conclusion about the ρ' and ω' states. Then, in order to obtain the parameters of ω' mesons, they are analyzed with a multichannel method belonging to the Breit–Wigner type and preserving unitarity in the case of overlapping resonances. We also apply the WA to the ratio $R_{e^+e^-}$.

Toward Thermodynamic Consistency of the Quasiparticle Picture

T. S. Biró, A. A. Shanenko, and V. D. Toneev

The purpose of the present article is to call attention to some realistic quasiparticle-based description of quark–gluon matter and its consistent implementation in thermodynamics. A simple and transparent representation of thermodynamic consistency conditions is given. This representation allows one to review critically and systematize available phenomenological approaches to the deconfinement problem with respect to their thermodynamic consistency. Particular attention is paid to the development of a method for treating the string screening in the dense matter of unbound color charges. The proposed method yields an integrable effective pair potential that can be incorporated into the mean-field picture. The results of its application are in reasonable agreement with lattice data on QCD thermodynamics.

CP Violation in $K_{S,L} \to \pi^+\pi^-\gamma$ and $K_{S,L} \to \pi^+\pi^- e^+e^-$ Decays

S. S. Bulanov

The dependence of $K_{S,L} \to \pi^+\pi^-\gamma$ decay probabilities on photon polarization is calculated. The phases of terms of amplitude that arise from the pion–pion interaction are obtained by using a simple realistic model

of pion–pion interaction via a virtual ρ meson, instead of chiral perturbation theory (ChPT). The results are compared with those of other authors and the origin of the discrepancies is explained. It is shown that the standard ChPT approach for $K_{S,L} \to \pi^+\pi^-\gamma$ decays cannot reproduce the contribution of the ρ meson to the P-wave $\pi\pi$ interaction. The deviation of the photon spectrum from pure bremsstrahlung due to the pion-loop contribution to the direct emission amplitude is calculated. It is shown that the interference between the terms of the amplitude with different CP parity appears only when the photon is polarized (linearly or circularly). Instead of measuring the linear polarization, one can study the angular correlation between the $\pi^+\pi^-$ and e^+e^- planes in the decay $K_{S,L} \to \pi^+\pi^-e^+e^-$.

Transition Form Factors and Light-Cone Distribution Amplitudes of Pseudoscalar Mesons in the Chiral Quark Model

A. E. Dorokhov, M. K. Volkov, and V. L. Yudichev

It is shown that a chiral quark model of the Nambu–Jona-Lasinio type can be used to describe "soft"-momentum parts of the amplitudes with a high momentum transfer. As a sample, the process $\gamma^* \to \gamma(\pi, \eta, \eta')$ where one of the photons, γ^*, has large spacelike virtuality is investigated. The $\gamma^* \to \gamma(\pi, \eta, \eta')$ transition form factors are calculated for a wide region of momentum transfers. The results are consistent with the calculations performed in the instanton-induced chiral quark model and agree with experimental data. The distribution amplitudes of pseudoscalar mesons are derived. Our calculations show that effective chiral quark models can be safely applied to the description of the processes with a high momentum transfer.

Tunneling between Asymmetric Potential Wells and Mixing of Normal and Superdeformed Nuclear Bands

A. Ya. Dzyublik

The equation for the nuclear deformational motion in an asymmetric potential with two minima is solved semiclassically by analogy with the familiar symmetric case. Taking into account the tunneling, we obtained formulas for the energies and wave functions similar to those that were previously derived for the two-band mixing. It enabled us to interpret the mixing of closely lying levels of normal and superdeformed rotational bands in ^{133}Nd as a manifestation of tunneling. In addition, the mixing of superdeformed levels with N normal configurations is analyzed in the framework of the theory of overlapping resonance levels.

Magnetic Black Holes with String-Loop Corrections

M. Z. Iofa

String-loop corrections to magnetic black holes are studied. The 4D effective action is obtained by compactification of heterotic string theory on the manifold $K3 \times T^2$ or on a suitable orbifold yielding $N = 1$ supersymmetry in 6D. In the resulting 4D theory with $N = 2$ local supersymmetry, the prepotential receives only one-string-loop perturbative correction. The loop-corrected black hole is obtained in two approaches: (i) by solving the system of the Einstein–Maxwell equations of motion derived from the loop-corrected effective action and (ii) by solving the system of spinor Killing equations (conditions for the supersymmetry variations of the fermions to vanish) and Maxwell equations. We consider a particular tree-level solution with the magnetic charges adjusted so that the moduli connected with the metric of the internal two-torus are constant. In this case, the loop correction to the prepotential is independent of coordinates, and it is possible to solve the system of the Einstein–Maxwell and spinor Killing equations in the first order in string coupling analytically. The set of the supersymmetric solutions of the loop-corrected spinor Killing equations is contained in a larger set of solutions of the equations of motion derived from the string-loop-corrected effective action. Loop corrections to the metric and dilaton are large at short distances from the center of the black hole.

Analysis of the Densities of s-Wave Neutron Resonances Separated with Respect to Spin

M. Kaczmarczyk

The density ratio of s-wave neutron resonances $z = \rho(J_1)/\rho(J_2)$ was analyzed on the basis of the experimental data for 22 nuclei and the Gilbert–Cameron formula for $\rho(J)$. Here, $J_1 = I_x - 1/2$ and $J_2 = I_x + 1/2$,

where I_x denotes the spin of the target nucleus in the ground state. Our aim was to verify whether the factor $\eta(I_x)$, as a multiplier, can be applied in the expression describing $\rho(J_1)$, with the assumption that $\rho(J_2)$ values stay unchanged or whether the factor $1/\eta(I_x)$ can be applied, as a multiplier with $\rho(J_2)$, while the $\rho(J_1)$ values stay unchanged. The final conclusions, e.g., the confirmation or the negation of the fact that it may be necessary to apply the $\eta(I_x)$ factor, depend on the values of "real" errors Δz of the z variable, which can be calculated if the optimal values of $\Delta\rho(J_1)$ and $\Delta\rho(J_2)$ are known. The requirement that the function $\eta(I_x)$ be introduced as a multiplier into, for example, the equation that describes $\rho(J_1)$ can be well founded only in the case where the "real" values of Δz are enclosed within the interval delimited by the values Δz corresponding to the two cases that are analyzed and which deal with the ways of the calculation of the errors $\Delta\rho(J_1)$ and $\Delta\rho(J_2)$.

Hybrid Adiabatic Potentials in the QCD String Model

Yu. S. Kalashnikova and D. S. Kuzmenko

The short- and intermediate-distance behavior of the hybrid adiabatic potentials is calculated in the framework of the QCD string model. The calculations are performed with the inclusion of a Coulomb force. A spin-dependent force and a so-called string correction term are treated as perturbation in the leading potential-type regime. Reasonably good agreement with lattice measurements takes place for adiabatic curves excited with magnetic components of field-strength correlatior functions.

Thermal Multifragmentation of Hot Nuclei and Liquid–Fog Phase Transition

V. A. Karnaukhov, S. P. Avdeyev, E. V. Duginova, L. A. Petrov†, V. K. Rodionov, H. Oeschler, A. Budzanowski, W. Karcz, M. Janicki, O. V. Bochkarev, E. A. Kuzmin, L. V. Chulkov, E. Norbeck, and A. S. Botvina

Multiple emission of intermediate-mass fragments (IMF) in the collisions of protons (up to 8.1 GeV), ^{4}He (4 and 14.6 GeV), and ^{12}C (22.4 GeV) with Au is studied with the 4π setup FASA. In all cases, the hot and diluted target spectator undergoes thermal multifragmentation. The fragment multiplicity and charge distributions are well described by the combined model including the modified intranuclear cascade followed by the statistical multibody decay of the hot system. An IMF–IMF correlation study supports this picture, giving a very short time scale of the process ($\leq$70 fm/c). This decay process can be interpreted as the first-order nuclear "liquid–fog" phase transition inside the spinodal region. The evolution of the mechanism of thermal multifragmentation with increasing projectile mass is investigated. The onset of the radial collective flow is observed for heavier projectiles. The analysis reveals information on the fragment space distribution inside the breakup volume: heavier IMF are formed predominantly in the interior of the fragmenting nucleus, possibly due to the density gradient.

Electromagnetic Transition Form Factors for the Weak Dilepton Decay $\Lambda \to ne^+e^-$

B. V. Martemyanov

In general, the weak radiative decay $\Lambda \to ne^+e^-$ depends on four independent electromagnetic transition form factors. These form factors can be fixed within the extended vector-meson-dominance model, where the asymptotic behavior of the form factors is in agreement with quark counting rules. The dependence of the branching ratio for the decay $\Lambda \to ne^+e^-$ on the relative weights of four electromagnetic form factors is investigated.

Uncertainty of the Two-Loop Renormalization-Group Upper Bound on the Higgs Mass

Yu. F. Pirogov and O. V. Zenin

A modified criterion of perturbative consistency within the Standard Model (SM) is proposed. It is based on the analytic properties of the two-loop SM running couplings. Under the criterion adopted, the Higgs mass up to 380 GeV might not give rise to the strong coupling prior to the Planck scale. This means that the light Higgs boson is possibly preferred for reasons other than the SM perturbative consistency, i.e., for reasons beyond the SM.

Muon Anomalous Magnetic Moment: A Consistency Check for the Next-to-Leading-Order Hadronic Contributions

A. A. Pivovarov

A duality-inspired model for verifying a consistency of the evaluation of the next-to-leading-order hadronic contributions to the muon anomalous magnetic moment with that of the leading order ones is proposed. Some of the next-to-leading-order hadronic contributions related to the photon vacuum polarization function are rather accurately reproduced in the model. A new numerical value is found for the light-by-light hadronic contribution that leads to the agreement of the Standard Model prediction for the muon anomalous magnetic moment with the recent experimental result.

Renormalization-Group Summation, Spectrality Constraints, and Analyticity of the Coupling Constant for Phenomenological Applications of Two-Point Correlation Functions in QCD

A. A. Pivovarov

Analytic structure in the strong coupling constant that emerges for some observables in QCD after duality averaging of renormalization-group-improved amplitudes is discussed, and the validity of the infrared renormalon hypothesis for the determination of this structure is critically reexamined. A consistent description of peculiar features of perturbation-theory series related to hypothetical infrared renormalons and corresponding power-law corrections is considered. It is shown that perturbation-theory series for the spectral moments of two-point correlation for hadronic currents in QCD can explicitly be summed in all orders by using the definition of the moments that avoids integration through the infrared region in momentum space. Such a definition of the moments relies on the analytic properties of two-point correlation functions in the momentum variable that allows for shifting the integration contour into the complex plane of momentum. For the sake of definiteness, an explicit case of gluonic-current correlation functions is discussed in detail.

On the Fermi and Gamow–Teller Strength Distribution in Medium-Heavy Mass Nuclei

V. A. Rodin and M. H. Urin

An isospin-self-consistent approach based on the random phase approximation with allowance for a continuum (CRPA) is used to describe the Fermi and Gamow–Teller strength distributions within a wide excitation-energy interval. To take into account nucleon pairing in open-shell nuclei, we formulate an isospin-self-consistent version of the pn-quasiparticle CRPA (pn-QCRPA) approach by incorporating the BCS model into the CRPA method. The isospin and configuration splittings of the Gamow–Teller giant resonance are analyzed in single-open-shell nuclei. The results obtained for ^{208}Bi, ^{90}Nb, and Sb isotopes are compared with available experimental data.

Novel Solutions to Renormalization-Group Equations for $\alpha(s)$ and $\beta(\alpha)$ in the large-N_c Limit

Yu. A. Simonov

A general solution to renormalization-group equations in the framework of background perturbation theory is written in the large-N_c limit. A simplified (model) approximation to the general solution is suggested that allows one to write $\beta(\alpha)$ and $\alpha(s)$ to any loop order. The resulting $\alpha_B(Q^2)$ coincides asymptotically at large $|Q^2|$ with standard (free) α_s, saturates at small $Q^2 \geq 0$, and has poles at timelike Q^2 in agreement with analytic properties of physical amplitudes in the large-N_c limit.

σ Meson in Hot and Dense Matter

M. K. Volkov, A. E. Radzhabov, and N. L. Russakovich

The important role of the scalar–isoscalar σ meson in low-energy physics is discussed. The behavior of the σ meson in a hot and dense medium is studied. It is shown that, in the vicinity of the critical values of the temperature and the chemical potential, the σ meson can become a sharp resonance. This effect can lead to a strong enhancement of the processes $\pi\pi \to \gamma\gamma$ and $\pi\pi \to \pi\pi$ near the two-pion threshold. Experimental observation of this phenomenon can be interpreted as a signal of approaching the domain where the chiral-symmetry restoration and the phase transition of hadron matter into quark–gluon plasma occur.